ABSTRACT

HAQUE, ARIFUL. Fabrication of Diamond and Q-carbon by Ultrafast Nanosecond Pulsed Laser Processing and Chemical Vapor Deposition for Electron Field Emission and Electrocatalysis Applications. (Under the direction of Dr. Jagdish Narayan and Dr. Mehmet Ozturk).

This study focuses on the understanding of the fabrication of high-quality diamond and Q-carbon nano and microstructures and composites by nanosecond pulsed laser annealing (PLA) and hot filament chemical vapor deposition (HFCVD) techniques and the structural-property correlation of these structures for electron field emission and electrocatalysis applications. The role of several major factors such as surface morphology, microstructure, sp^3/sp^2 ratio, density of states near the Fermi level, and interface and conductivity of these carbon based structures are taken into account to elucidate and study the properties relevant to these applications. This thesis comprises of two major segments, i.e. the first one is on the fabrication, processing, and characterization (experimental study and modeling) of novel diamond microstructures, Q-carbon, and CNT-diamond hybrid structures, and the second one is on the applications of these structures such as the electron field emission (EFE) device application of Q-carbon and the electrocatalysis applications of tubular diamond microstructures with magnificent double layer capacitance owing to its large electroactive surface area for unique microstructures, and enhanced conductivity.

At first, the pseudo-topotactic growth of single-crystal diamond fibers and nanostructures by nanosecond laser melting of amorphous carbon nanofibers (CNFs) and crystalline multi-wall carbon nanotubes (MWCNTs) at ambient temperature and pressure in air is extensively studied. Rapid laser melting through a super undercooled state and subsequent quenching convert the tips of CNFs and MWCNTs into phase-pure <110> nanodiamonds along the growth directions. Subsequent laser pulses melt regions below <110> nanodiamonds that provide seeds for epitaxial growth. By repeating this process, the length of <110> nanodiamond fibers can be increased, as

each pulse results in ~50nm nanodiamond region, depending upon the initial size of CNFs and MWCTs. The simulation results pinpoint the distribution of the optimum energy density for the direct conversion of CNTs into diamond via the formation of liquid carbon and subsequent ultrafast quenching. The nature of C-C bonding characteristics was studied by high-resolution electron-energy-loss spectroscopy to establish the formation of diamond phase by the characteristic peak at 292 eV for sp^3 bonding (σ^*), and absence of 284 eV peak for sp^2 (π^*) graphitic bonding. The characteristic diamond Raman peak at 1332 cm^{-1} is found to downshift to 1321-1324 cm^{-1} because of phonon confinement in nanodiamonds. These nanodiamond structures can be doped with both n- and p-type dopants with concentrations far higher than thermodynamic solubility limit due to solute trapping during quenching from the liquid phase. Thus, these nanodiamond structures provide ideal platform for nanosensing, computing and communication, including efficient field emitting devices. The non-equilibrium PLA technique is also used to fabricate the Q-carbon which is a recently discovered new phase of carbon with 80-85% sp^3 hybridized carbon and having diamond tetrahedra with a very high packing efficiency owing to the ultrafast quenching mediated growth from the liquid phase of carbon. Traditionally the growth of CVD diamond on optically transparent substrates like sapphire (for optoelectronic applications) presents a great challenge because of the large thermal misfit between the film and the substrate, absence of any carbide layer during diamond growth, and low nucleation density during chemical vapor deposition (CVD) growth process. This issue is addressed by using the Q-carbon as an intermediate layer for large-area diamond film deposition on c-sapphire by hot filament chemical vapor deposition (HFCVD). The high-density diamond tetrahedra in Q-carbon acts as the seed for diamond nucleation with a nucleation density of ~10^9-10^{10} cm^{-2} and successively helps growing wafer-scale diamond film on sapphire. A comparative study on the deposition of diamond film on

uncoated sapphire, diamond-like carbon (DLC, grown by pulsed laser deposition) coated sapphire, and Q-carbon coated sapphire substrates by HFCVD was carried out. The results show the growth of large-area diamond thin film on the Q-carbon/sapphire substrate, whereas the depositions of diamond on DLC/sapphire or uncoated sapphire substrates give cluster-like/patches of discontinuous diamond thin film formation with cracks and delamination due to the thermal stress. Molecular vibrational spectroscopy and diffraction studies of the diamond film on Q-carbon/sapphire show a smaller residual stress (1.7 GPa) compared to the diamond on DLC/sapphire (~3.1GPa) or diamond on uncoated sapphire (~3.9GPa) substrates. The calculated non-diamond content in the diamond crystals on Q-carbon coated sapphire is found to be only 0.12%, around 2.5, and 3.5 times better than that of diamond on DLC coated sapphire and uncoated sapphire, respectively. Furthermore, the conductive diamond structures with high surface area are very appealing for various applications but their synthesis presents a great challenge. A simple one-step method for the synthesis of conductive diamond tube with porous tube wall from carbon nanotube (CNT) hollow fiber via pulsed laser annealing and hot filament chemical vapor deposition (HFCVD) is also presented. These diamond tubes exhibit high double layer capacitances of 11.65-18.07 mF cm^{-2}, three orders of magnitudes higher than the equivalent flat diamond films. The number density of diamond, the average size of diamond microspheres, and nanocrystallite content on the microspheres are controlled by HFCVD time and laser annealing parameters of CNT hollow fibers. Considerably improved electrochemical performances of these diamond tubes are explained by their significantly enhanced electroactive surface area and the presence of a very small fraction (0.73%-1.03%) of sp^2 carbon in diamond tubes for electron conduction. This effective method for the synthesis of diamond tubes having large surface area

makes it an ideal candidate for electrochemical applications such as electrocatalysis, electrosynthesis, electroanalysis, energy storage and conversion.

Finally, I have also investigated the room temperature and high temperature (up to 500 K) electric-field enhancement characteristics of the Q-carbon fabricated by the nonequilibrium PLA technique. Under the optimum fabrication conditions, a dense microstructured morphology of Q-carbon composite was obtained, which is important for local electric field enhancement in field-emission device applications. At room temperature the Q-carbon requires only ~2.4V/μm applied electric field to turn-on the EFE. The EFE properties of the Q-carbon composite structure improve with temperature by lowering the turn-on field and increasing the current density. At 500 K we observed a turn-on field of ~ 2.34V/μm, and a maximum current density was found to be ~ 53μA/cm^2 at 2.66V/μm. The mechanism of electron emission from Q-carbon over the temperature range (300K-500K) is explained by the Fowler-Nordheim (F−N) theory, which describes the emission of electrons from the front surface of an emitter via tunneling to a suitable anode. The Q-carbon field emitters also show very stable EFE characteristics (within 7% fluctuations) over time for current intensities between 7.5μA/cm^2 and 47μA/cm^2. Our findings thus hold a great promise for the development of Q-carbon films in applications ranging from field emitters and frictionless motors to heterostructures for novel micro and nano-electronic devices. The essence of this discovery is melting of carbon under highly undercooled state and quenching to convert amorphous quenched carbon, CNT-diamond hybrid, and fabricate diamond microstructures with desirable structural and electronic properties for EFE and electrocatalytic applications which will open new opportunities in the field of electronics and energy applications.

Fabrication of Diamond and Q-carbon by Ultrafast Nanosecond Pulsed Laser Processing and Chemical Vapor Deposition for Electron Field Emission and Electrocatalysis Applications

by
Ariful Haque

A dissertation submitted to the Graduate Faculty of
North Carolina State University
in partial fulfillment of the
requirements for the degree of
Doctor of Philosophy

Materials Science & Engineering and Electrical Engineering

Raleigh, North Carolina
2020

APPROVED BY:

_____	_____
Dr. Jagdish Narayan Committee Co-chair	Dr. Mehmet Ozturk Committee Co-chair
_____	_____
Dr. Claude Reynolds Jr.	Dr. Yuntian Zhu
_____	
Dr. Bongmook Lee	

DEDICATION

To my parents and my lovely wife.

BIOGRAPHY

Ariful Haque was born in Rangpur, Bangladesh. After completing his schooling, Arif went to Dhaka, the capital city of Bangladesh, for a bachelor degree in Electrical and Electronic Engineering (EEE) from the Bangladesh University of Engineering and Technology (BUET). After his bachelor's, he worked as a lecturer in the Electrical Engineering department at Dhaka International University and Primeasia University in Bangladesh for about a year. Then he went to the Missouri State University (MSU) for his Master of Science degree in Materials Science. He completed the MS degree from MSU in 2015 with the highest honor. His MS thesis was on "Investigation of Electrical and Magneto Transport Properties of Reduced Graphene Oxide Thin Films". In 2016, Arif moved to NC State University to work with Professor Jagdish Narayan for his Ph.D. In parallel with the Ph.D. study, he has also completed the Master of Nanoengineering (MNAE) degree from NC State University in 2019 with a concentration in nanoelectronics and nanophotonics.

ACKNOWLEDGMENTS

First of all, I want to express my gratitude to the almighty for presenting me such a wonderful life and the opportunity to learn and live with peace of mind. I also want to thank Him for the blessing to offer me nice and caring parents. My mother Mst. Zabun Nahar and father Md. Nurul Haque made a lot of sacrifice throughout their life to ensure my healthy upbringing, quality life, and best possible education. In this Ph.D. journey, my wife, Sharaf Sumaiya, was always there for me with love, care, and support which helped me to walk on a smooth and hassle-free learning path. My elder sister, Rafia Marzan, and younger brother, Taushiful Haque, both played decisive roles in my early development which prepared me to take this challenging route. I owe my success and well-being to them and their unbridled support, love, and encouragement. My in-laws, Mostofa Zamal and Irin Pervin, have always provided me their love and blessings from the very first day I met them in the Ph.D. life, and their encouragement was a big motivational factor to endure this journey. I would want to mention Nancy Parish and Kent Parish from Springfield, Missouri, who always played a big role in facing the challenges as an align in this country and made me feel home here through their care, support, love, and good wishes.

I want to express my sincere gratitude to my Ph.D. advisor, Professor Jay Narayan, who was very supportive from the very first day of my Ph.D. journey. He has guided, motivated, and supervised me in a methodical way to conduct the ever-challenging experiments throughout the time and always pushed me towards the boundary to attain excellence. It was a big privilege to have such an eminent scientist and professional as a Ph.D. supervisor who achieved so many recognitions, awards, and honors in his career including North Carolina Science Award (highest NC honor), NAE, NAI, NAS, O. Max Gardner Award, and so on.

I want to thank my committee members, Professor Mehmet Ozturk, Professor Lews Renolds Jr., Professor Yuntain Zhu, and Professor Bongmook Lee, all the faculties in Materials Science and Engineering department and Electrical Engineering department who enlightened me with knowledge, training, skills, and technical discussions at different stages of my stay at NC State University. All the staff members in the department, especially Edna Deas and George Myrtle, made the administrative, paperwork, and IT/tool related staffs easy and smooth, and they were always there for assistance when I needed them. The whole journey would not be enjoyable and insightful without the presence of my colleagues and peers like Dr. Ritesh Sachan, Dr. Sudhakar Nori, Dr. Punam Pant, Dr. Srinivasa Rao, Dr. Namik Kemal Temizer, Dr. Anagh Bhaumik, Dr. Adele Moatti, Mr. Siddharth Gupta, Mr. Pratik Joshi, Miss Sanchali Das, Dr. Abdelrahman Zkria from Kyushu University, and Dr. Yanming Liu from Dalian University of Technology. I am truly indebted to NC State University to offer me such a nice in-class and out of the class learning environment, state of the art facilities like Analytical Instrument Facilities (AIF), and all other supports which helped me to achieve my research and academic goals with a joyful mind. I want to thank the lab managers in the AIF, including Charles Mooney, Roberto Garcia, Fred Anderson, Elaine Zhou, and Toby Tung, who trained and helped me in learning different instruments during the Ph.D. journey. I also want to acknowledge the National Science Foundation for supporting me with the research assistantship, DMR-1735695.

TABLE OF CONTENTS

LIST OF TABLES

LIST OF FIGURES

1. Introduction

Carbon is one of the most prospective and versatile elements on earth with many allotropes owing to the fact that it can exist in linear (sp), trigonal (sp^2), and tetrahedral (sp^3) coordination systems in nature[1]. It is the sixth most abundant material on earth, which holds numerous promises from modern technological applications viewpoint ranging from deep sea drilling to micro and nano-electronics, and quantum computing and nanosensing [2–4]. Besides drilling and cutting carbon-based materials, such as diamond, carbon nanotube, and Q-carbon, have excellent prospects and a wide variety of applications in the field of electron field emission, high-power devices, harsh environment electronics, electrocatalysis etc owing to its unique band-structures, outstanding charge carrier mobility, high thermal conductivity, excellent structural stability, and highest number density of atoms in the form of diamond and Q-carbon [5–8]. However, one of the major drawbacks of these materials and their hybrids for practical applications is the complex fabrication processes with limited yield and lower quality using conventional routes. These are metastable materials, which require high-temperature and high-pressure processing for phase stability. The transformation of one phase of carbon to another is of immense scientific interest with profound technological impact. Recent successes in the synthesis and conversion of new forms of carbon, i.e., Q-carbon [9], the quenchable transparent liquid phase of carbon [10], single crystal phase pure diamond nano and microstructures via nonequilibrium routes etc, have drawn significant experimental and theoretical interest for a variety of applications. The conversion of one carbon phase to another using the nonequilibrium route is the most feasible way to fabricate these metastable phases of carbon. Except graphite, the other thermodynamically metastable forms of carbon exist in nature due to the strong carbon-carbon bonding strength. From the phase diagram of carbon, it is evident that diamond is the stable phase beyond 17 GPa at room temperature,

although it is stable under ambient conditions once it is formed [11]. A substantially large activation energy barrier of more than 0.8 eV must be overcome or bypass to transform back from sp^3-bonding states to graphitic states. From the Clausius-Clapeyron equation, thermodynamically very high-temperature and high-pressure environments are required for the transformation of carbon phase into diamond or other metastable phases of carbon [11].

In this study, a novel nonequilibrium pulsed laser annealing (PLA) technique is used to convert thermodynamically stable phases of carbon, i.e. graphitic carbon/carbon nanotube (CNT)/amorphous carbon nanofiber (CNF), into metastable phases like diamond and Q-carbon with improved functionalities and quality. The atomic spacing of carbon nanotubes and diamond are 0.2468 nm [12] and 0.2522 nm (in (1 0 0) plane), respectively, with only 2.5% incompatibility. Thus the transformation of CNTs to diamond is thought to be even easier compared to that from other forms of carbon during the pulsed laser induced melting and subsequent quenching process. Careful selection of the laser parameters is very important for irradiating CNTs to convert into diamond. Earlier researchers have observed an increased realignment of the thin CNTs with an increase of the laser energy density [13]. Studies also reported that high energy pulsed laser heating would lead to an apparent growth process of additional small diameter CNTs. The use of excessive energy density (over 1.5 J/cm^2) results in the broken or blown off CNTs due to overheating and ablation effect [13]. Researchers have also used laser irradiation treatment of aligned CNTs to produce clean and uniform surfaces [14]. Further increase in the energy density produced too high of a temperature resulting in the burning/etching/ablation and trimming of the aligned CNTs. The final temperature determines the undercooling and quenching rate during pulsed laser annealing, which has been controlled by the selection of optimum laser parameters. Hence the direct conversion of CNTs and CNFs into diamond is only possible by the proper understanding of the

kinetics and thermodynamics. Upon irradiating the CNTs/CNFs with nanosecond pulsed laser at a suitable energy density, the tips and bends of the structures can be melted in a highly undercooled state (due to the geometry constraint of the temperature distribution and 1D heat flow). The highly undercooled state of carbon is a metastable phase and nanodiamonds nucleation will occur from this state. The whole process (rapid melting, solidification, and growth) takes place in less than 200-250 ns [15]. Therefore such a highly nonequilibrium phase transformation is ideal for the formation of single-crystal diamond and this single-crystal diamond can be doped with dopants of both p and n-types at doping concentration far greater than the thermodynamic solubility limit owing to the liquid phase mediated growth.

On the other hand, the interest on the deposition of large-area diamond thin film on a suitable optically transparent substrate like Al_2O_3 has enormously increased owing to the fact that most of the attractive diamond properties, such as the wide bandgap, optical transparency, and high thermal conductivity, could be utilized for different applications only when it is in the form of a continuous large area thin film on such kind of a substrate. Synthesis of adequate quality diamonds on optically transparent substrates like single-crystal Al_2O_3 is quite challenging because of the thermal mismatch, poor adhesion, low nucleation density, and substantial lattice mismatch. On the basis of carbon-substrate interactions during the CVD process, the substrate materials used for diamond deposition can be classified into three major groups, i.e. materials showing (i) little or no carbon reaction or solubility with the substrate, (ii) weak carbide formation, and (iii) strong carbide formation. Sapphire is very stable and has no carbon solubility and it also does not react with carbon to form a carbide layer to improve the adhesion. The difference in the coefficient of thermal expansion between diamond and sapphire is very large (at room temperature, $\alpha_{\text{diamond}} \sim 1 \times 10^{-6}$ K^{-1}, $\alpha_{\text{sapphire}} \sim 6 \times 10^{-6}$ K^{-1}). This leads to a large residual compressive stress in the diamond thin

film upon cooling. The highly anisotropic stresses in diamond film can be identified by the split of the signature Raman peak of diamond with a pronounced upshift [16]. Researchers have observed peak splitting at 1332.7 and 1348 cm^{-1} due to very high residual stress which ultimately leads to the delamination of the continuous diamond film.

Due to complex nucleation, adhesion, and stress-related issues, the deposition of diamond on sapphire by the CVD technique is relatively difficult compared to the growth of diamond on carbide forming substrates. Because of the non-carbide forming affinity of sapphire during CVD diamond nucleation and growth, researchers have observed dispersed clusters of diamond film on the uncoated substrate after long growth times [17]. The nucleation density of diamonds on a smooth sapphire surface without any conditioning/roughening/pretreatment is only about 10^4 cm^{-2} which results in scattered isolated individual diamond clusters on the substrate [18]. Due to the dissociation of the methane and the addition of excess gaseous hydrogen into the gas mixture in HFCVD, the plasma gas at the substrate interface is likely to have a high concentration of hydrogen. The availability of excess hydrogen at the surface could enhance the diamond formation and suppress the formation of graphite phase and can provide a higher concentration of active sites for diamond nucleation. However, this technique has also been proven futile for large area diamond deposition on smooth sapphire substrates. Researchers have also observed a compressive stress of ~3.7 GPa, even grown at low temperatures (525 ^{0}C) in their studies [19]. This amount of stress is enough to cause the delamination of the diamond film. Coating the substrate surface with graphite [20], amorphous carbon [20,21], diamond-like carbon [22–24], C60, and mechanical oil [25] have also been employed by other researchers to enhance diamond nucleation. However, these coatings are responsible for the formation of a graphitic interlayer in-between the diamond film and the substrate, causing a poor adhesion. Although roughening the substrate surface with an abrasive

powder has been the most commonly used method, which prone to enhance contamination. From the experimental studies, we have shown that diamond nucleation can be promoted by the deposition of a thin layer of PLD grown DLC on uncoated sapphire. Although the obtained yield of diamond on DLC coated sapphire has been improved, however, this interlayer cannot provide a sufficient amount of nucleation sites to produce continuous diamond thin films. The dispersed morphology of diamond on sapphire is achieved when diamond nucleation is sparse and confined to a very few sites on the substrate (sapphire in this experiment). On the other hand, enhanced nucleation is obtained under the presence of a DLC interlayer [26]. Hence, the nucleation density is increased when the DLC layer is introduced where the film adhesion is quite poor. Last but not least, we have observed the deposition of a large area continuous diamond film when the Q-carbon layer was introduced on the c-sapphire substrate. The highly packed diamond tetrahedra present in the Q-carbon helps to dramatically enhance the nucleation density which is one of the major findings of this study [27].

Over the years, scientists have also been trying to develop a reliable method to pattern diamond on different mirror polished single-crystal substrates as a lot of microelectronic applications require patterned polycrystalline diamond thin films on suitable substrates [28]. At present different techniques such as plasma etching, chemical etching, selective growth etc. are used for patterning of diamond thin film. However, all of these techniques have their own limitations. Diamond is very inert to the chemical solutions; therefore, it is very difficult to pattern diamond by chemical etching. Moreover, finding a suitable masking material for diamond etching, which can withstand the highly corrosive/erosive solution, is also difficult. On the other hand, reactive ion etching of diamond with oxygen results in poor etching efficiency. A solution to this problem could be the utilization of patterned Q-carbon on sapphire as a substrate. In addition, Q-carbon

provides a strong adhesion as Q-carbon formed at the melting improves interfacial adhesion The patterned Q-carbon with suitable size and shape can be fabricated on sapphire using selective area pulsed laser annealing by utilizing a suitable optical system and shadow masking. Thus the patterned diamond can easily be grown on the substrate in this process for the electronic applications. We have shown a sharp diamond interface between the Q-carbon coated and the uncoated regions on sapphire. All in all, advances have been made by using the Q-carbon coating on sapphire in this study, which addresses the stringent requirements of coping up with huge thermal expansion mismatch, ensuring strength and mechanical integrity, patterning related issues while maintaining the sapphire properties unaffected.

The unique properties of diamond make it a promising material for a variety of applications such as optics, electronic devices, tribology, thermal management, biomedicine, sensor, (photo-, electro-) catalysis [29–34]. To realize its wide-ranging applications, a simple and low-cost method for the synthesis of high-quality diamond is highly desirable. As different diamond structures are favorable for different applications, steering diamond structures is an effective method to adjust their properties and improve their respective performances. For example, diamond twins show higher hardness than single crystals [35]; a continuous diamond film covering the entire substrate is required for electrochemical applications [36,37]; diamond structures with high surface areas and exposed sites can enhance its performance in sensor and catalysis applications [38,39]. The equilibrium methods of direct conversion of carbon into diamond require very high-temperature (~5000K) and pressure (~12 GPa) in the form of diamond particles with a limited yield. For the synthesis of diamond coatings, chemical vapor deposition (CVD) integrated with hot-filament, microwave, and radio frequency plasma are used, where nano/micro-diamond seeds sprinkled on substrates are often used for diamond nucleation [40,41]. However, diamond is formed with low

yield due to limited diamond nucleation and growth rates in addition to poor adhesion. Considerable efforts have been made to enhance diamond nucleation and growth. Nonequilibrium methods for direct conversion of graphitic/amorphous carbon into nanodiamond include shock-wave [42], spark plasma sintering [43], ballistic fracturing [44], and laser annealing [45–47]. The direct conversion of carbon nanofibers/nanotubes into nanodiamonds by nanosecond laser annealing is already achieved in this study [48,49]. The formed nanodiamonds provide effective nucleation sites to facilitate high-quality diamond film growth by HFCVD. The most common approach for preparing novel structured diamond is diamond growth on templates or reactive ion/plasma etching of planar diamond films. Porous diamond structures were obtained by diamond growth on the conductive polymer, SiO_2 spheres, and SiC [50–52], followed by chemical etching of the templates. Diamond nano-/microwires/rods/channels were synthesized with Si and carbon nanotubes as templates [53–56]. Meanwhile, reactive ion/plasma etching of planar diamond films was found to be effective for diamond nano-/microwires/cones/glasses preparation [57,58]. The major obstacles limiting the preparation of various diamond structures of high quality are the complicated processes of these methods and low yield.

In this study, we report a promising strategy to synthesize novel structured diamond with high quality from amorphous and graphitic carbon materials via HFCVD. Carbon microfibers, porous carbon, and carbon nanotube hollow fibers are used as nucleation seeds to promote diamond growth. By using different carbon precursors and controlling the pulses of laser annealing carbon precursors, we have successfully prepared diamonds with various microstructures, including diamond microfibers and diamond microspheres consisted of fivefold twinned microcrystallites, phase pure diamond film and diamond tube with porous tube wall. Nanosecond pulsed laser annealing is effectively used to facilitate diamond growth and control the diamond morphology.

The method we followed for novel structured diamond preparation is simple and cost-effective, which overcomes the complicated and time-consuming processes of commonly used methods, and increases the diamond nucleation and growth rates.

Diamond materials with high surface areas, porous structure and good conductivity are highly desirable for various electrochemical applications, which can provide plenty of exposed active sites, fast mass transfer, and rapid electron transfer rates for redox systems, leading to enhanced electrochemical performance[59,60]. The most common studied diamond structure is flat diamond film consisted of microcrystallites and nanocrystallites on silicon or metal substrates. Many efforts have been made to synthesize diamond materials with increased surface areas and/or porous structures, including diamond foam (also called network or porous diamond) with pore size ranging from nanometers to micrometers, nano-/microwires (also called rods, needles), cones, grasses etc [61]. Diamond foam has been prepared by depositing diamond film on SiO_2 template and removing the template by chemical etching [62,63], and diamond films have been grown homoepitaxially on porous polymer and SiC to obtain composite materials [64,65]. Diamond nano-/microwires and cones are usually synthesized by top-down and bottom-up methods. In a top-down method, diamond nano/micro-structure is obtained by reactive ion etching or plasma etching of diamond flat films with etching masks [66,67]. The gases used for etching are oxygen/tetrafluoromethane, argon/hydrogen, and oxygen. The structures of the as-prepared diamond are dependent upon the masks, etching conditions, initial morphologies, and microstructures of diamond films. In a bottom-up technique, diamond nano-/microwires and cones are prepared from depositing diamond crystallites on templates such as Si nanowires/microrods [68,69], where the morphology of templates determines the characteristic of as-prepared structures. During these deposition processes, doping has been prove to be effective for enhancing

diamond conductivity [69,70]. Moreover, these methods are complicated, time consuming, and cumbersome with low yield. Thus simple, template-free methods with low-cost and high-throughput are needed for conductive diamond synthesis. An alternative method for nano-/micro-structured diamond preparation is the conversion of graphitic carbon materials [71,72] which can avoid the complicated etching process and the use of expensive templates/masks. We studied a simple and cost-effective technique for the synthesis of three-dimensional structured diamond tube with porous tube wall from CNT hollow fibers PLA and HFCVD. The PLA treated CNTs can provide nucleation sites to accelerate diamond growth. The optimum amount of residual unconverted carbon at the interfaces of diamond tubes endows them with desired electrical conductivity for electron transfer [73,74]. The effects of HFCVD time and PLA on diamond tube growth and its electrochemical performance were investigated. Double layer capacitance measurements demonstrated that these diamond tubes have significantly enhanced electroactive surface area compared with the equivalent flat diamond films.

Electrons from the surface of a solid can be emitted into the vacuum by different processes such as thermal excitation known as thermionic emission [75], photonic excitation known as photoemission, lowering the work function and tuning the electron affinity [76], or applying sufficient voltage for field emission which is also known as cold cathode field emission. The cold cathode field emitters can potentially emit high-density electrons at room temperature under suitable vacuum conditions. On the other hand, most of the conventionally used electron emitters emit electrons into vacuum utilizing the thermionic emission mechanism. However, the thermionic emitters demonstrate several disadvantages which include poor efficiency, instability in the emission current density, low lifetime of the emitters, and produce heat, resulting in raising the temperature of the surrounding devices. Therefore, field emitters are desirable for different state-

of-the-art applications, such as flat panel displays [77,78], lamps [79], gas discharge tubes [80], and x-ray [81] and microwave generators, due to the possibility of obtaining large emission current density at comparatively low applied electric fields, better stability and durability, longer lifetime of the cathode, and low fabrication cost. Over the last few decades, tremendous efforts have been devoted to investigate electron field emission properties of different materials. Nevertheless, due to different structural, morphological, and electronic property related limitations, most of the conventional electron field emitters do not concurrently demonstrate all of the characteristics mentioned above which are required for the realization of practical electronic devices, displays, and sensors. Under the circumstances, the carbon-based field emitters are playing a leading role in reviving attention to field emission technologies since last two decades due to their exceptional electron emitting properties coupled with negative electron affinity (NEA) or very low positive electron affinity [82–85]. Many of the carbon-based materials possess a tunable bandgap characteristic, excellent thermal conductivity, high atomic density, high carrier mobility, in most of the cases good electrical conductivity, the remarkable chemical stability and biocompatibility, and very high Young's modulus [86–88]. Therefore, for several decades, these carbon-based field emitters with different size, shape, aspect ratio, hybrid- nanostructures, and dopant types and doping concentrations have been studied extensively for field emission applications [89–92]. The electric fields required for electron emission from most of the carbon-based field emitters are considerably lower than those required for emission from Si, Ge, GaAs, or metal surfaces [93–96]. Moreover, carbon-based systems can sustain exceptionally large electric fields because of their high breakdown voltage, on the order of 1000 V/μm [97]. Therefore this class of materials is considered as the most promising next-generation materials for a wide range of potential applications, especially in construction of the high-performance field emission devices. Thus, the

intriguing properties of Q-carbon arising from its unique structural, optical, magnetic, electronic, and mechanical properties have given rise to numerous fundamental and applied areas of research [98]. Promising applications ranging from superhard composite coatings, novel micro- and nano-electronic devices, atomic sensors and biomarkers, spintronic devices, nonvolatile memory, superconducting magnetic resonance imaging (MRI) and nuclear magnetic resonance (NMR) devices and field emission (FE) devices are feasible after the discovery of this new phase of carbon [98–100]. Among these possibilities, the fabrication of practical FE devices is the most foreseeable one in the near future. Although there has been tremendous interest in cold cathode field emission from carbon materials ranging from diamond [101], diamond-like-carbon [102], vertically aligned carbon nanotubes [103], and amorphous carbon structures [104], electron emission from Q-carbon created immense interests in this field due to its outstanding structural, electronic, and mechanical properties coupled with the simple and large-scale fabrication capability on rigid to flexible substrates such as tungsten carbide, steel, sapphire, plastic, and glass [105,106].

In comparing and analyzing the emission properties, it is implied that new type of field emitters (Q-carbon) have the most promising characteristics for advanced applications. Therefore, the last segment of this thesis focuses on attractive emission-related properties of Q-carbon field emitters. The Q-carbon field emitters not only provide more electrically conductive channels for electron transport and tunneling but also exhibit high field enhancement factor with lower work function, weaker screen effect of the neighboring emitters and high density of emission sites. Therefore, the Q-carbon field emitters show a very low emission threshold field, a high emission current density, long-term stability, and reproducible performances. A comprehensive study on the emission characteristics and mechanism of Q-carbon field emitter is conducted for our

comprehensive understanding and further improvements in the next generation carbon-based field emission devices.

References

[1] E.H. Falcao, F. Wudl, Carbon allotropes: beyond graphite and diamond, J. Chem. Technol. Biotechnol. 82 (2007) 524–531. https://doi.org/10.1002/jctb.1693.

[2] B. Li, L. Li, B. Wang, C.Y. Li, Alternating patterns on single-walled carbon nanotubes, Nat. Nanotechnol. 4 (2009) 358–362. https://doi.org/10.1038/nnano.2009.91.

[3] K. Tsukagoshi, N. Yoneya, S. Uryu, Y. Aoyagi, A. Kanda, Y. Ootuka, B.W. Alphenaar, Carbon nanotube devices for nanoelectronics, Phys. B Condens. Matter. 323 (2002) 107–114. https://doi.org/10.1016/S0921-4526(02)00993-6.

[4] M. Freitag, Nanoelectronics goes flat out, Nat. Nanotechnol. 3 (2008) 455–457. https://doi.org/10.1038/nnano.2008.219.

[5] A. Mainwood, Recent developments of diamond detectors for particles and UV radiation, Semicond. Sci. Technol. 15 (2000) R55–R63. https://doi.org/10.1088/0268-1242/15/9/201.

[6] Y. Wu, Y. Lin, A.A. Bol, K.A. Jenkins, F. Xia, D.B. Farmer, Y. Zhu, P. Avouris, High-frequency, scaled graphene transistors on diamond-like carbon, Nature. 472 (2011) 74–78. https://doi.org/10.1038/nature09979.

[7] C.J.H. Wort, R.S. Balmer, Diamond as an electronic material, Mater. Today. 11 (2008) 22–28. https://doi.org/10.1016/S1369-7021(07)70349-8.

[8] A. Haque, J. Narayan, Stability of electron field emission in Q-carbon, MRS Commun. 8 (2018) 1343–1351. https://doi.org/10.1557/mrc.2018.172.

[9] J. Narayan, A. Bhaumik, S. Gupta, A. Haque, R. Sachan, Progress in Q-carbon and related materials with extraordinary properties, Mater. Res. Lett. 6 (2018) 353–364. https://doi.org/10.1080/21663831.2018.1458753.

[10] E.D. Miller, D.C. Nesting, J.V. Badding, Quenchable Transparent Phase of Carbon, Chem. Mater. 9 (1997) 18–22. https://doi.org/10.1021/cm960288k.

[11] A. Reza Kamali, D. J. Fray, Preparation of nanodiamonds from carbon nanoparticles at atmospheric pressure, Chem. Commun. 51 (2015) 5594–5597. https://doi.org/10.1039/C5CC00233H.

[12] S. Iijima, T. Ichihashi, Single-shell carbon nanotubes of 1-nm diameter, Nature. 363 (1993) 603–605. https://doi.org/10.1038/363603a0.

[13] T. Nakamiya, S. Aoqui, K. Ebihara, Experimental and numerical study on pulsed-laser annealing process of diamond-like carbon thin films, Diam. Relat. Mater. 10 (2001) 905–909. https://doi.org/10.1016/S0925-9635(00)00536-7.

[14] T. Nakamiya, T. Ueda, T. Ikegami, K. Ebihara, R. Tsuda, Thermal analysis of carbon nanotube film irradiated by a pulsed laser, Curr. Appl. Phys. 8 (2008) 400–403. https://doi.org/10.1016/j.cap.2007.10.056.

[15]A. Haque, R. Sachan, J. Narayan, Synthesis of diamond nanostructures from carbon nanotube and formation of diamond-CNT hybrid structures, Carbon. 150 (2019) 388–395. https://doi.org/10.1016/j.carbon.2019.05.027.

[16] M.C. Rossi, S. Salvatori, F. Galluzzi, Surface Distribution of Stress State and Diamond Phases in [100] Oriented Diamond Films, Phys. Status Solidi A. 172 (1999) 97–103. https://doi.org/10.1002/(SICI)1521-396X(199903)172:1<97::AID-PSSA97>3.0.CO;2-K.

[17] R.K. Singh, D.R. Gilbert, J. Laveigne, Growth of adherent diamond films on optically transparent sapphire substrates, Appl. Phys. Lett. 69 (1996) 2181–2183. https://doi.org/10.1063/1.117158.

[18] O. Ternyak, R. Akhvlediani, A. Hoffman, Study on diamond films with ultra high nucleation density deposited onto alumina, sapphire and quartz, Diam. Relat. Mater. 14 (2005) 323–327. https://doi.org/10.1016/j.diamond.2004.10.033.

[19] R.K. Singh, D.R. Gilbert, J. Laveigne, Growth of adherent diamond films on optically transparent sapphire substrates, Appl. Phys. Lett. 69 (1996) 2181–2183. https://doi.org/10.1063/1.117158.

[20] V.V.S.S. Srikanth, Review of advances in diamond thin film synthesis, Proc. Inst. Mech. Eng. Part C J. Mech. Eng. Sci. 226 (2012) 303–318. https://doi.org/10.1177/0954406211422788.

[21] A.A. Morrish, P.E. Pehrsson, Effects of surface pretreatments on nucleation and growth of diamond films on a variety of substrates, Appl. Phys. Lett. 59 (1991) 417–419. https://doi.org/10.1063/1.105448.

[22] J. Singh, M. Vellaikal, Nucleation of diamond during hot filament chemical vapor deposition, J. Appl. Phys. 73 (1993) 2831–2834. https://doi.org/10.1063/1.353034.

[23] K.V. Ravi, C.A. Koch, H.S. Hu, A. Joshi, The nucleation and morphology of diamond crystals and films synthesized by the combustion flame technique, J. Mater. Res. 5 (1990) 2356–2366. https://doi.org/10.1557/JMR.1990.2356.

[24] K.V. Ravi, C.A. Koch, Nucleation enhancement of diamond synthesized by combustion flame techniques, Appl. Phys. Lett. 57 (1990) 348–350. https://doi.org/10.1063/1.103688.

[25] S. Yugo, T. Kanai, T. Kimura, T. Muto, Generation of diamond nuclei by electric field in plasma chemical vapor deposition, Appl. Phys. Lett. 58 (1991) 1036–1038. https://doi.org/10.1063/1.104415.

[26] K.V. Ravi, C.A. Koch, H.S. Hu, A. Joshi, The nucleation and morphology of diamond crystals and films synthesized by the combustion flame technique, J. Mater. Res. 5 (1990) 2356–2366. https://doi.org/10.1557/JMR.1990.2356.

[27] A. Haque, P. Pant, J. Narayan, Large-area diamond thin film on Q-carbon coated crystalline sapphire by HFCVD, J. Cryst. Growth. 504 (2018) 17–25. https://doi.org/10.1016/j.jcrysgro.2018.09.036.

[28] R. Ramesham, C. Ellis, Selective growth of diamond crystals on the apex of silicon pyramids, J. Mater. Res. 7 (1992) 1189–1194. https://doi.org/10.1557/JMR.1992.1189.

[29] A. Sipahigil, R.E. Evans, D.D. Sukachev, M.J. Burek, J. Borregaard, M.K. Bhaskar, C.T. Nguyen, J.L. Pacheco, H.A. Atikian, C. Meuwly, R.M. Camacho, F. Jelezko, E. Bielejec, H. Park, M. Lončar, M.D. Lukin, An integrated diamond nanophotonics platform for quantum-optical networks, Science. 354 (2016) 847–850. https://doi.org/10.1126/science.aah6875.

[30] P. Maletinsky, S. Hong, M.S. Grinolds, B. Hausmann, M.D. Lukin, R.L. Walsworth, M. Loncar, A. Yacoby, A robust scanning diamond sensor for nanoscale imaging with single nitrogen-vacancy centres, Nat. Nanotechnol. 7 (2012) 320–324. https://doi.org/10.1038/nnano.2012.50.

[31] N. Yang, S. Yu, J. V. Macpherson, Y. Einaga, H. Zhao, G. Zhao, G. M. Swain, X. Jiang, Conductive diamond: synthesis, properties, and electrochemical applications, Chem. Soc. Rev. 48 (2019) 157–204. https://doi.org/10.1039/C7CS00757D.

[32] N. Wächter, C. Munson, R. Jarošová, I. Berkun, T. Hogan, R.C. Rocha-Filho, G.M. Swain, Structure, Electronic Properties, and Electrochemical Behavior of a Boron-Doped Diamond/Quartz Optically Transparent Electrode, ACS Appl. Mater. Interfaces. 8 (2016) 28325–28337. https://doi.org/10.1021/acsami.6b02467.

[33] T. Sun, F.A.M. Koeck, C. Zhu, R.J. Nemanich, Combined visible light photo-emission and low temperature thermionic emission from nitrogen doped diamond films, Appl. Phys. Lett. 99 (2011) 202101. https://doi.org/10.1063/1.3658638.

[34] E. Abubakr, A. Zkria, Y. Katamune, S. Ohmagari, K. Imokawa, H. Ikenoue, T. Yoshitake, Formation of low resistivity layers on singlecrystalline diamond by excimer laser irradiation, Diam. Relat. Mater. 95 (2019) 166–173. https://doi.org/10.1016/j.diamond.2019.04.013.

[35] Q. Huang, D. Yu, B. Xu, W. Hu, Y. Ma, Y. Wang, Z. Zhao, B. Wen, J. He, Z. Liu, Y. Tian, Nanotwinned diamond with unprecedented hardness and stability, Nature. 510 (2014) 250–253. https://doi.org/10.1038/nature13381.

[36] C.A. Martínez-Huitle, M.A. Rodrigo, I. Sirés, O. Scialdone, Single and Coupled Electrochemical Processes and Reactors for the Abatement of Organic Water Pollutants: A Critical Review, Chem. Rev. 115 (2015) 13362–13407. https://doi.org/10.1021/acs.chemrev.5b00361.

[37] Y. Liu, Y. Zhang, K. Cheng, X. Quan, X. Fan, Y. Su, S. Chen, H. Zhao, Y. Zhang, H. Yu, M.R. Hoffmann, Selective Electrochemical Reduction of Carbon Dioxide to Ethanol on a Boron- and Nitrogen-Co-doped Nanodiamond, Angew. Chem. Int. Ed. 56 (2017) 15607–15611. https://doi.org/10.1002/anie.201706311.

[38] D. Luo, L. Wu, J. Zhi, Fabrication of Boron-Doped Diamond Nanorod Forest Electrodes and Their Application in Nonenzymatic Amperometric Glucose Biosensing, ACS Nano. 3 (2009) 2121–2128. https://doi.org/10.1021/nn9003154.

[39] T.A. Silva, H. Zanin, Paul.W. May, E.J. Corat, O. Fatibello-Filho, Electrochemical Performance of Porous Diamond-like Carbon Electrodes for Sensing Hormones,

Neurotransmitters, and Endocrine Disruptors, ACS Appl. Mater. Interfaces. 6 (2014) 21086–21092. https://doi.org/10.1021/am505928j.

[40] D. Das, R.N. Singh, A review of nucleation, growth and low temperature synthesis of diamond thin films, Int. Mater. Rev. 52 (2007) 29–64. https://doi.org/10.1179/174328007X160245.

[41] J.J. Gracio, Q.H. Fan, J.C. Madaleno, Diamond growth by chemical vapour deposition, J. Phys. Appl. Phys. 43 (2010) 374017. https://doi.org/10.1088/0022-3727/43/37/374017.

[42] O.A. Shenderova, I.I. Vlasov, S. Turner, G. Van Tendeloo, S.B. Orlinskii, A.A. Shiryaev, A.A. Khomich, S.N. Sulyanov, F. Jelezko, J. Wrachtrup, Nitrogen Control in Nanodiamond Produced by Detonation Shock-Wave-Assisted Synthesis, J. Phys. Chem. C. 115 (2011) 14014–14024. https://doi.org/10.1021/jp202057q.

[43] F. Zhang, J. Shen, J. Sun, Y.Q. Zhu, G. Wang, G. McCartney, Conversion of carbon nanotubes to diamond by spark plasma sintering, Carbon. 43 (2005) 1254–1258. https://doi.org/10.1016/j.carbon.2004.12.019.

[44] S. Ozden, L.D. Machado, C. Tiwary, P.A.S. Autreto, R. Vajtai, E.V. Barrera, D.S. Galvao, P.M. Ajayan, Ballistic Fracturing of Carbon Nanotubes, ACS Appl. Mater. Interfaces. 8 (2016) 24819–24825. https://doi.org/10.1021/acsami.6b07547.

[45] L. Zhu, M. Yao, J. Dong, K. Hu, R. Liu, C. Gong, Y. Wang, B. Liu, Direct Conversion of Graphene Aerogel into Low-Density Diamond Aerogel Composed of Ultrasmall Nanocrystals, J. Phys. Chem. C. 122 (2018) 13193–13198. https://doi.org/10.1021/acs.jpcc.8b03809.

[46] J. Narayan, A. Bhaumik, S. Gupta, A. Haque, R. Sachan, Progress in Q-carbon and related materials with extraordinary properties, Mater. Res. Lett. 6 (2018) 353–364. https://doi.org/10.1080/21663831.2018.1458753.

[47] R. Ye, X. Han, D.V. Kosynkin, Y. Li, C. Zhang, B. Jiang, A.A. Martí, J.M. Tour, Laser-Induced Conversion of Teflon into Fluorinated Nanodiamonds or Fluorinated Graphene, ACS Nano. 12 (2018) 1083–1088. https://doi.org/10.1021/acsnano.7b05877.

[48] A. Haque, R. Sachan, J. Narayan, Synthesis of diamond nanostructures from carbon nanotube and formation of diamond-CNT hybrid structures, Carbon. 150 (2019) 388–395. https://doi.org/10.1016/j.carbon.2019.05.027.

[49] J. Narayan, A. Bhaumik, R. Sachan, A. Haque, S. Gupta, P. Pant, Direct conversion of carbon nanofibers and nanotubes into diamond nanofibers and the subsequent growth of large-sized diamonds, Nanoscale. 11 (2019) 2238–2248. https://doi.org/10.1039/C8NR08823C.

[50] F. Gao, M.T. Wolfer, C.E. Nebel, Highly porous diamond foam as a thin-film micro-supercapacitor material, Carbon. 80 (2014) 833–840. https://doi.org/10.1016/j.carbon.2014.09.007.

[51] C. Hébert, E. Scorsone, M. Mermoux, P. Bergonzo, Porous diamond with high electrochemical performance, Carbon. 90 (2015) 102–109. https://doi.org/10.1016/j.carbon.2015.04.016.

[52] H. Zhuang, N. Yang, H. Fu, L. Zhang, C. Wang, N. Huang, X. Jiang, Diamond Network: Template-Free Fabrication and Properties, ACS Appl. Mater. Interfaces. 7 (2015) 5384–5390. https://doi.org/10.1021/am508851r.

[53] M. Chandran, S. Elfimchev, S. Michaelson, R. Akhvlediani, O. Ternyak, A. Hoffman, Fabrication of microchannels in polycrystalline diamond using pre-fabricated Si substrates, J. Appl. Phys. 122 (2017) 145303. https://doi.org/10.1063/1.5006608.

[54] C. Hébert, J.P. Mazellier, E. Scorsone, M. Mermoux, P. Bergonzo, Boosting the electrochemical properties of diamond electrodes using carbon nanotube scaffolds, Carbon. 71 (2014) 27–33. https://doi.org/10.1016/j.carbon.2013.12.083.

[55] H. Zanin, P.W. May, D.J. Fermin, D. Plana, S.M.C. Vieira, W.I. Milne, E.J. Corat, Porous Boron-Doped Diamond/Carbon Nanotube Electrodes, ACS Appl. Mater. Interfaces. 6 (2014) 990–995. https://doi.org/10.1021/am4044344.

[56] Y. Liu, S. Chen, X. Quan, H. Yu, Efficient Electrochemical Reduction of Carbon Dioxide to Acetate on Nitrogen-Doped Nanodiamond, J. Am. Chem. Soc. 137 (2015) 11631–11636. https://doi.org/10.1021/jacs.5b02975.

[57] S. Kunuku, K.J. Sankaran, C.-Y. Tsai, W.-H. Chang, N.-H. Tai, K.-C. Leou, I.-N. Lin, Investigations on Diamond Nanostructuring of Different Morphologies by the Reactive-Ion Etching Process and Their Potential Applications, ACS Appl. Mater. Interfaces. 5 (2013) 7439–7449. https://doi.org/10.1021/am401753h.

[58] C. Terashima, K. Arihara, S. Okazaki, T. Shichi, D.A. Tryk, T. Shirafuji, N. Saito, O. Takai, A. Fujishima, Fabrication of Vertically Aligned Diamond Whiskers from Highly Boron-Doped Diamond by Oxygen Plasma Etching, ACS Appl. Mater. Interfaces. 3 (2011) 177–182. https://doi.org/10.1021/am1007722.

[59] N. Yang, J.S. Foord, X. Jiang, Diamond electrochemistry at the nanoscale: A review, Carbon. 99 (2016) 90–110. https://doi.org/10.1016/j.carbon.2015.11.061.

[60] N. Wächter, C. Munson, R. Jarošová, I. Berkun, T. Hogan, R.C. Rocha-Filho, G.M. Swain, Structure, Electronic Properties, and Electrochemical Behavior of a Boron-Doped Diamond/Quartz Optically Transparent Electrode, ACS Appl. Mater. Interfaces. 8 (2016) 28325–28337. https://doi.org/10.1021/acsami.6b02467.

[61] K.D. Behler, A. Stravato, V. Mochalin, G. Korneva, G. Yushin, Y. Gogotsi, Nanodiamond-Polymer Composite Fibers and Coatings, ACS Nano. 3 (2009) 363–369. https://doi.org/10.1021/nn800445z.

[62] F. Gao, M.T. Wolfer, C.E. Nebel, Highly porous diamond foam as a thin-film micro-supercapacitor material, Carbon. 80 (2014) 833–840. https://doi.org/10.1016/j.carbon.2014.09.007.

[63] H. Kato, J. Hees, R. Hoffmann, M. Wolfer, N. Yang, S. Yamasaki, C.E. Nebel, Diamond foam electrodes for electrochemical applications, Electrochem. Commun. 33 (2013) 88–91. https://doi.org/10.1016/j.elecom.2013.04.028.

[64] H. Zhuang, N. Yang, H. Fu, L. Zhang, C. Wang, N. Huang, X. Jiang, Diamond Network: Template-Free Fabrication and Properties, ACS Appl. Mater. Interfaces. 7 (2015) 5384–5390. https://doi.org/10.1021/am508851r.

[65] C. Hébert, E. Scorsone, M. Mermoux, P. Bergonzo, Porous diamond with high electrochemical performance, Carbon. 90 (2015) 102–109. https://doi.org/10.1016/j.carbon.2015.04.016.

[66] S. Kunuku, K.J. Sankaran, C.-Y. Tsai, W.-H. Chang, N.-H. Tai, K.-C. Leou, I.-N. Lin, Investigations on Diamond Nanostructuring of Different Morphologies by the Reactive-Ion Etching Process and Their Potential Applications, ACS Appl. Mater. Interfaces. 5 (2013) 7439–7449. https://doi.org/10.1021/am401753h.

[67] C. Terashima, K. Arihara, S. Okazaki, T. Shichi, D.A. Tryk, T. Shirafuji, N. Saito, O. Takai, A. Fujishima, Fabrication of Vertically Aligned Diamond Whiskers from Highly Boron-Doped Diamond by Oxygen Plasma Etching, ACS Appl. Mater. Interfaces. 3 (2011) 177–182. https://doi.org/10.1021/am1007722.

[68] D. Luo, L. Wu, J. Zhi, Fabrication of Boron-Doped Diamond Nanorod Forest Electrodes and Their Application in Nonenzymatic Amperometric Glucose Biosensing, ACS Nano. 3 (2009) 2121–2128. https://doi.org/10.1021/nn9003154.

[69] Y. Liu, S. Chen, X. Quan, H. Yu, Efficient Electrochemical Reduction of Carbon Dioxide to Acetate on Nitrogen-Doped Nanodiamond, J. Am. Chem. Soc. 137 (2015) 11631–11636. https://doi.org/10.1021/jacs.5b02975.

[70] H. Zanin, P.W. May, D.J. Fermin, D. Plana, S.M.C. Vieira, W.I. Milne, E.J. Corat, Porous Boron-Doped Diamond/Carbon Nanotube Electrodes, ACS Appl. Mater. Interfaces. 6 (2014) 990–995. https://doi.org/10.1021/am4044344.

[71] A. Haque, R. Sachan, J. Narayan, Synthesis of diamond nanostructures from carbon nanotube and formation of diamond-CNT hybrid structures, Carbon. 150 (2019) 388–395. https://doi.org/10.1016/j.carbon.2019.05.027.

[72] A. Haque, P. Pant, J. Narayan, Large-area diamond thin film on Q-carbon coated crystalline sapphire by HFCVD, J. Cryst. Growth. 504 (2018) 17–25. https://doi.org/10.1016/j.jcrysgro.2018.09.036.

[73] Y. Lin, X. Sun, D. Sheng Su, G. Centi, S. Perathoner, Catalysis by hybrid sp 2 /sp 3 nanodiamonds and their role in the design of advanced nanocarbon materials, Chem. Soc. Rev. 47 (2018) 8438–8473. https://doi.org/10.1039/C8CS00684A.

[74] X. Duan, W. Tian, H. Zhang, H. Sun, Z. Ao, Z. Shao, S. Wang, sp2/sp3 Framework from Diamond Nanocrystals: A Key Bridge of Carbonaceous Structure to Carbocatalysis, ACS Catal. 9 (2019) 7494–7519. https://doi.org/10.1021/acscatal.9b01565.

[75] C. Kleint, A. Modinos. Field, thermionic, and secondary electron emission spectroscopy. Plenum Press, New York and London 1984, 375 S., Preis $ 78.00, ISBN 0–306–41321–3, Cryst. Res. Technol. 23 (1988) 900–900. https://doi.org/10.1002/crat.2170230711.

[76] S. Wang, J. Wang, P. Miraldo, M. Zhu, R. Outlaw, K. Hou, X. Zhao, B.C. Holloway, D. Manos, T. Tyler, O. Shenderova, M. Ray, J. Dalton, G. McGuire, High field emission reproducibility and stability of carbon nanosheets and nanosheet-based backgated triode emission devices, Appl. Phys. Lett. 89 (2006) 183103. https://doi.org/10.1063/1.2372708.

[77] Y. Cheng, O. Zhou, Electron field emission from carbon nanotubes, Comptes Rendus Phys. 4 (2003) 1021–1033. https://doi.org/10.1016/S1631-0705(03)00103-8.

[78] N.S. Lee, D.S. Chung, I.T. Han, J.H. Kang, Y.S. Choi, H.Y. Kim, S.H. Park, Y.W. Jin, W.K. Yi, M.J. Yun, J.E. Jung, C.J. Lee, J.H. You, S.H. Jo, C.G. Lee, J.M. Kim, Application of carbon nanotubes to field emission displays, Diam. Relat. Mater. 10 (2001) 265–270. https://doi.org/10.1016/S0925-9635(00)00478-7.

[79] Raman Spectra of Carbon Nanotubes, in: Phys. Prop. Carbon Nanotub., PUBLISHED BY IMPERIAL COLLEGE PRESS AND DISTRIBUTED BY WORLD SCIENTIFIC PUBLISHING CO., 1998: pp. 183–206. https://doi.org/10.1142/9781860943799_0010.

[80] R. Rosen, W. Simendinger, C. Debbault, H. Shimoda, L. Fleming, B. Stoner, O. Zhou, Application of carbon nanotubes as electrodes in gas discharge tubes, Appl. Phys. Lett. 76 (2000) 1668–1670. https://doi.org/10.1063/1.126130.

[81] H. Sugie, M. Tanemura, V. Filip, K. Iwata, K. Takahashi, F. Okuyama, Carbon nanotubes as electron source in an x-ray tube, Appl. Phys. Lett. 78 (2001) 2578–2580. https://doi.org/10.1063/1.1367278.

[82] F.J. Himpsel, J.A. Knapp, J.A. VanVechten, D.E. Eastman, Quantum photoyield of diamond(111)-A stable negative-affinity emitter, Phys. Rev. B. 20 (1979) 624–627. https://doi.org/10.1103/PhysRevB.20.624.

[83] J. Robertson, Mechanisms of electron field emission from diamond, diamond-like carbon, and nanostructured carbon, J. Vac. Sci. Technol. B Microelectron. Nanometer Struct. Process. Meas. Phenom. 17 (1999) 659–665. https://doi.org/10.1116/1.590613.

[84] C. Wenger, J. Kitzmann, A. Wolff, M. Fraschke, C. Walczyk, G. Lupina, W. Mehr, M. Junige, M. Albert, J.W. Bartha, Graphene based electron field emitter, J. Vac. Sci. Technol. B Nanotechnol. Microelectron. Mater. Process. Meas. Phenom. 33 (2015) 01A109. https://doi.org/10.1116/1.4905937.

[85] E. Manikandan, G. Kavitha, J. Kennedy, Epitaxial zinc oxide, graphene oxide composite thin-films by laser technique for micro-Raman and enhanced field emission study, Ceram. Int. 40 (2014) 16065–16070. https://doi.org/10.1016/j.ceramint.2014.07.129.

[86] Y. Zhu, S. Murali, W. Cai, X. Li, J.W. Suk, J.R. Potts, R.S. Ruoff, Graphene and Graphene Oxide: Synthesis, Properties, and Applications, Adv. Mater. 22 (2010) 3906–3924. https://doi.org/10.1002/adma.201001068.

[87] A. Haque, P. Pant, J. Narayan, Large-area diamond thin film on Q-carbon coated crystalline sapphire by HFCVD, J. Cryst. Growth. 504 (2018) 17–25. https://doi.org/10.1016/j.jcrysgro.2018.09.036.

[88] J. Narayan, A. Bhaumik, R. Sachan, A. Haque, S. Gupta, P. Pant, Direct conversion of carbon nanofibers and nanotubes into diamond nanofibers and the subsequent growth of large-sized diamonds, Nanoscale. (2019). https://doi.org/10.1039/C8NR08823C.

[89] C. Nützenadel, O.M. Küttel, O. Gröning, L. Schlapbach, Electron field emission from diamond tips prepared by ion sputtering, Appl. Phys. Lett. 69 (1996) 2662–2664. https://doi.org/10.1063/1.117551.

[90] A. Wisitsora-at, W.P. Kang, J.L. Davidson, Y. Gurbuz, D.V. Kerns, Field emission enhancement of diamond tips utilizing boron doping and surface treatment, Diam. Relat. Mater. 8 (1999) 1220–1224. https://doi.org/10.1016/S0925-9635(99)00008-4.

[91] E. Manikandan, J. Kennedy, G. Kavitha, K. Kaviyarasu, M. Maaza, B.K. Panigrahi, U.K. Mudali, Hybrid nanostructured thin-films by PLD for enhanced field emission performance for radiation micro-nano dosimetry applications, J. Alloys Compd. 647 (2015) 141–145. https://doi.org/10.1016/j.jallcom.2015.06.102.

[92] D.E. Motaung, M.K. Moodley, E. Manikandan, N.J. Coville, In situ optical emission study on the role of C2 in the synthesis of single-walled carbon nanotubes, J. Appl. Phys. 107 (2010) 044308. https://doi.org/10.1063/1.3311563.

[93] K.L. Ng, J. Yuan, J.T. Cheung, K.W. Cheah, Electron field emission characteristics of electrochemical etched Si tip array, Solid State Commun. 123 (2002) 205–207. https://doi.org/10.1016/S0038-1098(02)00287-9.

[94] V.N. Tondare, B.I. Birajdar, N. Pradeep, D.S. Joag, A. Lobo, S.K. Kulkarni, Self-assembled Ge nanostructures as field emitters, Appl. Phys. Lett. 77 (2000) 2394–2396. https://doi.org/10.1063/1.1316076.

[95] F. Giubileo, A. Di Bartolomeo, L. Iemmo, G. Luongo, M. Passacantando, E. Koivusalo, T.V. Hakkarainen, M. Guina, Field Emission from Self-Catalyzed GaAs Nanowires, Nanomaterials. 7 (2017) 275. https://doi.org/10.3390/nano7090275.

[96] G. Fursey, I. Brodie, P. Schwoebel, eds., Field Electron Emission from Metals, in: Field Emiss. Vac. Microelectron., Springer US, Boston, MA, 2005: pp. 1–17. https://doi.org/10.1007/0-387-27419-7_1.

[97] J. Robertson, Mechanisms of electron field emission from diamond, diamond-like carbon, and nanostructured carbon, J. Vac. Sci. Technol. B Microelectron. Nanometer Struct. Process. Meas. Phenom. 17 (1999) 659–665. https://doi.org/10.1116/1.590613.

[98] J. Narayan, A. Bhaumik, S. Gupta, A. Haque, R. Sachan, Progress in Q-carbon and related materials with extraordinary properties, Mater. Res. Lett. 6 (2018) 353–364. https://doi.org/10.1080/21663831.2018.1458753.

[99] J. Narayan, A. Bhaumik, R. Sachan, A. Haque, S. Gupta, P. Pant, Direct conversion of carbon nanofibers and nanotubes into diamond nanofibers and the subsequent growth of large-sized diamonds, Nanoscale. 11 (2019) 2238–2248. https://doi.org/10.1039/C8NR08823C.

[100] A. Haque, P. Pant, J. Narayan, Large-area diamond thin film on Q-carbon coated crystalline sapphire by HFCVD, J. Cryst. Growth. 504 (2018) 17–25. https://doi.org/10.1016/j.jcrysgro.2018.09.036.

[101] N. Jiang, K. Eguchi, S. Noguchi, T. Inaoka, Y. Shintani, Structural characteristics and field electron emission properties of nano-diamond/carbon films, J. Cryst. Growth. 236 (2002) 577–582. https://doi.org/10.1016/S0022-0248(01)02219-9.

[102] C. Li, P.X. Yan, X.C. Li, E.M. Chong, Electron field emission from diamond-like carbon nanodot arrays, Phys. E Low-Dimens. Syst. Nanostructures. 42 (2010) 1343–1346. https://doi.org/10.1016/j.physe.2009.11.018.

[103] J. Kennedy, F. Fang, J. Futter, J. Leveneur, P.P. Murmu, G.N. Panin, T.W. Kang, E. Manikandan, Synthesis and enhanced field emission of zinc oxide incorporated carbon

nanotubes, Diam. Relat. Mater. 71 (2017) 79–84. https://doi.org/10.1016/j.diamond.2016.12.007.

[104] B.S. Satyanarayana, A. Hart, W.I. Milne, J. Robertson, Field emission from tetrahedral amorphous carbon, Diam. Relat. Mater. 7 (1998) 656–659. https://doi.org/10.1016/S0925-9635(97)00296-3.

[105] A. Haque, J. Narayan, Electron field emission from Q-carbon, Diam. Relat. Mater. 86 (2018) 71–78. https://doi.org/10.1016/j.diamond.2018.04.008.

[106] A. Haque, J. Narayan, Stability of electron field emission in Q-carbon, MRS Commun. 8 (2018) 1343–1351. https://doi.org/10.1557/mrc.2018.172.

2. Experimental

2.1 Deposition and Processing techniques

2.1.1 Hot Filament Chemical Vapor Deposition (HFCVD)

HFCVD is a nonplasma technique, also known as pyrolytic technique, for the fabrication of a variety of high quality films and structures like diamond, diamond like carbon, organosilicon films of novel structure, etc. Metallic filaments, such as tungsten, tantalum, or rhenium, are used in the HFCVD chamber for resistive heating to dissociate the source gas at high temperature. This dissociation process produces the reactive precursors for the growth of thin films. The flow rate of the precursor gases and the final temperature of the heated filaments control the reactive precursor concentration and kinetics. The substrate temperature is also controlled independently to govern the film quality. The HFCVD films do not suffer from the UV irradiation and ion bombardment associated with plasma exposure. A simplified schematic of HFCVD process is shown in Fig. 2.1.

2.1.2 Pulsed Laser Deposition (PLD)

PLD is a versatile technique to grow thin films and multilayers of complex materials. It consists of a vacuum chamber inside which a target holder and a substrate holder are placed. The energy source is a pulsed laser source located outside the chamber. So the thin film can be grown in high vacuum and under ambient gas environment. The high power laser is directed towards the target using a set of optical components to focus and raster the beam over the target. The laser beam interacts with the target to vaporize the material and grow the thin film. Using this technique a stoichiometry transfer between the target and substrate takes place which allows the deposition of different types of materials such as oxides, carbides, nitrides, semiconductors, high-temperature superconductors, and even metals [1]. The pulsed nature of the PLD process even allows preparing complex polymermetal compounds and multilayers as well as polymers and fullerenes. The

preparation in inert gas or any other advantageous gas atmosphere makes it even possible to tune important film properties such as stress, texture, reflectivity, magnetic properties etc. by varying the kinetic energy of the deposited particles. Thus PLD is an alternative deposition technique for the growth of high-quality thin films. Fig. 2.2 shows a simplified schematic diagram of a PLD system.

2.1.3 Pulsed Laser Annealing

Laser annealing is a very broader class of phenomena ranging from laser induced melting or growth to alloying, controlled patterning for display devices and so on. In the PLA system a pulsed laser source is used to anneal the sample. In earlier studies this technique was extensively used to remove the structural damage produced during the ion implantation of Si. This process is very efficient to activate the dopant atoms and thus the process is very suitable for microelectronics. Judicious selection of the laser parameters can lead to the melting and subsequent quenching of a solid which can lead to the phase transformation. Thus we can grow metastable phases, utilizing this non-equilibrium ultrafast process, which is almost impossible to attain through the conventional equilibrium routes. This is the only route to bypass thermodynamics through kinetics which will open new opportunities in modern microelectronic systems. Moreover, as the PLA leads to a liquid route phase transformation, the material can be doped with a dopant concentration over retrograde solid solubility limit. Therefore the PLA process has a great implication in materials science and modern microelectronics industry.

2.2 Characterization techniques

2.2.1 X-ray diffraction

X-ray diffraction also known as XRD is a non-destructive analytic technique for identification and quantitative determination of different types of crystalline forms sometimes termed as

'phases'. The identification is performed by comparing the X-ray diffraction pattern with standard data. Crystalline samples consist of parallel rows of atoms separated by a 'unique' distance. Diffraction occurs when the radiation enters a crystalline substrate and is scattered. The intensity of the pattern and the angle of diffraction depend on the orientation of crystal lattice with radiation. The XRD principle is mainly based on the constructive interference of monochromatic X-rays and a crystalline sample. The X-ray is generated by a cathode ray tube. This X-ray is filtered to produce monochromatic radiation, collimated to concentrate, and directed towards the sample. The interaction between the X-ray and sample produces constructive interference when the conditions match to Bragg's law. This law relates the lattice spacing in the crystal sample, wavelength of the X-ray radiation and the angle of diffraction. The sample is scanned through a range of 2θ angles in all possible diffractions. The diffracted X-ray intensity is then processed and counted. When the Bragg's condition is satisfied, the number of counts rises and the XRD pattern gives a peak. Conversion of the diffraction peaks to d-spacing helps to identify the crystal structure. This is because each crystalline material has a unique set of d-spacing [2]. The XRD is typically used to measure the average spacing between the layers or rows of atoms, to determine the orientation of a single crystal or grain, to find the crystal structure of an unknown material, and also to measure the size, shape and internal stress in thin film samples. Fig. 2.3 illustrates the basic principle of XRD.

***θ-2θ scan*:** The geometry of the diffractometer for the θ-2θ scan is such that as the sample rotates at an angle of θ with regards to the X-ray beam, and the detector rotates at the angle of 2θ to sense the reflected beam. The θ-2θ scans are based on Bragg's law which is a special case of Laue diffraction, where angles for coherent and incoherent scattering from crystal lattice planes upon the incident of the X-ray beam will be determined. The general relationship between the incident

beam, incident angle, and the spacing between lattice planes is $n\lambda=2dsin\theta$, where λ is the wavelength of the X-ray beam, θ is the angle of the incident beam, and d is the d-spacing of the crystal lattice. Reflections at a given angle (2θ) corresponds to the lattice plane distances (d) that coherently reflected from those family of planes (hkl) (out-of-plane in case of thin films). If the film is textured or epitaxial, there is only one family of planes aligned parallel with respect to substrate planes. In order to check the in-plane alignment, Φ-scan can be employed.

2.2.2 Scanning electron microscopy (SEM)

The scanning electron microscope (SEM) has a high-energy electron beam which interacts with the sample and provides information regarding chemical composition, structure, and microstructure of the materials. When the electron beam hits the atoms, multiple situations can be envisaged. It can knock out the outer layer electrons which are called secondary electrons. It can dislodge the inner layer electron (also are considered secondary electrons) and as a result electrons from outer orbit transition to the inner orbit and generate X-ray. It can bounce and deflect by the positive core which is called a backscattered electron. The schematic Figure 2.4 represents secondary and backscattered electrons.

The secondary electrons (SE) are being detected and used for imaging mode as a result of inelastic interaction. These electrons have low energy and as a result, they give information about the surface (a few nm). These electrons later are accelerated to have enough energy to be analyzed and displayed. The brightness of the signal depends on the number of secondary electrons. The secondary electrons emitted from edges and steep surfaces are more due to the increased incident angle. Thus, these areas tend to be brighter. This property helps us build a topography map of the surface. The backscattered electrons (BSE) are high energy electrons that are deflected through elastic interaction. The higher the atomic number, the more backscattered electrons are deflected.

Thus, the heavier atoms show up brighter in the image. As a result, these electrons give information regarding the atomic map. The detector needs to be mounted above the sample to collect BSE electrons. These electrons can also be collected by electron backscattered diffraction (EBSD) detector providing different information. The generated X-ray can also be collected, which gives information related to elemental map and concentration.

2.2.3 Electron backscattered diffraction (EBSD)

Electron backscattered diffraction (EBSD) is an effective and powerful structural characterization technique to obtain the structure, phase, and crystal orientation of both single and polycrystalline materials. The ordered atoms in crystalline sample inelastically scatter a fraction of the incident electrons from the point of interest, with a small loss of energy, to form a divergent source of electrons close to the surface of the sample. A portion of these electrons is incident on atomic planes at angles that satisfy the Bragg equation for corresponding crystal structure which provides information about the lattice planes and orientation. These electrons produce an image on the phosphor screen containing characteristic Kikuchi bands of associated crystal structures. Primarily these characteristic Kikuchi bands are indexed by the miler indices utilizing the standard software and a standard library where the simulated/standard Kikuchi patterns are stored. Each set of Kikuchi bands from a polycrystalline material is associated with individual grain. The EBSD technique is also used to extract the alignment information across the interface in single crystalline heterostructure. The resolutions of modern EBSD instruments are in the order of 10-100 nm which is very suitable to study the phase transformation process by laser solid interaction at a nanoscale level. The resolution can be further enhanced in the transmission Kikuchi diffraction mode.

2.2.4 Transmission electron microscopy (TEM)

Transmission electron microscope is a very powerful and versatile tool to extract information related to crystallinity, structure, atomic scale imaging, and bonding characteristic of the material in the electron-energy-loss mode. It uses a high energy coherent electron beam that transmits through the TEM sample with thickness of less than 100 nm. The maximum resolution (d) is limited to the wavelength of the photons (λ) and the aperture in a conventional optical microscope.

$$d = \frac{\lambda}{2n\ sin\alpha}$$

where n is the refraction index, and α is the maximum half angle of the cone that is defined by the aperture. Similar to an optical microscope, in an electron microscope, the electron wavelength (λe) is a defining factor in resolution;

$$\lambda_e = \frac{h}{\sqrt{2m_0E\ (1 + \frac{E}{2m_0c^2})}}$$

where h is the Plank's constant, m_0 is the mass of the electron, E is the energy of the electron beam, and c is the speed of light. Thus at E=100 KeV, the wavelength of the source is only about 2.5 pm. The actual achievable resolution is limited to 0.1 nm due to different types of aberrations, such as object lens aberration, spherical aberration, and chromatic aberration.

***Selected-area electron diffraction (SAED)*:** When the electron beam is scattered by the sample lattice the elastically scattered electrons satisfies the Bragg's condition and form the SAED pattern. Thus the diffractions spots provide the phase and structural property of the material. When the material is amorphous SAED gives a thick single ring and polycrystalline materials generate multiple rings and these rings are indexed by the Miller indices (set of planes). In case of single crystal material the SAED generates a pattern with a set of spots and each of the spot correspond to specific a lattice plane.

***Electron energy loss spectroscopy (EELS)*:** Due to the broad range of inelastic interactions of the high energy electrons with the specimen atoms, ranging from phonon interactions to ionization processes, EELS offers unique possibilities for advanced materials analysis. The energy and momentum of the incident electron changes upon the interaction with the TEM sample. The change or loss in energy can be detected by the EEL spectrometer to obtain characteristic information of the sample. Core-loss excitations occur when tightly bound core electrons are promoted to a higher energy state by the incident electron. It can not only be used to map the elemental composition of a specimen, but also for studying the physical and chemical properties including stoichiometry, chemical bonding, valence and conduction band electronic properties, surface properties, and element-specific pair distance distribution functions of a wide range of materials.

***Scanning transmission electron microscopy (STEM)*:** In the scanning transmission electron microscopy (STEM) mode, the advantages of both TEM and SEM principles are taken by creating a focused convergent electron beam or probe at the sample surface upon adjusting the microscope lenses. The fine electron beam scans across the specimen and generates different signals which are collected on a point by point basis to generate the image. This enables to obtain enhanced spatial resolution of the imaging. This technique also offers the ability to provide information on elemental composition and electronic structure at the ultimate sensitivity, that of a single atom. A bright field detector and a dark field detector are available to generate bright field and dark field images. The bright field detector includes the transmitted beam whereas the dark field detector excludes the transmitted beam, therefore, in bright field image the holes appear bright whereas in dark field image the holes appear dark. Such complementary view of the specimen enables to obtain maximum possible information. Fig. 2.5 illustrates the interaction of incident electron beam

with the TEM sample and different detector positions. Fig. 2.6 illustrates the schematic of TEM and STEM optics.

***Electron transparent sample preparation*:** The sample preparation is one of the most critical parts in transmission electron microscopy. The sample preparation can be done by advanced focused ion beam (FIB) technique, or conventional mechanical polishing and successive ion milling, or the combination of both. Conventionally the sample preparation is done in a way to keep the surface intact and the superficial area of the specimen is prevented from any damage. To do this, the most common method consists in firstly mechanically thinning the back side of the specimen until the thickness becomes less than a few tens of microns, followed by an additional thinning method to reach the electron transparency. On the other hand, focused ion beam (FIB) tools and next the combined focused ion-beam/scanning electron microscope (FIB/SEM) systems are used to prepare fine TEM samples on specific localized zones with a spatial accuracy of about ten nanometers. Such fine samples are prepared by controlling the ion beam current, voltage, and angle of the sample with respect to the incident beam direction. The whole sample preparation is observed in the chamber using a second electron beam of SEM.

2.2.5 Raman spectroscopy

Raman spectroscopy is a non-destructive characterization technique comprises of the spectral measurements which provides information about molecular vibrations to identify and quantify different types of samples. This technique is also used to extract other important information of a material, such as phase, composition, chemical bonding, crystal structure, chemical environment and to identify the number of layers of a 2 dimensional materials. In this technique a monochromatic source of light, usually a laser source is used to illuminate a sample. The oncoming monochromatic light can be considered as the oscillating electromagnetic field with electrical part

E. Under this electric field the molecular polarizability α is determined to find out the Raman effect. Hence the resulting induced electric dipole moment, P= αE causes a perturbation in the molecule. In this way a periodic deformation is generated in the sample which causes the molecule to vibrate with its characteristic frequency υ_m. The sample absorb a fraction of the oncoming photon and reemits them. In comparison with the oncoming monochromatic frequency, the frequency of the reemitted photons shifts up, down or remains the same. If a molecule of a sample does not possess any Raman active mode and absorbs a photon with frequency υ0, it will return back to its original vibrational state by emitting the original frequency, υ0. This type of scattering is called elastic Rayleigh scattering. On the other hand, if a Raman active molecule absorbs light with frequency υ_0, a part of the energy of the photon is transmitted to the Raman active mode with the characteristic frequency υ_m. As a result, the resulting frequency of the scattered photon is reduced to $\upsilon_0 - \upsilon_m$ which is called Stokes frequency and the whole phenomenon is known as stokes scattering [3].

On the other hand, there is another type of scattering which is known as antistokes Raman scattering. At the time of interaction with photon with frequency, υ_0 if the Raman active molecule already exists in the excited vibrational state, the excessive photon energy is released by the excited molecule. Hence, the resulting frequency of the scattered light rises up to $\upsilon_0 + \upsilon_m$. This frequency is known as Anti-Stokes frequency or sometimes just ‘anti-stokes’. In the photon interaction process about 99.99999% of the scattered photons undergoes elastic scattering which is not useful to receive the desirable characteristic information about a sample. Only about 10-5% of the scattered photons are shifted in energy from the original frequency. However the stokes band is usually more intense than that of anti-stokes. Plotting the shifted light intensity versus the frequency provides the characteristic Raman peaks of the sample which is known as the Raman

spectrum. In Fig 2.7 the difference between the incident photon energy and scattered photon energy is represented by the arrows with different lengths. Numerically, the Raman shift $\bar{\upsilon}$ is the energy difference between the initial and final vibrational levels in the unit of wave numbers (cm^{-1}), which is calculated using the following expression where $\boldsymbol{\lambda}_{\text{incident}}$ is the wavelength of the incident photon and $\boldsymbol{\lambda}_{\text{scattered}}$ is the wavelength of the scattered photon.

$$\bar{\upsilon} = \frac{1}{\lambda_{incident}} - \frac{1}{\lambda_{scattered}}$$

A proper lens and optical filter setup is essential to obtain optimal data in Raman measurement. An objective lens is used through which the excitation light is focused on the sample. A band pass filter is used to eliminate the unwanted radiations. An edge filter is also used to block the frequencies coming from Rayleigh scattering.

2.3 Figures

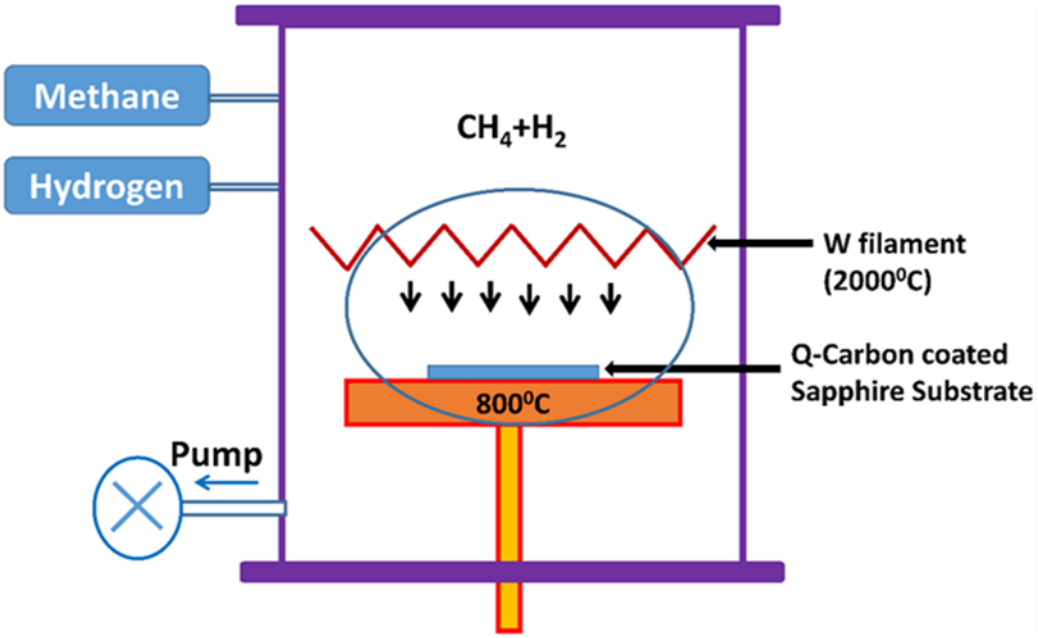

Figure 2. 1: Schematic of a HFCVD system

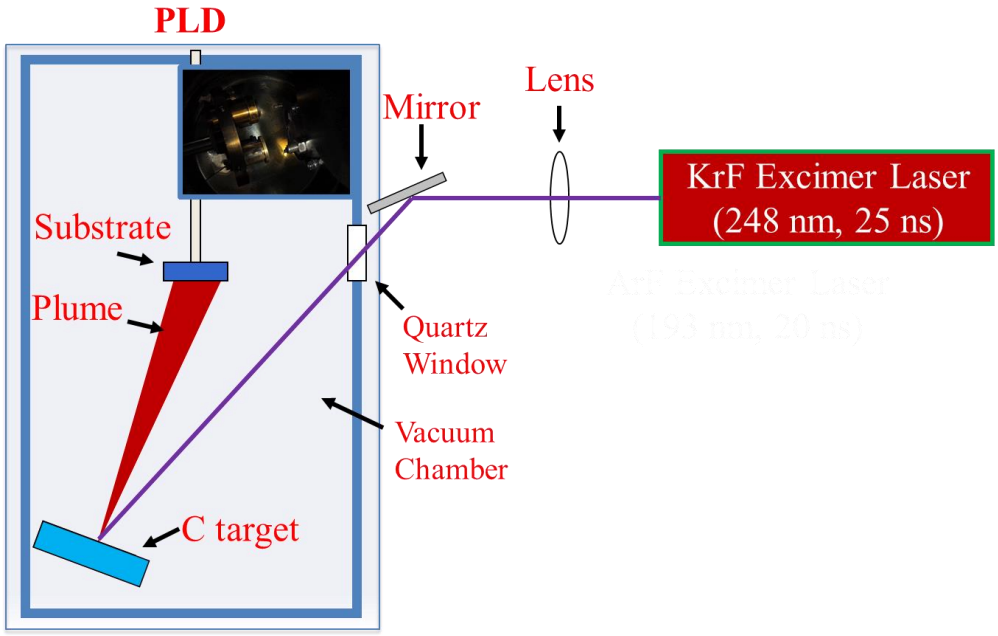

Figure 2. 2: Schematic illustration of pulsed laser deposition technique.

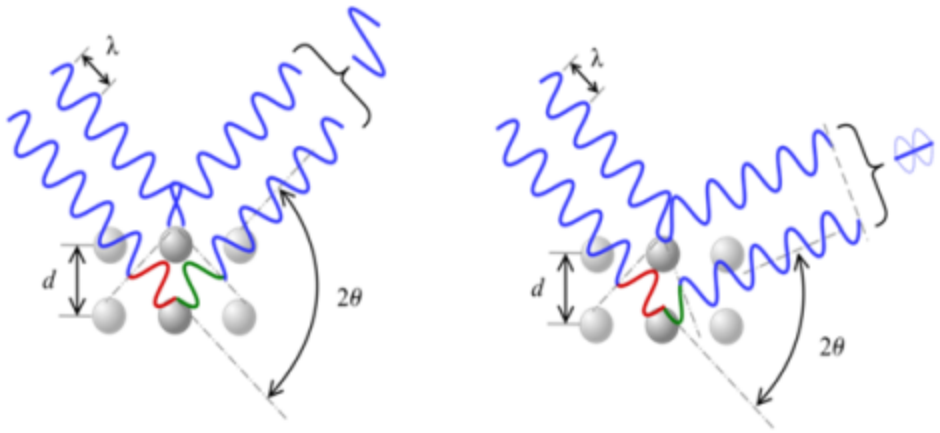

Figure 2. 3: Illustration of Bragg's law. Depending on the angle the interference can either be constructive (left) or destructive (right).

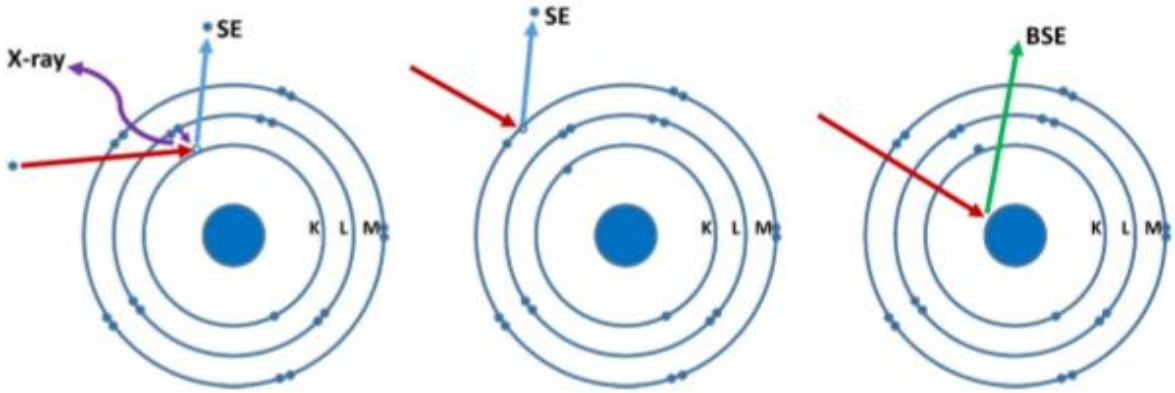

Figure 2. 4: Emission of secondary electrons (SE), backscattered electrons (BSE), and X-ray upon the incident of the electron beam.

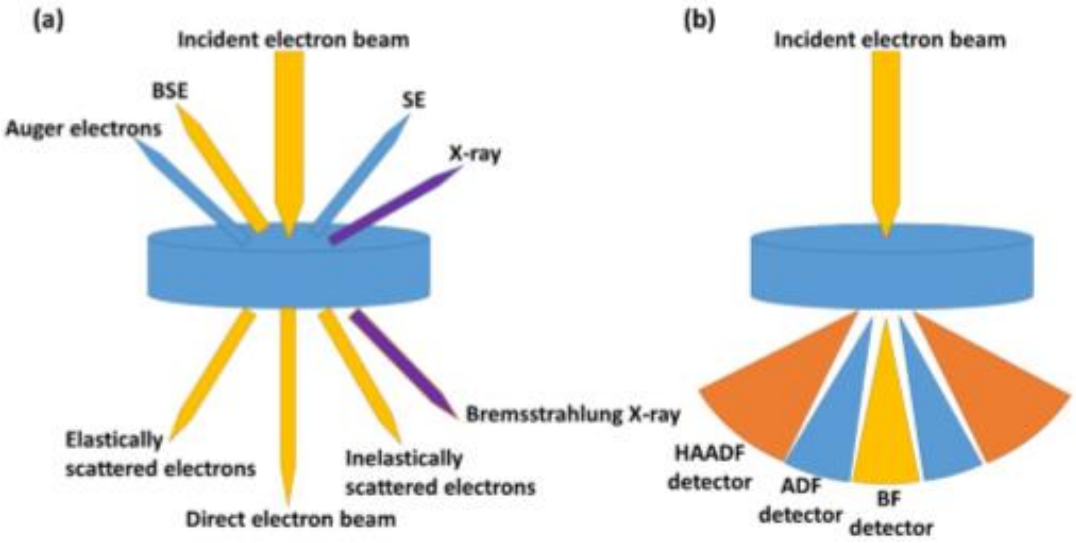

Figure 2. 5: (a) Different phenomena upon electron beam interaction with material. And (b) HAADF detector angle > 50 mrad, ADF detector>10 mrad, and BF detector < 10 mrad.

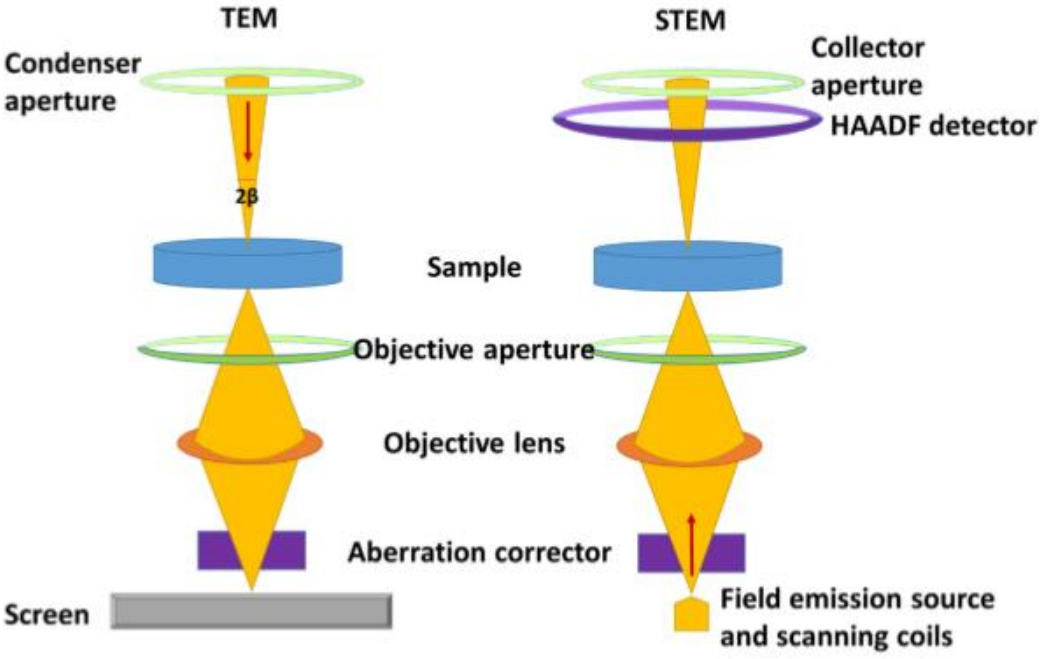

Figure 2. 6: Schematic illustration of the TEM and STEM optics.

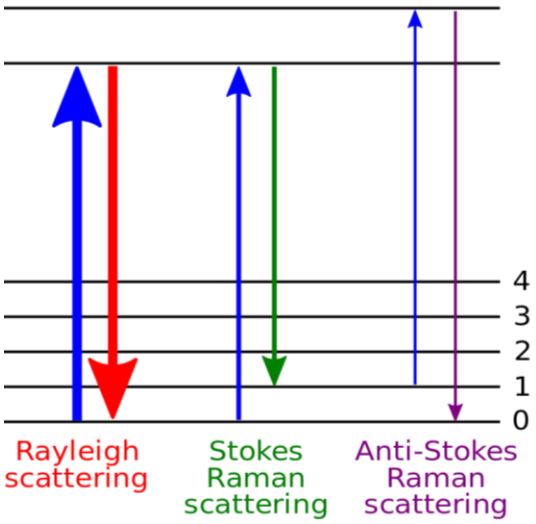

Figure 2. 7: Electronic and virtual states along with vibrational levels in Raman spectroscopy.

References

[1] R. Eason, Pulsed Laser Deposition of Thin Films: Applications-Led Growth of Functional Materials, John Wiley & Sons, 2007.

[2] A. Higginbotham, S. Patel, J.A. Hawreliak, O. Ciricosta, G.W. Collins, F. Coppari, J.H. Eggert, M.J. Suggit, H. Tang, J.S. Wark, Single photon energy dispersive x-ray diffraction, Rev. Sci. Instrum. 85 (2014) 033906. https://doi.org/10.1063/1.4867456.

[3] J.R. Ferraro, Introductory Raman Spectroscopy, Elsevier, 2003.

.

3. Synthesis of diamond nanostructures from carbon nanotube and formation of diamond-CNT hybrid structures

Ariful Haque[1], Ritesh Sachan[2] and Jagdish Narayan[1]

[1]Department of Materials Science and Engineering, North Carolina State University, Raleigh, North Carolina 27695.7916, USA

[2]Department of Mechanical and Aerospace Engineering, Oklahoma State University, Stillwater, Oklahoma, 74078, USA

3.1 Abstract

We report direct conversion of multiwall carbon nanotubes (CNTs), synthesized by chemical vapor deposition, into diamond by nanosecond pulsed laser melting process at ambient temperature and pressure in air without any catalysts. The Raman spectroscopy of the CNTs after the laser irradiation showed the characteristic diamond peak at around 1324-1325 cm^{-1}. The downshift of this peak from its theoretical position (at 1332 cm^{-1}) is explained by phonon confinement in nanostructured diamond. The SEM and TEM images show the formation of diamond mostly at the tip and bends of the CNTs. The grain size distribution and the shape of the converted nanodiamonds suggest that the transformation takes place by melting of the CNTs in a super undercooled state by nanosecond laser pulses, and subsequent rapid quenching to convert it into phase-pure diamond. The EBSD analysis illustrates the phase-pure single crystal diamond formation at the tips and bends of the CNTs. The high-resolution electron energy-loss spectrum in the STEM contains characteristic σ* peak at 292 eV for sp^3 bonding of diamond. This study on the laser-induced direct conversion of CNTs to diamond marks a major breakthrough in the

formation of diamond nanostructures and diamond-CNT hybrid for a variety of potential applications.

3.2 Introduction

Carbon nanotubes, the tubular form of graphite sheets (100% sp^2 bonded carbon), are one of the most promising forms of carbon which is expected to be implemented in many nano-scale device applications owing to its exceptional properties such as large thermal conductivity, good electron mobility, excellent electrical conductivity, and dual band-gap properties (metallic and semiconductor as a function of chirality) [1,2]. On the other hand, diamond (consisting of 100% sp^3-bonded carbon) has tremendous chemical inertness, extreme hardness, biocompatibility, unique electrochemical properties, large bandgap, and negative electron affinity (observed in H-terminated diamond) [3–5]. It is one of the most studied and most promising materials for cold cathode electron source, heat sink substance for electronic devices, hermetic corrosion resistant coating for bio-devices, protective coating in machining tools, photon-enhanced thermionic emission (PETE) solar cells, and the structural material for micro- and nano-electromechanical systems (MEMS/NEMS) [6–10]. In fact, the diamond-based PETE solar cells fabricated by the defect engineering of diamond, obtained by the laser treatment, has shown immense potential [11–13]. Diamond is also widely used to fabricate radiation detectors to detect electromagnetic radiation with energy of greater than 5.5 eV. These includes UV, X-rays, γ rays, high energy particle radiation such as α-particles, electrons, neutrons, pions and other exotic particles[14]. However, the diamond cannot be directly integrated in most of these applications due to different processing limitations [15,16]. It is understood that a combination of carbon nanotubes and nanocrystalline diamond provides hybrids with unprecedented properties that can be advantageously used in electronics, field emission, and load transfer applications. This hybrid

material can have excellent electrical and thermal conductivities, and field emission characteristics comparable to or better than pure diamond (as pure diamond without hydrogen termination has very limited electrical conductivities). The diamond/CNT hybrid structures may thus find applications in various fields that require a combination of excellent mechanical, thermal, and electrical properties. As an example, diamond tipped carbon nanotube will provide an ideal high-efficiency field emitter, where electrons can be carried via nanotube for enhanced field emission by diamond tips.

Since the discovery of carbon nanotubes in 1991 [1] different routes have been tried to transform CNTs into diamond to form CNT/diamond hybrid structure [17–19]. Synthesis of diamond from CNTs was achieved by shock wave synthesis [20], chemical vapor (CVD) deposition by nanotube coating [21], high-pressure-high-temperature (HPHT) treatments [22], and hydrogen plasma post-treatment [23]. Most of these processes lead to diamond structures with limited yield and defects which make them unsuitable for electronic applications. Generally, pressures above several GPa and high-temperature conditions are required and catalysts such as Ni, Co, and other metals or alloys are necessary for the conversion process. The catalyst induced formation of diamond often yields contaminated diamond crystals. Researchers also reported direct synthesis of diamond from CNTs by microwave plasma enhanced chemical vapor deposition (MPCVD) [24]. During the transformation of CNTs to diamond in MPCVD a solid-gas-solid transformation mechanism was involved with limited yield and control over the resulting microstructure. The transformation of CNTs into diamond has been reported by spark plasma sintering at 1500º C temperature and 80 MPa pressure [25]. In this process, the diamond structures are sheathed with an amorphous carbon layer which may hinder its electronic device based applications. Moreover, the stringent requirement of high pressure, high-vacuum, and complicated

formation procedure of the spark plasma at a tremendously large current (>1000 A) are some major drawbacks of this synthesis process. It is important to note that none of these diamond formation methods invoke melting as the mechanism for conversion of CNTs into diamond. Moreover, most of these studies do not provide evidence of diamond structure by TEM and SEM (EBSD) techniques and bonding characteristics by EELS for σ* peak, Raman spectrum with the characteristic peak at 1332 cm^{-1}, and the phonon confinement effect in the Raman spectrum in the case of nanostructured diamond, as the synthesis routes are driven by the solid-to-solid or solid-gas-solid equilibrium phase conversions.

Apart from the above growth and structural quality related limitations, little evidence of direct bonding between the CNTs and diamond was observed in most of the diamond-CNT hybrid structures owing to the limitation of the solid-to-solid phase transformation. This could lead to poor emission efficiency owing to the presence of trap states at the interface between the CNT and diamond and high interfacial resistance as well. Furthermore, the lack of direct bonding weakens the hybrid structure at the interface, leading to an inefficient mechanical load transfer between these two structures (matrix and reinforcement). To overcome these problems, we followed an ultrafast pulsed laser annealing technique to directly convert the tips and bends of the CNTs into diamond at ambient temperature and pressure in air. This undercooling driven conversion of CNTs into diamond involves melting in a super undercooled state using nanosecond laser pulses and quenching rapidly to transform into phase-pure diamond. Subsequent laser pulses can be used to enhance and expand the diamond regions. So far diamond has been doped successfully with p-type dopants. These diamond structures can be also fabricated with n- and p-type dopants with concentrations far higher than equilibrium thermodynamic solubility limits as a result of rapid quenching from liquid and solute trapping phenomenon. Single crystal diamond with such high

level of doping concentration has several exciting applications, i.e. high-temperature superconductivity, power electronics, and efficient field emission devices. Attaining such high doping concentration (otherwise impossible to realize) in single crystal diamond is only possible by this novel discovery of the controlled, direct, ultrafast, and non-equilibrium transformation of carbon into diamond. Thus, this novel process of fabricating single crystal diamond structures and diamond-CNT hybrids using the highly non-equilibrium technique points towards a new promising direction for fabricating next-generation diamond-CNT based devices.

3.3 Experimental details

The double-walled and multi-walled CNTs were grown using a thermal CVD system. The substrate, a polished Si wafer, was placed at the center of the horizontal quartz tube inside the furnace (30 cm in length and 4 cm in diameter). The $FeCl_2$ powder (~99.9% pure, Kojundokagaku Laboratory) in a quartz boat was also placed inside the quartz tube which acts as a catalyst during the synthesis of the CNTs. The chamber pressure was maintained at 10^{-3} Torr during the heating cycle, and the chamber was purged with acetylene (98%) using a mass flow controller once the furnace temperature reached 820°C. At this stage, the furnace temperature remained constant and the pressure was maintained at 10 Torr. In this chloride mediated CVD method of growing CNTs the constant gas flow was maintained for 2 hours and no metallic film on the substrate was found. The CVD grown CNTs were mounted on a laser irradiation holder and the surface was irradiated with a pulsed ArF laser (*Lambda Physik, 193 nm* wavelength, and 20 ns pulse duration) in the air. We have used the previously developed SLIM software to simulate and control the details of laser–solid interactions and to determine the range of optimum laser energy density for the diamond conversion as well [26]. The laser energy density was ~ 0.75-0.8 J/cm^2 which leads to a highly undercooled state to form diamond. The irradiated size for the PLA process is 1 cm^2. We have

used a Calcium Fluoride (CaF_2) Plano-Convex confocal lens from Edmund optics with a focal length of 50 cm. This lens possesses low index of refraction and transmits more than 90% of the radiation at 193 nm. After the first pulse, the ultrafast pulsed laser annealing technique melts the CNT tips and bends where there is limited heat flow for undercooling to occur. The laser-converted diamond regions can be expanded after subsequent laser pulses. The degree of undercooling is critical to the formation of phase-pure diamond. Fig. 3.1 depicts the proposed schematic of the detail of the CNT to diamond conversion by PLA for a diamond capped CNT field emission device.

The high-resolution scanning electron microscopy (SEM) was performed on the CNTs before and after pulsed laser irradiation using an ultra-high-resolution FEI Verios 460L SEM instrument, operating at 2 kV. The Raman spectroscopy data of the nanostructured diamond and CNT were obtained using a WITec Confocal Raman microscope system (triple monochromator, gratings 2400 lines/mm) with an x100 objective lens which focuses the laser beam in a spot of 2 μm. All of the spectra were recorded by CCD matrix with a very high-spectral resolution (<300 nm). The excitation of the Raman scattering was performed by a 532 nm diode-pumped solid-state laser. A low laser power of ~20 mW was used to avoid any local heating of the sample. The sharp peak at ~520.6 cm^{-1} associated with crystalline Si was used to calibrate the instrument during the acquisition of the Raman spectra. The FEI Titan 80–300 keV aberration-corrected scanning transmission electron microscope, operating at 200 keV, was used to perform annular dark field (ADF) imaging. The convergence and collection semi-angles used for ADF imaging are 19.2 and 36 mrad. The electron energy-loss (EEL) spectra were acquired with a collection semi-angle of 28 mrad. The electron probe current used for all the experiments was 35 ± 2 pA. The EELS data acquisition was carried out at 29 mrad collection angle.

To determine the diamond crystal structure and detailed orientation relationships, we conducted electron backscattered (EBSD) measurements using FEI Quanta 3D FEG FIB-SEM system to map out the Kikuchi diffraction patterns. In this system, an EBSD HKL NordlysNano detector with lateral resolution of less than 5 nm was used to obtain the Kikuchi diffraction pattern. In this experiment, the stationary electron beam with 15 KV energy and 11 nA current interacts with the tilted sample (70^{o}) and the diffracted electrons from the diamond surface form a three-dimensional pattern. The diffraction pattern is characteristic of the crystal structure, and hence this pattern has been used to determine crystal structures and orientation relationships with the substrate. In our study, this particular technique was advantageous to determine the crystal structure of nano and micro-crystalline regions.

3.4 Results and discussions

3.4.1 SEM

We performed field emission SEM analysis to examine changes in the CNTs before and after PLA and to investigate the size distributions and growth characteristics of the nanodiamonds formed by the PLA process. Fig. 3.2 (a-c) show the SEM image of the CVD grown CNTs (1-D structure) before PLA. The diameters of these nanowires are in the range of 10–50 nm and their lengths are up to several micrometers. At a higher magnification, in Fig. 3.2 (b-c), no evidence of diamond or any other phase is found. Fig. 3.3 (a) shows a high-resolution SEM image of the CNTs after PLA, and it clearly illustrates the structural changes at the tips and bends of the CNTs. The structural changes at the tips and bends are marked by red arrows. The nanosecond pulsed laser heating leads to the formation of molten carbon and upon quenching the molten (from undercooled state) carbon crystallizes rapidly to form a diamond structure, which has been characterized in detail below. Fig. 3.3 (b) shows absence of diamond formation in the middle of the CNTs (far from

the tips) due to less undercooling. However, the formation of diamond is clearly evident at the tip and bends regions (red arrows). The change from a uniform tubular structure to a granular structure especially at the tip and curves/bends of the CNTs is evident by the high-resolution SEM images in Fig. 3.3 (c-f), signifying the liquid phase mediated formation of the diamond phase. The contrast of those granular diamond particles is different compared to that of the unconverted tubular CNTs due to the shrinkage of the molten carbon. The presence of fine crystals in Fig. 3.3 (e-f) (less than 30 nm in size) suggest that these nano-diamonds were directly transformed from the CNTs via the molten state of carbon. Moreover, the process is more efficient when the tip and bends are directly irradiated by the laser pulses with a minimum angle between the CNT axis and the incident direction of the laser irradiation. The nanosecond laser parameters and heat confinement by the one-dimensional CNTs determine the temperature distribution and undercooling plays a critical role in nucleation and growth of nanodiamonds. The nanosecond laser pulses help to achieve the undercooled state of carbon and upon subsequent quenching leads to the formation of nanodiamonds from CNTs. The nanosecond laser heating and temperature distributions are confined spatially and temporally. Therefore, the tips (and bends) of CNTs melt and achieve undercooling needed for transformation into diamond. Thus, the right amount of laser energy density for irradiation and the heat flow geometry to achieve necessary undercooling are very crucial for the formation of phase-pure diamond from CNTs. Some of the surface nuclei grow into nanodiamond structures normal to the substrate along the diameter. Fig. 3.3 (e-f) also illustrate the formation of nanodiamonds at the surface of the CNTs due to the conversion of the ridges into diamond due to the undercooling effect. Here, the nanodiamond beads are formed which signifies direct evidence of carbon melting during the conversion process. Details of the conversion at the tip are evidenced by an ultra-high-resolution SEM image in Fig. 3.3 (g). This also illustrates that

up to a few tens of nanometers (in length) of the CNT has been converted into a diamond nano-rod with a radius of ~25 nm after laser irradiation. It is also important to mention that presence of no element other than carbon was detected on the samples by the EDX.

It can be observed from the SEM images that diamond nucleates and grows at the tips and bends of CNTs without destroying the parent CNT structures. The structure of the CNT does not collapse after the laser irradiation. Moreover, the converted diamond tips are considerably sharp (Fig. 3.3 (f)) due to the shrinkage from the molten state of carbon during the conversion process and a smaller amount of carbon available in the hollow nanotube structure. These results show the direct formation of sharpest diamond nanoneedles and CNTs with sharpest diamond tips which can produce the largest possible field enhancement factor due to the large aspect ratio in the field emission process.

3.4.2 Raman spectroscopy

Fig. 3.4 (a-b) represent the room-temperature Raman spectra of the as-grown CNTs and the laser irradiated CNTs, respectively. The CVD grown CNT has characteristic D and G Raman bands at ~1350-1352 cm^{-1} and 1592 cm^{-1}, respectively. The Raman spectrum of the laser irradiated CNTs demonstrates a sharp peak at ~1324-1325 which is consistent with the Raman mode of a diamond crystal [27,28]. The red shift in the characteristic diamond band (from its normal position, at 1332 cm^{-1}) can be explained by a phonon confinement effect due to small grain size [29]. The intensity of the two characteristic Raman peaks, i.e.- peak related to the defect-mode (I_D) and the peak related to the graphite-mode (I_G), and the shift in the graphite-mode were analyzed to study the effect of the pulsed laser irradiation on the unconverted regions of the CNTs. The I_D/I_G ratio of the as-synthesized CNT is found to be ~ 0.5. After the laser irradiation the I_D/I_G ratio increases to ~1.4, implying the increase in the relative density of dangling bonds and crystal defects in the

CNT structures, as shown in [30]. Therefore, it is evident that the effect of the pulsed laser irradiation at the unconverted regions (middle of the CNTs) was insufficient to bring changes in the structure/bonding characteristics in a structural sense (e.g. conversion from sp^2 bonded CNTs to sp^3 bonded nanodiamond structures and/or size and distribution of the tubes), however, it induced some changes in the microscopic sense (e.g. defect density in the graphite structure of CNTs). In addition, the shift in the G-band position from 1567-1571 cm^{-1} to 1590-1594 cm^{-1}, significant amount of upshift from the original position of ordered CNTs [31], implies the presence of defects in the unconverted CNT regions due to the degeneration of the graphite structure in MWCNTs induced by the pulsed laser irradiation [32]. The insets of Fig. 3.4 (a-b) show the detail of the G-peak before and after laser irradiation. Furthermore, upon laser irradiation the graphite peaks are found to be broader due to the structural disorder. Thus the pulsed laser irradiation induces some structural changes in the unconverted CNT regions which are consistent with other studies related to the effect of the incident energetic photons on the graphite structure of CNT body at the microscopic scale [30,32,33]. The FWHMs of the diamond peaks at 1324-1325 cm^{-1} in the Raman spectra are all broad. Such broad peaks are known to be associated with nanodiamond crystallites (phonon confinement effect) [29]. The Raman results agree well with the SEM observations that diamond was directly transformed from the carbon nanotubes during the laser annealing process.

3.4.3 Electron backscattered diffraction

The phase detection and the information about the crystallographic orientation of the fixed diamond structures in an SEM instrument by means of EBSD-analysis are shown in Fig. 3.5. The Kikuchi pattern is generated by the diffracted electron beam showing the diamond crystal structure at the point where the electron beam interacts with the sample surface. The detected backscattered

patterns of electrons are analyzed by identifying and matching the angles between the detected bands to that of the standard diamond pattern. Thus, the extracted information is matched with the crystallographic information to confirm the formation of diamond phase. Fig. 3.5(a) shows the point of interaction of the incident electron beam on the sample in the high-resolution SEM image to generate a diffraction pattern. Fig. 3.5(b) shows the Kikuchi lines which closely match up with the ideal diamond pattern after a quick analysis of observed lines in the Aztec software and the indexed diffraction patterns are shown by the red lines. The possible solutions for the crystal orientation are sorted in the software library to find the best fit, and the orientation matrix is calculated which is shown in the inset of Fig. 3.5(b). Regarding the orientation, because the diffraction pattern is bound to the crystal structure of the sample, as the crystal orientation changes the resultant diffraction pattern also changes. The positions of the Kikuchi bands can, therefore, be used to calculate the orientation of the diffracting crystal. As it is evident from the well-defined electron backscattered diffraction pattern the out-of-plane orientation of the crystalline diamond tip is <101>. The <110> crystallization has been explained by a model of rapid explosive recrystallization of DLC structures [34]. The size of the electron probe was ~10 nm to obtain these three-dimensional diffraction patterns, and the characteristic EBSD patterns do not change much along the same nanofiber tip. This negligible crystallographic change in the relative orientation along a diamond tip refers to single crystal growth of the diamond rods at the CNT tips, where required undercooling is retained. Fig. 3.5 (c) shows another spot on the same nanorod (~15 nm far from the previous point) from where the EBSD pattern was obtained. The obtained EBSD pattern matched to that of the diamond and is shown in Fig. 3.5 (d). The relative orientation of the diamond nano-crystallite at this spot is shown in the inset of Fig. 3.5 (d). The relative crystal

orientation of diamond at this new point closely matches to that of the previous region, thus confirming the formation of <110>single crystal diamond upon laser annealing process.

We also obtained the Kikuchi diffraction pattern from the middle region of a CNT where the rate of undercooling was insufficient for the diamond conversion. The point of interaction is shown in Fig. 3.5 (e). The Kikuchi diffraction pattern (Fig. 3.5(f)) matches with that of the CNT suggesting the retention of the CNT structure in the middle and base of the CNTs. The relative crystal orientation at this point is shown in the inset of Fig 3.5 (f).

3.4.4 STEM and electron-energy loss spectroscopy

A detailed STEM/EELS analysis is performed on nanosecond laser annealed CNTs, as shown in Fig. 3.6. Fig. 3.6 (a) shows multiple as grown CNTs before laser annealing. A representative HAADF image of laser annealed CNTs is presented in Fig. 3.6(b), demonstrating the formation of nanodiamonds in various regions on CNTs. The average size of the nanodiamonds is estimated to be ~3 ±1 nm, while CNTs are measured to be ~7±1 nm thick. Fig. 3.6 (c-d) (taken from different regions in the sample) further show the formation of nanodiamonds on individual CNT. These two HAADF images clearly illustrate the emergence of nanodiamonds at the terminals/tips and the bends of CNTs. This supports the proposed hypothesis of diamond formation through ultrafast melting of CNT and quenching from super undercooled state. Various nanodiamonds are also observed on the body of CNTs formed under similar conditions but through partial melting of CNTs. The core loss EEL spectra (*K*-absorption edge) obtained from the nanodiamonds, CNT and nanodiamonds, and unannealed CNT are shown in Fig. 3.6 (e-g), respectively. The spectra are shown along with the reference CNT and diamond EEL spectra for the comparison. The EEL spectrum obtained from the nanodiamonds exhibit the near edge fine structure peaks at 292, 297, 305, and 326 eV, however, are broader than the typical reference spectrum from diamonds. The

broadening in the characteristic peaks is attributed to the strained nature of nanodiamonds. An EEL spectrum (Fig. 3.6(f)) is taken from one of the overlapping diamond and CNT regions which are found very frequently in the sample. The additional strong π* (284 eV) peak is clearly observed in Fig. 3.6(f), appearing due to the presence of the underlying CNT. The EEL spectrum obtained from the CNT appears to be consistent with the typical reference spectraum. It should be mentioned that under intense electron flux with prolonged acquisition time diamonds were found to convert into nanodiamonds and amorphous graphitic phase of carbon due to the small probe-size during EELS [35]. No chemical composition other than carbon was detected on the samples by the core loss spectra EEL spectroscopy.

3.4.5 Mechanism of the diamond formation

The formation of diamond occurs by the homogeneous nucleation from the highly undercooled state of carbon nanotube in the molten state. The change in Gibbs free energy (ΔG_T) associated with the formation of diamond tips consists of a gain in volume energy ($\sim r^3$) at the expense of surface energy ($\sim r^2$), where r is the radius of the diamond nucleus. So there are two contributions to the total free energy change which can be expressed by the following equation:

$$\Delta G_T = \frac{-4}{3}\pi r^3 \frac{\rho}{M_m}\frac{\Delta H_m}{T_m}\Delta T_u + 4\pi r^2 r_s \qquad (1)$$

Where ρ, T_m, M_m, ΔH_m, and r_s refer to the density of diamond, melting temperature, molar mass, latent heat of melting, and the surface free energy between diamond nuclei and the undercooled state of carbon in CNTs. The term ΔT_u $(= T_m - T_r)$ is the degree of undercooling, where T_m indicates the melting point of the initial carbon structure (~4000 K) and T_r indicates the nucleation temperature. With an increase in the value of ΔT_u, ΔG_T becomes more negative and a conversion of CNTs to diamond at the tip is favorable. The critical radius (r^*) of the nucleus and the change

in Gibbs free energy can be obtained by differentiating the equation (1) with respect to r and setting the result equal to zero:

$$\frac{d\Delta G_T}{dr} = -4\pi r^2 \frac{\rho}{M_m} \frac{\Delta H_m}{T_m} \Delta T_u + 4\pi (2r) r_s = 0 \qquad (2)$$

Equation (2) leads to the following two expressions to determine the two critical parameters-

$$r^* = \frac{2 r_s T_m M_m}{\Delta H_m \Delta T_u \rho} \qquad (3)$$

$$\Delta G_T^* = \frac{16\pi r_s 3 T_m^2 M_m^2}{3\, \Delta H_m^2 \Delta T_u^2 \rho^2} \qquad (4)$$

Equation (3) and (4) renders that increasing ΔT_u reduces the critical radius of diamond nuclei and the change in Gibbs free energy occurs even at a faster rate. The rate of nucleation (I) is given by the equation:

$$I \sim exp(-\frac{\Delta G_T^*}{kT_r}), \qquad (5)$$

Where, k is the Boltzmann constant. Therefore the rate of nucleation increases with decreasing ΔG_T^*, thereby facilitating the formation of diamond. Considering r_s = 0.6 Jm^{-2}, T_m =4000 K, ΔH_m=1.0 eV/atom, ΔT_u=1000 K, and ρ = 3.5 $gmcm^{-3}$, we determined a rough estimate of r^* ~2.0 nm for the diamond formation. Similar calculations were verified experimentally in earlier works on silicon [36,37] and diamond [34]. High ΔT_u would result in a very small ΔG_T^* (as $\Delta G_T^* \; \alpha \; 1/\Delta T_u^2$) leading to a very high rate of nucleation. But the critical radius of the diamond nuclei would be too small to facilitate the subsequent formation of diamond. So a tradeoff between ΔG_T^* and r^* are needed to attain suitable conditions for the direct conversion of single crystal growth from CNTs. This is done by the careful selection of the laser energy density for the undercooling.

The growth or crystallization velocity (v) is another important parameter for single crystal diamond formation by the laser-solid interaction. The v is directly related to the undercooling by the following equation [38]:

$$v = \frac{D_\alpha f}{\lambda f_D}\left(1 - e^{\frac{-\Delta T_u \Delta S}{kT}}\right) \qquad (6)$$

Where D_α refers to the diffusivity in the liquid state (~10^{-8} m^2/s in liquid state), f is the fraction of available sites, λ is the atomic jump distance, f_D is the geometrical factor associated with diffusion, k Boltzmann constant, T temperature of the molten state, and ΔS is the change in entropy. The value of chemical free energy barrier for the phase transformation of CNT to crystalline diamond decreases with increasing ΔT_u. Large ΔT_u simultaneously results in a high velocity of the melt-front during the solidification. Thus, the values of undercooling dictate the conversion of CNT into diamond *via* the molten phase of carbon. A slow cooling rate (low undercooling and low solidification velocity), produces crystalline graphite whereas a high cooling rate (large undercooling and large solidification velocity) results in the formation of crystalline diamond. Too high of a velocity of the melt front would produce amorphous carbon due to the lack of available time for the melted carbon atoms to take proper lattice sites of the crystal structure.

Generally, the conversion of the sp^2-bonded state to diamond requires extremely high-temperatures (5000 K) and pressures (12 GPa) [34]. However, these extreme requirements could be overcome through kinetics by bypassing the equilibrium thermodynamic route via a highly non-equilibrium laser melting and subsequent quenching phenomena. The processes by which these transformations are initiated and proceed have been understood by the recent discovery of the liquid phase mediated transformation of amorphous carbon films to Q-carbon and diamond [34]. We have followed the analogous direct transformation route to from nanodiamonds from CNTs by nanosecond laser melting of carbon and ultrafast quenching from the molten state of carbon. Rapid melting and quenching from highly undercooled state is the key to the formation of diamond. Careful selection of the laser parameters is very important for irradiating CNTs to convert into diamond. The final temperature determines the undercooling and quenching rate during pulsed

laser annealing which has been controlled by the selection of optimum laser parameters. Hence the direct conversion of CNTs into diamond is possible by the proper understanding of the kinetics and thermodynamics. The direction of the incident laser beam onto the CNTs is very important for the diamond conversion. During melting of amorphous carbon a highly undercooled state is created due to the restriction of heat flow in 1-D CNTs. The undercooled state is subsequently quenched to form nanostructures of diamond. Thus, the key consideration is undercooling which depends upon thermal properties and heat flow geometry. By simulation of the heat flow [26] and considering thermal properties for specific shapes, we can obtain laser parameters needed for the conversion into diamond. The tips and bends of CNTs directly absorb the irradiated laser energy with maximum energy density when the laser pulses irradiate the CNTs at a minimum angle, and there occurs high localized temperatures (due to restriction of the heat flow) because of high undercooling. This leads to the nucleation of diamond (from the undercooled melt of carbon) at the tips and bends of CNTs. This heat flow restriction is more relevant at the tip and at the bends where the undercooling reaches to the maximum. If the laser hits the CNTs horizontally, the heat dissipates along two directions and the undercooling is not enough for diamond formation. At the middle, the molten carbon of the CNTs may quench back to sp^2-bonded structure again due to insufficient undercooling.

3.5 Conclusions

In summary, diamond is directly formed from CNTs as a result of nanosecond laser melting of the sp^2-bonded carbon of CNTs in a super-undercooled state and subsequent ultrafast quenching. The process takes place at room temperature and pressure in air and can be scaled up easily for industrial applications by translating the sample or scanning the 100-200 Hz pulses of laser beam. The EBSD and Raman spectroscopy of the laser irradiated CNTs illustrate the structural and

bonding characteristics of diamond. The core loss EEL spectra (*K*-absorption edge) were acquired at different points on the samples, both irradiated and unirradiated, to pinpoint the diamond formation using the ultrafast route. The mechanism for forming the cubic diamond nanostructures (via the non-equilibrium route) at the tips and bends along the radial directions of CNTs is also discussed. The process can be used to fabricate phase-pure diamond rods across the scale ranging from a few nanometers to micrometers and beyond depending upon the initial size of carbon nanotubes for different applications such as wear-resistant coatings, thermal management of integrated circuits, electrochemistry, field emission devices, and electrical field shielding in MEMS and microelectronics. With these results we conclude that the controlled non-equilibrium liquid phase mediated synthesis method can be very useful to fabricate highly pure diamond from sp^2-bonded carbon phases for a host of novel applications.

3.6 Figures

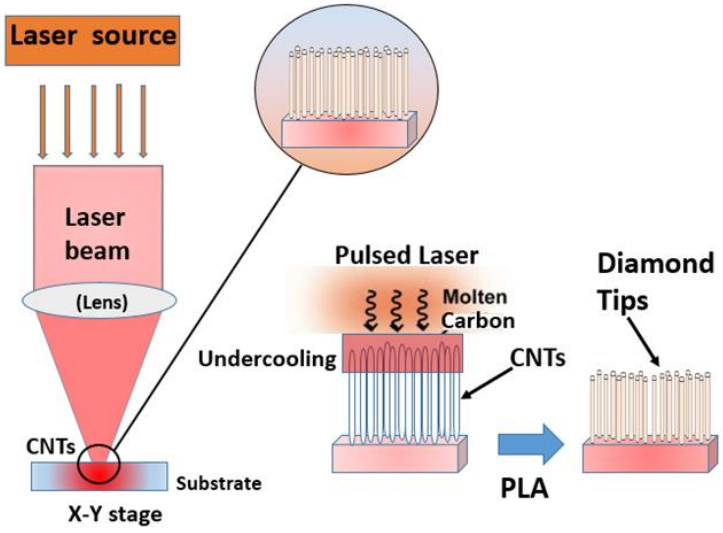

Figure 3.1**:** The proposed schematic illustration of the CNT to diamond conversion by PLA for field emission applications. The diamond tips can act as the ideal field emission sites and the carbon nanotubes with a large conductivity are the key to the electron flow to the diamond tips.

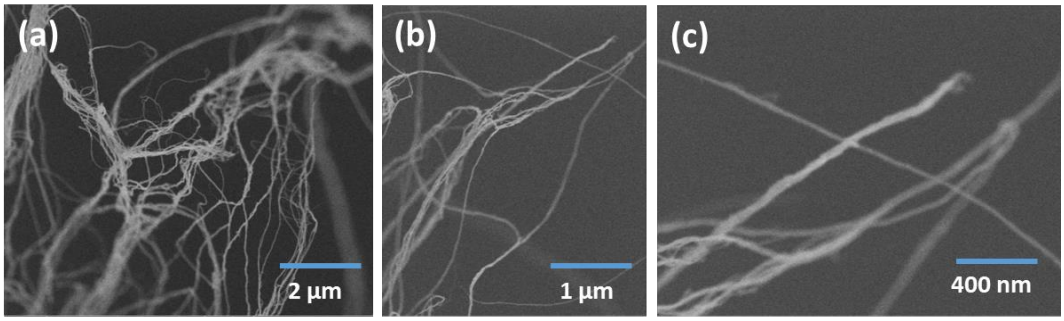

Figure 3.2**:** High-resolution SEM images of the CNT before PLA. (a) Shows the low-magnification image, (b) and (c) show high-magnification image with no evidence of diamond at the tip of CNTs.

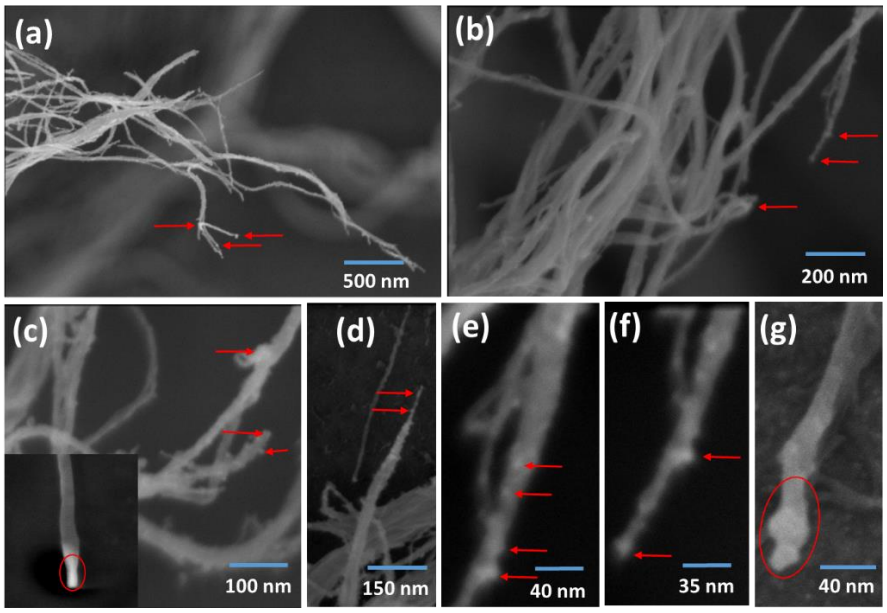

Figure 3. 3**:** High resolution SEM images of the CNT after PLA. (a) SEM micrograph showing the conversion of carbon nanotubes into diamond after 10 pulses of ArF laser (pulse duration 20ns) at 0.75-0.8 Jcm^{-2}; (b) shows no formation of diamond at the middle of CNTs, and (c) and (d) details of conversion process starting from the tips; the inset of figure (c) illustrates the conversion of the CNT tip into diamond nanorod; (e) and (f) nucleation of diamond in the middle of the nanotube and growth of diamond nanorods normal to the tube; and (g) the ultra-high-resolution SEM image shows the detail of the conversion at a single tip. This also illustrates that up to a few tens of nanometers (in length) of the CNT has been converted into a diamond nano-rod.

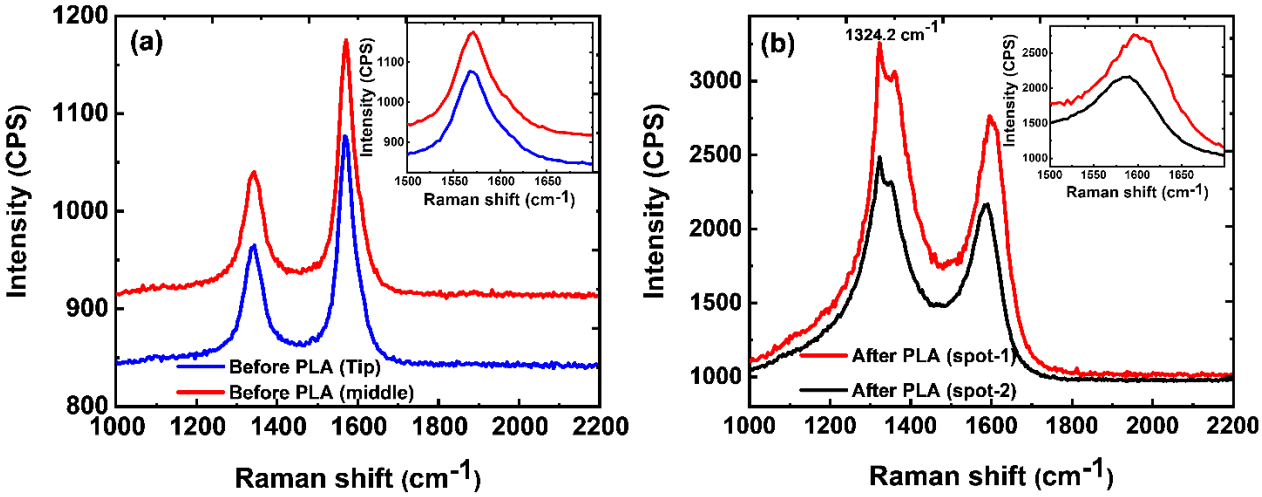

Figure 3. 4**:** (a) Raman spectra of the CNTs before PLA shows prominent D and G peaks. (b) Raman spectra after PLA. A prominent diamond peak at 1324.2 cm^{-1} illustrates the conversion of the CNT to diamond. The red shift of the peak form 1332 cm^{-1} is due to the phonon confinement effect. Inset of each figures illustrate the detail of corresponding G peaks.

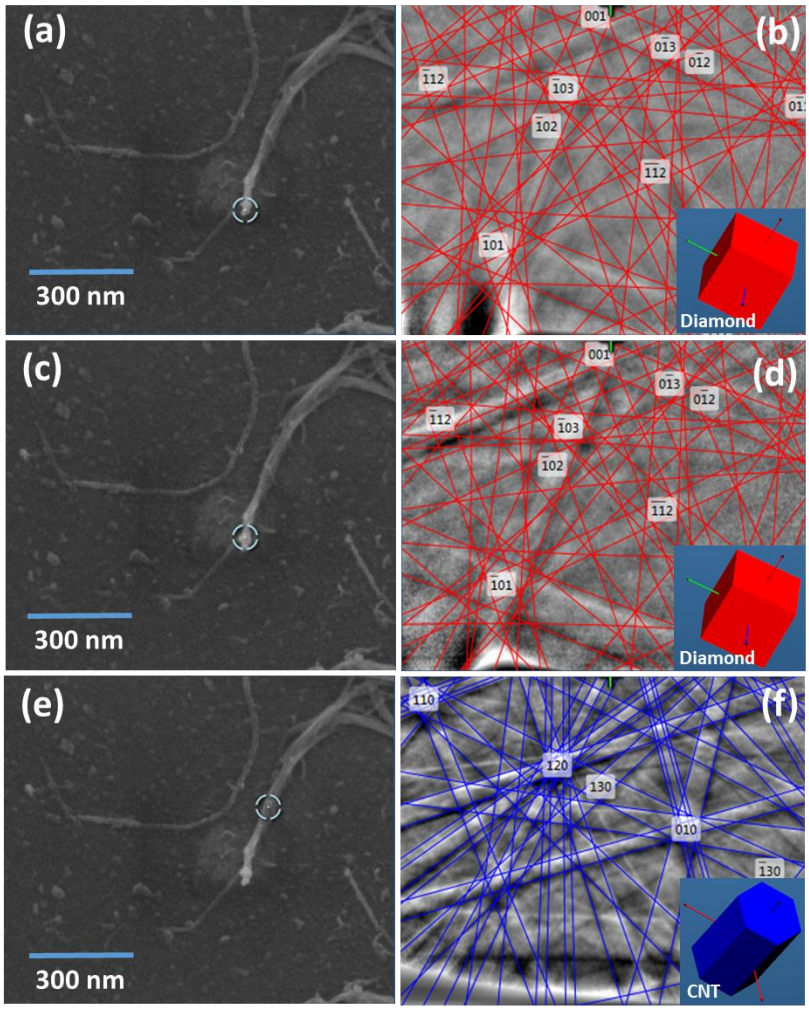

Figure 3. 5**:** EBSD patterns of diamond (b & d) and CNT (f) and corresponding SEM micrographs are presented in (a), (c), and (e), respectively. The relative orientation of diamond from the laser treated CNTs are shown in the inset of (b) and (e) by the red cubes. The inset of (f) represents the relative crystal orientation of the CNT structure.

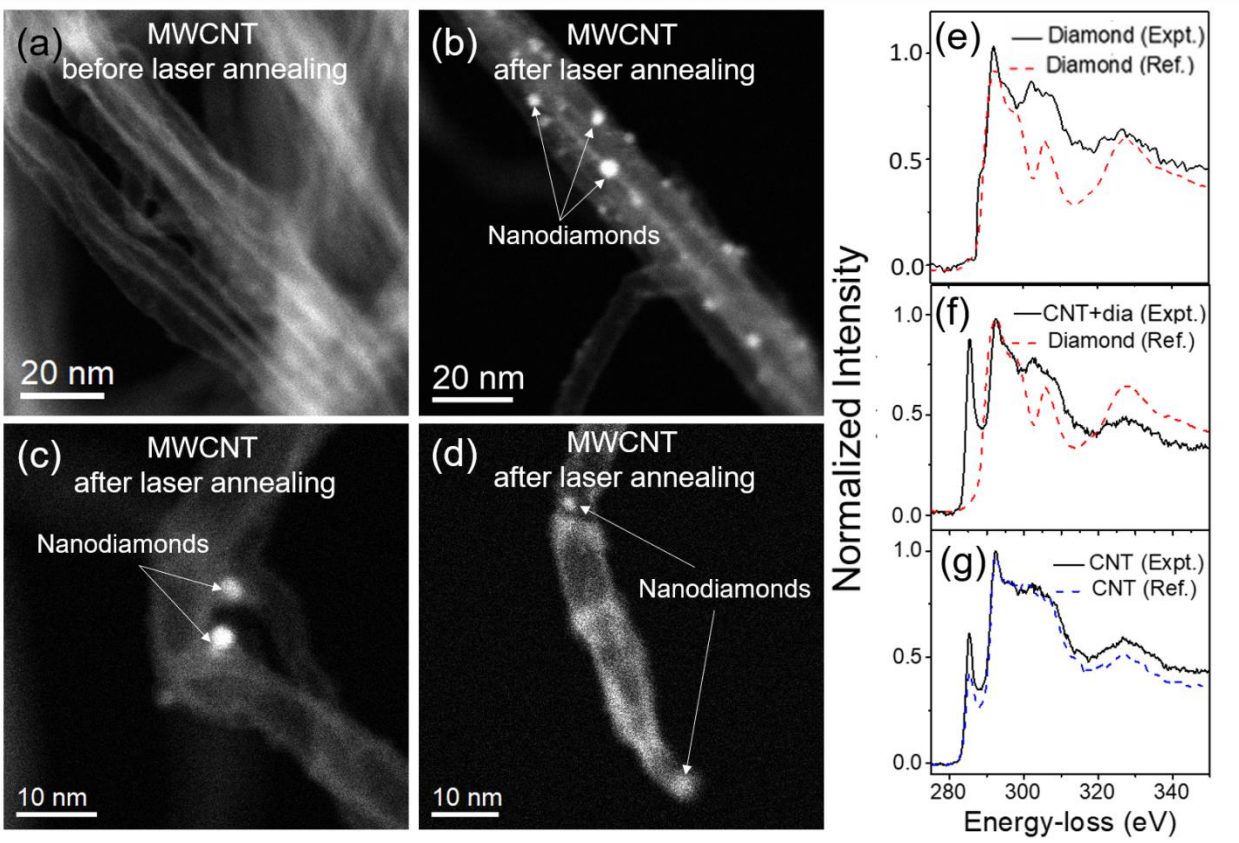

Figure 3. 6**:** (a) HAADF image of multiple as-grown CNTs, (b) HAADF image of CNT after the laser annealing showing the formation of nanodiamonds, (c) and (d) HAADF image showing the formation of nanodiamonds at a bend and the end of a single CNT, EELS spectra obtained of the regions of (e) diamond, (f) CNT and diamond and (g) pure CNT. The reference EEL spectra of the diamond and CNT are also shown in (e-g) for comparison.

References

[1] S. Iijima, Helical microtubules of graphitic carbon, Nature. 354 (1991) 56–58. https://doi.org/10.1038/354056a0.

[2] D. Tasis, N. Tagmatarchis, A. Bianco, M. Prato, Chemistry of Carbon Nanotubes, Chem. Rev. 106 (2006) 1105–1136. https://doi.org/10.1021/cr050569o.

[3] Q. Huang, D. Yu, B. Xu, W. Hu, Y. Ma, Y. Wang, Z. Zhao, B. Wen, J. He, Z. Liu, Y. Tian, Nanotwinned diamond with unprecedented hardness and stability, Nature. 510 (2014) 250–253. https://doi.org/10.1038/nature13381.

[4] H. Clevenson, M.E. Trusheim, C. Teale, T. Schröder, D. Braje, D. Englund, Broadband magnetometry and temperature sensing with a light-trapping diamond waveguide, Nat. Phys. 11 (2015) 393–397. https://doi.org/10.1038/nphys3291.

[5] A. Zkria, T. Yoshitake, Temperature-dependent current–voltage characteristics and ultraviolet light detection of heterojunction diodes comprising n-type ultrananocrystalline diamond/hydrogenated amorphous carbon composite films and p-type silicon substrates, Jpn. J. Appl. Phys. 56 (2017) 07KD04. https://doi.org/10.7567/JJAP.56.07KD04.

[6] V.N. Mochalin, O. Shenderova, D. Ho, Y. Gogotsi, The properties and applications of nanodiamonds, Nat. Nanotechnol. 7 (2012) 11–23. https://doi.org/10.1038/nnano.2011.209.

[7] A. Haque, J. Narayan, Electron field emission from Q-carbon, Diam. Relat. Mater. 86 (2018) 71–78. https://doi.org/10.1016/j.diamond.2018.04.008.

[8] Y. Tao, J.M. Boss, B.A. Moores, C.L. Degen, Single-crystal diamond nanomechanical resonators with quality factors exceeding one million, Nat. Commun. 5 (2014) 3638. https://doi.org/10.1038/ncomms4638.

[9] A. Zkria, H. Gima, T. Yoshitake, Application of nitrogen-doped ultrananocrystalline diamond/hydrogenated amorphous carbon composite films for ultraviolet detection, Appl. Phys. A. 123 (2017) 167. https://doi.org/10.1007/s00339-017-0798-4.

[10] A. Haque, J. Narayan, Stability of electron field emission in Q-carbon, MRS Commun. 8 (2018) 1343–1351. https://doi.org/10.1557/mrc.2018.172.

[11] P. Calvani, A. Bellucci, M. Girolami, S. Orlando, V. Valentini, R. Polini, D.M. Trucchi, Black diamond for solar energy conversion, Carbon. 105 (2016) 401–407. https://doi.org/10.1016/j.carbon.2016.04.017.

[12] M. Girolami, L. Criante, F. Di Fonzo, S. Lo Turco, A. Mezzetti, A. Notargiacomo, M. Pea, A. Bellucci, P. Calvani, V. Valentini, D.M. Trucchi, Graphite distributed electrodes for diamond-based photon-enhanced thermionic emission solar cells, Carbon. 111 (2017) 48–53. https://doi.org/10.1016/j.carbon.2016.09.061.

[13] P. Calvani, A. Bellucci, M. Girolami, S. Orlando, V. Valentini, A. Lettino, D.M. Trucchi, Optical properties of femtosecond laser-treated diamond, Appl. Phys. A. 117 (2014) 25–29. https://doi.org/10.1007/s00339-014-8311-9.

[14] D.R. Kania, M.I. Landstrass, M.A. Plano, L.S. Pan, S. Han, Diamond radiation detectors, Diam. Relat. Mater. 2 (1993) 1012–1019. https://doi.org/10.1016/0925-9635(93)90266-5.

[15] C.J.H. Wort, R.S. Balmer, Diamond as an electronic material, Mater. Today. 11 (2008) 22–28. https://doi.org/10.1016/S1369-7021(07)70349-8.

[16] A. Haque, S. Sumaiya, An Overview on the Formation and Processing of Nitrogen-Vacancy Photonic Centers in Diamond by Ion Implantation, J. Manuf. Mater. Process. 1 (2017) 6. https://doi.org/10.3390/jmmp1010006.

[17] S.G. Rao, L. Huang, W. Setyawan, S. Hong, Nanotube electronics: Large-scale assembly of carbon nanotubes, Nature. 425 (2003) 36–37. https://doi.org/10.1038/425036a.

[18] R.H. Baughman, A.A. Zakhidov, W.A. de Heer, Carbon Nanotubes--the Route Toward Applications, Science. 297 (2002) 787–792. https://doi.org/10.1126/science.1060928.

[19] J. Narayan, A. Bhaumik, R. Sachan, A. Haque, S. Gupta, P. Pant, Direct conversion of carbon nanofibers and nanotubes into diamond nanofibers and the subsequent growth of large-sized diamonds, Nanoscale. 11 (2019) 2238–2248. https://doi.org/10.1039/C8NR08823C.

[20] Y.Q. Zhu, T. Sekine, T. Kobayashi, E. Takazawa, M. Terrones, H. Terrones, Collapsing carbon nanotubes and diamond formation under shock waves, Chem. Phys. Lett. 287 (1998) 689–693. https://doi.org/10.1016/S0009-2614(98)00226-7.

[21] Y.-Q. Hou, D.-M. Zhuang, G. Zhang, M.-S. Wu, J.-J. Liu, Preparation of diamond films by hot filament chemical vapor deposition and nucleation by carbon nanotubes, Appl. Surf. Sci. 185 (2002) 303–308. https://doi.org/10.1016/S0169-4332(01)00988-6.

[22] H. Yusa, Nanocrystalline diamond directly transformed from carbon nanotubes under high pressure, Diam. Relat. Mater. 11 (2002) 87–91. https://doi.org/10.1016/S0925-9635(01)00532-5.

[23] L.T. Sun, J.L. Gong, Z.Y. Zhu, D.Z. Zhu, S.X. He, Z.X. Wang, Y. Chen, G. Hu, Nanocrystalline diamond from carbon nanotubes, Appl. Phys. Lett. 84 (2004) 2901–2903. https://doi.org/10.1063/1.1704856.

[24] Q. Yang, S. Yang, C. Xiao, A. Hirose, Transformation of carbon nanotubes to diamond in microwave hydrogen plasma, Mater. Lett. 61 (2007) 2208–2211. https://doi.org/10.1016/j.matlet.2006.08.060.

[25] J. Shen, F.M. Zhang, J.F. Sun, Y.Q. Zhu, D.G. McCartney, Spark plasma sintering assisted diamond formation from carbon nanotubes at very low pressure, Nanotechnology. 17 (2006) 2187–2191. https://doi.org/10.1088/0957-4484/17/9/018.

[26] R.K. Singh, J. Narayan, A novel method for simulating laser-solid interactions in semiconductors and layered structures, Mater. Sci. Eng. B. 3 (1989) 217–230. https://doi.org/10.1016/0921-5107(89)90014-7.

[27] A. Haque, P. Pant, J. Narayan, Large-area diamond thin film on Q-carbon coated crystalline sapphire by HFCVD, J. Cryst. Growth. 504 (2018) 17–25. https://doi.org/10.1016/j.jcrysgro.2018.09.036.

[28] R. Sachan, A. Bhaumik, P. Pant, J. Prater, J. Narayan, Diamond film growth by HFCVD on Q-carbon seeded substrate, Carbon. 141 (2019) 182–189. https://doi.org/10.1016/j.carbon.2018.09.058.

[29] Prawer Steven, Nemanich Robert J., Raman spectroscopy of diamond and doped diamond, Philos. Trans. R. Soc. Lond. Ser. Math. Phys. Eng. Sci. 362 (2004) 2537–2565. https://doi.org/10.1098/rsta.2004.1451.

[30] H. Li, T. Xu, C. Wang, J. Chen, H. Zhou, H. Liu, Humidity dependence on the friction and wear behavior of diamond-like carbon film in air and nitrogen environments, Diam. Relat. Mater. 15 (2006) 1585–1592. https://doi.org/10.1016/j.diamond.2005.12.048.

[31] S. Yick, A. Mai-Prochnow, I. Levchenko, J. Fang, M.K. Bull, M. Bradbury, A.B. Murphy, K. (Ken) Ostrikov, The effects of plasma treatment on bacterial biofilm formation on vertically-aligned carbon nanotube arrays, RSC Adv. 5 (2014) 5142–5148. https://doi.org/10.1039/C4RA08187K.

[32] A.C. Ferrari, Raman spectroscopy of graphene and graphite: Disorder, electron–phonon coupling, doping and nonadiabatic effects, Solid State Commun. 143 (2007) 47–57. https://doi.org/10.1016/j.ssc.2007.03.052.

[33] C.-H. Li, H.-C. Liu, S.-C. Tseng, Y.-P. Lin, S.-P. Chen, J.-Y. Li, K.-H. Wu, J.-Y. Juang, Enhancement of the field emission properties of low-temperature-growth multi-wall carbon nanotubes by KrF excimer laser irradiation post-treatment, Diam. Relat. Mater. 15 (2006) 2010–2014. https://doi.org/10.1016/j.diamond.2006.09.017.

[34] J. Narayan, A. Bhaumik, S. Gupta, A. Haque, R. Sachan, Progress in Q-carbon and related materials with extraordinary properties, Mater. Res. Lett. 6 (2018) 353–364. https://doi.org/10.1080/21663831.2018.1458753.

[35] S. Talapatra, J.-Y. Cheng, N. Chakrapani, S. Trasobares, A. Cao, R. Vajtai, M.B. Huang, P.M. Ajayan, Ion irradiation induced structural modifications in diamond nanoparticles, Nanotechnology. 17 (2005) 305–309. https://doi.org/10.1088/0957-4484/17/1/052.

[36] J. Narayan, C.W. White, Pulsed laser melting of amorphous silicon layers, Appl. Phys. Lett. 44 (1984) 35–37. https://doi.org/10.1063/1.94594.

[37] J. Narayan, C.W. White, O.W. Holland, M.J. Aziz, Phase transformation and impurity redistribution during pulsed laser irradiation of amorphous silicon layers, J. Appl. Phys. 56 (1984) 1821–1830. https://doi.org/10.1063/1.334192.

[38] S.T. Picraux, D.M. Follstaedt, Surface Modification and Alloying: Aluminum, in: J.M. Poate, G. Foti, D.C. Jacobson (Eds.), Surf. Modif. Alloy. Laser Ion Electron Beams, Springer US, Boston, MA, 1983: pp. 287–321. https://doi.org/10.1007/978-1-4613-3733-1_11.

4. Pseudo-topotactic growth of diamond nanofibers

J. Narayan[1], A. Bhaumik[1], A. Haque[1]

[1]Department of Materials Science and Engineering, North Carolina State University, Raleigh, NC, 27695, USA

4.1 Abstract

We report pseudo-topotactic growth of single-crystal diamond fibers by nanosecond laser melting of amorphous carbon nanofibers (CNFs) and crystalline multi-wall carbon nanotubes (MWCNTs). A rapid laser melting in a super undercooled state and subsequent quenching convert the tips of CNFs and MWCNTs into phase-pure <110> nanodiamonds along the growth directions. Subsequent laser pluses melt regions below <110> nanodiamonds that provide seeds for epitaxial growth. By repeating this process, the length of <110> nanodiamond fibers can be increased, as each pulse results in ~50nm nanodiamond region, depending upon the initial size of CNFs and MWCTs. This conversion process can be carried at ambient temperature and pressure in air. The epitaxial nature of <110> nanodiamond fibers has been confirmed by systematic electron-back-scatter-diffraction studies along the fiber in high-resolution scanning electron microscopy, and high-resolution TEM imaging and diffraction. The nature of C-C bonding characteristics was studied by high-resolution electron-energy-loss spectroscopy to establish the formation of diamond phase by the characteristic peak at 292 eV for sp^3 bonding (σ^*), and absence of 284 eV peak for sp^2 (π^*) graphitic bonding. The characteristic diamond Raman peak at 1332 cm^{-1} is found to downshift to 1321cm^{-1} because of phonon confinement in nanodiamonds associated with nanofibers. These nanodiamond structures can be doped with both n- and p-type dopants with concentrations far higher than thermodynamic solubility limit due to solute trapping during

quenching from the liquid phase. Thus, these nanodiamond structures provide ideal platform for nanosensing, computing and communication, including efficient field emitting devices.

4.2 Introduction

Direct conversion of carbon into diamond occurs thermodynamically under equilibrium at high temperatures (5000K) and pressure (12 GPa) in an inert atmosphere. These temperatures and pressures can be reduced somewhat in the presence of catalysts. Because of the high-temperature and pressure requirements, diamond in the form bulk grits has limited yield and is often contaminated as a result of fast diffusion at high temperatures. Recently, we reported direct conversion of amorphous carbon films into phase-pure diamond in the form of nanodots, nanoneedles, microneedles, microdiamonds and single-crystal thin films at ambient temperature and pressure in air [1]. In this nonequilibrium conversion process, carbon is melted by nanosecond laser pulses in a super undercooled state and quenched rapidly, where kinetics overrules thermodynamics. These diamond structures were doped with *n*- and *p*-type dopants, where concentrations were found to exceed equilibrium thermodynamic solubility limits as a result of rapid quenching from liquid and solute trapping phenomenon [2]. We were able to control nature and number density of defects in diamond more precisely from liquid phase growth, where defect density can be minimized for solid-state devices, as the annealing of as-grown defects in these materials require annealing temperatures exceeding 1700^0C. Recently, we reported direct conversion of carbon fibers and tubes into diamond after pulsed laser melting and quenching [3]. In both nanofibers and nanotubes, the degree of undercooling was found to be critical for the conversion into diamond. If the undercooling was not enough, molten carbon was quenched back to amorphous carbon with a mixture of sp^3 to sp^2 bonding. Our previous works focused on thin film conversion and did not address the formation of single-crystal diamond nanofibers.

Other studies have reported the conversion of carbon nanotubes into diamond through the formation of carbon onion phase *via* solid-phase transformation. One study involved CO_2 CW laser irradiation of carbon nanotubes on a cast iron substrate [4]. In another study, the formation of diamond nanocrystals at the tips of carbon nanofibers was reported after spark plasma sintering at 1500^0C and atmospheric pressure as a result of the formation by an intermediate phase of carbon onion [5]. Similarly, the conversion of tips of multi-walled carbon nanotubes (MCNTs) into diamond was found after spark plasma sintering at 1200^0C, again invoking the formation of an intermediate carbon onion phase [6]. Ballistic fracturing of CNTs can also lead to formation of nanodiamonds [7], which is similar to diamond formation at high pressures and temperatures (4.5 GPa at 1300^0C) [8]. The formation of different forms of amorphous carbon, including nanodiamonds by using pulsed laser irradiation (266 nm NdYAG laser with 3 ns pulse duration and 40-100 $mJcm^{-2}$) of MWCNTs in nitrogen atmosphere has been reported [9]. However, characteristic Raman (near 1332 cm^{-1}) and EELS (at 292 eV) peaks for the diamond phase were not observed. It is envisaged that required undercooling for diamond formation under these laser irradiation conditions is not achieved, which is the key to the formation of diamond phase. However, none of these previous methods invoked melting and undercooling as the mechanism for conversion of carbon-based structure into diamond. The essence of our work is melting under highly undercooled state and quenching to convert entire volume into phase-pure diamond. The first-order phase transformation associated with melting plays a critical role in the formation of phase-pure diamond, unlike other processes.

More recently, the conversion of carbon nanotubes into T-carbon and pseudo topotactic growth has been reported by using pico-second laser irradiation, which does not involve melting [10]. In

this work, topotactic growth was attributed to electronic excitations without clarifying the mechanism of first-order phase transformation needed for topotactic growth.

We introduced an interesting idea of nanosecond laser melting of carbon and direct conversion of carbon nanofibers and nanotubes into diamond nanofibers [3,11]. Thus nanosecond laser melting resulted in first-order phase transformation needed for topotactic growth. In this paper, we showed rather direct evidence of topotactic growth to form single-crystal diamond nanofibers, carried out very detailed high-resolution TEM, SEM (EBSD), EELS, and Raman characterization, and provided first model for topotactic growth based upon our earlier work on unseeded crystallization [12]. These nanostructures are ideally suited for applications ranging from enhanced catalysis to field emission.

4.3 Experimental

We synthesized CNFs in a tube furnace (CVD chamber) with flowing Ar (450 sccm) and H_2 (10 sccm) at 800°C by introducing 25 sccm of C_2H_4 for 30 min with additional details [3]. These CNFs are irradiated in air with ArF laser pulses (pulse duration = 20ns, wavelength = 193nm, energy density = 0.6-1.0 Jcm^{-2}). The laser beam size is about 10x10mm, which can be varied with the out of laser energy. The restriction of heat flow in one-dimensional caused melting of amorphous carbon in a highly undercooled state. The subsequent quenching from the undercooled state resulted in the formation of nanostructures of diamond. As the number of nanosecond laser pulses is increased, the length of converted diamond region is increased to cover the entire length of the fiber. The laser processing can be scaled up to produce 100-200 cm^2 area per second by using 100-200Hz (repetition rate) ArF Excimer laser. The CNFs (before and after PLA processing) are dispersed in ethanol and capture onto copper TEM grids. To facilitate the bleeding of electronic charges, the sample is sandwiched between two copper grids and then

mounted in the TEM sample holder. The multi-walled CNTs were grown using a thermal CVD system. The substrate, a smooth Si wafer, was placed at the center of the horizontal quartz tube inside the furnace (30 cm in length and 4 cm in diameter). The $FeCl_2$ powder (~99.9% pure) in a quartz boat was also placed inside the quartz tube which acted as a catalyst during the synthesis of the CNTs. Detailed high resolution TEM/STEM and EBSD measurements did not show the presence of any Fe nanoparticles associated with CNTs before and after laser annealing. The EDAX analysis showed only trace amount of Fe in CNTs. The chamber pressure was maintained at 10^{-3} Torr during the heating cycle, and the chamber was purged with acetylene (98%) using a mass flow controller once the furnace temperature reached to 820°C. At this stage, the furnace temperature remained constant and the pressure was maintained at 10 Torr for two hours for CNT growth. The CVD grown CNTs were mounted on a laser irradiation holder, and the surface was irradiated with a pulsed ArF laser (Lambda Physik, 193 nm wavelength, and 20 ns pulse duration) in the air. The laser energy density was ~ 0.65-0.8 J/cm^2, which leads to a highly undercooled state needed to form diamond. The ultrafast pulse- laser annealing technique melts the CNT tips and bends from which rapid explosive recrystallization occurs upon quenching to form phase-pure single crystal diamond structures. We have characterized these structures by TEM, SAED, EBSD, SEM, and Raman spectroscopy (using 532 nm laser). High-resolution SEM (and EDX) and EBSD (electron-scatter-back diffraction) measurements were carried out in FEI Verios 460L SEM and FEI Quanta 3D FEG FIB-SEM, respectively. The EBSD technique provides accurate three-dimensional (Kikuchi) diffraction patterns for phase identification, where structural morphology is simultaneously determined by high-resolution SEM. A HORIBA Xplora PLUS confocal Raman microscope having 0.5 □m spatial resolution and 532 nm excitation source was used for determining the Raman active vibrational characteristics of carbon and diamond nanofibers and

nanotubes. The Raman spectroscopy provides a distinctive identification of diamond and related materials. Aberration-corrected STEM-FEI Titan 80-300 was used to acquire HRTEM and HAADF images and EEL spectra of diamond nanofibers. In this experiment, the microscope was operated at an accelerating voltage of 200 kV and the electron probe current of 38 ± 2 pA. The convergence and collection angles in the experiments were 19 and 65 mrad, respectively. The EELS data were acquired with a collection angle of 28 mrads.

4.4 Results and discussion

The primary focus of this work is on the formation of single-crystal diamond nanofibers as a function of number of laser pulses. We present a model of crystal growth to explain epitaxial growth of diamond nanofibers as a function of number of laser pulses during melting of amorphous carbon nanofibers and nanotubes. The formation of beads at the tips of nanofibers and nanotubes provides a direct evidence for the melting. The diamond formation starts at the tips and bends, which propagates with the number of pulses to cover entire lengths of fibers and tubes. From this work, we have established that there is a critical diameter for a complete conversion into diamond. Above this critical size, diamond nanocrystallites are formed on the surface, some of these grow rapidly to form diamond nanorods perpendicualr to the fiber. Fig. 4.1(a) shows high-resolution SEM micrograph of a typical pristine carbon nanofiber before laser irradiation, where the structure is amorphous, as determined by EBSD (SEM). After a single laser shot, fiber tips melt as beads (Fig. 4.1(b)) and turn into diamond. Diamond phase identification has been carried out carefully using EBSD (SEM), HRTEM, EELS and Raman. The orientation of diamond nanocrystal was determined by EBSD after the first pulse, and it was found to be <110>, as a result of rapid unseeded crystallization.[11] The growth of <110> crystallites after rapid crystallization has been extensively studied and modeled for silicon. After 5, 10 and 20 laser pulses, we see successive

conversion into diamond in Fig. 4.1(c-e), respectively. With each shot, there is a successive increase by about 50-100nm, as labelled in Fig. 4.1(b-d). From the characteristics of diamond formation with increasing number of laser pulses, it is argued that each shot melts about 50-100nm long region, which is quenched from a highly undercooled state to form diamond. The length of diamond converted region depends upon the fiber diameter and orientation of the fiber with respect the laser beam. For each successive laser shots, previous diamond grain provides a template for epitaxial topotactic growth of diamond, as only carbon below the diamond seed melts. This epitaxial topotactic growth is quite unique for the formation of diamond nanofibers from carbon nanofibers and nanotubes.

Fig. 4.2 shows a similar topotactic growth from the top of diamond fibers from multi-wall carbon nanotubes (MWCNTs) with increasing number of laser pulses. Fig. 4.2(a) shows high-resolution SEM from as-grown pristine nanotubes before laser annealing. The formation of diamond at the tips is shown after single laser pulse (energy density = 0.65 Jcm^{-2}) in Fig. 4.2(b) and (c). As the number of pulses is increased, the epitaxial conversion starts from the top and moves downwards with each pulse, as shown for 5 and 10 pulses in Fig. 4.2(d) and Fig. 4.2 (e), respectively. The carbon to diamond process in the case of nanotubes is similar to that of nanofibers, and it is more efficient for both nanotubes and fibers which are aligned with the laser beam. The diameter of carbon nanotubes (mostly double-walled) ranged from 10-50nm with over 300nm in length. These results show the formation of sharpest diamond nanoneedles by this direct conversion of carbon nanotubes into diamond.

The crystal structure determination of as-grown DNFs was carried out by the electron beam scatter diffraction (EBSD) technique in the high-resolution SEM. The EBSD patterns provide 3-D Kikuchi patterns with characteristic crystal structure and detailed three-dimensional orientation

relationship. The size of electron probe used for EBSD is ~10 nm and thus it is ideal for determination of structure along the length of the diamond fiber. Epitaxial growth was investigated by EBSD patterns along the length of the fibers, as shown in Fig. 4.3. The <110> EBSD patterns provide diamond phase identification, as shown by unique color-coding. The <110> orientation was found to be unchanged along the carbon fiber, which demonstrates epitaxial topotactic growth, where diamond crystallites grow with the number of laser pulses with top crystallite providing as a seed for subsequent crystal growth.

The atomistic details of epitaxial growth were studied by using high-resolution TEM. Fig. 4.4(a-c) show high-resolution TEM micrographs in [-110] zone axis with increasing magnification. The orientation of {111} planes of diamond with 0.206nm spacing with respect to <110> growth axis is clearly depicted. Fig 4.4(b) also shows the interface between two epitaxial crystallites with some nanopockets of amorphous carbon trapped in the interface region. However, there is enough connection between two crystallites (lower left of Fig. 4.4(b)) to provide an epitaxial template for growth. Two sets of {111} planes along with <110> are clearly imaged in Fig. 4.4(c), which is a characteristic diamond-cubic-lattice structure [12]. The Fourier-transformed diffraction pattern in the inset of Fig. 4.4(c) clearly shows<110> growth direction, as shown in the schematic of Fig. 4.4(d). The schematic shows <110> closed-packed chains, which are formed during rapid crystallization. This <110> growth can occur without a seed, that is how the first diamond crystallite is formed, which acts as a template for successive laser pulses and formation of diamond crystallites. According to our model, the formation of <110> diamond nanocrystallites at the tips of carbon nanofibers and nanotubes occurs by the process of unseeded crystallization of diamond cubic lattice structure. The <110> orientation is preferred due to <110> closed-packed chains, which provide growth sites for rapid growth. The details of this model with experimental results

were presented earlier for silicon <110> growth under unseeded condition [12]. These <110> crystallites at the tips after the first pulse provide seeds for topotactic growth.

The bonding characteristics of carbon nanofibers before and pulsed laser annealing were investigated by electron energy loss spectroscopy, as shown in Fig. 4.5. The EEL spectrum of carbon nanofibers before annealing contains π^* peak at 285 eV corresponding to sp^2 bonded carbon. After laser annealing, the EEL spectrum shows the characteristic σ^*peak corresponding to sp^3 bonded carbon in diamond. A small intensity of π^* peak is attributed to some disordered carbon present at the interfaces. Fig. 4.6 shows Raman results from carbon nanofibers before and after PLA treatment. The Raman peak corresponding to nanodiamonds is observed ~1321 cm^{-1} in the CNF samples after the PLA processing. The downshift of ~11 cm^{-1} (from 1332 cm^{-1} in microdiamonds) and spectral broadening are attributed to phonon confinement [13] in nanodiamonds (formed after PLA). The D, G and 2D peaks originate primarily from unconverted amorphous carbon. Therefore, Raman spectra provide a reliable and consistent evidence for the formation of nanodiamomds as a result of nanosecond laser melting and quenching, and direct conversion of CNFs and nanotubes into DNFs after the PLA treatment.

Fig. 4.7 shows a theoretical calculation of temperature (a) and melt depth (b) as function of time of laser annealing. The carbon is melted in a highly undercooled state, and subsequent quenching leads to direct conversion of carbon into diamond. The melting starts after about 10ns of the incidence of the laser pulse, melt-in front rapidly penetrates up until the end of the laser pulse. After that solidification occurs to forma diamond. As shown in the plot, solidification velocity is of the order 2-5ms^{-1}. The temperature profile in Fig 4.7(a) shows that amorphous carbon melts ~4000K in a highly undercooled state, close to 1000K below the equilibrium melting of carbon. The pulsed laser annealing process is carried out in atmospheric pressure and room

temperature in air. No other sources of heat are applied during the conversion. The temperature ~4000 K is attained after laser-carbon interaction, which results in a melting. This undercooled state results in the formation of diamond upon quenching. During the transformation of CNTs and CNFs, the temperature rises locally to 4000K, but it is for very short time, less than 50ns in this case. As a result, overall temperature rise of the system is less than 5K. These calculations were performed by using SLIM (simulation of laser interaction with materials) program [14]. The nanosecond pulsed laser annealing of nanofibers leads to melting of carbon, and subsequent quenching from a highly undercooled state leads to a direct conversion of carbon into diamond. Our earlier studies on melting of amorphous carbon films on sapphire (0001) substrates showed that molten carbon was converted into diamond at an undercooling ~1000K, and into a new form of carbon (named Q-carbon) at a higher undercooling at ambient temperatures and pressures in air [1,15–17].

The formation of DNFs involves nucleation and growth of diamond from highly undercooled molten carbon, which results from nanosecond laser melting. The nucleation and growth of diamond starts from the tips of carbon nanofibers with <110> oriented diamond seed of about 50nm length. During next pulse this <110> diamond acts as a seed to create next 50nm segment. This is referred to as topotactic growth, where the diamond seed after the pulse provides a template for the next pulse. Thus, by increasing the number of pulses, an entire length of nanofiber can be converted into epitaxial diamond nanofibers. Using the homogeneous diamond nucleation model, we estimated the critical size of the nucleus ~2nm. From SLIM simulation [14], we estimated growth velocity and time of growth to be $5.0ms^{1}$ and 10ns, respectively. This leads to 50nm long diamond crystallite with <110> orientation via unseeded crystallization. The details of diamond nucleation and growth modeling are published in an earlier paper [1,3,18]. These results on

diamond are entirely consistent with our previous work on melting of amorphous silicon by nanosecond lasers [19–21]. Since these DNFs are formed after rapid laser melting and quenching, they can be doped with p- and n-type dopants. Using CVD based methods, diamond structures could be doped only with boron (p-type) dopants. Under rapid quenching, we are able increase p- and n-type dopant concentrations far beyond the thermodynamic solubility limits. Using this approach, DNFs can be doped with N and Si to create N-V and Si-V centers for applications related to atomic sensing, quantum communication, and quantum computing. The DNFs and their heterostructures will also have exciting applications ranging from drug delivery to cellular sensors [22]. Another important consideration for diamond structures and devices relates to control of defects and elimination of defects during crystal growth itself. Higher formation and migration of point defects in diamond lead to defect annealing temperatures exceeding 1700^0C, at which diamond oxidizes and reverts to equilibrium graphite phase [23]. Since the nanosecond laser annealing is completed with a microsecond, which is nucleation time for defects such as dislocations, it is possible to create dislocation-free crystals using the nanosecond laser melting and quenching approach.

4.5 Summary

We have obtained epitaxial growth of diamond nanofibers by nanosecond laser melting of carbon nanofibers and nanotubes in a super undercooled state and subsequent quenching. First laser pulse melts the tips of carbon nanofibers and nanotubes and results in the formation of <110> diamond crystallites via unseeded crystallization. These <110> diamond seeds provide epitaxial template for diamond growth with increasing number of pulses. The formation of diamond phase occurs by direct conversion of carbon into diamond at ambient temperature and pressure in air. The structural characteristics of diamond have been confirmed by high-resolution SEM and EBSD

and high-resolution TEM/STEM , and bonding characteristics by STEM/EELS and Raman. This process can be applied to cover a large area over 100 to 200 cm^2 area per second using 100 to 200 Hz (repetition rate per second). The diamond-tipped carbon nanofibers and carbon nanotubes grown on conducting substrates provide ideal platform for field emitting devices needed for next-generation contact-less energy-transfer systems and motors. These nanofibers can be doped selectively with *n*- and *p*-type dopants with concentrations far exceeding thermodynamic solubility limits, by incorporating dopants before melting for a variety of potential applications ranging from atomic sensors to efficient catalysts and field emitters. This discovery of conversion of carbon nanofibers and nanotubes into diamond nanofibers at ambient temperature and atmospheric pressure in air will open a new frontier for synthesis and processing of diamond nanostructures for a variety of applications, ranging from quantum computing, sensing and communication to field emission.

4.6 Figures

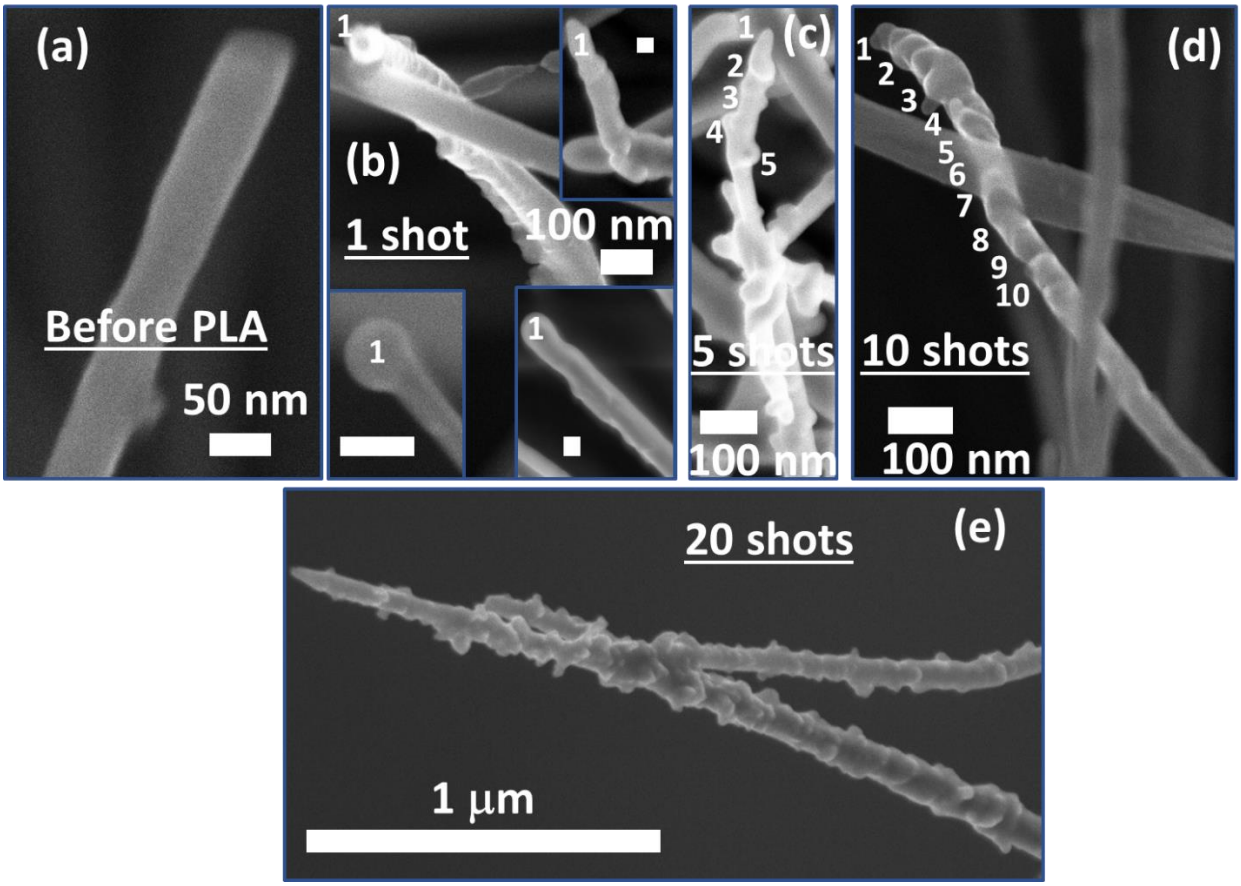

Figure 4. 1**:** SEM micrographs of CNFs before PLA (a), after 1 laser shot showing the formation of diamond at the tip (b), after 5 laser shots (c), after 10 laser shots (d), and after 20 laser shots (e).

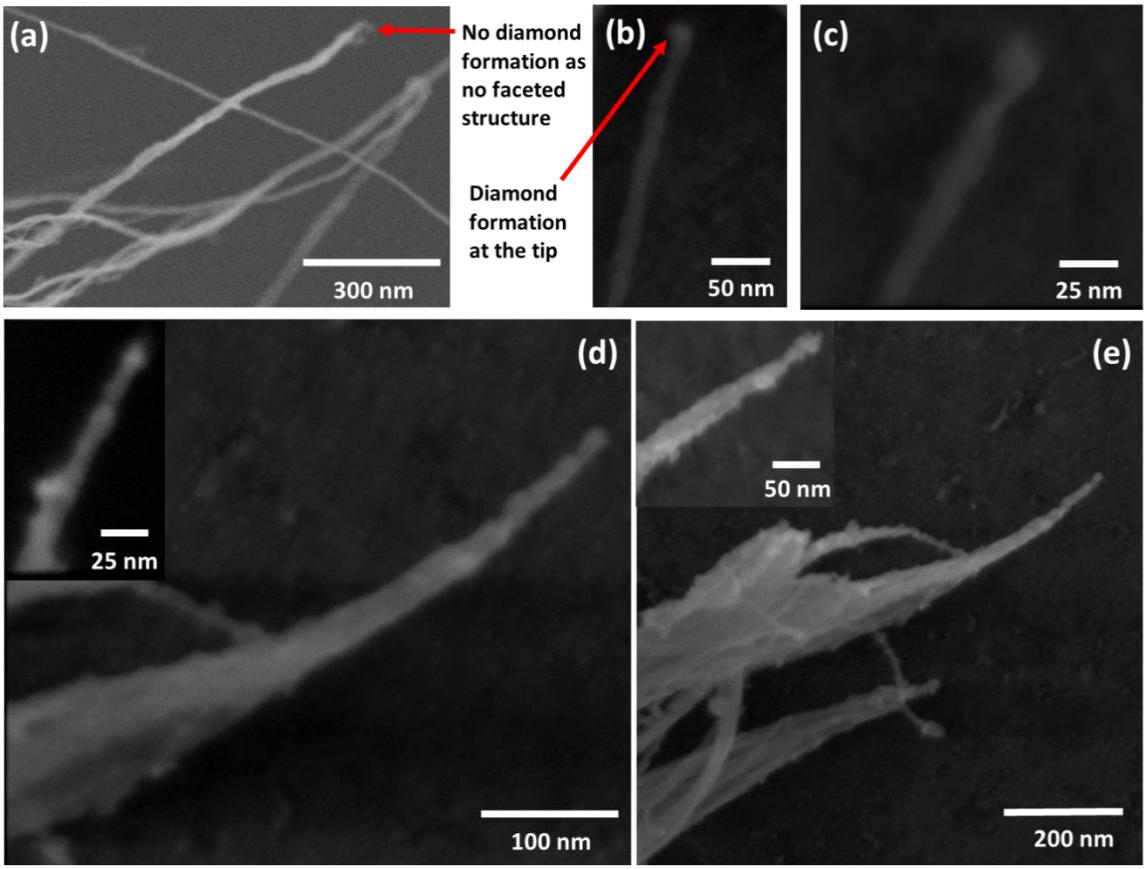

Figure 4. 2**:** Detail of the conversion of carbon nanotubes into diamond nanorods starting from the tips; (a) CVD grown CNTs without PLA. (b) and (c) high-resolution SEM micrographs showing conversion of carbon nanotubes into diamond only at the tip after a single pulse of an ArF laser (pulse duration 20 ns) at 0.65 J cm^{-2}, (d) shows the propagation of the diamond formation after 5 laser pulses, and (d) illustrates more diamond conversion (more faceted structures are seen) after 10 laser pulses. It is noted that the converted nanodiamonds at the tip do not get affected by the successive laser pulses as they can dissipate the heat through the structure to the unconverted CNT region owing to the high thermal conductivity of diamond.

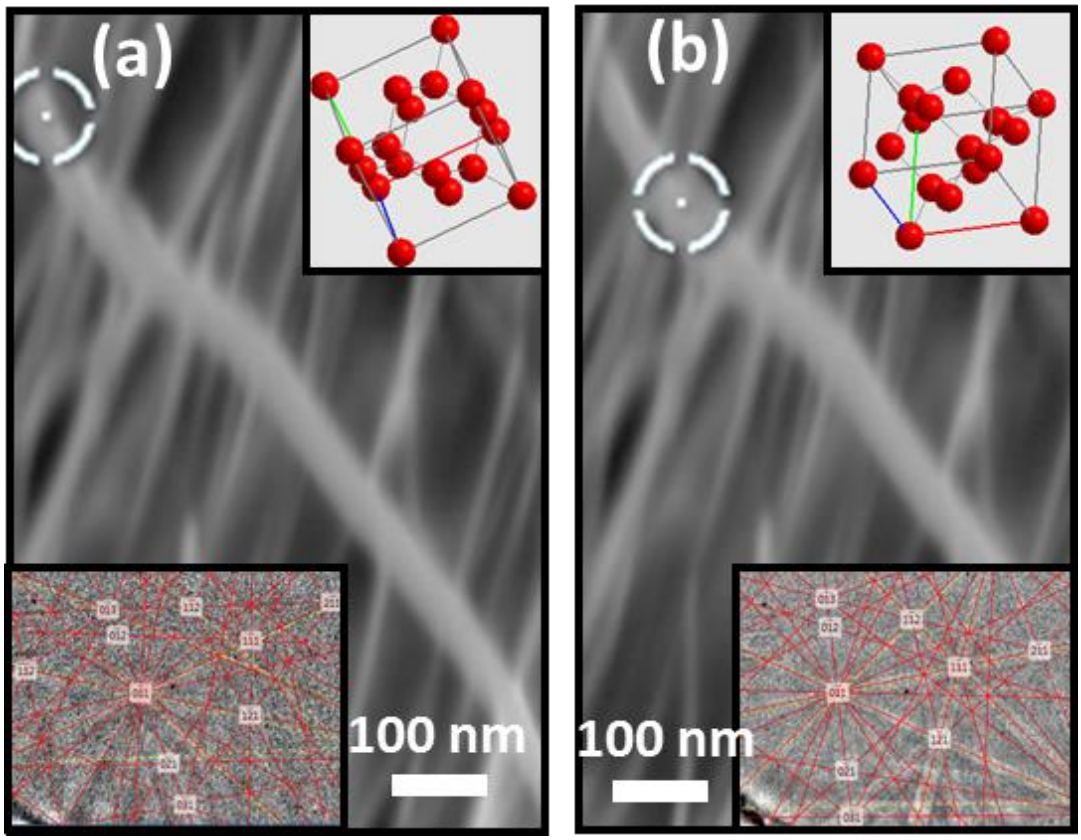

Figure 4. 3**:** EBSD-SEM micrographs of (a) tip of the CNF after PLA, and (b) just below the tip of the same CNF after PLA with the insets showing the Kikuchi diffraction pattern and the corresponding crystal orientation of the diamond (formed at the tip of CNF after the PLA).

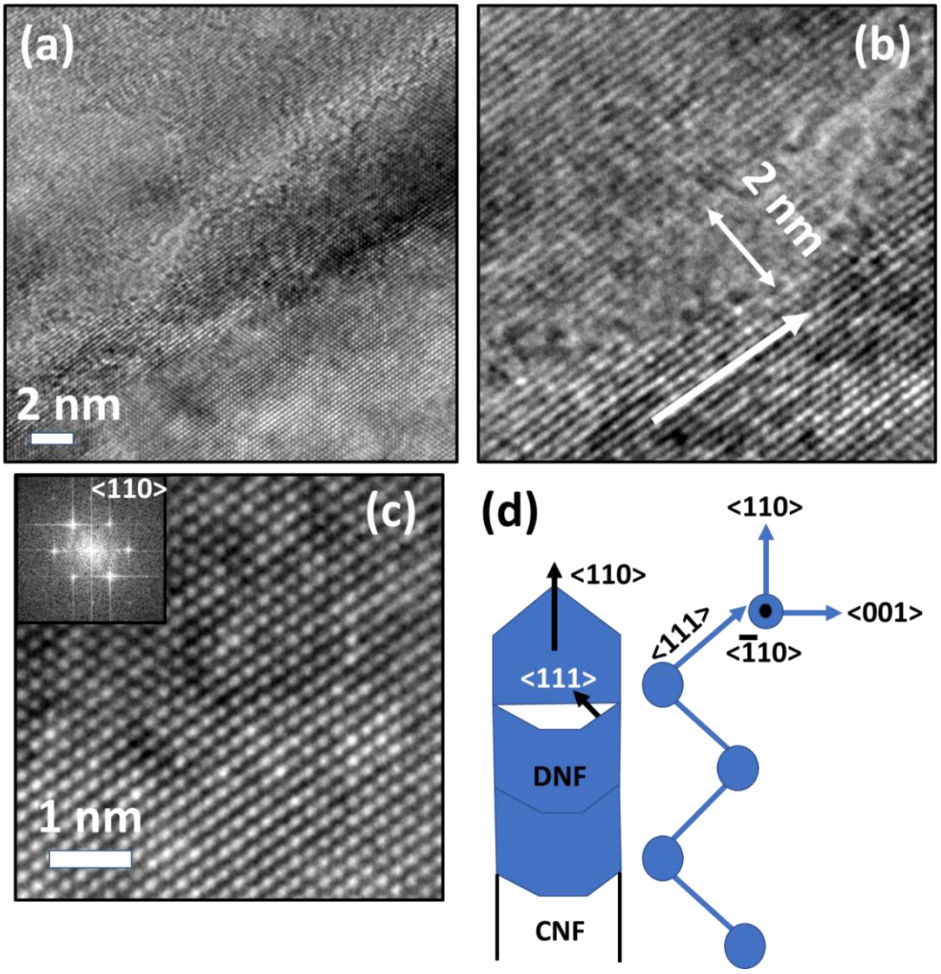

Figure 4. 4**:** (a-c) High-resolution TEM micrographs in [-110] zone axis with increasing magnification, and (d) Model for the topotactic growth of diamond after the PLA where the <110> crystallites at the tips after the first pulse provide seeds for further growth. Figure 4 (b) clearly shows the interface between two epitaxial crystallites with nanopockets of amorphous carbon trapped (~ 2 nm) in the interface region. However, there is enough connection between two crystallites (lower left of Fig. 4(b)) to provide an epitaxial template for growth. The two sets of {111} planes along with <110> columns are clearly imaged in Figure 4 (c), which is a characteristic diamond-cubic-lattice structure. The Fourier-transformed diffraction pattern in the inset of Fig. 4(c) clearly shows the <110> growth direction, as shown in the schematic of Figure 4(d).

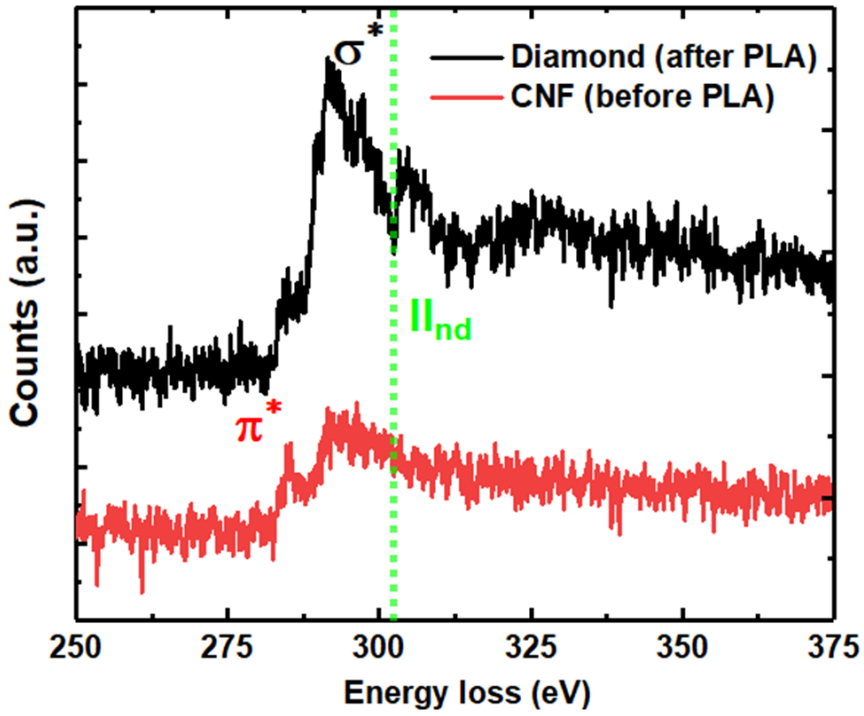

Figure 4. 5**:** EELS of CNF before PLA and after PLA showing the formation of diamond (after PLA) having the characteristic σ* peak and IInd absolute band gap.

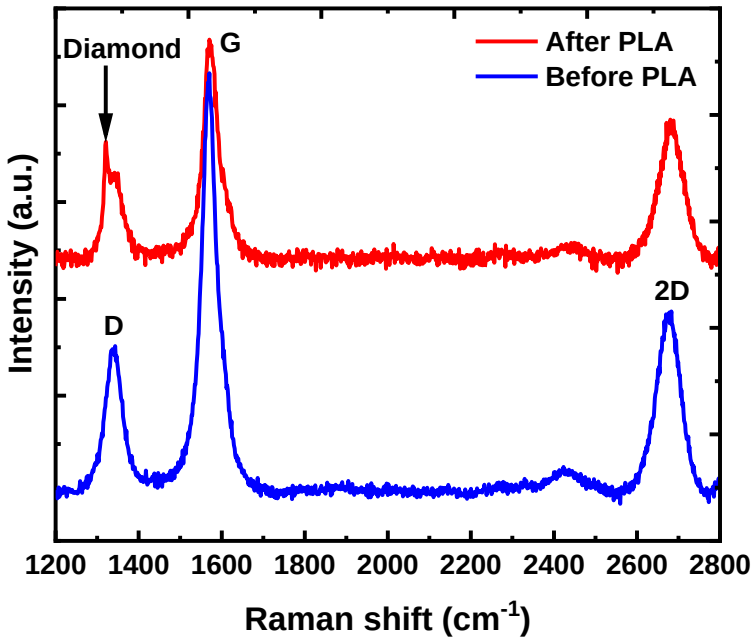

Figure 4. 6**:** Raman spectrum of CNF before PLA and after PLA showing the formation of diamond after the PLA. The diamond peak is formed at 1321 cm^{-1} due to phonon confinement.

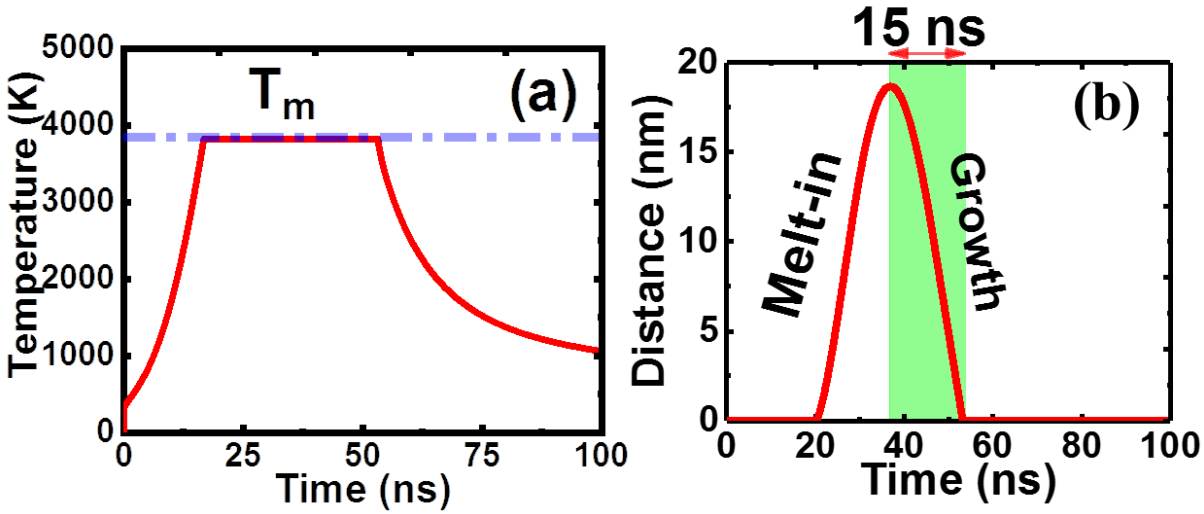

Figure 4. 7**:** Simulation of laser interaction with materials (SLIM) program showing the temperature *vs* time profile (a) and melt-in and growth regions (b).

References

[1] J. Narayan, A. Bhaumik, Research Update: Direct conversion of amorphous carbon into diamond at ambient pressures and temperatures in air, APL Mater. 3 (2015) 100702. https://doi.org/10.1063/1.4932622.

[2] J. Narayan, A. Bhaumik, S. Gupta, A. Haque, R. Sachan, Progress in Q-carbon and related materials with extraordinary properties, Mater. Res. Lett. 6 (2018) 353–364. https://doi.org/10.1080/21663831.2018.1458753.

[3] J. Narayan, A. Bhaumik, R. Sachan, A. Haque, S. Gupta, P. Pant, Direct conversion of carbon nanofibers and nanotubes into diamond nanofibers and the subsequent growth of large-sized diamonds, Nanoscale. 11 (2019) 2238–2248. https://doi.org/10.1039/C8NR08823C.

[4] B. Wei, J. Zhang, J. Liang, D. Wu, The mechanism of phase transformation from carbon nanotube to diamond, Carbon. 36 (1998) 997–1001. https://doi.org/10.1016/S0008-6223(97)00232-7.

[5] C. Luo, X. Qi, C. Pan, W. Yang, Diamond synthesis from carbon nanofibers at low temperature and low pressure, Sci. Rep. 5 (2015) 13879. https://doi.org/10.1038/srep13879.

[6] F. Zhang, J. Shen, J. Sun, Y.Q. Zhu, G. Wang, G. McCartney, Conversion of carbon nanotubes to diamond by spark plasma sintering, Carbon. 43 (2005) 1254–1258. https://doi.org/10.1016/j.carbon.2004.12.019.

[7] S. Ozden, L.D. Machado, C. Tiwary, P.A.S. Autreto, R. Vajtai, E.V. Barrera, D.S. Galvao, P.M. Ajayan, Ballistic Fracturing of Carbon Nanotubes, ACS Appl. Mater. Interfaces. 8 (2016) 24819–24825. https://doi.org/10.1021/acsami.6b07547.

[8] W.K. Wang, L.M. Cao, Transformation of Carbon Nanotubes to Diamond at High Pressure and High Temperature, Russ. Phys. J. 44 (2001) 178–182. https://doi.org/10.1023/A:1011373920458.

[9] Á. Pérez del Pino, E. György, L. Cabana, B. Ballesteros, G. Tobias, Ultraviolet pulsed laser irradiation of multi-walled carbon nanotubes in nitrogen atmosphere, J. Appl. Phys. 115 (2014) 093501. https://doi.org/10.1063/1.4864776.

[10] J. Zhang, R. Wang, X. Zhu, A. Pan, C. Han, X. Li, D. Zhao, C. Ma, W. Wang, H. Su, C. Niu, Pseudo-topotactic conversion of carbon nanotubes to T-carbon nanowires under picosecond laser irradiation in methanol, Nat. Commun. 8 (2017) 683. https://doi.org/10.1038/s41467-017-00817-9.

[11] A. Haque, R. Sachan, J. Narayan, Synthesis of diamond nanostructures from carbon nanotube and formation of diamond-CNT hybrid structures, Carbon. 150 (2019) 388–395. https://doi.org/10.1016/j.carbon.2019.05.027.

[12] J. Narayan, Nature of unseeded crystallization in semiconductors, Mater. Lett. 2 (1984) 219–222. https://doi.org/10.1016/0167-577X(84)90027-2.

[13] Prawer Steven, Nemanich Robert J., Raman spectroscopy of diamond and doped diamond, Philos. Trans. R. Soc. Lond. Ser. Math. Phys. Eng. Sci. 362 (2004) 2537–2565. https://doi.org/10.1098/rsta.2004.1451.

[14] R.K. Singh, J. Narayan, A novel method for simulating laser-solid interactions in semiconductors and layered structures, Mater. Sci. Eng. B. 3 (1989) 217–230. https://doi.org/10.1016/0921-5107(89)90014-7.

[15] A. Haque, J. Narayan, Electron field emission from Q-carbon, Diam. Relat. Mater. 86 (2018) 71–78. https://doi.org/10.1016/j.diamond.2018.04.008.

[16] A. Haque, J. Narayan, Stability of electron field emission in Q-carbon, MRS Commun. 8 (2018) 1343–1351. https://doi.org/10.1557/mrc.2018.172.

[17] A. Haque, P. Pant, J. Narayan, Large-area diamond thin film on Q-carbon coated crystalline sapphire by HFCVD, J. Cryst. Growth. 504 (2018) 17–25. https://doi.org/10.1016/j.jcrysgro.2018.09.036.

[18] J. Narayan, A. Bhaumik, Research Update: Direct conversion of h-BN into pure c-BN at ambient temperatures and pressures in air, APL Mater. 4 (2016) 020701. https://doi.org/10.1063/1.4941095.

[19] J. Narayan, C.W. White, Pulsed laser melting of amorphous silicon layers, Appl. Phys. Lett. 44 (1984) 35–37. https://doi.org/10.1063/1.94594.

[20] J. Narayan, C.W. White, O.W. Holland, M.J. Aziz, Phase transformation and impurity redistribution during pulsed laser irradiation of amorphous silicon layers, J. Appl. Phys. 56 (1984) 1821–1830. https://doi.org/10.1063/1.334192.

[21] D.H. Lowndes, R.F. Wood, J. Narayan, Pulsed-Laser Melting of Amorphous Silicon: Time-Resolved Measurements and Model Calculations, Phys. Rev. Lett. 52 (1984) 561–564. https://doi.org/10.1103/PhysRevLett.52.561.

[22] R. Narayan, Diamond-Based Materials for Biomedical Applications, Elsevier, 2013.

[23] A.M. Zaitsev, On the way to mass-scale production of perfect bulk diamonds, Proc. Natl. Acad. Sci. U. S. A. 105 (2008) 17591–17592. https://doi.org/10.1073/pnas.0809748105.

5. Mechanism of the ultrafast laser-assisted conversion of CNT to diamond and successive large area diamond thin film

Ariful Haque[1, §], Siddharth Gupta[2, §], and Jagdish Narayan[2, *]

[1]Department of Materials Science and Engineering, North Carolina State University, Raleigh, North Carolina 27695.7916, USA

5.1 Abstract

In this work, we studied the mechanism of direct conversion of multi-wall carbon nanotubes (CNTs), synthesized by chemical vapor deposition, into diamond by ultrafast nanosecond pulsed laser melting process using nanosecond excimer laser pulses at ambient temperature and pressure in air by complementary experimental and simulation techniques, and used those nanodiamonds as precursor to grow wafer-scale high-quality diamond film by hot filament chemical vapor deposition (HFCVD). The conditions under which diamond nucleates and grows from CNTs are extensively examined by different characterization techniques and the kinetics and thermodynamics of the phase transformation mechanism has been discussed using finite element method (FEM) simulation/SLIM analysis. Raman spectroscopy of the CNTs after the laser irradiation probes the characteristic diamond peak at 1324-1326 cm^{-1} to illustrate the formation of nanocrystalline diamond with phonon confinement effect. The high-resolution scanning electron and transmission electron microscope images show the formation of diamond mostly at the tip and bends of the CNTs. The direct phase transformation of CNT nanofibers into <110> oriented single-crystal diamond tips was observed by electron back-scattered Kikuchi diffraction analysis, and high-resolution TEM imaging and FFT patterning. The diamond nanostructures are utilized as seeds to synthesis large-area high-quality diamond thin film on different substrates at a tremendous

growth rate of ~800 nm/hr in HFCVD. Overall, this facile and ultrafast route to directly convert CNTs to diamond creates an immense technological and scientific potential for next-generation solid-state devices ranging from quantum sensors to enhanced field emitters.

5.2 Introduction

Diamond is one of the most precious and promising materials on earth not only due to its aesthetic value but also for some of its extraordinary structural, mechanical, and electronic properties such as extreme hardness, wide bandgap, large charge carrier mobility, and high-temperature superconductivity when doped with boron. It is also regarded as one of the most promising next-generation composite materials due to some of its extraordinary physical properties such as high tensile strength, excellent radial elastic deformability, tremendous chemical inertness, biocompatibility, unique electrochemical properties, large bandgap, and negative electron affinity [1,2] [3]. It is one of the most studied and most effective materials for hermetic corrosion-resistant coating for bio-devices, protective coating in machining tools, cold cathode electron source, heat sink substance for electronic devices, and the structural material for micro- and nano-electromechanical systems (MEMS/NEMS) [4–7]. However, diamond cannot be directly implemented in most of these applications due to different growth, interfacial bonding, and doping-related issues. Although diamond possesses the highest hardness (Vickers hardness in the range of 70–150 GPa) due to its low fracture toughness (K_{IC} ~5 MPa.$(m)^{1/2}$) this material is quite brittle which hinders its direct application in load transfer systems [1]. A combination of diamond and tough carbon nanotube (CNT) can be a good solution. Similar to the sp^2-bonded graphitic structure, double-walled and multi-walled CNTs consist of multiple graphite sheets in the rolled structure having flexibility, large thermal conductivity, good electron mobility and unique dimension (aspect ratio greater than 10^6 [8]) for field emission applications.

A composite of CNT and diamond is expected to have unique mechanical and electronic properties suitable for different applications. For example, for load-bearing applications CNT can provide the toughness (to overcome the brittleness of standalone diamond) and diamond can provide the hardness, and for field emission applications the CNT with large free carrier concentration (one free electron from each sp^2-bonded carbon) and high aspect ratio can provide the conductive pathway for the electrons to reach to the diamond tip having negative electron affinity. Therefore, investigation of a suitable route to directly convert CNT into diamond is of great scientific, technological, and economic interest. However, the understanding and development of a suitable and controlled technique to directly grow diamond from CNTs to form a diamond-CNT hybrid structure have been unsuccessful due to the existing limitations of the conventional and equilibrium diamond fabrication routes. Most of these processes involve extreme conditions, requiring catalysts such as Ni, Co, and other metals or alloys, and the yield products are, in most cases, poor in quality. For instance, the high-pressure high-temperature (HPHT) technique for the conversion of CNTs into diamond requires extreme conditions of pressure between 5.5 and 14.5 GPa and temperature of 1150–1800 K [9,10]. In most of the cases the HPHT technique of the diamond conversion from CNTs has been proven to be inefficient and time taking with limited control over the process. The solid-gas-solid transformation mechanism involved in the conversion of diamond from CNTs by microwave plasma-enhanced chemical vapor deposition (MPCVD) also shows limited control. The initiative to the formation of diamond/CNT hybrid by MPCVD was reported, but the complex pretreatment of CNTs in pure hydrogen plasma is required which made the process inefficient and mainly the diamond was formed with the consumption of MWCNTs in the MPCVD chamber [11]. Another group reported CNT to diamond conversion by spark plasma sintering at 1500º C and 80 MPa; however, in this process, the diamond structures

are covered with the amorphous carbon layer to limit many of its applications, especially electronic devices based applications including electron field emission[12]. Gong *et al.* reported the conversion of CNT into diamond by hydrogen plasma post-treatment method [13]. This process yields diamond nanorods having an undesirable core-sheath structure with the inner core being diamond crystal and the outer shell being amorphous carbon. Overall, as the synthesis routes are mainly driven by the solid-state or solid-gas-solid equilibrium phase conversions, most of those studies do not show sufficient characteristic evidences on the formation of nanodiamond structures, i.e., distinctive microscopic imaging, or characteristic Raman peak at 1332 cm^{-1}, and the proof of phonon confinement effect in the Raman spectrum from diamond nanostructures.

To address these critical issues, in this study we report on the direct conversion of multi-wall carbon nanotubes (CNTs), synthesized by chemical vapor deposition, into diamond by ultrafast nanosecond pulsed laser melting process using nanosecond excimer laser pulses (193 nm wavelength) at ambient temperature and pressure in air. This undercooling driven ultrafast phase transformation phenomenon via the liquid route involves the melting of CNT in a super undercooled state using nanosecond laser pulses and quenching rapidly to transform into the phase-pure diamond. The obtained diamond nanostructures showed a single-crystal growth phenomenon in electron backscattered diffraction (EBSD) analysis and phonon confinement effect in the Raman spectrum. The experimental evidences on the phase transformation mechanism are explained by the kinetics and thermodynamics modeling and simulations using the transient solid-laser interaction in materials (SLIM) analysis. Furthermore, we have used these diamond nanostructures as seeds to grow large-area high-quality diamond thin films on different substrates. These diamond nanostructures and CNT-diamond hybrid formed by quenching from the liquid-state at an ultrafast

speed, and large area thin films are ideally suited for applications ranging from enhanced catalysis and load transfer to efficient field emission.

5.3 Experimental techniques

Growth of CNT. The double-walled and multi-walled CNTs were grown using a thermal CVD system. The substrate, a polished Si wafer, was placed at the center of the horizontal quartz tube inside the furnace (30 cm in length and 4 cm in diameter). The $FeCl_2$ powder (~99.9% pure, Kojundokagaku Laboratory) in a quartz boat was also placed inside the quartz tube which acts as a catalyst during the synthesis of the CNTs. The chamber pressure was maintained at 10^{-3} Torr during the heating cycle, and the chamber was purged with acetylene (98%) using a mass flow controller once the furnace temperature reached 820°C. At this stage, the furnace temperature remained constant and the pressure was maintained at 10 Torr. In this chloride mediated CVD method of growing CNTs the constant gas flow was maintained for 2 hours and no metallic film on the substrate was found.

PLA conversion of CNT into diamond. The CVD grown CNTs were mounted on a laser irradiation holder and the surface was irradiated with a pulsed ArF laser (*Lambda Physik, 193 nm* wavelength, and 20 ns pulse duration) in the air. We have used the previously developed SLIM software to simulate and control the details of laser–solid interactions and to determine the range of optimum laser energy density for the diamond conversion as well [14]. The laser energy density was ~ 0.7-0.8 J/cm^2 which leads to a highly undercooled state to form diamond. We have used a Calcium Fluoride (CaF_2) Plano-Convex confocal lens from Edmund optics with a focal length of 50 cm. This lens possesses low index of refraction and transmits more than 90% of the radiation at 193 nm. After the first pulse, the ultrafast pulsed laser annealing technique melts the CNT tips and bends where there is limited heat flow for undercooling to occur. The laser-converted diamond

regions can be expanded after subsequent laser pulses. The degree of undercooling is critical to the formation of phase-pure diamond.

HFCVD. A standard HFCVD system was used to synthesize the diamond films on different substrates. The system uses a stainless steel cylindrical water-cooled chamber, a tungsten filament holder (4 wires) assembly at the middle, a heated substrate holder, a sealable gas inlet and pumping ports. The chamber also contains a thermocouple temperature sensor, a sealable gas inlet and pumping port, and a necessary flow rate controller and electrical systems. The specimen substrates are placed on the Molybdenum heater block (700°C) below the filament. The chamber is initially evacuated with a mechanical pump to 10^{-3} Torr. When the desired base pressure is reached, the pumping port valve is closed and methane and hydrogen gas at a ratio of 1:50 is then allowed to flow over the hot filaments (2000°C) into the chamber to the desired pressure (low working pressures ~20 Torr). The filament temperature was measured with a two-color pyrometer while the substrate temperature was measured by a K-type thermocouple inserted on the substrate holder, placed on the backside of the substrate. The set of multiple filaments and the rotation of the substrate stage during the deposition facilitates the formation of a uniform diamond thin film over the large substrate area. Gas composition (%vol. CH_4 and H_2), total gas pressure (P), total mass flow, and substrate and filament temperatures were monitored throughout the deposition time. Cooling from growth down to room temperature was conducted at a constant cooling rate of 10 °C/min for all samples to minimize the thermal shock.

Raman spectroscopy. We have used a WITec confocal Raman spectrometer (with a triple monochromator, gratings 2400 lines/mm) to detect the fingerprint of diamond and non-diamond phases, and the stress present in the film. A continuous laser beam of 532 nm wavelength from a diode-pumped solid-state laser was focused at a spot of ~2 μm diameter. The spectrum resolution

was ~0.5 cm^{-1}. Optimum laser power (~40 mW) was used to illuminate the sample to avoid heating of the sample during the spectrum acquisition. Raman spectra at different points of the samples were acquired with an exposure time of 5 s, the spectrum being the sum of 10 acquisitions.

SEM. High-resolution SEM images at high-magnification enable us to understand the mechanism behind the phase transformation better. Scanning electron microscopy was also undertaken to characterize the morphological surface features of the nucleated diamond films. The high-resolution SEM imaging with the sub-nanometer resolution was carried out on the PLA grown Q-carbon and HFCVD grown diamond films using the FEI Verios 460L SEM.

EBSD. A powerful non-destructive technique, electron backscattered diffraction (EBSD), is used to determine the details of atomic structure of crystalline phases (diamond and CNTs) at nanoscale. During the EBSD data acquisition, a beam of electrons (20KV & 5 nA) is directed at a point of interest on the tilted diamond structures. These electrons are diffracted to form a set of paired large-angle cones that correspond to each diffracting plane. The image produced on the phosphor screen contains characteristic Kikuchi bands of the corresponding diamond crystal, which are formed where the regions of enhanced electron intensity intersect the screen. The pattern seen is a gnomonic projection of the diffracted cone, making the band edges appear hyperbolic.

XRD. X-ray diffraction (XRD) measurements (θ - 2θ scan) were conducted on the diamond films (Bruker D8 Discover) using Cu kα radiation source from a sealed tube operating at 40 kV and 25 mA and state of the art LENXEYE XE detector. This detector filters fluorescence and K-β radiation to overcome the intensity losses and absorption edges associated with secondary monochromators and metal filters. The data were collected in the Bragg-Brentano reflection geometry in the 2θ range of 30-100 at 0.01 step size and a dwell time of 0.5 seconds per scan point.

HRTEM. The TEM specimen for PLA processed CNT sample was fabricated using the ultrasonication exfoliation technique in the methanol medium. The dispersed solution (10 μL) was then manually transported to the TEM grid and left to dry up. TEM images and SAED patterns are captured by high-resolution transmission electron microscopy (S/TEM, FEI, Talos-F200) operating at 200 keV, equipped with a proprietary "XFEG" high-brightness Schottky emission field-emission-gun electron source, which provides beams ~5× brighter than previous Schottky-FEG technologies.

Laser-solid melt interaction simulations. To study melt kinetics upon performing PLA, a temporal and spatial Gaussian is utilized as a heat source. The annealing was modeled using transient solid-laser interaction in materials (SLIM) code. The annealed region had a finer mesh size of 1 nm which increased to coarser values up to 100 nm in the subdomain. The outer boundaries of the film were approximated with adiabatic conditions, while the annealed surface had radiative and conductive losses incorporated in it. The thermal conductivities were approximated as 3 W/m-K, 2.90 W/cm-K, and 15 W/cm-K for amorphous solid [15], liquid carbon [16], and MWCNTs [17] at high temperatures, respectively. The motion of melt-front during the onset of melting and regrowth was performed incorporating the phase change at solid/melt interface for C, with the latent heat of melting and heat conduction as the driving force propagating the melt interface.

Ab-initio MD simulations. The sp^2-bonded graphitic carbon structure was generated by ultrafast quenching from the liquid state through extensive *ab initio* Molecular Dynamics simulations using the large-scale atomic/molecular massively parallel simulator (LAMMPS) code. The simulations were performed utilizing the angular dependent potential (ADP) designed for simulating the carbon melt subsequent phase transformations on ultrafast quenching [18,19]. Liquid carbon (216 atoms) was initially equilibrated at 7000 K in an NVT ensemble (constant number of atoms,

volume, and temperature) for 20 ps with the timesteps set as 2 fs. To simulate the effect of undercooling, at this stage isotropic pressure of 5-50 GPa was applied to the system under the NPT (constant number of atoms, pressure, and temperature) ensemble, while the system was gradually cooled to 2000 K in 500 ps by extracting heat from the system periodically, forming an amorphous solid (i.e., graphitic carbon and amorphous diamond at 1 GPa and 50 GPa, respectively). The as-obtained amorphous structure was further stabilized in an NPT ensemble at 300 K with atmospheric pressure for 20 ps. The structure factor calculations for the quenched structures were computed based on the radial distribution functions (RDF) using the Baxter-Dixon-Hutchinson factorization method [20].

5.4 Results and Discussion

Fig. 5.1 illustrates the high-resolution SEM images of CNTs at different magnifications before and after the PLA to illustrate the mechanism of phase transformation. Fig. 5.1(a) shows a high-resolution SEM image at relatively low magnification from the as-grown pristine nanotubes before laser annealing. No evidence of diamond is observed in the nanotubes. Fig. 5.1(b-c), the high-resolution images of CNTs at nanoscale, clearly illustrates the CNT structure throughout, without any trace of diamond. The SEM images of the PLA converted nanodiamond structures are shown in Fig. 5.1(d-f). Fig. 5.1(d) illustrates the overall laser irradiated region (1 PLA shots) where the formation of diamond is shown by the red and yellow circles at the tip and bends of the nanotubes, respectively. It can also be noted that the diamond structures are only formed where the CNTs are not completely horizontally lying on the substrate. This is due to the reason that heat cannot be confined locally to provide enough undercooling in horizontally placed CNTs due to the geometry effect. Fig. 5.1(e) shows a high-resolution SEM image of the conversion of a single CNT tip after irradiation with 2 laser shots. Fig. 5.1(f) shows another spectacular conversion of a CNT tip into a

sharp diamond nanorod after 10 PLA shots. More number of shots increases the length of the diamond rod where the previously formed diamond works as a seed for the pseudomorphic topotactic growth.

The shape and size distribution of the converted nanodiamonds suggest that the transformation takes place by the direct conversion of nanotubes via a nonequilibrium ultrafast process which involves melting of the CNTs in a super undercooled state by nanosecond laser pulses, and subsequent rapid quenching to convert it into phase-pure diamond. The results obtained from the SEM analysis also suggest that the size of the diamond nano-rods and grains can be controlled by the number of pulses and heat flow geometry as the nanosecond pulsed laser heating and temperature distributions are confined spatially and temporally. It is also important to note that the size distribution of the diamond nano-rods and grains is particularly dependent on the initial nanotube diameter. The diameter of carbon nanotubes ranged from 10-50nm (mostly multi-walled) with over 300nm in length. The unconverted CNTs do not collapse upon laser irradiation and retain their original shape which is necessary to maintain a high aspect ratio for electron field emission based applications. These results show the formation of sharpest diamond nanoneedles by this direct conversion of carbon nanotubes into diamond which has lots of potential applications.

EBSD. The crystal structure determination of the samples after the laser irradiation was carried out by the EBSD technique in the high-resolution SEM. The electron probe size used for EBSD is ~10 nm and thus it is ideal for determination of structure along the length of the diamond fiber. Fig. 5.2 shows the probing spots on the laser irradiated samples for EBSD analysis in a high-resolution SEM image, corresponding obtained and resolved Kikuchi patterns for each of those points, and the relative orientations by cubic and hexagonal shapes of diamond and CNT, respectively. The ordered carbon atoms in the CNT and diamond inelastically scatter a fraction of

the incident electrons from the point of interest, with a small loss of energy, to form a divergent source of electrons close to the surface of the sample. A portion of these electrons is incident on atomic planes at angles that satisfy the Bragg equation for graphitic carbon sheet and diamond crystal in case of CNT and diamond, respectively. These electrons produce an image on the phosphor screen containing characteristic Kikuchi bands of the diamond and CNT crystal structures. The high-resolution image of the laser irradiated sample is shown in Fig. 5.2(a) where Kikuchi bands are obtained from the marked spots. In Fig. 5.2(b-c) (spot 1 and 2), the <110> EBSD patterns of diamond upon resolving the Kikuchi patterns using AzTec software provide ubiquitous evidence of the formation of diamond crystal structure at the point of interest (shown by the red mark on the 1 D structures). The <110> orientation of the cube was found to be unchanged along the carbon fiber at the tip region, which demonstrates epitaxial topotactic growth, where diamond crystallites grow with the number of laser pulses with already formed crystallites providing as a seed for subsequent crystal growth. Fig. 5.2(c), the EBSD pattern of spot 3 (far from the tip region), clearly illustrates the existence of the sp^2 bonded graphitic CNT structure, which supports the SEM analysis and the proposed mechanism of diamond conversion. Fig. 5.2 (d) also shows the resolved EBSD pattern of another spot (spot-4) from the top of another CNT lying flat on the substrate. The horizontally placed CNTs cannot be converted into diamond due to limited undercooling owing to the geometric constraints, hence, the resolved pattern of spot 4 shows the graphitic crystallinity.

High-resolution transmission electron microscopy. The first order phase transformation of MWCNT tip into nanodiamond is further elucidated by performing high-resolution S/TEM imaging and fast-Fourier transform (FFT) analysis. Fig. 5.4(a) reflects the structure of MWCNT singular tube with concentric tubes exhibiting interlayer spacing of 0.335 nm across (002) planes,

which are conjoined by the weak van der Walls forces. The exceptional properties of these layered CNT tubes arise from the combination of radial weak van der Walls interaction and strong sp^3 bonding. The tube layers were noted to vary from 40-60 in the following experiments. Fig. 5.4(b) reflects the MWCNT configuration utilized in performing the PLA experiments. Notably, only the CNT tip facing the nanosecond laser beam perpendicularly converted into diamond, as can be noted with the change in contrast. The CNT tube in the left does not show conversion into diamond due to low undercooling generated across the tube. The structural transformation is further emphasized with the high-resolution image in Fig. 5.4(c), revealing the change-over from radial lattice fringes arising from (002) planes of CNT to (111) cross-fringes arising from diamond. Notably, we did not observe any presence of intermediate structures like carbon onions.

This transformation resulted in diamond size varying from 8-10 nm, as shown in Fig. 5.5(a). Notably, on traversing from left-right the first-order phase transformation from CNT to diamond can be noted, with densification of lattice suggesting CNT to diamond tip conversion, as a result of the thermal flux entrapment which considerably improves undercooling in the melt state. The respective FFT acquisitions from regions labeled A and B (shown in Fig. 5.5(b-c)), reflect definite addendum of D(111) dots arising from (111) cross-fringes of diamond, together with the (002) and (004) MWCNT diffused rings. This configuration of (111) spots in FFT pattern arises across the <110> zone-axis during diamond regrowth. As this is a plan view acquisition, the *<110>* zone-axis is the out-of-plane orientation of these liquid phase regrown nanodiamonds. Such regrowth dynamics are consistent with the ultrafast topotactic regrowth of diamonds from molten carbon during PLA processing of amorphous carbon [21], carbon nanofibers [22], and polymeric tapes, with the regrowth ending in less than 100 ns. It is interesting to note that we did not observe (200) peaks in this case, which are generally associated with double-diffraction of (1-11) and (11-1)

planes of diamond. Perhaps the ultrathin nature of MWCNT and diamond tip reduced the probability of double-diffraction. It is interesting to note that, on performing the FFT acquisitions on the complete MWCNT structure in Fig. 5.5(d-e), we observed a diffused (111) ring with speckled spots in between, suggesting the formation of nanodiamonds throughout this PLA processed MWCNT structure.

Raman spectroscopy. Fig. 5.6 (a) shows the Raman spectra of the CVD grown CNT and the PLA converted nanodiamond regions. The as-grown CNT has characteristic D and G Raman bands at ~1350-1352 cm^{-1} and 1592 cm^{-1}, respectively. The 2D peak, which is the first overtone of D peak, also observed at ~2700 cm^{-1}. Raman microprobe spectroscopy also identifies the nanodiamond phase in the laser irradiated samples as having a characteristic T_{2g} peak at ~1322–1324 cm^{-1} which is consistent with the mode of bulk diamond crystal with peak shifted to a slightly lower wavenumber. The downshift of ~8-10 cm^{-1} (from 1332 cm^{-1} in microdiamonds) and spectral broadening are due to a certain component of tensile stress/phonon confinement [23] in nanosized diamonds formed after the PLA. The *D*, *G* and *2D* peaks originate primarily from unconverted graphitic carbon regions which were illuminated by the green laser during spectral acquisition. Moreover, no D′ peak, arises due to the defect-induced single-phonon intra-valley scattering process, at 1604 cm^{-1} in the CNTs before and after PLA eliminates the presence of perturbations within the sp^2 lattice induced by voids and edge defects [24]. Studies on the microscopic changes in the graphitic structures of CNTs after laser treatment (pulsed laser wavelength 248 nm) showed some significant changes upon the incident energetic photons by Raman spectroscopy which revealed crucial information after fine analysis [25,26]. Upon laser irradiation the shift in the G-band position from 1580 cm^{-1} to 1592 cm^{-1}, an upshift from the theoretical position of graphite, implies the defect induced graphitic structure of the unconverted CNT region. Since the I_D/I_G ratio

indicates the relative density of dangling bonds and defects to the more crystalline graphite structure in the CNTs, the increase in the I_D/I_G ratio from 0.72 to 1.4 indirectly refers to the increase in the disordered amorphous carbon density in the unconverted tube walls after the PLA[27]. Previous studies on the microscopic changes in the graphitic structures of CNTs showed similar changes due to the incident energetic photons by Raman spectroscopy [25,26]. Li *et al.* reported that an increasing I_D/I_G ratio, which was attributed to the pulsed laser irradiation (248 nm wavelength) with energy densities in-between 0.08 to 0.15 J/cm^2 , gives rise to an enhancement of emission current density [26]. Other studies also explained improvements in emission characteristics by the dangling bond formation or laser cleaning at the surface of the MWCNT samples [28,29]. Thus, the formation of diamond capped CNTs with a high density of dangling bonds in the unconverted CNT regions can form an ideal platform for the high current density field emitters.

In case of CNT irradiated with a laser energy density of 0.4 J/cm^2 a slight increase of D peak is observed and the I_D/I_G ratio was determined to be ~1. The intensity of the 2D peak did not change substantially which refers to the retention of the crystallinity of the CNTs irradiated at low energy density. On the other hand, when the CNTs were irradiated with a laser energy density (0.9 J/cm^2) much higher than the optimum range (0.65 J/cm^2), a drastic fall in the 2D peak intensity was observed. The obtained I_D/I_G ratio at this laser energy density was also found to be the highest among all the laser irradiated samples (~1.55), implying a tremendous enhancement in the defect density. Moreover, the position of the G peak provides important information regarding the defect density on the MWCNT as a function of the energy density during laser irradiation. The G peak of the as grown CNTs (1568 cm^{-1}) shifts significantly towards right (blue shift) with increasing PLA energy density. The position of this peak was found to be at 1582 cm^{-1}, 1592cm^{-1}, and 1602

cm^{-1} for the CNTs irradiated with 0.4 J/cm^{-2}, 0.65 J/cm^{-2}, and 0.9 J/cm^{-2}, respectively. Thus the pulsed laser irradiation induces some structural changes in the unconverted CNT regions which are consistent with other studies related to the effect of the incident energetic photons on the graphite structure of CNT body at the microscopic scale [25,26,30]. Fig. 5.6(b) shows the Raman spectrum obtained from the diamond after HFCVD (3 hr) on the laser-treated CNT on Si. The presence of a sharp characteristic T_{2g} peak at 1333 cm^{-1} refers to the highly crystalline diamond. The vanishing G-peak (associated with sp^2 graphitic carbon) at 1580cm^{-1} refers to the high quality and magnificent phase purity. In the case of the Raman spectrum from the diamond crystal in the untreated region, the G-peak is more pronounced, referring to the presence of unconsumed carbon fibers compared to the laser-treated samples. The Raman spectrum of a piece of crystalline Si having a peak at 520 cm^{-1} is also shown as a reference.

Melting carbon explanation and simulation results: Liquid carbon refers to the liquid phase of carbon resulting from the melting of pure carbon in a solid phase (graphite, amorphous carbon, diamond, carbon nanotube, carbon fibers, or a variety of other carbons). In this study, the conversion of CNTs into diamond is driven by the undercooling process via the formation of a liquid state of carbon upon PLA. Although the liquid state of carbon can be produced by different conventional equilibrium techniques with arduous efforts, such as resistive heating [31] or laser heating of graphite by exploiting the poor interplanar thermal conductivity of graphite [32], these routes cannot lead to the phase conversion to transform into diamond due to the lack of understanding and limited control over the process. The phase diagram for carbon shows that liquid carbon is stable at atmospheric pressure only at very high temperatures (above ~4450 K)[33]. Since carbon has the highest melting point of any elemental solid, first of all, it is very difficult to melt the carbon utilizing the conventional heat treatment or equilibrium routes. Again in conventional

processes, the crucible in which the carbon is melted must itself be made of carbon to avoid contamination of the melt, and sufficient heat must be focused on the sample volume to produce the necessary temperature rise to attain melting [16,32]. Thus the carbon crucible, by default, leads to regraphitization during the cooling down of liquid carbon due to the homogenous nucleation in those equilibrium processes. Although diamond and graphitic carbon have different melting temperatures, the same liquid carbon is obtained upon melting either solid phase. Therefore controlled undercooling may lead to an energetically favorable route to produce diamond from the liquid state of carbon.

Attaining the liquid carbon state does not guarantee the formation of diamond as quenching and undercooling play critical roles in the phase transformation. The undercooling and thereby the resolidification velocity of the melt front dictates the formation of the solid states of carbon, i.e. the diamond, graphite, or Q-carbon. Since the vaporization temperature for carbon (~4700K) is only slightly higher than the melting point ~ 4450 K), the vapor pressure over liquid carbon is high, which again emphasizes the importance of the control over the spatial and temporal heat flow during the process [16]. Only the ultrafast laser-induced melting of carbon can generate the required undercooling to transform the liquid state of carbon into diamond (after the melting of CNTs) as the preferable range of the regrowth velocity for such conversion is very narrow (4-6 m/s) [21,34].

In the PLA mediated conversion of CNTs into diamond the CNTs were irradiated by nanosecond laser pulses with an energy density of 0.65-0.7 J/cm^2. The temperature of the tubes as a function of time was determined from the energy in the laser pulse and the measured heat capacity for CNTs [35] over the temperature range up to the melting point, assuming that the whole portion of the absorbed laser pulse was converted into thermal energy in the tube. For PLA

experiments, above the melt threshold (E_d), surface melting of thin films occurs. For MWCNT tubes used in these experiments 20-80 layers, the E_d is determined to be 0.4 J/cm^2 as revealed in Fig. 5.6(a). For phase transformation of molten carbon into Q-carbon, α-carbon or crystalline phases, it is essential first to melt the carbon tubes. In the non-equilibrium route of PLA, the heat flow is spatially and temporally confined, making it an ideal technique for melt processing of materials which have a tendency to undergo sublimation, like carbon. Once the melting of carbon is achieved, the melt cools down rapidly, leading to regrowth rates of 10^{10}-10^{11} K/s. The profile reveals the onset of melting at ~4 ns, with the maxima in temperature at 20 ns which corresponds to the nanosecond laser pulse width of 20 ns, signifying the cool-down of the film once the incoming heat flux truncates with solidification completing in <50 ns. Fig. 5.6(b) shows the progression of melt front with time for various PLA energy densities. Notably, post the onset of melting, on a further rise in PLA energy densities, an exponential increase in melt depth is noted (Fig. 5.6(c)), which can be utilized to engineer the formation of diamond structures with varied aspect ratios. These simulations elucidate the criterion and thermal dynamics of molten carbon, and the mechanism behind liquid phase regrowth of *<110>* oriented nanodiamonds during melt regrowth.

Further, we utilized ab initio molecular dynamics calculations to simulate the liquid phase regrowth of diamond. The simulations are based on "liquid quench method" [36,37] generally used for randomization and formation of disordered solids, where carbon is melted and subsequently quenched under isotropic pressure. In this case, to equilibrate the structures formed under HPHT condition, the pressure is first released at 2000 K to 760 Torr (see Experimental section for details**),** and then subsequent quenching to room temperature is performed. The Nose-Hoover thermostat is used to equilibrate the liquid melt [38]. The quenching to room temperature was performed

under NVT conditions with a Langevin thermostat [39]. The ultrafast quenching of the melt phase shifts the temperature at which the solidification occurs, generating the undercooled liquid which triggers the rapid non-equilibrium solidification. For carbon, increased undercooling triggers the formation of diamond and densely-packed Q-carbon phases, which are formed far from equilibrium [21,40,41]. These HPHT simulations are performed by applying isotropic pressure on the carbon melt during quenching.[20] It is worth mentioning that high-pressure quench resulted in the evolution of a densely-packed phase with ~90% sp^3 content. These results are in-agreement with super-undercooling (>1000 K) driven formation of densely packed Q-carbon phase on rapid quenching of molten carbon. The structural model of the regrown solid reveals extensive tetrahedral bonded states, as highlighted in red, shown in Fig. 5.6(d). These simulation results provide further evidence that carbon polymorphs like MWCNT can be regrown into diamonds under the highly undercooled conditions.

The growth velocity (solidification velocity) of the diamond is estimated to be ~4 ms^{-1} from the length of the converted diamond region at the tips (SEM and TEM images). This estimation is consistent with the presented theoretical modeling and previous molten phase mediated growth of diamond and c-BN [21,34,41–44]. The atomic spacing of carbon nanotubes and diamond are 0.2468 nm [45] and 0.2522 nm (in (100) plane), respectively, with only 2.5% incompatibility. Thus the transformation of CNTs to diamond is thought to be even easier compared to that from other forms of carbon during the pulsed laser-induced melting and subsequent quenching process. Careful selection of the laser parameters is very important for irradiating CNTs to convert into diamond. Earlier, researchers have observed an increased realignment of the thin CNTs with an increase of the laser energy density [46]. Studies also reported that high energy pulsed laser heating would lead to an apparent growth process of additional small diameter CNTs. The use of excessive

energy density (over 1.5 J/cm^2) resulted in the broken or blown off CNTs due to overheating and ablation effects [46]. Researchers have also used laser irradiation treatment of aligned CNTs to produce clean and uniform surfaces [47]. Further increase in the energy density produced too high of a temperature resulting in the burning/etching/ablation and trimming of the aligned CNTs. Thus the direct conversion of CNTs into diamond is possible only the proper understanding of the kinetics and thermodynamics. Upon irradiating the CNTs with nanosecond pulsed laser at a suitable energy density, the tips and bends of the CNTs can be melted in a highly undercooled state (due to the geometry constraint of the temperature distribution and 1D heat flow). The final temperature determines the undercooling and quenching rate during pulsed laser annealing which has been controlled by the selection of optimum laser parameters. The highly undercooled state of carbon is a metastable phase, and nanodiamonds nucleation occurs from this state. The whole process (rapid melting, solidification, and growth) takes place in less than 200-250 ns. Therefore such a highly nonequilibrium phase transformation is ideal for the formation of single crystal diamond and this single crystal diamond can be doped with dopants of both p and n-types at doping concentration far higher than thermodynamic solubility limit. Single crystal diamond with such a high level of doping concentration has several exciting applications, i.e. high-temperature superconductivity, power electronics, and efficient field emission devices. Attaining such high doping concentration (otherwise impossible to realize) in single crystal diamond is only possible by this novel discovery of the controlled, direct, ultrafast, and nonequilibrium transformation of carbon into diamond. The simulation results are in excellent agreement with the experimental evidence, and the calculated results of the temperature distribution using SLIM supports the nonequilibrium phase transformation phenomenon from CNT to diamond in catalysis free and very controlled process at ultrafast speed.

Formation of large-area diamond films by HFCVD. The first laser pulse melts the tips of carbon nanofibers and nanotubes and results in the formation of <110> diamond crystallites via unseeded crystallization. These <110> diamond seeds provide the template for diamond growth with an increasing number of pulses. The nanodiamond is grown by melting and resolidification was used to grow larger diamond crystals further by using a standard HFCVD process (3 hr). Fig. 5.7 shows the large area diamond growth by HFCVD on the laser converted diamonds from CNTs. As there is no time loss for nucleation (due to the preexisting PLA nanodiamonds), remarkably large diamond crystals, owing to a high growth rate of ~800 nm/hr, was obtained. The formation of sizeable triangular diamond facets is observed in the high-resolution SEM image in Fig. 5.7(a). The low magnification image in Fig. 5.7(b) shows the formation of a large-area diamond thin film assisted by the laser converted nanodiamond embryo on the Si substrate. Fig. 5.7(c) shows shallow diamond coverage after 3hr HFCVD on untreated CNTs (left side).

The unconverted CNTs are totally consumed during the HFCVD process, as shown in the left side of Fig. 5.7 (c). The etching rate of sp^2 carbon (mainly CNTs) is 10 times faster than that of sp^3 carbon (already formed diamond) upon interaction with active hydrogen species during growth [48]. This process assists the growth of sp^3 diamond phase as the rate of formation of sp^3 diamond is greater than the etching rate [49]. It should be mentioned that the source for carbon in diamond growth is enhanced due to additional carbon containing species from the fibers. In the treated samples, nanodiamond nuclei formed after laser annealing provides very effective nucleation sites. In untreated samples, diamond nucleation starts from the surface roughness at pits, which may provide strain centers for diamond nucleation and subsequent growth.

Fig. 5.7(d) represents the Raman area mapping to understand the growth of HFCVD diamond on c-sapphire better. An area of 92 μm x 56 μm was divided into 200 x 200 pixels (200 points per

line and 200 lines per image) to collect data (with an integration time of 0.5 s) for the ultrahigh-resolution Raman area mapping images. The sample was focused by the 532 nm laser and each line on the sample was precisely rasterized by a motorized stage during the spectra acquisition for the area mapping. The Raman mapping was acquired by selecting the diamond region (1330-1335 cm^{-1}), which clearly illustrates the formation of a large-area diamond on the bottom side (irradiated CNT region) and almost no diamond formation on the top side (unirradiated masked region). The distinctive sharp boundary refers to the high nucleation density and favorable growth throughout the laser-irradiated CNT side with no crack and/or delamination. This refers to high-quality diamond growth throughout the laser-irradiated CNT region. Fig. 5.8 illustrates the XRD pattern of the HFCVD diamond thin films on Si substrates. The diffraction peaks at ~43.90º (2θ) corresponds to diamond (111). The sharp (111) diamond peak (less FWHM) refers better crystallinity and the absence of any other peak dismisses the possibility of the formation of any other secondary or impurity phase during the process. The vanishingly small {220} reflection of diamond is visible at ~76° (2θ), implying high quality and textured nature of the film. The SEM image in Fig. 5.7(a) also demonstrates the prevalence of triangular facets on the diamond surface which supports the textured nature of the diamond. Since the X-ray can penetrate the diamond film of thickness more than 100 μm [50], the XRD pattern is also showing the (100) peak of Si substrate. Almost no shift in the diamond peak from its original position implies stress free film deposition and thereby no change in d_{111}. Thus no formation of crack or delamination is observed in the large area diamond film.

5.5 Conclusions

In this study, a novel route of the formation of diamond by ultrafast direct conversion of sp^2 carbon at ambient temperature and pressure in air is investigated by complementary experimental

and simulation evidences. The structural characteristics of diamond have been confirmed by high-resolution SEM and EBSD and high-resolution TEM/STEM, and Raman spectroscopy. All these characterization techniques were employed at different points on the samples, both irradiated and un-irradiated, to elucidate the diamond formation mechanism using the ultrafast route. The experimental results are explained by the simulation outcomes which show that the whole process (melt, quench, and solidification) completes within 200ns for the nucleation and growth of diamond. Such an ultrafast process could be very effective in a way that the nanotubes can be doped selectively with *p*- and *n*-type dopants with concentrations far higher than thermodynamic solubility limits, by incorporating dopants before melting for a variety of potential applications ranging from quantum sensors to efficient catalysts and field emitters. These diamond nanostructures, formed by an undercooling driven clean process, provide seeds for the subsequent growth of high-quality large-area diamond by HFCVD on different substrates. Overall, this study on the controlled conversion of graphitic structures into diamond is a matter of great scientific interest with a tremendous technological impact since these nanostructures stand to revolutionize the fields related to nanomechanical systems, nanosensing, quantum computing, and quantum communication.

5.6 Figures

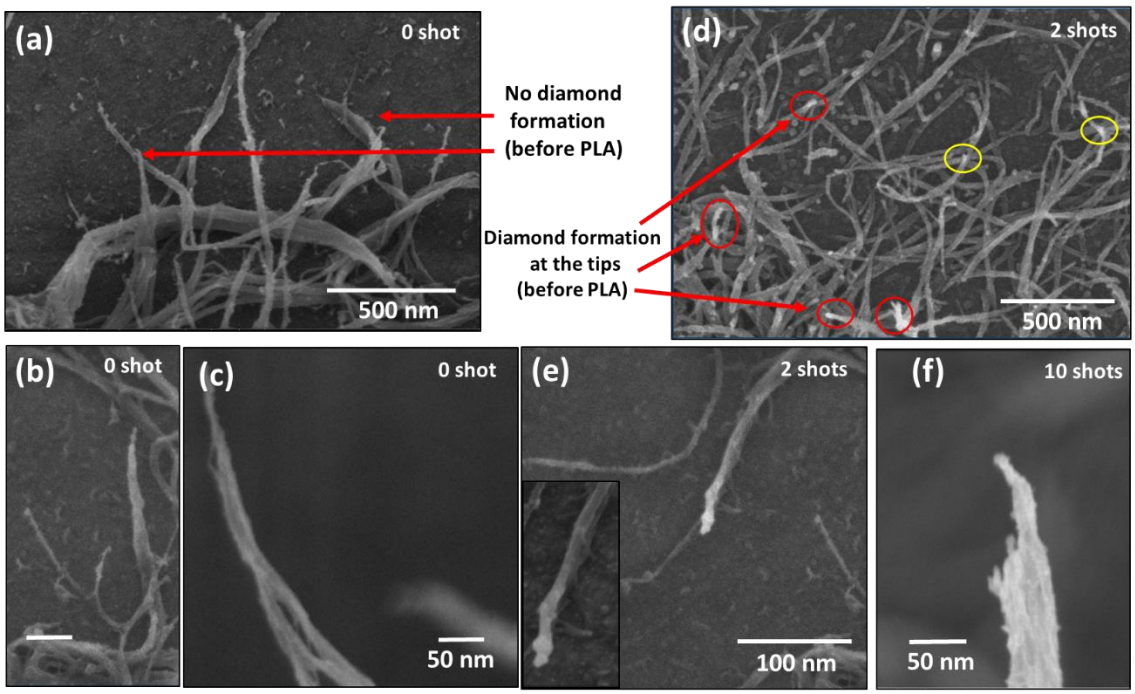

Figure 5. 1**:** Detail of the conversion of carbon nanotubes into diamond nanorods starting from the tips; (a) CVD grown CNTs without PLA. (b) and (c) high-resolution SEM micrographs showing no diamond trace in the as-grown CNTs, (d) illustrates the conversion of carbon nanotubes into diamond only at the tip (marked by red circles) and bends (yellow circles) after irradiating with a 2 pulses of an ArF laser (pulse duration 20 ns), (e) shows the propagation of the diamond formation after 2 laser pulses, and (f) illustrates more diamond conversion (more faceted structures are seen) after 10 laser pulses. It is noted that the converted nanodiamonds at the tip do not get affected by the successive laser pulses as they can dissipate the heat through the structure to the unconverted CNT region owing to the high thermal conductivity of diamond.

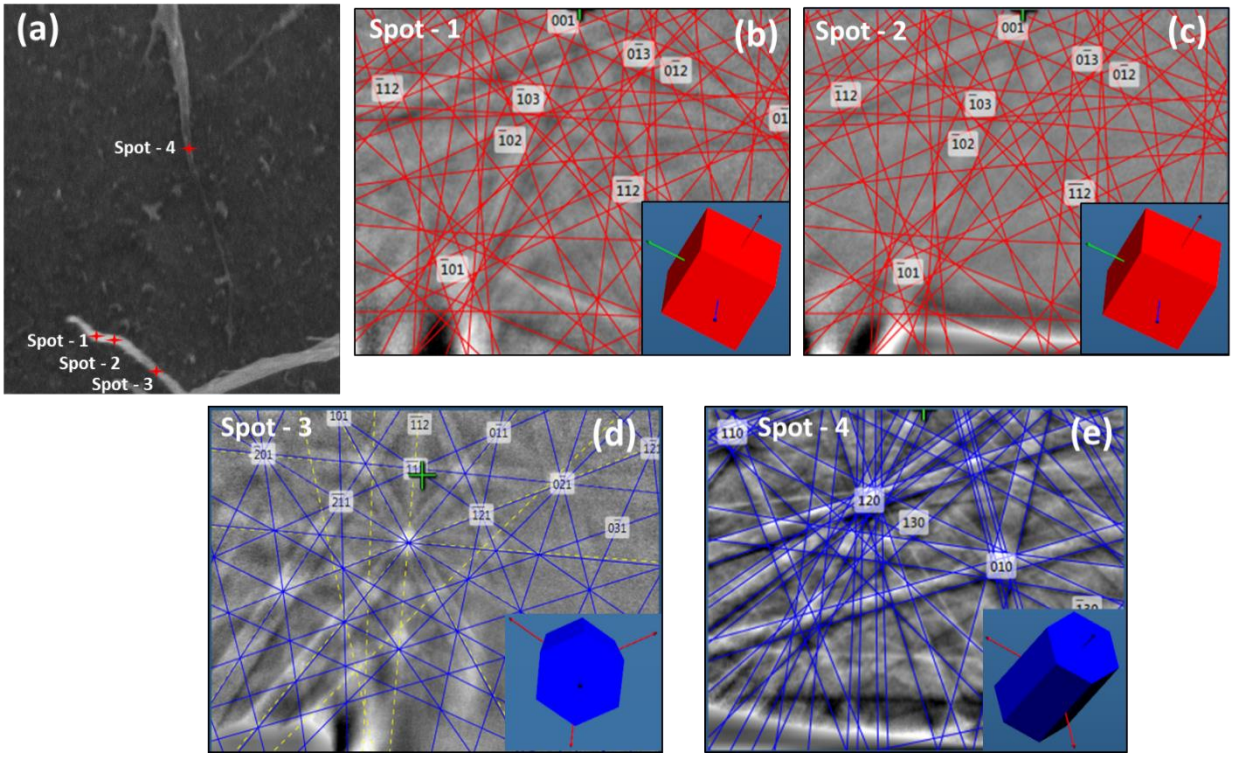

Figure 5. 2**:** Detail structural characterization of the conversion of carbon nanotubes into diamond nanorods. (a) The high-resolution image of the region of interest. The point of interest for structural characterization are marked as spot 1-4. (b) and (c) The obtained backscattered diffraction patterns from spot-1 and 2 match closely to that of diamond and the crystallographic orientation of the grown diamond are shown in the insets of the corresponding figures. (d) and (e) show the Kikuchi patterns obtained from spot-3 and 4, respectively. In the middle region of a CNT (spot-3), where the rate of undercooling is insufficient for diamond conversion, the pattern matches only with that of CNT. The absorbed laser energy is insufficient for the CNT (spot-4), lying horizontally on the substrate and off from the incident laser direction, to convert into diamond.

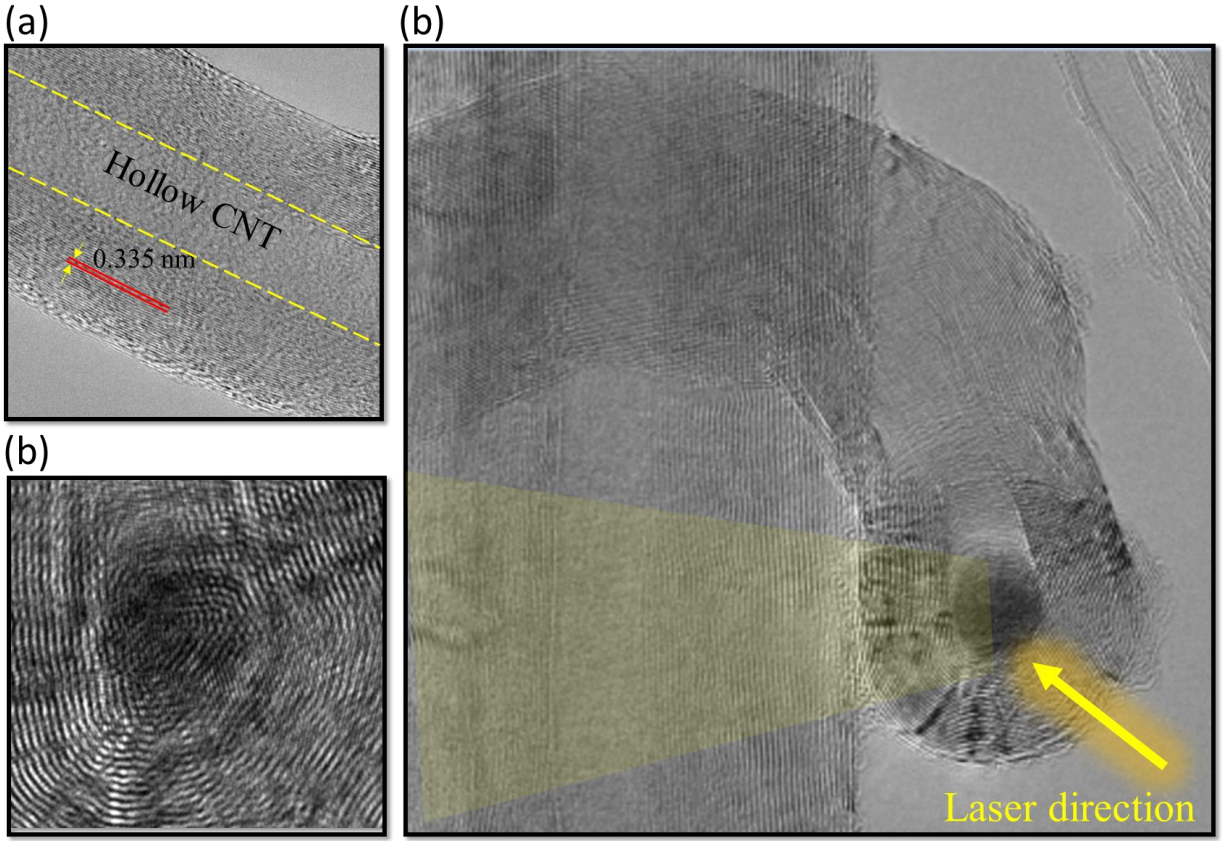

Figure 5. 3**:** High resolution scanning/transmission electron microscopy of multi-walled carbon nanotubes, revealing (a) the hollow nature of crystalline MWCNT with d spacing of 0.335 nm arising from (002) planar spacing. (b) Highlights the conversion of MWCNT into diamond at the tip located approximately perpendicular to the nanosecond laser pulse. (c) Shows the first-order phase transformation from MWCNT to diamond tip, with change in lattice fringe nature form disordered circular patterns, to cross-fringes associated with (111) planar spacing for nanodiamond.

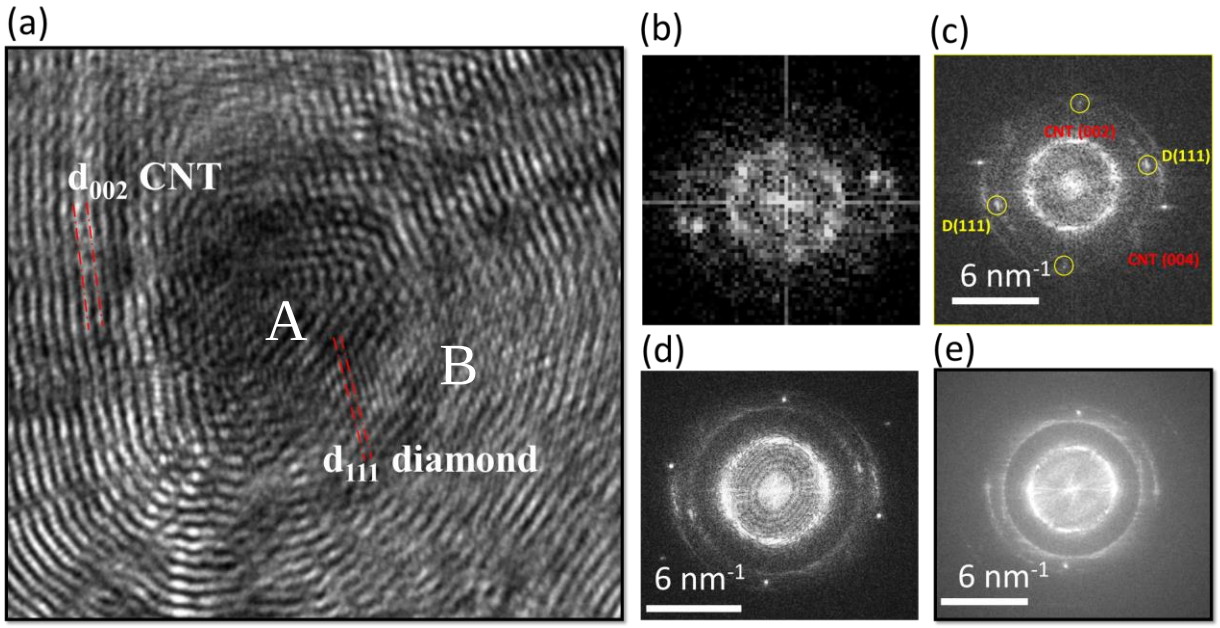

Figure 5. 4**:** TEM image of the nanodiamond region showing the formation of nanodiamonds at the MWCNT tip with a size of ~8-10 nm. It also highlights the shrinkage in d-spacing from first-order phase transformation of CNT (d_{002} = 0.335 nm) to diamond (d_{111} =0.026 nm). (b) and (c) reveal the local FFT acquisitions from the tip (A) and tip periphery (B) of the PLA processed MWCNT revealing the distinct <111> spots in the. Notably, the FFT acquisitions across the whole image also reveal the <111> diffraction ring, as highlighted in (d) and (e), suggesting the formation of nanodiamonds at multiple places in the PLA processed MWCNT.

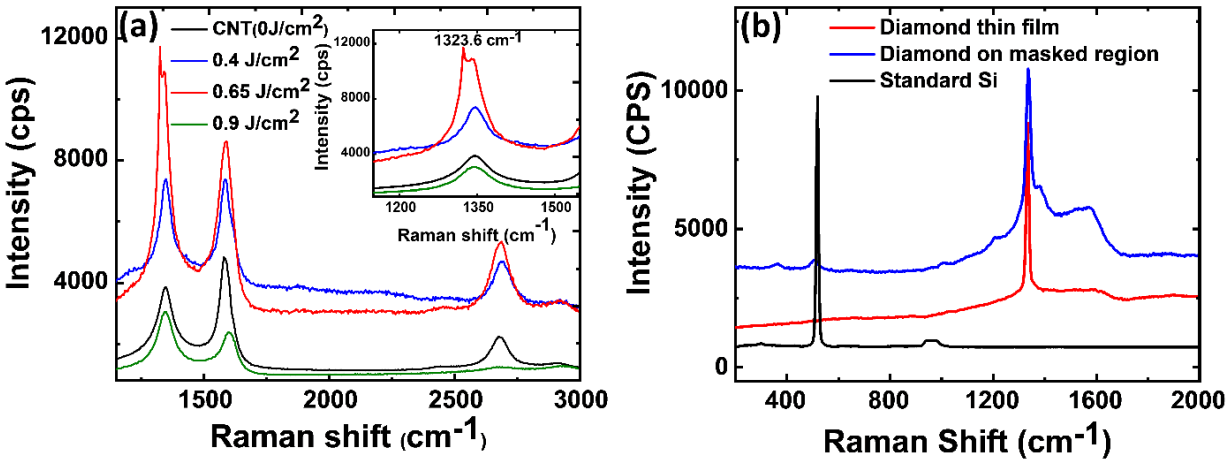

Figure 5. 5**: (a)** Detail Raman on the conversion of carbon nanotubes into diamond structures by PLA. The red shifted characteristic T_{2g} peak of diamond is observed when the CNT is irradiated with 0.65 J/cm^2 laser energy density. (b) Raman spectra of the diamond thin film grown on the laser irradiated region, diamond structures on the unirradiated CNT region (masked area), and standard Si for reference.

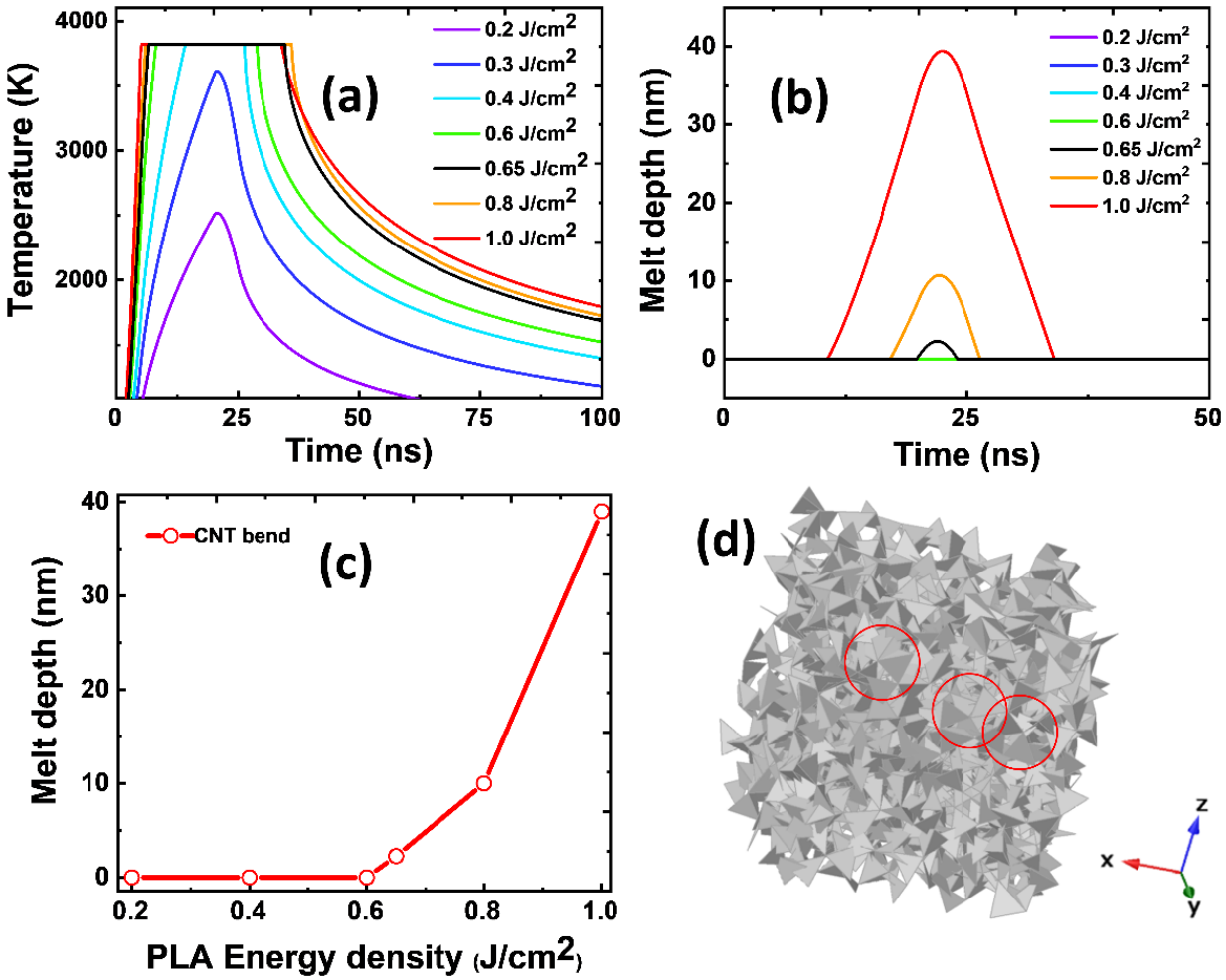

Figure 5. 6**:** Computational simulation of the tetrahedral carbon structure. (a) Temperature-time profiles for multi-walled CNT laser annealing at various PLA energy densities; (b) highlights the melting and melt depth at the respective PLA energy densities; (c) suggests onset of melting at 0.6 J/cm^2 in case of MWCNT, and the exponential rise in melt depth post onset (d) reveals the structural model for tetrahedrally bonded nanodiamond units in the ultrafast quenched liquid phase regrown solid.

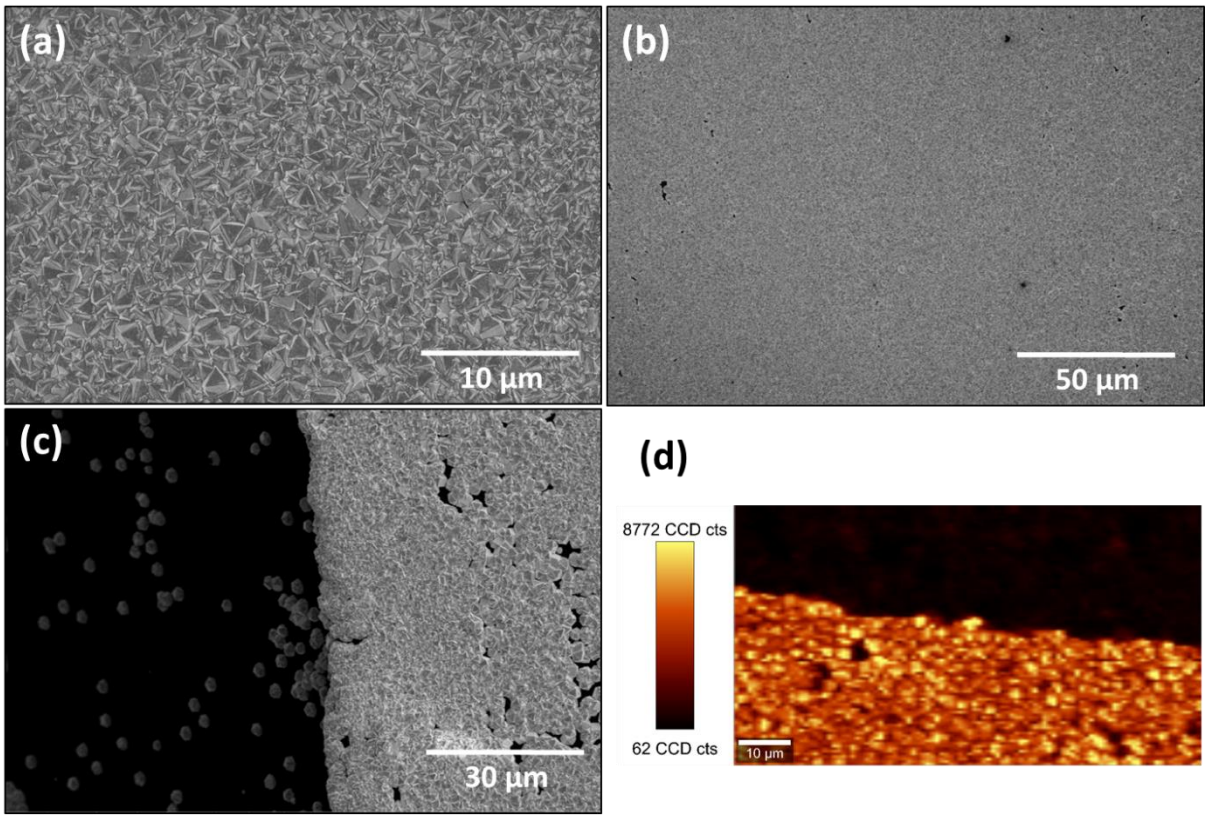

Figure 5. 7**:** Detail of the HFCVD diamond thin film formation assisted by the PLA diamond seeds converted from the CNTs on Si substrate. (a) High-resolution image shows the triangular faceting structures referring to the (111) texture growth of diamond, (b) shows the formation of large area diamond thin film, (c) shows the large area diamond thin film formation on the right side of the substrate, where the CNT was irradiated by the ArF laser to form nanodiamond. The left side was covered by the shadow mask during the PLA process and therefore, sparse HFCVD diamond formation is observed due to the lack of nucleation sites (owing to the absence of PLA converted nanodiamonds). The sharp boundary of the diamond film refers to the boundary of the shadow mask during the PLA process. (d) The Raman area mapping of the diamond peak depicts the presence of a continuous diamond entity in the unmasked laser irradiated region (bottom side). An almost complete absence of graphitic entity on the bottom side refers to the high quality diamond thin film deposition.

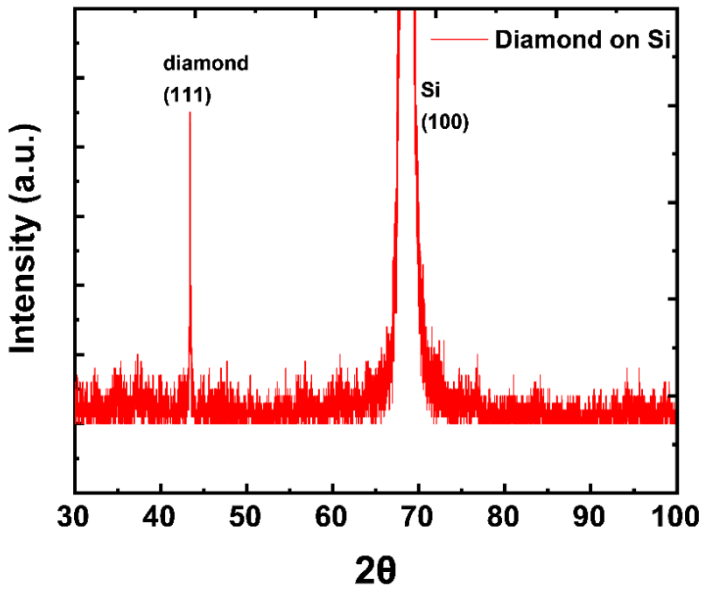

Figure 5. 8**:** X-ray two theta scan of the HFCVD diamond thin film on Si substrate showing a sharp (111) diamond peak.

References

[1] Q. Huang, D. Yu, B. Xu, W. Hu, Y. Ma, Y. Wang, Z. Zhao, B. Wen, J. He, Z. Liu, Y. Tian, Nanotwinned diamond with unprecedented hardness and stability, Nature. 510 (2014) 250–253. https://doi.org/10.1038/nature13381.

[2] H. Clevenson, M.E. Trusheim, C. Teale, T. Schröder, D. Braje, D. Englund, Broadband magnetometry and temperature sensing with a light-trapping diamond waveguide, Nat. Phys. 11 (2015) 393–397. https://doi.org/10.1038/nphys3291.

[3] L. Hu, D.S. Hecht, G. Grüner, Carbon Nanotube Thin Films: Fabrication, Properties, and Applications, Chem. Rev. 110 (2010) 5790–5844. https://doi.org/10.1021/cr9002962.

[4] V.N. Mochalin, O. Shenderova, D. Ho, Y. Gogotsi, The properties and applications of nanodiamonds, Nat. Nanotechnol. 7 (2012) 11–23. https://doi.org/10.1038/nnano.2011.209.

[5] A. Haque, J. Narayan, Electron field emission from Q-carbon, Diam. Relat. Mater. 86 (2018) 71–78. https://doi.org/10.1016/j.diamond.2018.04.008.

[6] Y. Tao, J.M. Boss, B.A. Moores, C.L. Degen, Single-crystal diamond nanomechanical resonators with quality factors exceeding one million, Nat. Commun. 5 (2014) 3638. https://doi.org/10.1038/ncomms4638.

[7] A. Haque, J. Narayan, Stability of electron field emission in Q-carbon, MRS Commun. 8 (2018) 1343–1351. https://doi.org/10.1557/mrc.2018.172.

[8] A. Raunika, S.A. Raj, K. Jayakrishna, M.T.H. Sultan, Carbon nanotube: A review on its mechanical properties and application in aerospace industry, IOP Conf. Ser. Mater. Sci. Eng. 270 (2017) 012027. https://doi.org/10.1088/1757-899X/270/1/012027.

[9] A. Merlen, P. Toulemonde, S. Le Floch, G. Montagnac, T. Hammouda, O. Marty, A. San Miguel, High pressure–high temperature synthesis of diamond from single-wall pristine and

iodine doped carbon nanotube bundles, Carbon. 47 (2009) 1643–1651. https://doi.org/10.1016/j.carbon.2009.02.014.

[10] M. Corrias, Ph. Serp, Ph. Kalck, G. Dechambre, J.L. Lacout, C. Castiglioni, Y. Kihn, High purity multiwalled carbon nanotubes under high pressure and high temperature, Carbon. 41 (2003) 2361–2367. https://doi.org/10.1016/S0008-6223(03)00279-3.

[11] A.J.S. Fernandes, M. Pinto, M.A. Neto, F.J. Oliveira, R.F. Silva, F.M. Costa, Nano carbon hybrids from the simultaneous synthesis of CNT/NCD by MPCVD, Diam. Relat. Mater. 18 (2009) 160–163. https://doi.org/10.1016/j.diamond.2008.08.015.

[12] J. Shen, F.M. Zhang, J.F. Sun, Y.Q. Zhu, D.G. McCartney, Spark plasma sintering assisted diamond formation from carbon nanotubes at very low pressure, Nanotechnology. 17 (2006) 2187–2191. https://doi.org/10.1088/0957-4484/17/9/018.

[13] J.L. Gong, L.T. Sun, D.Z. Zhu, Z.Y. Zhu, S.X. He, T. Yue, Z.X. Wang, Diamond nanorods from carbon nanotubes by hydrogen plasma treatment, Int. J. Nanosci. 05 (2006) 307–313. https://doi.org/10.1142/S0219581X06004401.

[14] R.K. Singh, J. Narayan, A novel method for simulating laser-solid interactions in semiconductors and layered structures, Mater. Sci. Eng. B. 3 (1989) 217–230. https://doi.org/10.1016/0921-5107(89)90014-7.

[15] M. Shamsa, W.L. Liu, A.A. Balandin, C. Casiraghi, W.I. Milne, A.C. Ferrari, Thermal conductivity of diamond-like carbon films, Appl. Phys. Lett. 89 (2006) 161921. https://doi.org/10.1063/1.2362601.

[16] J. Steinbeck, G. Dresselhaus, M.S. Dresselhaus, The properties of liquid carbon, Int. J. Thermophys. 11 (1990) 789–796. https://doi.org/10.1007/BF01184345.

[17] D.J. Yang, Q. Zhang, G. Chen, S.F. Yoon, J. Ahn, S.G. Wang, Q. Zhou, Q. Wang, J.Q. Li, Thermal conductivity of multiwalled carbon nanotubes, Phys. Rev. B. 66 (2002) 165440. https://doi.org/10.1103/PhysRevB.66.165440.

[18] Z. Zeng, L. Yang, Q. Zeng, H. Lou, H. Sheng, J. Wen, D.J. Miller, Y. Meng, W. Yang, W.L. Mao, H. Mao, Synthesis of quenchable amorphous diamond, Nat. Commun. 8 (2017) 1–7. https://doi.org/10.1038/s41467-017-00395-w.

[19] Carbon - EAM potentials, (n.d.). https://sites.google.com/site/eampotentials/Carbon (accessed February 11, 2020).

[20] M. Dixon, P. Hutchinson, A method for the extrapolation of pair distribution functions, Mol. Phys. 33 (1977) 1663–1670. https://doi.org/10.1080/00268977700101381.

[21] J. Narayan, A. Bhaumik, S. Gupta, A. Haque, R. Sachan, Progress in Q-carbon and related materials with extraordinary properties, Mater. Res. Lett. 6 (2018) 353–364. https://doi.org/10.1080/21663831.2018.1458753.

[22] J. Narayan, A. Bhaumik, A. Haque, Pseudo-topotactic growth of diamond nanofibers, Acta Mater. 178 (2019) 179–185. https://doi.org/10.1016/j.actamat.2019.08.008.

[23] S. Prawer, R.J. Nemanich, Raman spectroscopy of diamond and doped diamond, Philos. Transact. A Math. Phys. Eng. Sci. 362 (2004) 2537–2565. https://doi.org/10.1098/rsta.2004.1451.

[24] S. Yick, A. Mai-Prochnow, I. Levchenko, J. Fang, M.K. Bull, M. Bradbury, A.B. Murphy, K. (Ken) Ostrikov, The effects of plasma treatment on bacterial biofilm formation on vertically-aligned carbon nanotube arrays, RSC Adv. 5 (2014) 5142–5148. https://doi.org/10.1039/C4RA08187K.

[25] A.C. Ferrari, Raman spectroscopy of graphene and graphite: Disorder, electron–phonon coupling, doping and nonadiabatic effects, Solid State Commun. 143 (2007) 47–57. https://doi.org/10.1016/j.ssc.2007.03.052.

[26] C.-H. Li, H.-C. Liu, S.-C. Tseng, Y.-P. Lin, S.-P. Chen, J.-Y. Li, K.-H. Wu, J.-Y. Juang, Enhancement of the field emission properties of low-temperature-growth multi-wall carbon nanotubes by KrF excimer laser irradiation post-treatment, Diam. Relat. Mater. 15 (2006) 2010–2014. https://doi.org/10.1016/j.diamond.2006.09.017.

[27] J.H. Lehman, M. Terrones, E. Mansfield, K.E. Hurst, V. Meunier, Evaluating the characteristics of multiwall carbon nanotubes, Carbon. 49 (2011) 2581–2602. https://doi.org/10.1016/j.carbon.2011.03.028.

[28] W.-J. Zhao, A. Sawada, M. Takai, Field Emission Characteristics of Screen-Printed Carbon Nanotube After Laser Irradiation, Jpn. J. Appl. Phys. 41 (2002) 4314. https://doi.org/10.1143/JJAP.41.4314.

[29] A. Sawada, M. Iriguchi, W.J. Zhao, C. Ochiai, M. Takai, Emission site control in carbon nanotube field emitters by focused ion and laser irradiation, J. Vac. Sci. Technol. B Microelectron. Nanometer Struct. Process. Meas. Phenom. 21 (2003) 362–365. https://doi.org/10.1116/1.1527597.

[30] H. Li, T. Xu, C. Wang, J. Chen, H. Zhou, H. Liu, Humidity dependence on the friction and wear behavior of diamond-like carbon film in air and nitrogen environments, Diam. Relat. Mater. 15 (2006) 1585–1592. https://doi.org/10.1016/j.diamond.2005.12.048.

[31] J. Heremans, C.H. Olk, G.L. Eesley, J. Steinbeck, G. Dresselhaus, Observation of metallic conductivity in liquid carbon, Phys. Rev. Lett. 60 (1988) 452–455. https://doi.org/10.1103/PhysRevLett.60.452.

[32] M.S. Dresselhaus, M. Endo, Relation of Carbon Nanotubes to Other Carbon Materials, in: M.S. Dresselhaus, G. Dresselhaus, P. Avouris (Eds.), Carbon Nanotub. Synth. Struct. Prop. Appl., Springer, Berlin, Heidelberg, 2001: pp. 11–28. https://doi.org/10.1007/3-540-39947-X_2.

[33] F.P. Bundy, Pressure-temperature phase diagram of elemental carbon, Phys. Stat. Mech. Its Appl. 156 (1989) 169–178. https://doi.org/10.1016/0378-4371(89)90115-5.

[34] R. Sachan, S. Gupta, J. Narayan, Nonequilibrium Structural Evolution of Q-Carbon and Interfaces, ACS Appl. Mater. Interfaces. 12 (2020) 1330–1338. https://doi.org/10.1021/acsami.9b17428.

[35] A.E. Aliev, M.H. Lima, E.M. Silverman, R.H. Baughman, Thermal conductivity of multi-walled carbon nanotube sheets: radiation losses and quenching of phonon modes, Nanotechnology. 21 (2009) 035709. https://doi.org/10.1088/0957-4484/21/3/035709.

[36] V.S. Dozhdikov, A.Y. Basharin, P.R. Levashov, Quenching of liquid carbon under intensive heat transfer to the cold diamond substrate: Molecular-dynamic simulation, J. Phys. Conf. Ser. 653 (2015) 012091. https://doi.org/10.1088/1742-6596/653/1/012091.

[37] R. Ranganathan, S. Rokkam, T. Desai, P. Keblinski, Generation of amorphous carbon models using liquid quench method: A reactive molecular dynamics study, Carbon. 113 (2017) 87–99. https://doi.org/10.1016/j.carbon.2016.11.024.

[38] D.J. Evans, B.L. Holian, The Nose–Hoover thermostat, J. Chem. Phys. 83 (1985) 4069–4074. https://doi.org/10.1063/1.449071.

[39] R.L. Davidchack, R. Handel, M.V. Tretyakov, Langevin thermostat for rigid body dynamics, J. Chem. Phys. 130 (2009) 234101. https://doi.org/10.1063/1.3149788.

[40] S. Gupta, R. Sachan, A. Bhaumik, J. Narayan, Enhanced mechanical properties of Q-carbon nanocomposites by nanosecond pulsed laser annealing, Nanotechnology. 29 (2018) 45LT02. https://doi.org/10.1088/1361-6528/aadd75.

[41] A. Haque, J. Narayan, Electron field emission from Q-carbon, Diam. Relat. Mater. 86 (2018) 71–78. https://doi.org/10.1016/j.diamond.2018.04.008.

[42] A. Haque, J. Narayan, Stability of electron field emission in Q-carbon, MRS Commun. 8 (2018) 1343–1351. https://doi.org/10.1557/mrc.2018.172.

[43] A. Haque, S. Sumaiya, An Overview on the Formation and Processing of Nitrogen-Vacancy Photonic Centers in Diamond by Ion Implantation, J. Manuf. Mater. Process. 1 (2017) 6. https://doi.org/10.3390/jmmp1010006.

[44] A. Zkria, A. Haque, M. Egiza, E. Abubakr, K. Murasawa, T. Yoshitake, J. Narayan, Laser-induced structure transition of diamond-like carbon coated on cemented carbide and formation of reduced graphene oxide, MRS Commun. 9 (2019) 910–915. https://doi.org/10.1557/mrc.2019.88.

[45] S. Iijima, T. Ichihashi, Single-shell carbon nanotubes of 1-nm diameter, Nature. 363 (1993) 603–605. https://doi.org/10.1038/363603a0.

[46] T. Nakamiya, S. Aoqui, K. Ebihara, Experimental and numerical study on pulsed-laser annealing process of diamond-like carbon thin films, Diam. Relat. Mater. 10 (2001) 905–909. https://doi.org/10.1016/S0925-9635(00)00536-7.

[47] T. Nakamiya, T. Ueda, T. Ikegami, K. Ebihara, R. Tsuda, Thermal analysis of carbon nanotube film irradiated by a pulsed laser, Curr. Appl. Phys. 8 (2008) 400–403. https://doi.org/10.1016/j.cap.2007.10.056.

[48] Z. Chuan-Yi, J. Xiao-Peng, M. Hong-An, L. Shang-Sheng, T. Yu, X. Hong-Yu, Grow Large High-Quality Diamonds with Different Seed Surfaces, Chin. Phys. Lett. 23 (2006) 214–216. https://doi.org/10.1088/0256-307X/23/1/062.

[49] A. Haque, P. Pant, J. Narayan, Large-area diamond thin film on Q-carbon coated crystalline sapphire by HFCVD, J. Cryst. Growth. 504 (2018) 17–25. https://doi.org/10.1016/j.jcrysgro.2018.09.036.

[50] J.J. Gracio, Q.H. Fan, J.C. Madaleno, Diamond growth by chemical vapour deposition, J. Phys. Appl. Phys. 43 (2010) 374017. https://doi.org/10.1088/0022-3727/43/37/374017.

6. Large-area diamond thin film on Q-carbon coated crystalline sapphire by HFCVD

Ariful Haque, Punam Pant, and Jagdish Narayan

Materials Science and Engineering, North Carolina State University, Raleigh, North Carolina 27695.7916, USA

6.1 Abstract

The growth of diamond on transparent substrates like sapphire presents a great challenge because of the large thermal misfit between the film and the substrate, absence of any carbide layer during diamond growth, and low nucleation density during chemical vapor deposition (CVD) growth process. In this study, we report on the use and the role of Q-carbon as an intermediate layer to successfully deposit large-area diamond film on c-sapphire by hot filament chemical vapor deposition (HFCVD). The Q-carbon consists of very high-density diamond tetrahedra which act as the embryo for diamond nucleation. Different techniques such as X-ray diffraction, scanning electron microscopy, and Raman spectroscopy show that continuous diamond films with good crystallinity and without any impurity phase can be deposited on the Q-carbon coated single crystal sapphire substrate. The Q-carbon layer is very adherent and it negates the thermal mismatch between the diamond film and the sapphire substrate. A small blue shift in the Raman peak of the diamond from its equilibrium position suggests the deposition of the CVD diamond film with minimal stress (1.14 GPa). This technique of growing large-area continuous diamond thin film with excellent crystalline quality on a single crystal sapphire substrate can serve as a platform for the development of next-generation corrosion and erosion resistant infrared windows, state-of-the-art optoelectronic devices, and advanced scanning probe microscopy systems.

6.2 Introduction

Diamond thin films have unique physical and chemical properties which are needed for different technological applications of immense commercial importance. Especially, the deposition of large-area diamond film on single crystal sapphire holds a lot of promise in various technological applications due to unique properties of the substrate, which include good optical transparency, high-melting point, high hardness and chemical inertness, etc. The applications of diamond on sapphire include diamond polishing wheels, corrosion and radiation resistant infrared windows, solid-state lasers, novel scanning probe microscopy applications such as nanoindentation and high-resolution imaging of soft samples, and so on [1,2]. In fact, a model laser gain element formed by integrating diamond and a solid-state laser material, such as Ti: Sapphire, has been designed to obtain an increased average output power up to a megawatt level [3]. All of these technological milestones can be achieved by establishing a successful deposition route to grow large-area and high-quality diamond on single crystal sapphire. Although a lot of comprehensive studies about chemical vapor deposition (CVD) of diamond on different substrates have been conducted over the past few decades, relatively little effort has been put on the development of large-area CVD diamond on single crystal sapphire substrate due to different technical obstacles. The utilization of sapphire as a substrate for CVD diamond growth is difficult due to low thermal conductivity (27.2 W/m-K) of sapphire, huge difference in thermal expansion coefficients between the diamond film and the sapphire substrate, low nucleation density, and poor adhesion [4,5]. Since the Gibbs free energy of formation of aluminium carbide (Al_4C_3) is much lower (-32.1 kJ/mole) compared to that of aluminium oxide (-1675 kJ/mole), the carbide layer to exist the diamond nucleation is not favored[6]. Over the years, attempts to grow large-area diamond thin film on transparent and hard substrates have received, at best, limited success.

Thermodynamically, sapphire is a very stable material, and its conversion from Al_2O_3 to an intermediate carbide layer during the fabrication of CVD diamond is unfavorable [7]. The absence of any carbide layer at the interface makes the diamond film poorly adherent on the sapphire substrate. The adherence is even worse due to the large thermal expansion coefficient mismatch between the sapphire and the diamond, which leads to a huge thermal stress (compressive) in the diamond film during the cooling process. To overcome adhesion and stress-related problems, researchers have proposed different techniques, such as an *in situ* two-step hot-filament chemical vapor deposition (HFCVD) [8], polishing the substrate surface by *in situ* pre-deposition of a carbon layer to form aluminum carbide at the surface during the HFCVD, microwave plasma chemical vapor deposition (MPCVD) [9], and using the plasma flame CVD which supplies activated diamond species to the substrate in the plasma flame [10]. However, all of these studies gave relatively low nucleation density (10^6 –10^7 sites/cm^2), and formation of large-area continuous diamond thin films was not obtained. The dc-biasing technique has been successfully used to deposit diamond on mirror-polished Si substrate with improved nucleation. However, this method cannot be applied to the insulating sapphire substrate [11]. The growth of polycrystalline diamond films on single crystal sapphire using HFCVD has been studied [12]. Problems related to the stress generation, poor adhesion at the film-substrate interface, delamination, and film cracking were observed for deposited areas greater than ~100μm^2. An alternative technique, by using patterned silicon on sapphire for CVD of diamond, was used to grow diamond on sapphire [7]. In this case, Si acts as a partial stress-relieving layer. However, the area of continuous diamond film greater than ~200μm^2 still delaminated. These problems restrict the deposition of large-area diamond film on sapphire and put an upper limit even after using a crystalline Si layer as an intermediate layer. Diamond nucleation on mirror polished optically transparent substrates is another major challenge.

To increase the nucleation density researchers tried faceting or mechanical scratch pretreatment, by abrading using ultra-sonication or annealing in air at high-temperature, on sapphire during the HFCVD of diamond thin film [13,14]. But these pretreatment techniques damage the surface of the polished substrate, and hinder practical applications of diamond on sapphire. In another study, researchers claimed to observe a high nucleation density and a rapid lateral growth rate enabled the diamond nuclei to coalesce and cover the entire surface of the substrate in a short time using HFCVD (after 20 minutes manual aberration of 1 μm diamond seeds on the sapphire substrate) [12]. However, further diamond deposition (4 hours) caused a large part of the diamond film to delaminate. Recently, large area diamond thin films on sapphire have been synthesized using the adamantime coating on the substrate [15]. A good quality diamond film on sapphire was obtained only after a very long deposition time of 48 hours.

In this study, we have investigated a novel route to grow large-area CVD diamond thin film on sapphire by using Q-carbon as an intermediate layer to overcome the inherent problems related to the nucleation and growth of diamond on single crystal sapphire. We have successfully demonstrated a simple technique for the direct deposition of large-area, and excellent quality diamond thin films on the Q-carbon coated sapphire substrate by HFCVD. The Q-carbon is a new phase of carbon discovered by our group recently, which consists of diamond tetrahedra with a very high packing efficiency due to the ultrafast quenching from the liquid phase of carbon by nanosecond pulsed laser annealing [16,17]. This layer helps to grow a very large-area diamond on sapphire without any cracking or delamination. The analyses from scanning electron microscopy (SEM), X-ray diffraction (XRD), and Raman spectroscopy show that the Q-carbon assists the diamond nucleation, and a large-area continuous diamond film with low compressive stress can be obtained. We have conducted a detailed analysis of stresses in these films and found that the Q-

carbon interlayer helps to reduce the effect of the thermal misfit strains which arise as a result of the difference in coefficients of thermal expansion between the diamond film and the smooth sapphire substrate.

6.3 Experimental

We have grown the large-area CVD diamond film using a two-step method, i.e. first, the formation of Q-carbon using nanosecond pulsed laser annealing (PLA) of the amorphous diamond-like carbon (DLC) film, and second the growth of diamond film on Q-carbon by HFCVD. To fabricate the Q-carbon, at first, we deposited ~500 nm thick amorphous carbon thin film on the c-plane sapphire substrate using pulsed laser deposition. The substrate was cleaned with acetone vapor for 10 minutes, with methanol for 5 minutes by ultra-sonication, and dried with nitrogen gas. The amorphous carbon film was deposited in a stainless steel chamber evacuated to a base pressure of $\sim 1 \times 10^{-6}$ torr. We used a pulsed krypton fluoride (KrF) excimer laser (λ = 248 nm, repetition rate 5 Hz/s, pulse width 20 ns, laser fluence of ~2 J/cm^2) during deposition. The as-deposited films were irradiated by an ArF laser (wavelength = 193 nm, pulse duration = 25 ns) pulse with an energy density in-between 0.6 to 0.7 Jcm^{-2} for conversion into Q-carbon. During the laser irradiation process, the as-deposited DLC film was melted in a super undercooled state and subsequently quenched to complete the whole process within 200-250 nanoseconds. After shrinkage from the PLD grown amorphous carbon layer, due to the super undercooling and subsequent quenching from the liquid state of carbon which is produced due to nanosecond pulsed laser irradiation, the generated Q-carbon layer thickness varies from 35–150 nm [18].

During HFCVD of diamond thin film, the Q-carbon coated c-sapphire was inserted into the HFCVD reactor. We used a set of 4 straight tungsten wires as hot filaments. The distance between the filament and the substrate was maintained at ~6-8 mm. Diamond thin films were deposited for

6 hours. The schematic diagram of the HFCVD reactor used to deposit diamond on Q-carbon/sapphire by employing methane and hydrogen gas mixtures is shown in Fig. 6.1 (a). The tungsten filament was gradually heated to a high-temperature (~2000^{o} C). The CVD growth was done under a flow rate of 2 sccm for methane and 100 sccm for hydrogen at a chamber pressure of 20 Torr. Pyrolysis of the gas mixture takes place inside the CVD chamber, which results in the generation of diamond-forming active gas species. Upon reaching the Q-carbon/sapphire substrate surface, these diamond-forming active gas species initiate the nucleation and the formation of diamond. The substrate was placed on a substrate holder, and the temperature of around 800^{o} C was maintained during growth. The set of multiple filaments and the rotation of the substrate stage during the deposition assisted the formation of a uniform diamond thin film over the large substrate area. Fig. 6.1 (b) represents the schematic of the physical and chemical processes occurring inside the chamber and shows the dissociation of precursor gases at high-temperature. The absorbed reactive species coalesce and subsequently form diamond clusters on the substrate under favorable conditions, which are also shown in this figure.

Raman spectroscopy and XRD are the two most powerful techniques to characterize diamond thin films in terms of structure and bonding, respectively. These techniques provide a fingerprint of the presence of diamond and non-diamond phases, and the stress present in the film. Raman spectra were obtained using a WITec confocal Raman microscope system (alpha300M) micro-Raman spectrometer (triple monochromator, gratings 2400 lines/mm) with an x100 objective which focuses the laser beam in a spot of 2 μm. All of the spectra were recorded by CCD matrix with a very high spectral resolution (<300 nm). The excitation of the Raman scattering was performed by a 532 nm diode-pumped solid-state laser. To avoid any local heating of the sample, a low laser power of ~40 mW was used. The X-ray diffraction (XRD) was performed on the

HFCVD diamond film using the Rigaku SmartLab x-ray diffractometer with a CuKα x-ray source (25KV, 15 mA). Diffraction data were collected with a 0.01 step size in the 2θ range of 30^0-100^0 and a constant dwell time of 0.5 seconds per scan point. Bragg-Brentano reflection geometry was used during the data acquisition process. High-resolution scanning electron microscopy (SEM) with the sub-nanometer resolution was carried out on the laser irradiated samples using the FEI Verios 460L SEM.

6.4 Results and discussion

6.4.1 Nucleation, growth, and microstructure of diamond

Nucleation of diamond requires the formation or preexistence of diamond nuclei which are the smallest stable diamond units that form on the substrate and then act as suitable sites for the subsequent diamond thin film growth. Understanding the diamond nucleation is crucial because it not only affects the final grain size and orientation of the diamond thin film but also the film thickness, morphology, uniformity, defect concentration, adhesion, surface roughness, and so on. Fig. 6.2 (a) shows an SEM micrograph of Q-carbon on c-sapphire, which has been used for the HFCVD diamond deposition. In conventional diamond depositions, seeds of nano/micro diamond are dispersed on the substrate, which act as diamond nucleation sites during the CVD process. Using Q-carbon, we obtained a relatively high diamond nucleation density (around 10^9 cm^{-2}) for diamond growth. Fig. 6.2 (b) shows the SEM micrograph of diamond on the Q-carbon/c-plane sapphire surface after 3 hours of HFCVD. The Q-carbon provides a high number density of nucleation sites by providing: (i) very active surface adsorption sites to connect with the diamond-forming gas species due to the presence of numerous diamond tetrahedra, and (ii) the distributed region of adsorption sites larger than the nuclei size for the subsequent crystal growth. Although considerable amount of work has been done in the past on the diamond nucleation mechanism

during the HFCVD process, the detailed steps which can explain the nucleation of the first diamond phase are still unclear. The hot filament generates atomic hydrogen, which react with carbon containing species to reduce and connect it with diamond/ diamond nuclei. The growth of diamond is affected by the generation of different hydrocarbon species in the gas phase at high-temperature inside the CVD chamber and adsorption of those species on the substrate surface via interfacial interactions. The Gibbs free energies at different stages depend upon the C–H bond energies in different CH_X species, i.e.CH_4, CH_3, CH_2, and CH, and formation energy of H_2. The reactions initiate from the dissociation of the molecular hydrogen by the hot filament at a very high-temperature to form highly active hydrogen radical followed by several steps (by which the atomic carbon is generated via the formation of CH_X species upon dissociation of methane) given below [19].

$H_2 \longrightarrow 2\,H^{\cdot}$ $\Delta G^0 = 75$ kJ/mol

$CH_4 + H^{\cdot} \longrightarrow CH_3 + H_2$ $\Delta G^0 = -42$ kJ/mol

$CH_3 + H^{\cdot} \longrightarrow CH_2 + H_2$ $\Delta G^0 = 17$ kJ/mol

$CH_2 + H^{\cdot} \longrightarrow CH + H_2$ $\Delta G^0 = -38$ kJ/mol

$CH + H^{\cdot} \longrightarrow C + H_2$ $\Delta G^0 = -84$ kJ/mol

$C + C_d \longrightarrow 2C_d$ $\Delta G^0 = -480$ kJ/mol

At the end, generated carbon atoms are added to the diamond structure via the final reaction. Although the formation of atomic hydrogen and the formation of CH_2 species are not thermodynamically favorable owing to the small positive changes in Gibbs free energy, the high-temperature environment ensures a thermodynamically favorable condition.[19] sp^1, sp^2 and sp^3 bonded carbon species coexist on the substrate surface and the etching of the sp^1 and sp^2 bonded carbon are ten times faster than etching of the stable sp^3 bonded carbon, which assists the growth

of sp^3 phase [20]. Around 10^4 activated hydrogen atoms are required to convert a carbon atom to the final sp^3 bonded state, therefore, we have used a high hydrogen to methane ratio (50:1) [21]. At the final stage, the disordered domains of the sp^3 bonded carbon convert into an ordered diamond structure with the same bonding type. The high density of the diamond tetrahedra in Q-carbon on the substrate surface helps to achieve a very high nucleation density during the diamond growth. The overall morphology of the obtained diamond thin films after 6 hours growth is shown by the high resolution SEM images in Fig. 6.3(a)-(c) at different magnifications. No visible crack/delamination was observed in the film implying that the Q-carbon layer helps to overcome the huge thermal mismatch between the film and the substrate. Fig. 6.3(c) is the low magnification image of the HFCVD diamond thin film, which corroborates that large-area continuous diamond thin film has been grown using this novel technique. For comparison, we have also grown the diamond on the clean c-sapphire without a Q-carbon layer under the same deposition conditions. The morphology of the diamond growth on sapphire without Q-carbon using the same HFCVD conditions for 6 hours is shown in Fig. 6.3(d). This image shows that the area of the substrate surface is barely covered with diamond crystals. Thus, we can conclude that the Q-carbon layer can enhance the coverage during diamond deposition. This is due to the presence of the diamond tetrahedra in the Q-carbon with a high packing efficiency, which can act as embryos for the diamond nucleation. The residual amorphous carbon is etched off by the reactive species. This etching of the amorphous carbon (driven by the highly reactive atomic hydrogen) occurs via the following thermodynamically favorable reaction [19].

$$C_a + 4H^{\cdot} \longrightarrow CH_4 \qquad \Delta G^0 = -470 \text{ kJ/mol}$$

6.4.2 Effect of thermal stress

Fig. 6.4(a) represents the percent of the linear thermal expansion of sapphire, AlN, silicon, and diamond in the temperature range between 0^o C and 1200^o C, which helps us to understand the effect of thermal stress on diamond film at different growth temperatures [22,23]. The relative thermal expansion at different temperatures also implies the magnitude and nature of the thermal stress in the diamond film grown at a particular temperature. To plot this figure, we have determined the percent of the thermal expansion by integrating the corresponding expression for the thermal expansion coefficient of each of the material over the temperature range. From Fig. 6.4(a) we can observe that the percent of thermal mismatch is the highest for the diamond-sapphire system compared to other systems at the deposition temperature (800-850^0C). Therefore, the growth of diamond on sapphire at such high-temperature has always been a challenging task.

The thermal misfit strain occurs due to the differences in coefficients of thermal expansion between the diamond thin film and the substrate. The coefficient of thermal expansion of the diamond film (α_d) is less than that of the substrates (α_s) considered in Fig. 6.4(a). As a result, the film will be under compressive stress and the substrate will be under tensile stress after cooling. The thermal misfit strain (ε_T) in the diamond thin film plane on a particular substrate can be expressed by equation 1.

$$\varepsilon_T = (\alpha_d - \alpha_s)\, \Delta T \qquad (1)$$

Where ΔT is the change in temperature and is negative during cooling down. Based on the thermal properties, the thermal strain of the diamond film on sapphire, AlN, and silicon substrates at different growth temperatures are illustrated in Fig. 6.4(b). The thermal strain that can be generated in the diamond film plane on Si or AlN is much less than that on the sapphire substrate over the entire temperature range. Therefore, the high-temperature growth of diamond on Si or AlN is

relatively easier from the thermal strain viewpoint. This plot shows that at 800^{o} C deposition temperature, a compressive strain of ~0.43% is expected to be generated in a diamond thin film on the c-sapphire substrate. Such a high compressive strain due to the thermal misfit can generate ~ 5.1 GPa stress in the film. The diamond film on sapphire can easily delaminate under such large amount of strain. Although researchers have been able to grow diamond on c-sapphire by electron–cyclotron–resonance chemical vapor deposition process using dispersed–particulate diamond suspension for nucleation at a lower temperature (500-550^{0} C), however, such low growth temperature is enough to generate approximately 3.5 GPa stress [24]. This amount of compressive stresses may cause delamination in the weakly bonded diamond film from the sapphire substrate. Although the optical evaluation of the continuous diamond film did not show any visible cracking or delamination, however, the edges of the film peeled off due to the built-in stress generated by the thermal misfit.

6.4.3 Raman Spectroscopy

Raman spectroscopy is a very effective technique to characterize the diamond film for different information. Fig. 6.5 shows the Raman spectra of the diamond film grown on the c-sapphire substrate. This spectrum shows a sharp distinct characteristic Raman peak of diamond at 1334.35 cm^{-1}, which refers to the crystalline diamond growth. This peak occurs due to the zone center Raman active TO(X) optical phonon mode of diamond, which has triply degenerate T_{2g} symmetry [25]. On the contrary, the synthetic diamond with defects present in the crystal is characterized by several additional features which have been attributed to different types of sp^2 and sp^3 defects. The natural diamond displays a sharp band at ~1332.5 cm^{-1} during the Raman spectroscopy [26]. The linewidth of this peak is observed to be ~2 cm^{-1}. Usually, this characteristic peak of diamond shifts from its equilibrium position towards right due to the compressive stress in the film, as explained

below. The peak position of the Raman signal is determined from the energy of the zone center optical phonons. The frequency of the first order phonon bands and, therefore, the relative position of the first order Raman line is related to the mass of the relevant atoms and the length and stiffness of the bonds in the crystal. Therefore, the position of the first order line will be sensitive to anything that changes these parameters. The equilibrium position of the atoms is changed under a stressed condition. Stress creates a contraction of the lattice, and the interatomic forces are changed due to the subtle anharmonicity of the bonds. This change in interatomic forces alters the phonon vibrational frequencies, which can be characterized by the change of the Raman peak position. The shift in the peak position measured for a thin film can be used to estimate the stress using hydrostatic [27], uniaxial [28] or biaxial [29] models. Researchers determined relationships between the observed Raman peak shifts and stress values in the framework of biaxial stress model to study the stress in the diamond thin films on different substrates [30]. Under the presence of biaxial stress, the Raman peak of polycrystalline diamond splits into singlet and doublet states and shifts from the equilibrium position. The linear expression between the stress and the peak shift due to the singlet and doublet states can be obtained by averaging the stress-peak shift relations. The shift of the singlet and doublet states can be expressed according to the following expressions developed by Ager and Drory [29].

$$\Delta\nu_s\ [cm^{-1}] = -0.93\sigma\ [GPa] \qquad (2)$$

$$\Delta\nu_d\ [cm^{-1}] = -2.61\sigma\ [GPa] \qquad (3)$$

At low-stress region, typically 0 – 8 GPa, the peak splitting is not resolved and a weighted shift relation, $\Delta\nu = (1/3)\nu_s + (2/3)\nu_d$, can be used to calculate the overall stress present in the diamond film. Therefore, for a diamond peak with no split, we can express the relation between the stress and the overall peak-shift as follow:

$\Delta\nu\ [cm^{-1}] = \nu_s - \nu_0 = -1.62\sigma\ [GPa]$ (4)

Where ν_0 is the equilibrium peak position of the diamond in the unstressed state (1332.5 cm^{-1}), ν_s corresponds to the position of the observed Raman peak in the stressed state. In this study, the deconvolution of the characteristic Raman peak into two individual peaks of singlet and doublet states reliably is very difficult due to comparatively small FWHM. The splitting of diamond peak to singlet and doublet only becomes observable at $\sigma > 8–9$ GPa [30]. From the position of the Raman peak, we obtained ~1.14 GPa compressive stress in the diamond film. Such a low value of compressive stress is due to the presence of intermediate Q-carbon layer which nullifies the effect of thermal strain. Other researchers have observed a compressive stress of ~3.7 GPa, even grown at low temperature (525 ^{0}C) in their studies [24]. Our stress value is the lowest ever obtained from diamond thin films grown on a single crystal sapphire substrate. The following expression can be used to determine the stress in the diamond film.

$\sigma_{th} = d\sigma/dT\ X\ \Delta T = [E/(1-\nu)]\ (\alpha_r - \alpha_s)\ X\ \Delta T = E(\varepsilon_d - \varepsilon_s)/(1-\nu)$ (5)

where E is the Young's modulus (1143 GPa) and ν is the Poisson ratio (0.07) of diamond, and ε_d and ε_s are temperature depended thermal expansions for the diamond film and the substrate, respectively. According to this expression, the maximum thermal stress that could be generated during the deposition of diamond under the chosen deposition conditions is obtained to be ~ - 5.1 GPa. According to equation 4, this value would result in ~ 8.28 cm^{-1} blue shift in the Raman peak. However, in this study, the original peak position of the Raman spectrum shows a much less shift. It is believed that the use of the Q-carbon on the sapphire substrate plays a crucial role to reduce the effect of thermal stress.

The Raman signal from a crystal of finite size also exhibits a smaller Raman shift and has a larger full width at half maximum (FWHM) than that from an infinite crystal lattice. In this study,

the FWHM of the diamond peak is determined to be ~8.5 cm^{-1}, which is smaller compared to that of diamond grown by other techniques on sapphire. In different studies researchers have determined FWHMs of around 15 cm^{-1} and 12 cm^{-1} in the stressed diamond on sapphire grown by microwave enhanced chemical vapor deposition and low-temperature low-pressure electron–cyclotron–resonance CVD techniques and obtained good crystallinity in the diamond films [24,31]. Nevertheless, the FWHM is greater than the instrumental resolution of ~1.2 cm^{-1}. The broadening of this peak also refers to the generation of high compressive stresses in the diamond film [29]. Combined contributions of some other factors, such as microstructural defects in the film, small domain size of the diamond crystals, and sp^2-bonded impurities, are also responsible for the broadening of this peak [32]. It is worthwhile to know that non-diamond carbon phases are codeposited with diamond during the growth of diamond thin films. These carbon- containing phases are also very sensitive to the Raman spectroscopy and can be characterized by their distinctive Raman signature, for example, graphite displays a single Raman band at 1580 cm^{-1}. Amorphous carbon or diamond-like carbon is characterized by a very broad Raman band centered in-between 1450 cm^{-1} and 1550 cm^{-1}. The exact shape and position of this band depend on the deposition process and the parameters used during the deposition [33]. In the as-deposited diamond film, the broad hump in the Raman spectra was centered at ~1510 cm^{-1}. Usually, the intensity of this peak in CVD diamonds on the sapphire substrate has been observed to be very high compared to the characteristic diamond peak [24,34]. The observed small intensity of amorphous carbon-related peak in this study refers to the excellent quality of the diamond thin film. Researchers also observed a small peak at ~1150 cm^{-1} in CVD diamond on sapphire, which promotes the trace sp^3-bonded carbon nanoclusters [13,33]. Nevertheless, the vanishing intensity of this peak in this study refers to the better quality of the diamond thin film grown by this process. The inset in Fig. 6.5

shows the Raman spectrum of Q-carbon film and gives the percentage of sp^3 carbon as approximately 80-82%. The rest of the carbon remains in sp^2 form.

6.4.4 XRD

We have conducted X-ray diffraction analysis to determine the crystallinity, phase composition, stress, and quality of diamond films grown on a sapphire substrate coated with Q-carbon. Fig. 6.6 represents a typical *θ-2θ* X-ray diffraction pattern obtained from the CVD diamond film on the c-sapphire substrate. This spectrum confirms the characteristic diamond peaks at (2θ) 43.94^0 and 75.42^0 corresponding to diamond {111} and {220} reflections, respectively [35]. The positions and FWHM of the XRD peaks imply very good crystalline quality of the deposited diamond film with little strain. The XRD spectrum does not show any peak other than sapphire (0006) peaks and diamond characteristic peaks, which eliminates the presence of any other phases in the sample. Stresses and strains play significant roles in determining the characteristics of the fundamental properties of thin film heterostructures, e.g., diamond on sapphire in this study. A generalized relationship between the stress and strain in a cubic (isotropic) crystal, a crystalline diamond thin film in this study, can be expressed by $\sigma_{zz}=\boldsymbol{\lambda}\varepsilon_{xx}+\boldsymbol{\lambda}\varepsilon_{yy}+(\boldsymbol{\lambda}+2\boldsymbol{\mu})\varepsilon_{zz}$, where $\boldsymbol{\lambda}$ is the Lamé constant, and $\boldsymbol{\mu}$ is the shear modulus [36]. In thin film heterostructures, there is no stress perpendicular to the film (free surface), so $\sigma_{zz}= 0$. Using the generalized expression one can obtain the following relationship between the strain in the perpendicular direction ε_{zz} with in-plane strains, ε_{xx} and ε_{yy}, and the Poisson's ratio of the film (ν).

$$\varepsilon_{zz}/(\varepsilon_{xx}+\varepsilon_{yy}) = -\nu/(1-\nu) \qquad (6)$$

Since $\varepsilon_{xx} = \varepsilon_{yy}$ in the basal plane for the diamond thin film, we simplify equation (6) as $\varepsilon_{zz}/\varepsilon_{xx} = -2\nu/(1-\nu)$. We have measured the strain (ε_{zz}) around (111) peak from the *θ-2θ* X-ray diffraction scan and obtained an in-plane lattice strain of around 1.45×10^{-3}. We can calculate the in-plane stress

in the diamond film using this value of the planar lattice strain by using the following expression (equation 7) [37].

$$\sigma = 2\,\varepsilon_{xx}\,\boldsymbol{\mu}\,(1+v)/(1-v) \qquad (7)$$

Where v is the Poisson's ratio. The calculated stress in the diamond film is ~1.57 GPa which seems to be consistent with the stress value determined from Raman analysis.

6.4.5 Discussions

There are significant advantages of using Q-carbon as a suitable intermediate layer for the fabrication of HFCVD diamond, which include: (i) the diamond tetrahedra present in the Q-carbon structure act as nucleation sites during the diamond growth, thus eliminating the requirement of a preexisting seed layer, (ii) no carbide formation is required at the film-substrate interface for adhesion, (iii) the melting point of Q-carbon is very high, which helps us to achieve the high-temperature CVD diamond growth and attain high growth rate (0.5 $\boldsymbol{\mu}$m/h) and improved quality of diamond thin films, (iv) there is no phase transition of the substrate or Q-carbon under the chosen deposition conditions, and (v) most importantly the Q-carbon helps to bypass the stringent requirement of low thermal misfit between the diamond and the transparent substrate, etc. Although researchers [38,39] have proposed that the abstraction of hydrogen from the hydrocarbon mixture in the gaseous phase sublimated and mixed in the plasma at high-temperature is one of the possible mechanisms for diamond nucleation on the substrate with a preexisting seed layer, it is important to discuss the possible mechanism of diamond nucleation and growth on Q-carbon coated sapphire. It has been shown that Q-carbon consists of 80-85% sp^3-bonded carbon which are closely packed in the form of individual diamond tetrahedra with a packing efficiency of >80% [16]. These diamond tetrahedra in Q-carbon act as the embryo for diamond nucleation. Therefore, the hydrocarbon species might decompose into nanosized diamond particles after releasing all of

its hydrogen atoms at the Q-carbon surface. A schematic of the diamond tetrahedron is shown in Fig. 6.7(a) and the illustration of the diamond nucleation is shown in Fig. 6.7(b). The edge carbon atoms in the diamond tetrahedra or in a cluster of the diamond tetrahedra (also called Q-diamond) present in the Q-carbon are very active for the diamond nucleation due to the dangling bond characteristics, which act as active sites for the diamond nucleation. Subsequently, the growth of large-area diamond thin film takes place. In the previous study, it was shown that the Q-carbon is well adhered to the sapphire substrate due to the nonequilibrium liquid phase mediated growth from the amorphous carbon film which is quenched from a super undercooled state by using high-power nanosecond laser pulses [16]. The Q-carbon consists of ~80% sp^3 carbon and the rest is sp^2 bonded carbon. The sp^3 carbon atoms form numerous diamond tetrahedra in the dense Q-carbon structure, which act as the nucleation sites for the diamond growth [16]. As a result, the adhesion of Q-carbon with sapphire is enhanced, and its sublimation or evaporation at high-temperature is reduced. This increases the chance for a very stable Q-carbon, consisting of numerous diamond tetrahedra, to remain on the surface and act as seed/embryo for diamond nucleation. The residual amorphous carbon layer might get etched off due to the reaction with the highly active hydrogen radicals during the HFCVD process.

Generally, deposition of CVD diamond on any substrate proceeds in two stages, namely, nucleation and growth. Over the years, different diamond nucleation methods have been developed. It is well established that diamond nucleation on any smooth non carbide forming surface such as mirror-polished sapphire substrate is very difficult. The nucleation density of diamond on smooth sapphire surface without any conditioning/pretreatment is only about 10^4 cm^{-2} which results in scattered isolated individual diamond crystallites on the substrate [13]. Diamond nucleation can be enhanced by scratching the substrate surface with diamond [40], SiC [41], cubic-

BN [42], Cu or stainless steel [43], etc. Although substrate scratching can improve the diamond nucleation, it can cause serious damage to the periodic arrangement of the surface structure/atoms and thus degrades the quality of heterostructure. Coating the substrate surface with graphite [11], amorphous carbon [11,44], diamond-like carbon [45–47], C60, and mechanical oil [48] have also been employed to enhance the diamond nucleation. However, these type of coatings may result the formation of a graphitic interlayer in-between the diamond film and the substrate causing poor adhesion. This technique of diamond nucleation on Q-carbon can help to overcome the aforementioned obstacles. The investigation of the nucleation process reveals a narrow window parameters for high-quality diamond nucleation. The crucial parameters are the substrate temperature, filament temperature, methane concentration, distance between the filaments and the substrate, and the nucleation/growth time. After nucleation the diamond crystals mainly increase laterally and after a sufficient amount of growth time the coalescence of the crystallites takes place. It is very important to obtain information about the thermal stress for different applications of diamond thin films such as optical protective coatings, fabrication of thin membranes, cutting tools and anti-friction coatings that undergo high mechanical loads frequently, etc. A large difference in the thermal behavior of the diamond thin film and a substrate can lead to problems related to cracking and delamination. Besides the intrinsic stress, the difference in the thermal expansion can lead to additional stress during cool down. In a diamond-sapphire system, this strain is compressive due to the negative value of the percent of thermal misfit. The high thermal strain in the diamond film plane on sapphire during the growth results in the formation of cracks, peeling off/delamination of the diamond film during cool down. Therefore, in this particular system (diamond on sapphire), the thermal mismatch plays a crucial role during film deposition as the thermal mismatch is comparable to the intrinsic part of the mismatch in the film-substrate system.

However, in this present experiment, we overcame the effect of this huge thermal mismatch by integrating the Q-carbon layer on the sapphire substrate using a highly non-equilibrium pulsed laser annealing technique before the deposition of CVD diamond.

The information about the maximum stress that can be accommodated without delamination of the film can serve as a platform to quantitatively assess the diamond adhesion to the substrate. The HFCVD diamond on Q-carbon/sapphire promotes the accommodation of thermal stress between the diamond film and the substrate and inhibits the delamination of the film from the substrate. Table 6.1 represents important substrate and film parameters (thermal expansion coefficient, Raman peak shift, measured stress, thermal stress) of different substrates which have been used for the growth of diamond thin film in different studies. These studies have shown that the diamond thin film can sustain a compressive stress of 2.835GPa without delamination [49]. Our measured compressive stress by Raman and XRD analyses are found to be considerably less than this value, which explains the large-area formation of diamond thin films on Q-carbon coated sapphire without delamination. The usefulness of diamond thin film on a substrate is considerably reduced if the diamond film has poor adhesion with the substrate. Our novel approach to fabricate large-area diamond films also improves the adhesion with the sapphire substrate. This has been achieved by the laser irradiation of the amorphous carbon layer to form a liquid state. The liquid carbon is quenched in a super undercooled state to form Q-carbon which is very adherent to the substrate. The diamond tetrahedra embedded in the Q-carbon are very adherent to the substrate due to the liquid phase mediated growth. Such adhesive diamond tetrahedra not only act as nucleation seeds for diamond growth but also in a way improve the overall adherence of the film with the substrate. To examine the extent of adhesion qualitatively, we have used the scotch tape

method. No peeling of the diamond film was observed in the SEM images even after using the scotch-tape for 3 times.

Among different applications of diamond on sapphire some notable examples are wear-resistant coatings, cutting tool applications, and windows in space applications. Additionally many microelectronic features require patterned polycrystalline diamond thin films [4]. Plasma etching, chemical etching, and/or selective growth are some of the patterning techniques used in the modern microelectronic technology. However, one of the major obstacles in obtaining patterned polycrystalline diamond is the highly resistive property/inertness of diamond to most of the chemical solutions. Therefore, diamond is very difficult to pattern by chemical etching and finding a suitable mask material, even if it could be chemically etched, to withstand the etchant is also very difficult. So far, reactive plasma etching of diamond with oxygen has resulted in limited success due to the poor etch selectivity between the diamond and the mask material [50]. Researchers also used alternative/non-conventional ions such as xenon ion and nitrogen dioxide to pattern diamond thin films [51]. However, these processes require complex equipment with low yield. Selective growth is another viable alternative process for patterning the diamond. Since diamond is grown over 800 C under extreme environment, we cannot use photoresist as a mask material. Therefore, researchers have used scratching or roughening techniques to grow diamond selectively. Such kind of selective regions on the substrates are obtained- (i) by using ethyl alcohol in an ultrasonic agitator along with standard photolithography and subsequent etching of the uncovered surface by Ar^+ ion beam up to 500-600 Å in depth [52], (ii) by using pulsed laser irradiation on silicon and copper substrate utilizing a shadow mask or by scanning a focused laser beam, which may not work for sapphire [53], or (iii) by using diamond paste to damage the substrate, photolithographically patterning, and finally plasma etching the wafer in the undesired

diamond growth areas to remove the damage or reducing the activation sites to restrain the growth of diamond [4]. However, such kind of techniques result in damaging or scratching all over the substrate surface which includes large density of sharp edges, strains, pitts, microscratches, mechanical defects etc. Therefore, these techniques for selective diamond growth restrict further microelectronic device processing due to the quality issue. The present technique of growing diamond could be an attractive alternative as Q-carbon can be selectively grown on single crystal sapphire substrate using the controlled laser irradiation process with a suitable optical setup. This could be a desirable approach to selectively pattern diamond on sapphire and various other substrates with minimum stress in the film and without creating or initiating any damage on the substrate.

6.5 Conclusions

We have demonstrated a simple and effective route for the direct deposition of large-area crystalline diamond film on c-sapphire using Q-carbon as an intermediate layer by HFCVD. The results from high resolution SEM, Raman spectroscopy, and XRD analysis show that the Q-carbon assists the diamond nucleation and a high-quality large-area continuous CVD diamond film on sapphire can be obtained. The Q-carbon helps to minimize the effect of thermal stress in the diamond film on single crystal sapphire and nullifies the stringent requirement of the conventional preexisting seed of nano/micro diamond on the substrate to deposit a continuous diamond thin film. The deposited CVD diamond film has a very small residual stress, compared to the other CVD diamond on sapphire, which has been determined by the Raman spectroscopy and XRD analysis. Less residual stress in the diamond film helps to deposit films with larger areas and higher thicknesses without any crack or delamination over the entire surface of the substrate. This process

of growing CVD diamond on sapphire can open a new frontier towards the fabrication of large-area crystalline diamond film at high-temperature on other transparent substrates as well.

Table 6. 1: Comparison among different parameters (thermal expansion coefficient α, Raman peak shift $\Delta\nu$, measured stress $\sigma_{measured}$, thermal stress σ_{th}) of the diamond thin film grown on different substrates and by different techniques [13,24,30,31].

Substrate	α (10^{-6} K^{-1})	$\Delta\nu$, cm^{-1}	$\sigma_{measured}$, GPa	σ_{th}, GPa
SiO_2	0.5	-1.0 – -3.7	+2.3	+2.1
Si	2.5	1.2 – 1.6	-1.0	-0.25
SiC	2.8	0.9 – 2.6	-1.6	-1.0
WC-Co (6%)	5.2	3.8 – 6.2	-3.8	-2.0
Mo	5.3	6.5–6.7	-4.1	-2.6
Sapphire (high-temperature CVD deposition)	7.5	0.7 & 16 (peak splitting)	Film delaminated	5.1
Sapphire (low temperature CVD deposition)	7.5	5.5	3.2 (from Raman)	3.7
Sapphire (Pt coated)	9.1	18	-	5.9
Q-carbon/Sapphire (Present study)	7.5	2.35	1.57 (from XRD) 1.14 (from Raman)	5.1

6.6 Figures

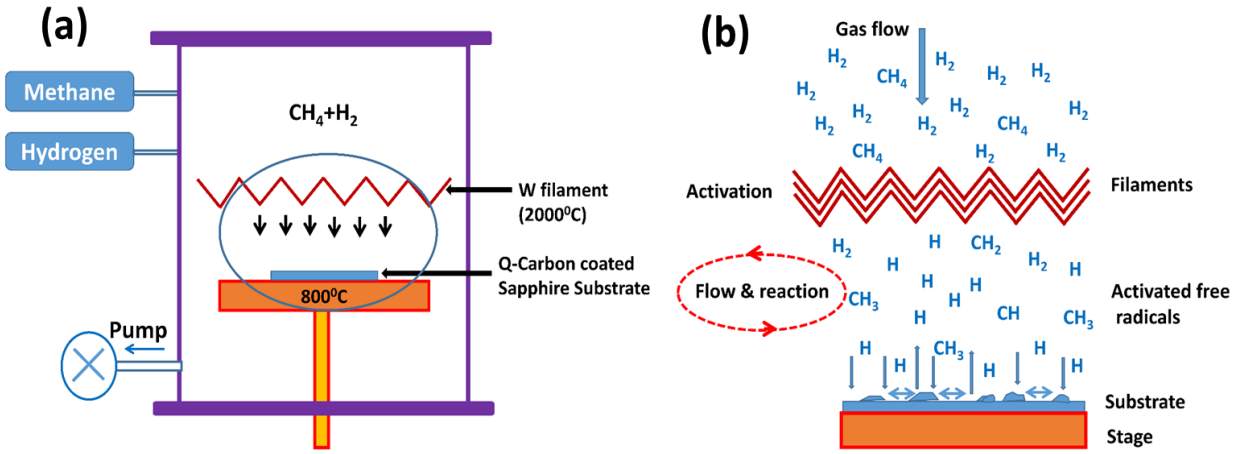

Figure 6. 1**:** (a) A schematic cross-section of the HFCVD system used for diamond growth, (b) schematic of the physical and chemical mechanisms occurring in the HFCVD reactor during diamond thin film deposition.

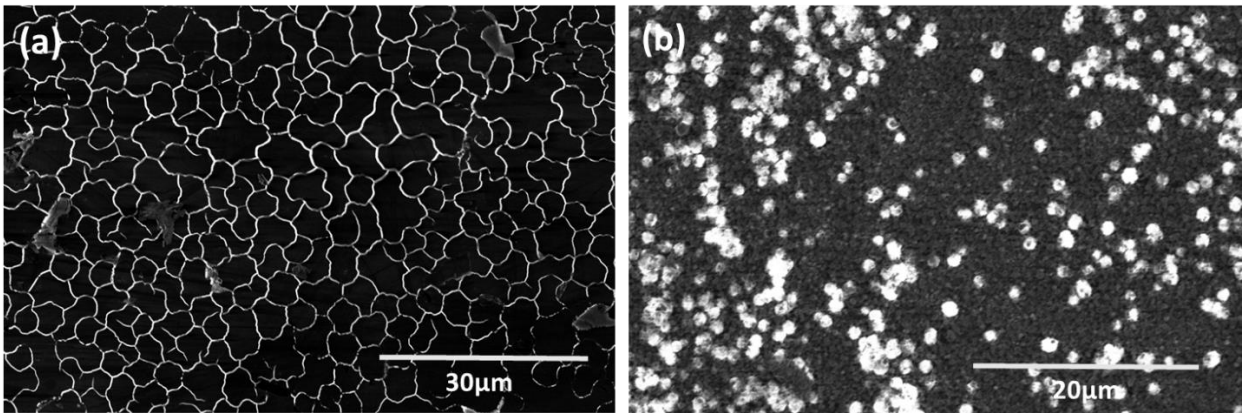

Figure 6. 2**:** SEM image (a) of Q-carbon on c-sapphire and (b) after 3 hours of HFCVD of diamond (~1.5 $\boldsymbol{\mu}$m thick) on Q-carbon coated C-sapphire.

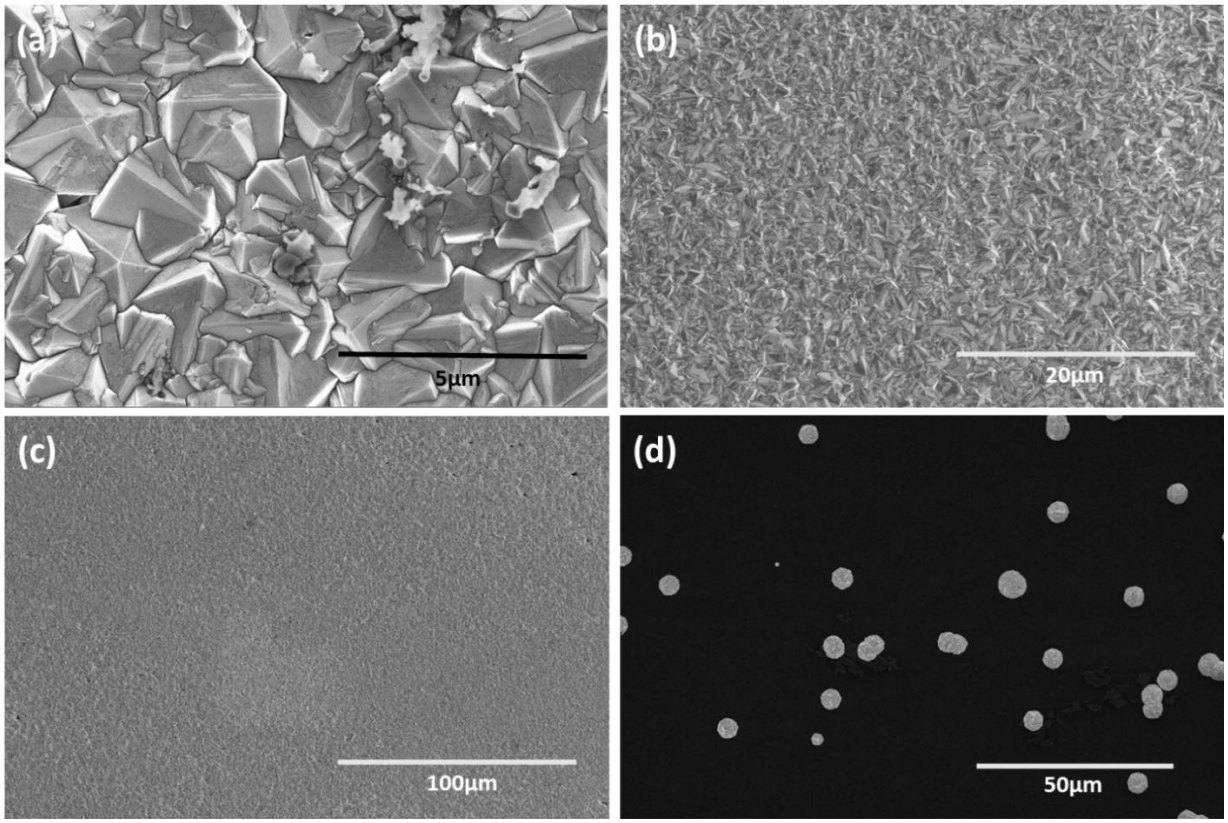

Figure 6. 3**:** (a)-(c) Large-area HFCVD diamond thin film (thickness ~3***µ***m) on Q-carbon coated c-sapphire at different magnifications, and (d) HFCVD diamond on untreated c-sapphire under the same deposition conditions without Q-carbon. All depositions were done for 6 hours.

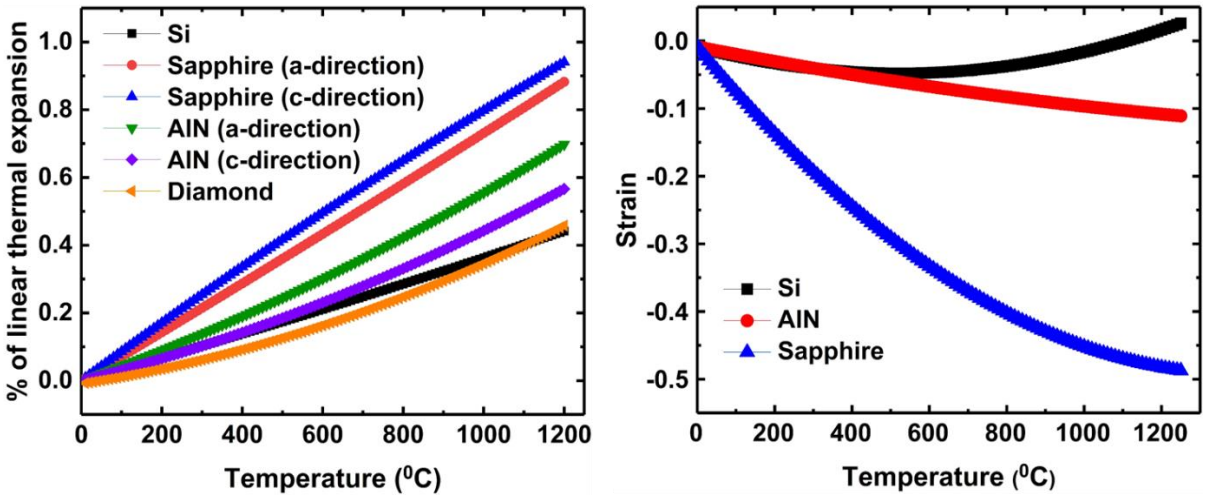

Figure 6. 4**:** (a) Plots of the cumulative thermal linear expansion coefficient for diamond, silicon, AlN and sapphire for comparison. The slope of each curve corresponds to the thermal expansion coefficient. (b) The thermal strain generated in the diamond thin film on different substrates (Si, AlN and Sapphire) at different temperature.

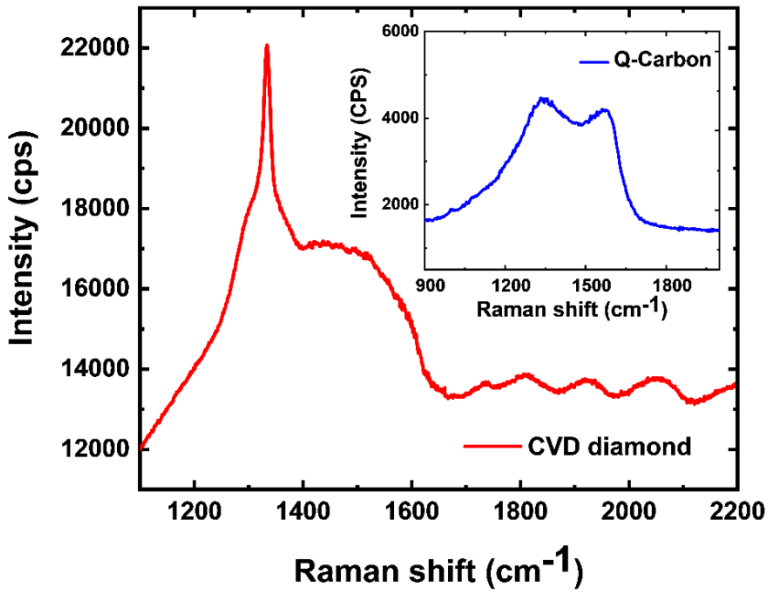

Figure 6. 5**:** Raman spectrum of the HFCVD diamond (thickness ~3μm) shows a sharp characteristic peak at 1333.85 cm^{-1}. The inset shows the Raman spectrum of Q-carbon.

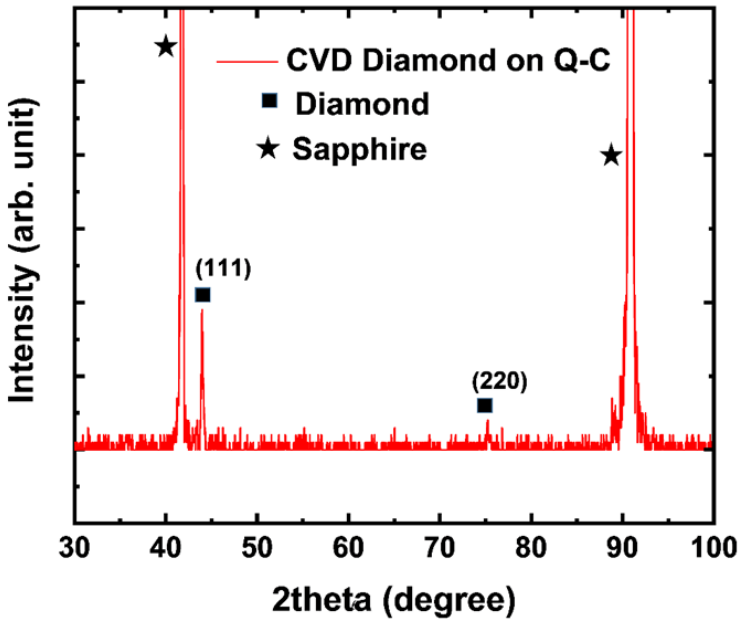

Figure 6. 6**:** XRD pattern of the HFCVD diamond thin film (thickness ~3μm) on Q-carbon coated c-sapphire.

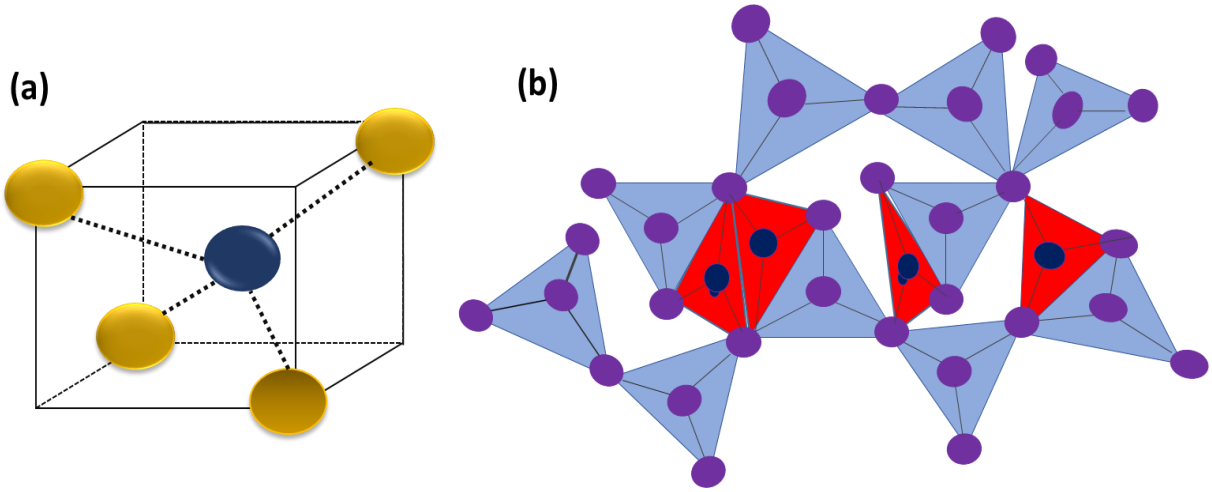

Figure 6. 7**:** (a) An individual diamond tetrahedron. (b) The formation of new diamond tetrahedra (red) bonded with the preexisting diamond tetrahedra present in the Q-carbon during the nucleation process.

References

[1] I. Friel, S.L. Geoghegan, D.J. Twitchen, G.A. Scarsbrook, Development of high quality single crystal diamond for novel laser applications, in: 2010: p. 783819. https://doi.org/10.1117/12.864981.

[2] B. Mesa, S. Magonov, Novel diamond/sapphire probes for scanning probe microscopy applications, J. Phys. Conf. Ser. 61 (2007) 770. https://doi.org/10.1088/1742-6596/61/1/154.

[3] R.L. Fork, W.W. Walker, R.L. Laycock, J.J.A. Green, S.T. Cole, Integrated diamond sapphire laser, Opt. Express. 11 (2003) 2532–2548. https://doi.org/10.1364/OE.11.002532.

[4] R. Ramesham, T. Roppel, Selective growth of polycrystalline diamond thin films on a variety of substrates using selective damaging by ultrasonic agitation, J. Mater. Res. 7 (1992) 1144–1151. https://doi.org/10.1557/JMR.1992.1144.

[5] M.D. Drory, J.W. Hutchinson, Diamond Coating of Titanium Alloys, Science. 263 (1994) 1753–1755. https://doi.org/10.1126/science.263.5154.1753.

[6] C.H. Prescott, W.B. Hincke, EQUILIBRIUM BETWEEN ALUMINUM CARBIDE AND NITROGEN AT HIGH TEMPERATURES, J. Am. Chem. Soc. 50 (1928) 3228–3237. https://doi.org/10.1021/ja01399a011.

[7] P.W. May, C.A. Rego, C.G. Trevor, E.C. Williamson, M.N.R. Ashfold, K.N. Rosser, N.M. Everitt, Deposition of diamond films on sapphire: studies of interfacial properties and patterning techniques, Diam. Relat. Mater. 3 (1994) 1375–1380. https://doi.org/10.1016/0925-9635(94)90153-8.

[8] A.V. Sumant, V.P. Godbole, S.T. Kshirsagar, Studies on hot filament chemical vapor deposition of diamond onto aluminum oxide, Mater. Sci. Eng. B. 39 (1996) L5–L9. https://doi.org/10.1016/0921-5107(96)01579-6.

[9] Y. Mo, Y. Xia, W. Wu, A nucleation mechanism for diamond film deposited on alumina substrates by microwave plasma CVD1Supported by the National Natural Science Foundation of China.1, J. Cryst. Growth. 191 (1998) 459–465. https://doi.org/10.1016/S0022-0248(98)00141-9.

[10] X. Qiao, O. Fukunaga, N. Shinoda, K. Yui, Enhancement of diamond nucleation on alumina substrates by the activated species transport method, Diam. Relat. Mater. 5 (1996) 1096–1102. https://doi.org/10.1016/0925-9635(96)00526-2.

[11] V.V.S.S. Srikanth, Review of advances in diamond thin film synthesis, Proc. Inst. Mech. Eng. Part C J. Mech. Eng. Sci. 226 (2012) 303–318. https://doi.org/10.1177/0954406211422788.

[12] K.G. Saw, I. Andrienko, A. Cimmino, P. Spizzirri, S. Prawer, J. du Plessis, Growth of diamond on α-(0001) sapphire substrates, Diam. Relat. Mater. 12 (2003) 1663–1669. https://doi.org/10.1016/S0925-9635(03)00189-4.

[13] O. Ternyak, R. Akhvlediani, A. Hoffman, Study on diamond films with ultra high nucleation density deposited onto alumina, sapphire and quartz, Diam. Relat. Mater. 14 (2005) 323–327. https://doi.org/10.1016/j.diamond.2004.10.033.

[14] K.G. Saw, J. du Plessis, Diamond growth on faceted sapphire and the charged cluster model, J. Cryst. Growth. 279 (2005) 349–356. https://doi.org/10.1016/j.jcrysgro.2005.02.072.

[15] Y.-C. Chen, L. Chang, Chemical vapor deposition of diamond on an adamantane-coated sapphire substrate, RSC Adv. 4 (2014) 18945–18950. https://doi.org/10.1039/C4RA01042F.

[16] J. Narayan, A. Bhaumik, S. Gupta, A. Haque, R. Sachan, Progress in Q-carbon and related materials with extraordinary properties, Mater. Res. Lett. 6 (2018) 353–364. https://doi.org/10.1080/21663831.2018.1458753.

[17] A. Haque, J. Narayan, Electron field emission from Q-carbon, Diam. Relat. Mater. 86 (2018) 71–78. https://doi.org/10.1016/j.diamond.2018.04.008.

[18] J. Narayan, A. Bhaumik, Novel phase of carbon, ferromagnetism, and conversion into diamond, J. Appl. Phys. 118 (2015) 215303. https://doi.org/10.1063/1.4936595.

[19] D. Das, R.N. Singh, A review of nucleation, growth and low temperature synthesis of diamond thin films, Int. Mater. Rev. 52 (2007) 29–64. https://doi.org/10.1179/174328007X160245.

[20] H. Sumiya, N. Toda, S. Satoh, Growth rate of high-quality large diamond crystals, J. Cryst. Growth. 237–239 (2002) 1281–1285. https://doi.org/10.1016/S0022-0248(01)02145-5.

[21] W.R.L. Lambrecht, C.H. Lee, B. Segall, J.C. Angus, Z. Li, M. Sunkara, Diamond nucleation by hydrogenation of the edges of graphitic precursors, Nature. 364 (1993) 607–610. https://doi.org/10.1038/364607a0.

[22] W.M. Yim, R.J. Paff, Thermal expansion of AlN, sapphire, and silicon, J. Appl. Phys. 45 (1974) 1456–1457. https://doi.org/10.1063/1.1663432.

[23] S.B. Qadri, C. Kim, E.F. Skelton, T. Hahn, J.E. Butler, Thermal expansion of chemical vapor deposition grown diamond films, Thin Solid Films. 236 (1993) 103–105. https://doi.org/10.1016/0040-6090(93)90651-5.

[24] R.K. Singh, D.R. Gilbert, J. Laveigne, Growth of adherent diamond films on optically transparent sapphire substrates, Appl. Phys. Lett. 69 (1996) 2181–2183. https://doi.org/10.1063/1.117158.

[25] J. Filik, J.N. Harvey, N.L. Allan, P.W. May, J.E.P. Dahl, S. Liu, R.M.K. Carlson, Raman spectroscopy of nanocrystalline diamond: An ab initio approach, Phys. Rev. B. 74 (2006) 035423. https://doi.org/10.1103/PhysRevB.74.035423.

[26] S.A. Solin, A.K. Ramdas, Raman Spectrum of Diamond, Phys. Rev. B. 1 (1970) 1687–1698. https://doi.org/10.1103/PhysRevB.1.1687.

[27] D.S. Knight, W.B. White, Characterization of diamond films by Raman spectroscopy, J. Mater. Res. 4 (1989) 385–393. https://doi.org/10.1557/JMR.1989.0385.

[28] M. Yoshikawa, G. Katagiri, H. Ishida, A. Ishitani, M. Ono, K. Matsumura, Characterization of crystalline quality of diamond films by Raman spectroscopy, Appl. Phys. Lett. 55 (1989) 2608–2610. https://doi.org/10.1063/1.101951.

[29] J.W. Ager, M.D. Drory, Quantitative measurement of residual biaxial stress by Raman spectroscopy in diamond grown on a Ti alloy by chemical vapor deposition, Phys. Rev. B. 48 (1993) 2601–2607. https://doi.org/10.1103/PhysRevB.48.2601.

[30] V.G. Ralchenko, E.D. Obraztsova, K.G. Korotushenko, A.A. Smolin, S.M. Pimenov, V.G. Pereverzev, Stress in Thin Diamond Films on Various Materials Measured by Microraman Spectroscopy, MRS Online Proc. Libr. Arch. 383 (1995). https://doi.org/10.1557/PROC-383-153.

[31] T. Tachibana, Y. Yokota, K. Kobashi, M. Yoshimoto, Heteroepitaxial growth of {111}-oriented diamond films on platinum{111}/sapphire{0001} substrates, J. Cryst. Growth. 205 (1999) 163–168. https://doi.org/10.1016/S0022-0248(99)00223-7.

[32] L. Bergman, R.J. Nemanich, Raman and photoluminescence analysis of stress state and impurity distribution in diamond thin films, J. Appl. Phys. 78 (1995) 6709–6719. https://doi.org/10.1063/1.360495.

[33] R.J. Nemanich, J.T. Glass, G. Lucovsky, R.E. Shroder, Raman scattering characterization of carbon bonding in diamond and diamondlike thin films, J. Vac. Sci. Technol. A. 6 (1988) 1783–1787. https://doi.org/10.1116/1.575297.

[34] A. Samoto, S. Ito, A. Hotta, T. Hasebe, Y. Ando, A. Sawabe, T. Suzuki, Investigation of heterostructure between diamond and iridium on sapphire, Diam. Relat. Mater. 17 (2008) 1039–1044. https://doi.org/10.1016/j.diamond.2008.02.007.

[35] M. Kamo, Y. Sato, S. Matsumoto, N. Setaka, Diamond synthesis from gas phase in microwave plasma, J. Cryst. Growth. 62 (1983) 642–644. https://doi.org/10.1016/0022-0248(83)90411-6.

[36] J.P. Hirth, J. Lothe, Theory of dislocations, McGraw-Hill, New York; London, 1968.

[37] J. Narayan, Recent progress in thin film epitaxy across the misfit scale (2011 Acta Gold Medal Paper), Acta Mater. 61 (2013) 2703–2724. https://doi.org/10.1016/j.actamat.2012.09.070.

[38] T. Nagano, N. Shibata, Diamond Synthesis by Microwave-Plasma Chemical Vapor Deposition Using CH3Cl and CH2Cl2 as Carbon Source, Jpn. J. Appl. Phys. 32 (1993) 5067. https://doi.org/10.1143/JJAP.32.5067.

[39] J. Jiang, Y. Tzeng, Mechanisms of suppressing secondary nucleation for low-power and low-temperature microwave plasma self-bias-enhanced growth of diamond films in argon diluted methane, AIP Adv. 1 (2011) 042117. https://doi.org/10.1063/1.3656241.

[40] Y. Mitsuda, Y. Kojima, T. Yoshida, K. Akashi, The growth of diamond in microwave plasma under low pressure, J. Mater. Sci. 22 (1987) 1557–1562. https://doi.org/10.1007/BF01132374.

[41] A. Sawabe, T. Inuzuka, Growth of diamond thin films by electron-assisted chemical vapour deposition and their characterization, Thin Solid Films. 137 (1986) 89–99. https://doi.org/10.1016/0040-6090(86)90197-5.

[42] N. Fujimori, T. Imai, A. Doi, Characterization of conducting diamond films, Vacuum. 36 (1986) 99–102. https://doi.org/10.1016/0042-207X(86)90279-4.

[43] C. -P Chang, D.L. Flamm, D.E. Ibbotson, J.A. Mucha, Diamond crystal growth by plasma chemical vapor deposition, J. Appl. Phys. 63 (1988) 1744–1748. https://doi.org/10.1063/1.339912.

[44] A.A. Morrish, P.E. Pehrsson, Effects of surface pretreatments on nucleation and growth of diamond films on a variety of substrates, Appl. Phys. Lett. 59 (1991) 417–419. https://doi.org/10.1063/1.105448.

[45] J. Singh, M. Vellaikal, Nucleation of diamond during hot filament chemical vapor deposition, J. Appl. Phys. 73 (1993) 2831–2834. https://doi.org/10.1063/1.353034.

[46] K.V. Ravi, C.A. Koch, H.S. Hu, A. Joshi, The nucleation and morphology of diamond crystals and films synthesized by the combustion flame technique, J. Mater. Res. 5 (1990) 2356–2366. https://doi.org/10.1557/JMR.1990.2356.

[47] K.V. Ravi, C.A. Koch, Nucleation enhancement of diamond synthesized by combustion flame techniques, Appl. Phys. Lett. 57 (1990) 348–350. https://doi.org/10.1063/1.103688.

[48] S. Yugo, T. Kanai, T. Kimura, T. Muto, Generation of diamond nuclei by electric field in plasma chemical vapor deposition, Appl. Phys. Lett. 58 (1991) 1036–1038. https://doi.org/10.1063/1.104415.

[49] J.J. Gracio, Q.H. Fan, J.C. Madaleno, Diamond growth by chemical vapour deposition, J. Phys. Appl. Phys. 43 (2010) 374017. https://doi.org/10.1088/0022-3727/43/37/374017.

[50] T.J. Whetten, A.A. Armstead, T.A. Grzybowski, A.L. Ruoff, Etching of diamond with argon and oxygen ion beams, J. Vac. Sci. Technol. A. 2 (1984) 477–480. https://doi.org/10.1116/1.572598.

[51] N.N. Efremow, M.W. Geis, D.C. Flanders, G.A. Lincoln, N.P. Economou, Ion-beam-assisted etching of diamond, J. Vac. Sci. Technol. B Microelectron. Process. Phenom. 3 (1985) 416–418. https://doi.org/10.1116/1.583276.

[52] K. Hirabayashi, Y. Taniguchi, O. Takamatsu, T. Ikeda, K. Ikoma, N. Iwasaki-Kurihara, Selective deposition of diamond crystals by chemical vapor deposition using a tungsten-filament method, Appl. Phys. Lett. 53 (1988) 1815–1817. https://doi.org/10.1063/1.99789.

[53] J. Narayan, X. Chen, Laser patterning of diamond films, J. Appl. Phys. 71 (1992) 3795–3801. https://doi.org/10.1063/1.350892.

7. Characteristics of diamond deposition on Al_2O_3, diamond-like carbon and Q-carbon

Ariful Haque[1], Siddharth Gupta[1] and Jagdish Narayan[1]

[1]Department of Materials Science and Engineering, North Carolina State University, Raleigh, North Carolina 27695.7916, USA

7.1 Abstract

We have conducted a comperative study on the deposition of diamond thin film on uncoated Al_2O_3, diamond-like carbon (DLC, grown by pulsed laser deposition) film on Al_2O_3, and Q-carbon (fabricated by nanosecond pulsed laser annealing) on Al_2O_3 substrates by hot filament chemical vapor (HFCVD) deposition. Scanning electron microscopy shows that the continuous large-area diamond thin film can be grown on the Q-carbon/Al2O3 substrate, whereas the deposition of diamond on DLC/Al_2O_3 or uncoated Al_2O_3 substrates gives cluster-like/patches of discontinuous diamond thin film formation. Raman spectroscopy of the diamond on Q-carbon/Al_2O_3 shows a considerably small residual stress (1.7 GPa) compared to the diamond on DLC/Al_2O_3 (3.1 GPa) or diamond on uncoated Al_2O_3 (3.9 GPa) substrate. The calculated non-diamond content in the diamond crystals on Q-carbon coated Al_2O_3 is found to be only 0.12%, around 2.5, and 3.5 times less than that of diamond on DLC coated Al_2O_3 and uncoated Al_2O_3, respectively. In consistent with the Raman analysis the X-ray diffraction analysis shows the crystalline growth of HFCVD diamond on Q-carbon/Al_2O_3 with relatively small in-plane stress compared to the diamond film on the rest two systems. We envisase that high-density of diamond tetrahedron in the Q-carbon structure provides a good platform for diamond growth with a very high nucleation density of around 10^9 cm^{-2} and can act as a seed layer for diamond growth without crack or delamination over the surface of the substrate. The optically transparent high-quality diamond film on Q-carbon

coated Al_2O_3 showed better adhesion property compared to that on DLC coated Al_2O_3 and uncoated Al_2O_3 as measured by a simple tape test. These results open a path towards the fabrication of large-area high-quality diamond on an optically transparent substrate for commercial applications.

7.2 Introduction

In view of the remarkable electrical, mechanical and thermal properties, such as high resistivity and thermal conductivity, perfect crystalline structure with high mechanical strength and optical transparency over a broad range of wavelengths, diamond thin films have numerous applications in a variety of current and future systems including abrasives, surgical cutting tools, MEMS, high-power high-temperature electronics, and wear-resistant coatings [1–4]. In particular, since the wide band gap diamond does not absorb infrared (IR) radiation and it possesses very high thermal conductivity, researchers consider this material as an ideal semiconductor for applications in advanced electronics such as heat sinks for cooling electronic components, IR radiation sensors, novel laser technologies including mid-IR semiconductor disk lasers and high-efficiency diamond Raman lasers, and a window in space applications [5–8]. All of these practical applications will be realized only when the continuous large-area diamond thin film can be grown on a suitable wide bandgap substrate with desirable properties like single-crystal Al_2O_3 for optoelectronic applications. The single-crystal Al_2O_3 possesses immense technological potential as a substrate material for different applications due to its high hardness, high melting point, chemical inertness, oxidation resistance, and good optical transparency. Its hardness promotes facile sample preparation and generally, it is free of surface defects and bubbles. Although Si and SiC are the most commonly used substrates for diamond growth, but due to their low optical bandgap researchers have been trying to develop a reliable method to fabricate large-area diamond on

single-crystal Al_2O_3 to utilize its unique properties as a substrate [9]. Thereby many state-of-the-art applications such as optical protective coatings, fabrication of thin membranes, cutting tools and antifriction coatings that undergo high mechanical loads and abrasion would become reality. Deposition of a diamond thin films on Al_2O_3 is largely hampered by the huge thermal mismatch between diamond and Al_2O_3. It has also been found that no interfacial bonding layer between the diamond thin film and the substrate, is formed during diamond growth on a single crystal Al_2O_3 surface, which leads to poor adhesion [10]. The nucleation density on the mirror polished Al_2O_3 substrate is also very poor. The generation of large residual compressive stress in the diamond film due to huge thermal mismatch between the diamond and Al_2O_3 also leads to the delamination of the film. In fact, significant amount of delamination was observed when deposited area exceeded $\sim$100 μm^2 [11]. Several solutions were proposed to address the issues related to low nucleation density, poor adhesion, film cracking, and considerably large residual compressive stress of diamond on Al_2O_3 but none of them was successful. Use of abrasive powders is an established technique for substrate pretreatment and diamond powder is among the most effective ones to improve the nucleation and growth rate of synthetic diamond [12]. However scratching and/or polishing with fine diamond particle increase the roughness and sometimes produce damage and contamination to the smooth substrates; thereby the substrates become incompatible with many applications requiring extremely smooth and clean surfaces, such as diamond films for electronic devices, optical window materials, and smooth wear-resistant coatings. Diamond nucleation on unscratched substrate surface has been recently achieved through the deposition of fullerene clusters and DLC films, which have been considered to play the role of nucleating agents [13–15]. It has been reported that diamond nucleation on graphite requires a long induction time and yields a poor nucleation density [16]. Researchers also tried highly sp^3 bonded DLC as a buffer layer on

Si and expected a dramatic enhancement in the nucleation density [17–19]. However, the results are not encouraging as the nucleation density never exceeded 10^9 cm^{-2} and the film-substrate adhesion was poor due to the absence of a layer-by-layer carbon growth characteristics [15]. Nevertheless, single-crystal Al_2O_3 has not been studied as a substrate in all of those interlayer dependent diamond fabrication processes. The formation of a carbide layer on silicon and molybdenum substrates prior to the nucleation of diamond crystallites has been identified in recent CVD experiments [20–22]. Such a layer usually improves the adherence of the diamond film to the substrate, which is necessary for different mechanical applications. But the absence of any carbide layer on Al_2O_3 inhibits the utilization of this substrate for the growth of large-area diamond thin film. The liquid phase mediated Q-carbon formed on the Al_2O_3 can provide the necessary nucleation sites and adherence to the diamond film for different applications.

For the practical utilization of diamond on Al_2O_3 it is necessary that the approach be scaled up to deposit diamond films over large area substrates and control over the structure and hence the desirable properties of the films be achieved. We have investigated the issues related to the nucleation of diamond and the morphology of the crystals and films by controlling the nucleation process at different surface conditions. In this study, we present the results from a set of experiments with a goal to enhance the nucleation density of diamond by HFCVD process on Al_2O_3 substrate and we have shown that the nucleation density and the morphology of diamond crystals are markedly influenced by the surface conditions of the substrate. We have conducted a comprehensive experimental study to grow diamond on Al_2O_3 using Q-carbon on Al_2O_3, DLC on Al_2O_3, and uncoated Al_2O_3 substrates and obtained a much improved nucleation and growth of high-quality diamond thin film on Q-carbon/Al_2O_3 compared to others. The obtained large area diamond thin film on Q-carbon/Al_2O_3 substrate has relatively less inplane stress due to the

presence of high-density diamond tetrahedra in the Q-carbon layer which also facilities to obtain high nucleation density.

7.3 Experimental section

DLC, Q-carbon and HFCVD diamond deposition. To fabricate the Q-carbon on Al_2O_3, at first the DLC films were deposited by pulsed by pulsed laser deposition (PLD) of a highly compact and pure (99.99%) graphite target using KrF excimer laser ($\boldsymbol{\lambda}$ = 0.248 pm, $\boldsymbol{\tau}$ = 25 ns, E = 2.0 J cm^{-2}). The deposition was carried out in a background pressure of 1X 10^{-6} Torr at room temperature with a substrate-target distance of ~ 4.0 cm. The DLC film was irradiated by ArF laser (wavelength = 193 nm, pulse duration = 20 ns) pulses with an energy density in-between 0.6 to 0.7 Jcm^{-2} for conversion into Q-carbon composite structure. During the pulsed laser annealing (PLA) process, the as-deposited films were melted in a super-undercooled state and subsequently quenched within 200-250 nanoseconds.

An optimum set of process parameters were used in the HFCVD of diamond fabrication on (i) Al_2O_3, (ii) DLC coated Al_2O_3, and (iii) Q-carbon coated Al_2O_3. A standard HFCVD system was used to synthesize the diamond on different substrates. The system uses a stainless steel cylindrical water-cooled chamber, a tungsten filament holder (4 wires) assembly at the middle, a heated substrate holder, a sealable gas inlet and pumping ports. The chamber also contains a thermocouple temperature sensor, a sealable gas inlet and pumping port, and a necessary flow rate controller and electrical systems. The specimen substrates are placed on the Molybdenum heater block (700°C) below the filament. The chamber is initially evacuated with a mechanical pump to 10^{-3} Torr. When the desired base pressure is reached, the pumping port valve is closed and methane and hydrogen gas at a ratio of 1:50 is then allowed to flow over the hot filaments (2000°C) into the chamber to the desired pressure (low working pressures ~20 Torr). The filament temperature was measured

with a two-color pyrometer while the substrate temperature was measured by a K-type thermocouple inserted on the substrate holder, placed on the backside of the substrate. The set of multiple filaments and the rotation of the substrate stage during the deposition facilitates the formation of a uniform diamond thin film over the large substrate area. Gas composition (%vol. CH_4 and H_2), total gas pressure (P), total mass flow, and substrate and filament temperatures were monitored throughout the deposition time. Cooling from growth down to room temperature was conducted at a constant cooling rate of 10 °C/min for all samples to minimize any effect due to thermal shock.

Raman spectroscopy. For the study of CVD diamond thin films the Raman spectroscopy is a technique as powerful as XRD since it provides a fingerprint of the presence of diamond and non-diamond phases, and the stress present in the film. We have used a WITec confocal Raman spectrometer (with triple monochromator, gratings 2400 lines/mm). A continuous laser beam of 532 nm wavelength from a diode-pumped solid-state laser was focused at a spot of ~2 μm diameter. The spectrum resolution was ~0.5 cm^{-1}. Optimum laser power (~40 mW) was used to illuminate the sample to avoid heating during the spectrum acquisition. Raman spectra at different points of the samples were acquired with an exposure time of 5 s, the spectrum being the sum of 10 acquisitions.

XRD. X-ray diffraction (XRD) measurements (θ - 2θ scan) were conducted on the diamond films (Bruker D8 Discover) using Cu kα radiation source from a sealed tube operating at 40 kV and 25 mA and state of the art LENXEYE XE detector. This detector filters fluorescence and K-β radiation to overcome the intensity losses and absorption edges associated with secondary monochromators and metal filters. The data were collected in the Bragg-Brentano reflection geometry in the 2θ range of 30-100 at 0.01 step size and a dwell time of 0.5 seconds per scan point.

SEM. Scanning electron microscopy (SEM) was undertaken to characterize the morphological surface features of the nucleated diamond films. The high-resolution SEM imaging with the sub-nanometer resolution was carried out on the PLA grown Q-carbon and HFCVD grown diamond films using the FEI Verios 460L SEM.

TEM. TEM cross-sectional samples are prepared by first mechanical polishing and then Ar ion milling to perforation around which large electron thin electron transparent specimen is generated. TEM images and SAED patterns are captured by high-resolution transmission electron microscopy (S/TEM, FEI, Talos-F200) operating at 200 keV, equipped with a proprietary "XFEG" high-brightness Schottky emission field-emission- gun electron source, which provides beams ~5× brighter than previous Schottky-FEG technologies.

7.4 Computational Methods

Laser-solid melt interaction simulations. The phase transformation of amorphous carbon into densely-packed Q-carbon on melt regrowth is analyzed by simulating the nanosecond laser-solid melt interactions. The time distribution for laser beam utilized in Gaussian. Near the sub-surface, the elemental regions were used as nodes of 1 nm size, which gradually increase in size on going towards the substrate. The thermal losses are incorporated into the code in the form of conduction and radiation, while adiabatic conditions were used as boundary approximations. The sp3 content in amorphous carbon was utilized as 0.03 W/cm K, while the thermal conductivity of liquid carbon is 2.9 W/cm K [21]. Latent heat is released on melting carbon, which drives the melt front forward. As the laser pulse is temporally confined (20 ns), the motion of melt front after ending of the laser pulse primarily involves phase change at solid/liquid phase boundary.

Ab-initio MD simulations. The phase transformations of as-deposited amorphous carbon into tetrahedrally bonded Q-carbon is studied by simulating the structure of liquid carbon and

quenching it under high-pressure conditions. *Ab-initio* molecular dynamics simulations are performed on a repeated 6x6x6 carbon atom cell, which has periodic boundaries in all three directions, utilizing the LAMMPS code. As these simulations are performed at high-temperature high-pressure (HPHT) conditions, angular dependent potential (ADP) designed explicitly for such simulations is utilized here to study the phase transformation from melt quenching.[28-29] The as-acquired solid carbon structure is stabilized by performing energy minimization, relaxing the 216 atoms in the cell. The solid carbon was heated to 7000 K to form the melt state. Post-equilibration, the melt was quenched for 20 picoseconds using a timestep of 2 femtoseconds using the Nose-Hoover thermostat. The quenching was performed under constant pressure (5-70 GPa), in order to mimic the undercooling conditions using the NPT (constant number of atoms, pressure, and temperature) ensemble. The quenching was performed until the temperature reaches 2000 K. At this temperature, the pressure inside the system was released to stabilize the system at room pressure. Subsequently, the system was quenched to 300 K. The structure for quenched materials was analyzed using the radial distribution functions (RDF) generated by following the Baxter-Dixon-Hutchinson factorization method [24].

7.5 Results and Discussion

Results on nucleation and growth characteristics of diamond films were obtained by making a microscopic comparison on diamond samples grown on different substrates treated differently, i.e., Q-carbon coated Al_2O_3, DLC coated Al_2O_3, and uncoated Al_2O_3. Fig. 7.1(a) shows the growth of diamond (4 hours) on a sample coated with DLC and Q-carbon. A shadow mask was used during the PLA process to convert part of the DLC into Q-carbon. The image clearly demonstrates better diamond growth on the Q-carbon region (bottom) compared to the DLC region. Fig. 7.1(b) shows the magnified image to illustrate better diamond coverage on the Q-carbon coated side compared

to the rest of the DLC area. The difference in the nucleation and growth of diamond on both sides is distinctive with a sharp boundary. The inset of Fig. 7.1(b) shows the microstructure of individual diamond crystal (~5μm) grown on DLC. Fig. 7.1(c) shows the scattered diamond growth on the DLC side from the same sample. The growth of diamond (6 hours) on uncoated (left) and Q-carbon coated (right) Al_2O_3 is shown in Fig. 7.1(d) where the sharp boundary implies the magnificent growth of diamond on the Q-carbon region and a drastic decrease in diamond nucleation without Q-carbon. Sparse growth of diamond on the uncoated Al_2O_3 is shown in Fig. 7.1(e). The formation of dispersed diamond clusters on the Al_2O_3 obtained from this figure implies the sparse nucleation density of diamond on untreated Al_2O_3. From Fig. 7.1(c) and (e) it can also be noted that the DLC coated substrate shows more coverage with the dispersed clusters of diamond films compared to the diamond on bare Al_2O_3. Fig. 7.1(f) shows the high-resolution image of diamond growth on Q-carbon. The faceted triangular morphology of diamond in this region refers to the preferential textured growth along <111> direction. Fig. 7.1(g) illustrates the wafer-scale coverage of HFCVD (6 hours) diamond on Q-carbon coated c-Al_2O_3. The longer growth time of diamond deposition on DLC coated Al_2O_3 leads to more areal coverage. However, the formation of crack and delamination takes place due to the large thermal mismatch. Fig. 7.1(h) illustrates the formation of crack and delamination of the diamond crystals on DLC coated Al_2O_3 (6 hours). It is interesting to note that average size of diamond on Q-carbon and DLC is approximately the same (~5$\boldsymbol{\mu}$m), which is little large than one on uncoated Al_2O_3 substrate. This shows that tetrahedra nuclei in Q-carbon in Q-carbon and DLC are ready to grow, although the number density of these nuclei in Q-carbon is much higher than in DLC. The smaller diamond microstructure size on uncoated Al_2O_3 signifies the delay related nucleation (DLC formation) and subsequent growth. From the nucleation and growth perspective, the Q-carbon coated Al_2O_3 is entirely covered with the

diamond thin film due to the high nucleation density. Therefore, the qualitative comparison of the diamond crystal growth shown in these images suggests that the nucleation density of diamond significantly increases from bare Al_2O_3 to DLC-Al_2O_3 to Q-carbon-Al_2O_3. The dramatic change in the density and the morphology of the diamond resulting from the presence of a DLC layer indicates that the growth conditions are also affected largely by the increase in nucleation density. This analysis suggests that the morphology of diamond crystals and films on Al_2O_3 is a strong function of the nucleation conditions/substrate conditions under the optimum growth conditions. In the case of the Q-carbon coated Al_2O_3 substrate, the nucleation density is further increased after the PLA of DLC on Al_2O_3, which promotes the growth of a large area continuous diamond film on Al_2O_3.

7.5.1 Thermal stress in the diamond film plane

Fig. 7.2 (a) represents a comparison of the percent of the linear thermal expansion coefficient of Al_2O_3 to other widely used substrate materials for diamond deposition at different temperatures (0-1200°C) [25,26]. This comparison helps us to better understand the effect of thermal stress on diamond film during high-temperature deposition, and the magnitude and the nature of the thermal stress in the diamond film as well. The observed thermal misfit is the largest for the diamond-Al_2O_3 system at ~700° C, referring to the difficulty of diamond deposition on Al_2O_3. From the plot, it can easily be realized that the diamond film grows under compressive stress and the substrate (α_s) under tensile stress as the coefficient of thermal expansion of Al_2O_3 is greater than that of diamond (α_d). The following expression correlates the thermal misfit strain (ε_T) with the stresses generated in the film and substrate during cooling down (ΔT)

$$\varepsilon_T = (\alpha_d - \alpha_s)\,\Delta T \qquad (1)$$

For a better understanding of the thermal strain, we have used equation (1) to plot and compare the thermal strain in the diamond films on different substrates at different temperatures (Fig. 7.2(b)). From this plot a compressive strain of ~0.4 % is generated in diamond on Al_2O_3 at 800° C deposition temperature, referring to the strain-induced delamination of the film. This amount of thermal mismatch induced compressive strain can generate ~ 5 GPa stress in the diamond. Singh *et al*. developed a low temperature(500-550^0 C) electron–cyclotron–resonance CVD process to grow diamond films on c-Al_2O_3 to overcome the stress-related problems [27]. Even this low deposition temperature generates 3.5 GPa stress, which is enough to cause delamination in the weakly bonded diamond film on noncarbide forming Al_2O_3. The thermal misfit strain is negative in the diamond-Al_2O_3 system, referring to the compressive strain. The amount of thermal misfit in this system is comparable to the intrinsic part of the misfit in the film-substrate system. The effect of a huge thermal misfit is compensated by the Q-carbon layer, formed by ultrafast and nonequilibrium nanosecond laser irradiation process, on the Al_2O_3. The information about the maximum stress that can be accommodated without delamination of the film can serve as a platform to quantitatively assess the diamond adhesion to the substrate. The HFCVD diamond on Q-carbon/Al_2O_3 promotes the accommodation of thermal stress between the diamond film and the substrate and inhibits the delamination of the film from the substrate. Table 7.1 represents different important substrates and film parameters (thermal expansion coefficient, Raman peak shift, measured stress, thermal stress) of different substrates, which have been used for the growth of diamond thin film in different studies.

7.5.2 X-Ray Diffraction

Fig. 7.3 illustrates the XRD patterns of the HFCVD diamond thin films and microstructures on Q-carbon coated Al_2O_3, DLC coated Al_2O_3 and uncoated Al_2O_3 substrates. The diffraction

peaks at ~43.90º (2θ) corresponds to diamond (111). The relative intensities of this peak for different samples are different due to the difference in the areal coverage in the thin film, which is consistent with the SEM observations. The sharper (111) diamond peak (less FWHM) from the film grown on Q-carbon coated Al_2O_3 refers better crystallinity compared to the diamond grown on DLC coated Al_2O_3 or uncoated Al_2O_3. The absence of {220} reflection in this film implies high quality and textured nature of the film. The SEM image in Fig. 7.1(e) also demonstrates the prevalence of triangular facets on the diamond surface which supports the textured nature of the diamond. The {220} reflection is visible at ~76° (2θ) in the case of the diamond grown on DLC coated Al_2O_3. In the case of HFCVD diamond grown on uncoated Al_2O_3, any diamond peak is hardly visible owing to the low areal coverage of diamond. Since the X-ray can penetrate the diamond film of thickness more than 100 μm [28], all the XRD patterns are also showing the (0001) peak of the Al_2O_3 substrate. No other peak present in all three XRD patterns implies the absence of any impurity phases in the HFCVD diamond films. The position of the diamond (111) peaks (2θ) were observed to be at 43.94º, 43.966º, and 43.98º for the diamond on Q-carbon coated Al_2O_3, DLC coated Al_2O_3, and untreated Al_2O_3, respectively. The shift in the diamond peak from its original position is due to the stress generated in the films and thereby change in d_{111}. The in-plane strain in the HFCVD diamond thin films can be obtained by the generalized relationship between the stress and strain in a cubic (isotropic) crystal. This stress-strain relationship can be expressed by

$$\sigma_{zz}=\boldsymbol{\lambda}\varepsilon_{xx}+\boldsymbol{\lambda}\varepsilon_{yy}+(\boldsymbol{\lambda}+2\boldsymbol{\mu})\varepsilon_{zz} \qquad (2)$$

where $\boldsymbol{\lambda}$ is the Lamé constant, and $\boldsymbol{\mu}$ is the shear modulus [29]. We consider $\sigma_{zz}= 0$ as there is no stress perpendicular to the film (free surface) in thin-film heterostructures. The following equation

can express the relationship between the perpendicular strain εzz with in-plane strains, ε_{xx} and ε_{yy}, and the Poisson's ratio of the film (ν).

$$\varepsilon_{zz}/(\varepsilon_{xx}+\varepsilon_{yy}) = -\nu/(1-\nu) \quad (3)$$

Eq. (6) can be simplified as $\varepsilon_{zz}/\varepsilon_{xx} = -2\nu/(1-\nu)$ by assuming the symmetricity in the in-plane strains $\varepsilon_{xx} = \varepsilon_{yy}$. From the θ-2θ X-ray diffraction patterns we have measured the strain (ε_{zz}) around (111) peak for all thee diamond samples and obtained in-plane lattice strains of around 1.45 x 10^{-3}, 3.6 x 10^{-3}, and 4.9 x 10^{-3}, for diamond on Q-carbon coated Al_2O_3, DLC coated Al_2O_3 and uncoated Al_2O_3, respectively. These in-plane strain values in the diamond films can be used to calculate the planar lattice strain by using the following relationship [30].

$$\sigma = 2\,\varepsilon_{xx}\,\boldsymbol{\mu}\,(1+\nu)/(1-\nu) \quad (4)$$

The calculated stress in the diamond films on Q-carbon coated Al_2O_3, DLC coated Al_2O_3 and uncoated Al_2O_3 are obtained to be ~1.6 GPa, 3.7 GPa, and 5.2 GPa, respectively. These values are consistent with the stress values determined from the Raman analysis. The thermal stress and the intrinsic stress related to non-diamond entities are two major sources of the residual stress in the diamond film. A greater non-diamond carbon content in diamond crystals results in higher residual stress. It is also important to mention that the texture of the diamond film on Q-carbon coated Al_2O_3 has no significant effect on the reduced residual stress, rather a low fraction of sp^2-carbon content in the film and liquid mediated interlayer Q-carbon plays a major role in achieving diamond films with lower residual stress. A low compressive residual stress on Al_2O_3 is also beneficial to the adhesion of the film [31]. Studies have shown that the diamond thin film can sustain a maximal compression stress of 2.84 GPa without delamination [32]. The calculated stress on the diamond film on Q-carbon coated Al_2O_3 is well below this value, which explains the crack or delamination free growth of large-area diamond.

7.5.3 Diamond SAED and Q-carbon HRTEM

The HRTEM image for the Q-carbon film formed on c-Al_2O_3 substrate is shown in Fig. 7.4(a), with a thickness of ~60 nm. Fig. 7.4(b) shows the selected area microdiffraction pattern acquired from Q-carbon/Al_2O_3 interface. It reveals the amorphous nature of Q-carbon with (111) and (002) diffraction rings arising from the prominent sp^3 tetrahedral bonding. On nanosecond laser irradiation, carbon melted and subsequent ultrafast regrowth led to amorphous Q-carbon regrowth. Due to the associated undercooling being the critical undercooling required for amorphization, no crystallites were noted in the diffraction pattern for Q-carbon. The densely-packed tetrahedra in Q-carbon are utilized as nucleation seeds for HFCVD experiments.

Fig. 7.4(c) reveals the highly textured <111> oriented ~550 nm thick diamond film deposited on the c-cut Al_2O_3 substrate. The HRTEM image in Fig. 7.4(d) shows the HRTEM image of microdiamond with (220) cross-fringes associated with diamond, acquired across the <100> zone-axis, revealing the formation of single-crystalline diamond post-HFCVD on Al_2O_3 substrate. The respective SAED pattern acquired at the area associated with the HRTEM image is shown in Fig. 7.4(e), confirming the single-crystalline nature of HFCVD grown diamond. On indexing the diffraction pattern, as the cross-sectional zone-axis is noted to be <100>, the other possible directions for out-of-plane HFCVD growth are <111> and <110>. As <110> growth direction is associated with ultrafast island growth, the formation of such a layered structure and the associated XRD results, suggest <111> out-of-plane microdiamond growth on Q-carbon, by HFCVD processing. We have also performed line-scan across the (220) planes as indicated in Fig. 7.4(f-g), revealing the d_{220} spacing of ~1.26 Å. The lattice spacing, is noted to be consistent across the measurement, suggesting minimal compressive strain inside the diamond film.

7.5.4 Simulation results

Laser-solid interaction SLIM modeling: The complex laser-solid interaction simulations are carried out by extremely accurate finite element SLIM programming to understand the structural transformation of DLC into Q-carbon nanocomposite [33,34]. As the laser beam dimensions are significantly larger than melt depth ~50-100 nm, column approximation was utilized to simulate the laser-solid interactions using 1-D finite element method. The approximation is viable as the heat flow perpendicular to the film has an order higher magnitude in comparison with film surface, causing it to collapse as a 1-D heat flow problem. The laser parameters- λ=193 nm, width of the pulse = 20 ns and corresponding reflectivity for solid DLC, and the liquid form is used as input parameters simulate the laser irradiation process. On analyzing the surface temperature-time plots in Fig. 7.5(a) at various irradiation energy densities it was found that 0.4 J cm^{-2} is the critical energy density to induce surface melting. At the onset of melting, the liquid gets heated up with maxima ~18 ns, as shown in the inset of Fig. 7.5(a). On increasing the laser pulse energy density, this heating gets further enhanced leading to high temperatures ~4600 K for 1 J cm^{-2} nanosecond laser irradiation. The liquid carbon is metallic and possesses the thermal conductivity of 290 W m^{-1} K^{-1} [35], so it cools down to melting temperatures as the pulse terminates. The maxima melt profiles at respective energy densities are shown in Fig. 7.5(b). The figure reveals that melt depth increases monotonically with laser pulse energy density. The increase in regrowth velocity translates into a rise in the interfacial instability and decrease in the cellular wavelength [36–38] of the periodic cell structure which is evident in Q-carbon filamentary structures.

Ab-initio modeling: The structure of melt regrown Q-carbon and α-carbon phases is simulated using the LAMMPS code. The simulations are based on “liquid quench method” [39,40] generally used for randomization and formation of disordered solids, where amorphous carbon is melted and

subsequently quenched under isotropic pressure. In this case, to equilibrate the structures formed under HPHT condition, the pressure is first released at 2000 K to 760 Torr (see Experimental section for details**),** and then subsequent quenching to room temperature is performed. The liquid melt was equilibrated utilizing the using a Nose-Hoover thermostat [41]. The quenching to room temperature was performed under NVT conditions using a Langevin thermostat [42].[10] For the quench (relaxation) of randomized coordinates, we use 10^{-4} Ry/Bohr as the criterion for the convergence of the force.

The undercooling in melt phase shifts the temperature at which the solidification occurs, thereby nucleating phases which are not accessible in equilibrium phase diagrams. In the case of carbon, these phases are diamond and densely packed Q-carbon phases, which are formed far from equilibrium [43,44]. As it is not possible to impart undercooling considerations in dense packing for the melt state in the MD simulations, the HPHT simulations are modeled in the melt state by applying pressure during quenching of the melt state in carbon [40]. Isotropic pressure was utilized to compress the bulk C melt state. Fig. 7.5(c) highlights the radial distribution functions (RDF) for quenched and stabilized structures with isotropic pressures of 5 GPa and 50 GPa. By setting a radial cut-off at 1.85 Å, the average coordination number (CN) of the generated structure is calculated to be 3.08, which reflects ~ 92% sp^2 bonded C atoms. Notably, usage of low pressure of 5 GPa leads to the formation of prominently sp^2 bonded C structure. Under the high pressure of 50 GPa, the ultrafast quenched melt leads to the formation of a densely-packed phase with ~80% sp^3 content. These results are in-agreement with super-undercooling driven formation of densely packed Q-carbon phase on ultrafast melt quenching of C films. Fig. 7.5(d) reveals the structural model of the Q-carbon and α-carbon phases obtained from simulations, revealing the fact that Q-carbon is tetrahedrally coordinated. These simulation results provide further evidence that

amorphous carbon can be converted into Q-carbon under HPHT conditions which mimic the highly undercooled conditions in the melt phase.

7.5.5 Raman spectroscopy

The Raman spectra of the diamond on Q-carbon coated Al_2O_3, DLC coated Al_2O_3 and uncoated Al_2O_3 substrate is shown in Fig. 7.6(a). The presence of diamond is revealed by a characteristic sharp line at around 1332 cm^{-1} which occurs due to the vibration of the two interpenetrating cubic sub-lattices of diamond [45]. This Raman peak confirms the successful deposition of crystalline diamond films on all three types of substrates. This signature Raman peak is attributed to the triply degenerate zone-center optical phonon in diamond structure, and is the only mode that is Raman active in the first-order [46,46,47]. The existence of a broad band at ~1550 cm^{-1} indicates the trace of certain amount of non-diamond (sp^2) carbon. Moreover, trace of any peak at ~1130 cm^{-1} corresponds to the nanocrystalline trancepolyacetylene in the grain boundaries of the diamond film [48,49]. No obvious evidence of this peak in all three diamond thin films refers to the absence of such noncrystalline phase of carbon. For stress analysis, we extensively studied the position of the diamond Raman peak in the Raman spectra taken on diamond thin films on three different substrate surface conditions. In case of the diamond on DLC coated Al_2O_3 and uncoated Al_2O_3 the T_{2g} peak upshifted to 1337 cm^{-1} and 1338.2 cm^{-1}, respectively, presumably as a result of thermally induced stresses between the diamond and Al_2O_3 [50]. On the other hand, since less significant shift in the diamond peak (1333.46 cm^{-1}) is observed in case of the diamond on Q-carbon coated Al_2O_3 , it is possible that the diamond film is no longer under considerable stress. The splitting of diamond peak to singlet and doublet states becomes observable when $\sigma > 8–9$ GPa [51]. In this study, the deconvolution of the characteristic Raman peak into two individual peaks of singlet and doublet states reliably is very difficult owing to the stress values <8 GPa. We have also calculated the

stress in the diamond films by the shift in the T_{2g} Raman peak. Researchers determined a relationship between the Raman peak shift and stress value in the framework of biaxial stress model to obtain the stress in the diamond thin films [51]. For an unsplitted diamond peak, this relationship between the stress and the overall peak-shift can be expressed as follow:

$$\Delta\nu\ [cm^{-1}] = \nu_s - \nu_0 = -1.62\sigma\ [GPa] \qquad (5)$$

Where ν_0 is the equilibrium position of the T_{2g} peak of diamond in the unstressed state (1332 cm^{-1}), and ν_s is the observed Raman peak position in the stressed state. From the position of the Raman peak (1333.46 cm^{-1}), we obtained ~0.9 GPa compressive stress in the diamond film deposited on Q-carbon coated Al_2O_3. Such a low value of compressive stress is owing to the intermediate Q-carbon layer which nullify the effect of thermal strain. On the other hand, the obtained stress in the diamond films on DLC coated Al_2O_3 and uncoated Al_2O_3 substrates are ~ 3.10 GPa and 3.90 GPa, respectively. These values are consistent with the in-plane stress values determined from the XRD analysis. The generation of huge in-plane stresses explains the formation of cracks in the diamond crystal (in the SEM image) and scarce growth of diamond on uncoated Al_2O_3 due to the poor nucleation and delamination.

The theoretical thermal stress in the diamond film on a particular substrate can be obtained by the following expression.

$$\sigma_{th} = d\sigma/dT\ X\ \Delta T = [E/(1-\nu)]\ (\alpha_r - \alpha_s)\ X\ \Delta T = E(\varepsilon_d - \varepsilon_s)/(1-\nu) \qquad (6)$$

where E is the Young's modulus (1143 GPa) and ν is the Poisson ratio (0.07) of the diamond, and ε_d and ε_s are temperature-dependent thermal expansions for the diamond film and the substrate, respectively. Under the chosen deposition conditions a maximum 5.1GPa stress can be generated in the diamond film on Al_2O_3 substrate. According to equation 5, this value would result in ~ 8.28 cm^{-1} blue shift in the Raman peak. The shift in the characteristic diamond Raman peak is ~ 6.2 cm^{-}

^{1} for the diamond film on uncoated Al_2O_3 substrate, which is close to the theoretical value. The diamond grown on DLC coated Al_2O_3 shows a peak shift of ~ 5.03 cm^{-1}, signifying little contribution of the DLC layer to release the stress on the diamond film. Hence thinly distributed growth of diamond is observed on DLC coated Al_2O_3. On the other hand, the diamond film on Q-carbon coated Al_2O_3 shows a very small peak shift (~1.46 cm^{-1}) in the Raman spectrum. It is supposed that the use of the Q-carbon on the Al_2O_3 substrate plays a crucial role to reduce the effect of thermal stress.

Line scan: The spectra of the Raman line scan patterns on diamond film grown on Q-carbon coated Al_2O_3 are illustrated in a 3D plot in Fig. 7.6(b). Along a 100μm line (Y-axis in the figure) 21 Raman spectra are collected at equal separation on the film. During the spectral acquisition, the equidistant points are illuminated by the focused 532nm laser beam, and a computer-controlled motorized stage precisely moved the sample. The presence of a sharp and symmetric diamond peak (T_{2g}) in each spectrum refers to the deposition of uniform, and high-quality diamond on the Q-carbon coated Al_2O_3. Significantly low and broad trace of the G-peak refers to the minimal graphitic entity along the line. The Raman spectra of the HFCVD diamond films were used to determine the quality index of the diamond films in this study. The quality index is defined as the ratio of the area under the peak associated with diamond to the area under the broad G peak associated with the nondiamond carbon, which can be expressed by the following equation [52].

$$\text{Quality index, } R = \frac{sp^3}{sp^2} = \frac{\int_{1325}^{1340} I(v)dv}{\int_{1440}^{1640} I(v)dv} \quad (7)$$

The smaller sp^2 content in the diamond film gives a larger quality index. The baseline for this integration was considered as the base points of the acquired spectra at 1000 cm^{-1} and 2000 cm^{-1}, respectively. The quality index was found to be better for the diamond growth on Q-carbon-Al_2O_3 (4.7) compared to the rest of the systems (1.6 and 1.1 for DLC coated Al_2O_3 and uncoated Al_2O_3,

respectively). The Raman spectra can also be used to pinpoint the amount of nondiamond content (C_{nd}) in each of the diamond films. The sensitivity of the Raman signal from the non-diamond carbon phase is about 75 times of diamond [53]. The following equation is used to calculate the nondiamond contents in the diamond films.

$$C_{nd} = \frac{1}{1+75(\frac{I_d}{I_{nd}})} \quad (8)$$

Where, I_d represents the Renan peak intensity for diamond entities, and I_{nd} represents the Raman peak intensity for the non-diamond carbon content. The calculated non-diamond content is found to be 0.12%, 0.28% and 0.41%, in case of diamond grown on Q-carbon coated Al_2O_3, DLC coated Al_2O_3, and uncoated Al_2O_3, respectively.

Area Mapping: Fig. 7.6(c-d) represent the Raman area mapping to better understand the growth of HFCVD diamond on c-Al_2O_3. An area of 92 μm x 56 μm was divided into 200 x 200 pixels (200 points per line and 200 lines per image) to collect data (with an integration time of 0.5 s) for the ultrahigh-resolution Raman area mapping images. The sample was focused by the 532 nm laser and the each line on the sample was precisely rasterized by a motorized stage during the spectra acquisition for the area mapping. The Raman mapping in Fig. 7.6(c) was acquired by selecting the diamond region (1330-1340 cm^{-1}) and in Fig. 7.6(d) was acquired by selecting the graphitic region (1440-1550 cm^{-1}). The diamond mapping image (Fig. 7.6(c)) clearly illustrates the formation of a large-area diamond on the right side (on the Q-carbon coated Al_2O_3 region) and almost no diamond formation on the left side (uncoated Al_2O_3 region). The distinctive sharp boundary refers to the high nucleation density, and favorable growth throughout the Q-carbon coated Al_2O_3 with no crack and/or delamination. The area mapping from the graphitic pick clearly illustrates huge graphitic content throughout the uncoated Al_2O_3 region (left side) due to unfavorable nucleation and growth

condition of diamond and very little trace of sp^2 content in the other side. This refers to the high-quality diamond growth throughout the Q-carbon coated Al_2O_3 region.

7.5.6 Diamond nucleation and growth on Q-carbon, DLC and bare Al_2O_3

Diamond nucleation is one of the most critical issues to develop the understanding of the diamond growth on polished, smooth, and non-carbide forming Al_2O_3 wafers. Understanding of diamond nucleation is absolutely essential for the formation of continuous uniform film consistently at an early stage of growth [54]. The nucleation density, the growth rate, and the morphology of the diamond crystals and films are found to be strongly influenced by the surface condition of the substrate. The substrates, on which the HFCVD diamond is deposited, can be classified into two main categories: (i) strong carbide formers, and (ii) substrates with no affinity for carbon. The latter substrates tend to have poor adhesion. Nucleation of diamond phase is generally difficult in both classes of substrates. This is clearly a difficult problem which is not well understood [55]. The transparent Al_2O_3 substrate has almost no affinity for carbon, therefore, no carbide layer is formed during diamond growth. It is well-known that carbide phases are formed on strong carbide forming substrates, on which nucleation of diamond is facilitated. However, no carbide layer is formed during CVD diamond growth on Al_2O_3 substrate due to the high stability of the Al_2O_3 structure [10]. The Gibbs free energy of formation of aluminum carbide (−32.1 KJ/mole) is much higher compared to that of aluminum oxide (−1675 kJ/mole), the carbide layer for the diamond nucleation is not favored on Al_2O_3 [56]. Therefore diamond nucleation is poor on bare Al_2O_3, which has been observed from the SEM micrograph in Fig. 7.1.

On Q-Carbon*:* In Q-carbon, the closed packed diamond tetrahedra are embedded on the surface of the substrate [57]. These diamond tetrahedra were formed as a result of quenching from a super

undercooled state by using a high-power nanosecond pulsed laser irradiation. During Q-carbon formation the laser pulse interacts with the DLC thin film on a suitable substrate and the carbon is melted in a super undercooled state (at 3800 K) and subsequently quenched resulting in a formation of highly packed (80% packing efficiency) diamond tetrahedra. These diamond tetrahedra act as a seed for the nucleation to grow diamond mocrocrystallites. This is the principal factor for the obtained high diamond nucleation densities during diamond growth on Q-carbon/Al_2O_3 system. The Q-carbon is embedded into the substrate and provides nucleation sites for further diamond growth. Thereby, the diamond formed on Q-carbon is very adherent to the substrate, which is essential for cutting tool, drilling, and microelectronic device applications.

On DLC*:* During CVD diamond growth, the local carbon concentration plays a significant role in diamond formation. The DLC film is responsible for the change in the local carbon concentration during the diamond deposition. Under these conditions, the nucleation density of diamond was increased by an order of magnitude and the growth rates by about 60%, as compared to diamond deposited on abraded molybdenum and molybdenum carbide [58]. The nucleation density, the distribution on the substrate, and the morphology of diamond on DLC-Al_2O_3 improved compared to the same on uncoated Al_2O_3. The following explanation can be invoked to explain the observed enhancement of diamond nucleation by diamond-like carbon layers. It has been suggested that the greater nucleation efficiency of diamond on DLC is a result of the solid-state transformation of amorphous carbon into diamond [59,60]. However, the synthesis of diamond on DLC is achieved by a reduction in the hydrocarbon species in the process gas mixture, which leads to the regasification of the amorphous carbon rather than a solid-state transformation of DLC to an ordered diamond structure [58]. Although all of these carbon species with different bonds coexist on the substrate surface, the etching rate of the sp^1 and sp^2 bonded carbon is ten times faster than

etching of the stable sp^3 bonded carbon, thereby growing the sp^3 phase [61]. Since the amorphous carbon is more reactive in the extreme ambient, which can be characterized by high hydrogen species concentrations, the regasification of the amorphous carbon is more likely. Thus, the regasification of the existing DLC layer locally increases the carbon concentration at the initial stage and promotes the high nucleation density of diamond [58]. In this experimental study, we have found that the DLC layer on Al_2O_3 leads to the local enhancement in the diamond deposition. However, the observed coverage of the diamond layer is incomplete consisting of patches of small uniform crystals. Even after 6 hours of growth, the DLC coated Al_2O_3 substrates were not covered with continuous diamond films. This diamond structure composed of uniform, small crystals, similar to the uncoated Al_2O_3 but with better coverage. By contrast, the diamond crystals on the Al_2O_3 sample without any coating were smaller in size and much less in density.

Adhesion. Further to elaborate, it has always been a daunting task to get adhesive CVD diamond on non-carbide forming substrates like Al_2O_3 or other optically transparent substrates, which possesses a big challenge for practical applications. Other than the weak interface interaction between the film and the substrate, the poor adhesion between the diamond thin film and the Al_2O_3 substrate is also attributed to the difference in the coefficient of thermal expansion. The usefulness of a poorly adhesive diamond on any substrate is considerably reduced. After long deposition runs at high temperature, peeling off the diamond film from the Al_2O_3 substrate were observed during the cooling process [62]. It has been also observed that a thin film of CVD diamond deposited on an Al_2O_3 substrate can be easily peeled off from the substrate during the peel-off adhesion test by the scotch tape method. In this experimental study, we present a laser irradiation based technique to improve the adhesion of diamond on Al_2O_3. For the nucleation, growth, and adhesion of diamond thin film on a nondiamond substrate with no affinity for carbon such as Al_2O_3, diamond

tetrahedra in the Q-carbon, and the reaction products on the substrate under the optimum conditions play a very critical role. Adhesion is primarily determined by the bonding characteristics and interfacial reactions between the film and the substrate [55]. The interfacial interaction between the Q-carbon and the Al_2O_3 is highly favorable to have very good attachment due to the liquid phase mediated growth of Q-carbon from a super undercooled state. This is a clean and nondestructive approach for promoting the nucleation and adhesion of diamond, as contrasted with the widely used techniques where the substrate is abraded with a suitable abrasive to create surface mechanical damage. Therefore, we did not observe any formation of cracks nor peeled-off areas in the diamond thin film deposited on Q-carbon coated Al_2O_3 substrates.

7.6 Summary

We described a novel laser method for enhancing the nucleation and for improving the quality of diamond films on c-Al_2O_3 substrate deposited by HFCVD. We have found that the DLC tetrahedra act as a nuclei for diamond growth, their number density determines the areal coverage of grown diamond crystals. The average size of diamond crystallites on DLC and Q-carbon is found to be the same (~5 μm), which is somewhat larger than on bare Al_2O_3. From our observation, we have concluded that diamond crystallites grow on DLC tetrahedra whose density is much high in Q-carbon than DLC films. The smaller size on bare Al_2O_3 is related to incubation period needed to form DLC tetrahedra during HFCVD, which provide nucleation sites for diamond growth. The improvement in adhesion is also accomplished owing to the liquid phase mediated growth of diamond tetrahedra in the Q-carbon on which the diamond nucleation and growth take place. To examine the effectiveness of Q-carbon for diamond nucleation, we have grown the diamond on Al_2O_3 without any coating under the same deposition conditions. We have observed a very limited coverage of scattered diamond clusters on uncoated Al_2O_3 due to the unfavorable substrate

conditions which lead to a poor nucleation density, huge stress generation, and poor adhesion. Moreover, to distinguish the role of Q-carbon from DLC on diamond nucleation and growth, we have examined the surface morphology of the diamond grown on the DLC coated Al_2O_3 without any laser irradiation in the same HFCVD conditions. Although the nucleation density and the areal coverage of diamond on the substrate improved compared to that on the uncoated Al_2O_3, however, we could not obtain a uniform coverage of diamond thin film on the entire substrate. The Q-carbon layer shows markedly superior characteristics on improving the nucleation, growth, and adhesion of diamond thin films on c-Al_2O_3, which is ascribed to the high density of the diamond tetrahedra in the Q-carbon. The diamond film grown on Q-carbon coated Al_2O_3 has shown significantly improved crystalline quality with very low non-diamond carbon content and very less residual stress, confirmed by Raman and XRD analysis, compared to that on DLC coated and uncoated Al_2O_3. The delamination related issue, which limits the fabrication of large-area diamond thin film on Al_2O_3, is also addressed in this experimental study. These results will provide some insight to the ever-challenging problem of diamond thin film deposition on single-crystal Al_2O_3 for different unprecedented and hi-tech applications.

Table 7. 1**:** Comparison of different important material properties of some of the commonly used substrates with Al_2O_3 for diamond growth [63].

Material	Crystal structure	Group of symmetry	Lattice constant(s) (Å)	Melting point (^{0}C)	Thermal expansion (10^{-6} K^{-1})	Hardness (Mohs)	Diamond nucleation density (cm^{-2})
Diamond	Cubic	Fd-3m	3.567	4027	1.5	10	
Si	Cubic	Fd-3m	5.43	1414	2.92	6-7	
SiC	Cubic	T^2_d-*F43m*	4.3596	3103	2.77	9.2-9.3	
	hexagonal	C^4_{6v}-	a =3.073				
		P6$_3$mc	c = 10.053				
Al_2O_3	Hexagonal	R3C	a = 4.758	2040	4.2	9	10^4
			c = 12.991				
MgO	Cubic	Fm-3m	4.216	2825	12.8	5.8	
Iridium	Cubic	Fm-3m	3.839	2484	6.8	6.5	
SrTiO3	Cubic	Pm3m	3.905	2080	10.3	6	

7.7 Figures

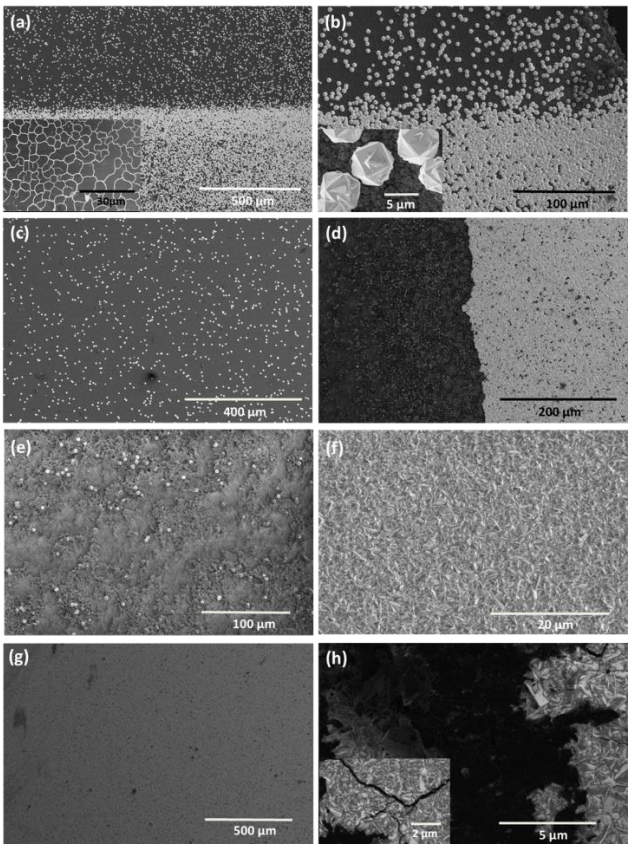

Figure 7. 1**:** (a) Growth of diamond on a c-Al_2O_3 substrate coated with DLC (top) and Q-carbon (bottom).The inset of figure (a) shows the Q-carbon formation on c-Al_2O_3. (b) A magnified image of the same sample illustrates better diamond coverage on the Q-carbon coated side compared to the rest of the DLC area. The inset shows the high-resolution image of individual diamond crystals. (c) Illustrates scattered diamond growth on the DLC coated Al_2O_3. (d) The growth of diamond (6 hours) on uncoated (left) and Q-carbon coated (right) Al_2O_3. (e) Spears growth of diamond on the uncoated Al_2O_3. (f) The high-resolution image of diamond growth on Q-carbon showing the faceted triangular morphology of diamond. (g) Shows the wafer-scale coverage of HFCVD (6 h) diamond on Q-carbon coated c-Al_2O_3. (h) Formation of crack and delamination of the diamond crystals on DLC coated Al_2O_3 (6 hours). The inset of (h) shows the magnified image of the crack formation due to stress in the film.

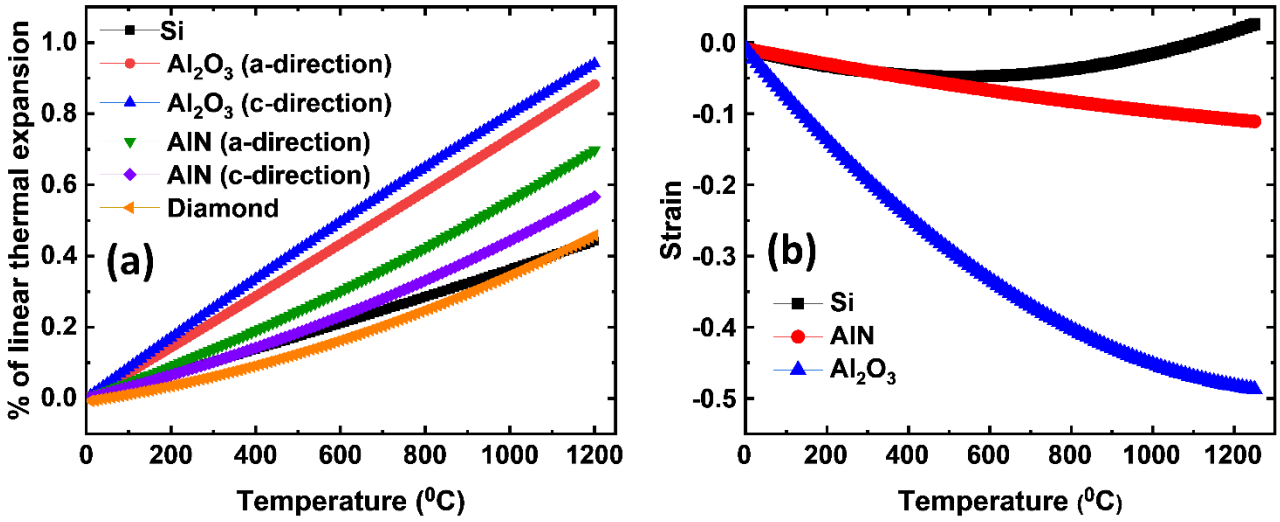

Figure 7. 2**:** (a) Plots of the cumulative thermal linear expansion coefficient for diamond, silicon, AlN, and Al_2O_3 for comparison. The slope of each curve corresponds to the thermal expansion coefficient. (b) Temperature-dependent lattice mismatch in a diamond-Al_2O_3 system.

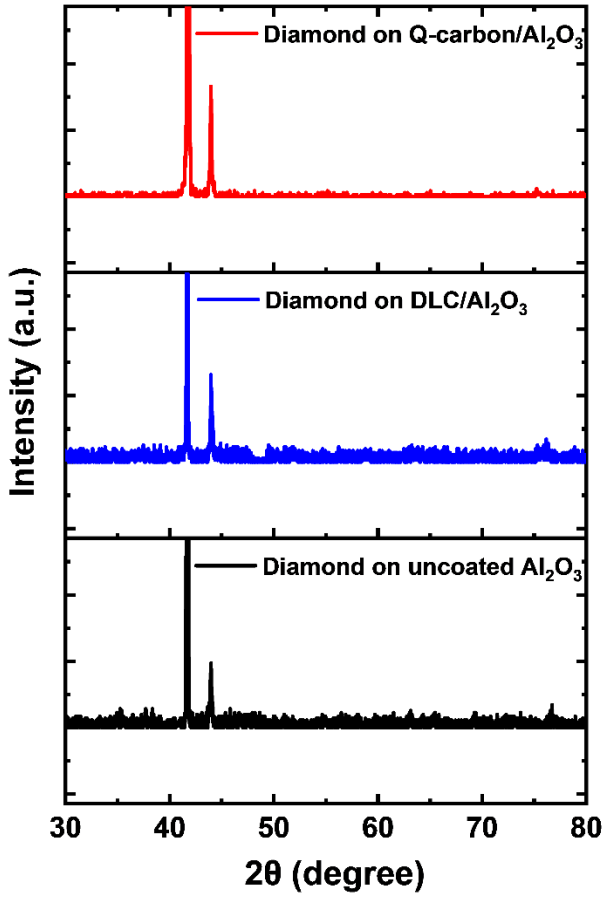

Figure 7. 3**:** X-ray diffraction patterns from $2\theta = 30°\text{-}80°$ for diamond on Q-carbon coated *c*-Al_2O_3 substrate, DLC coated Al_2O_3, and uncoated Al_2O_3.

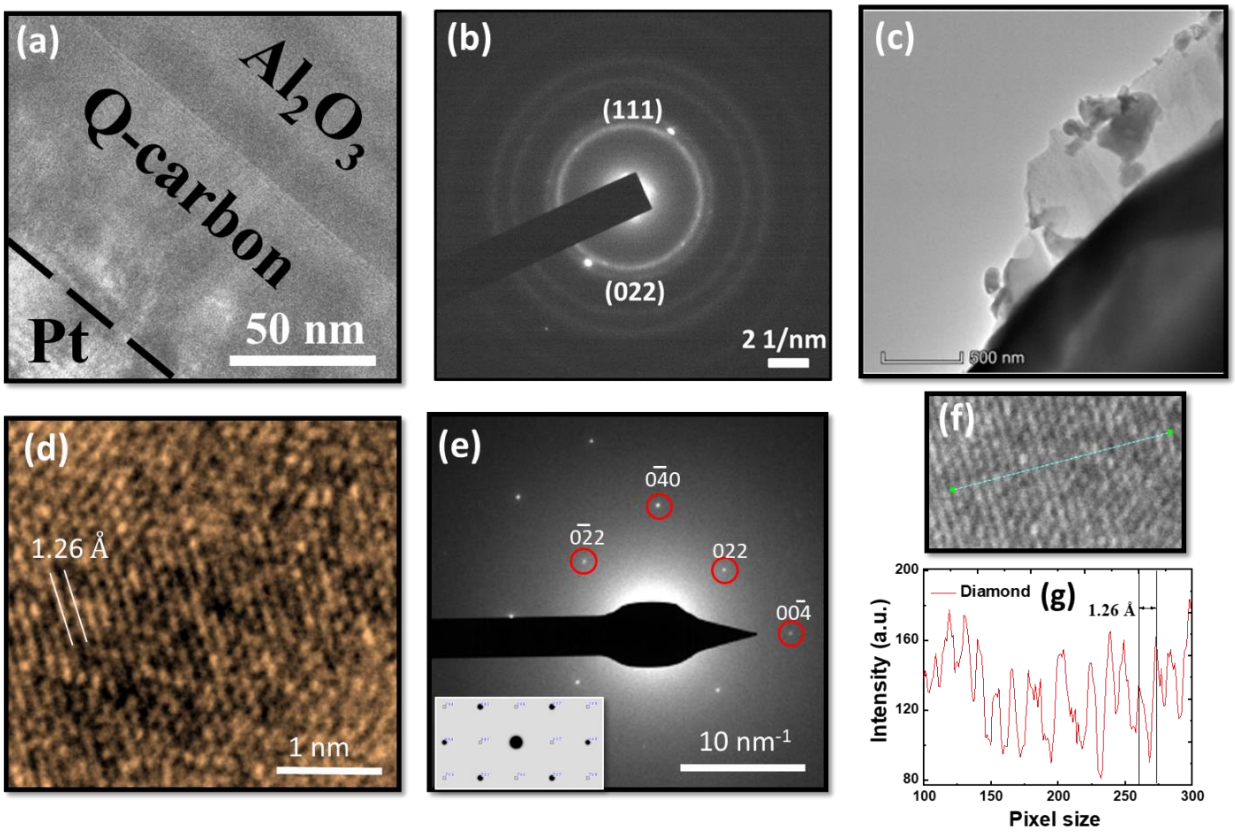

Figure 7. 4**:** Diamond SAED and Q-carbon HRTEM. (a) The HRTEM image for the Q-carbon film formed on c-Al_2O_3 substrate is shown in, with a thickness of ~60 nm. (b) Shows the selected area micro-diffraction pattern acquired from Q-carbon/Al_2O_3 interface. (c) Reveals the highly textured <*111*> oriented ~50 nm thick diamond film deposited on c-cut Al_2O_3 substrate. (d) Shows the HRTEM image of microdiamond with (220) cross-fringes, acquired across the <*100*> zone-axis, revealing the formation of single-crystalline diamond post-HFCVD on Al_2O_3. (e) The respective SAED pattern acquired at the area associated with the HRTEM image**,** confirming the single-crystalline nature of the HFCVD grown diamond. (f) and (g) reveal the line-scan across the (220) planes, revealing the d_{220} spacing of ~1.26 Å.

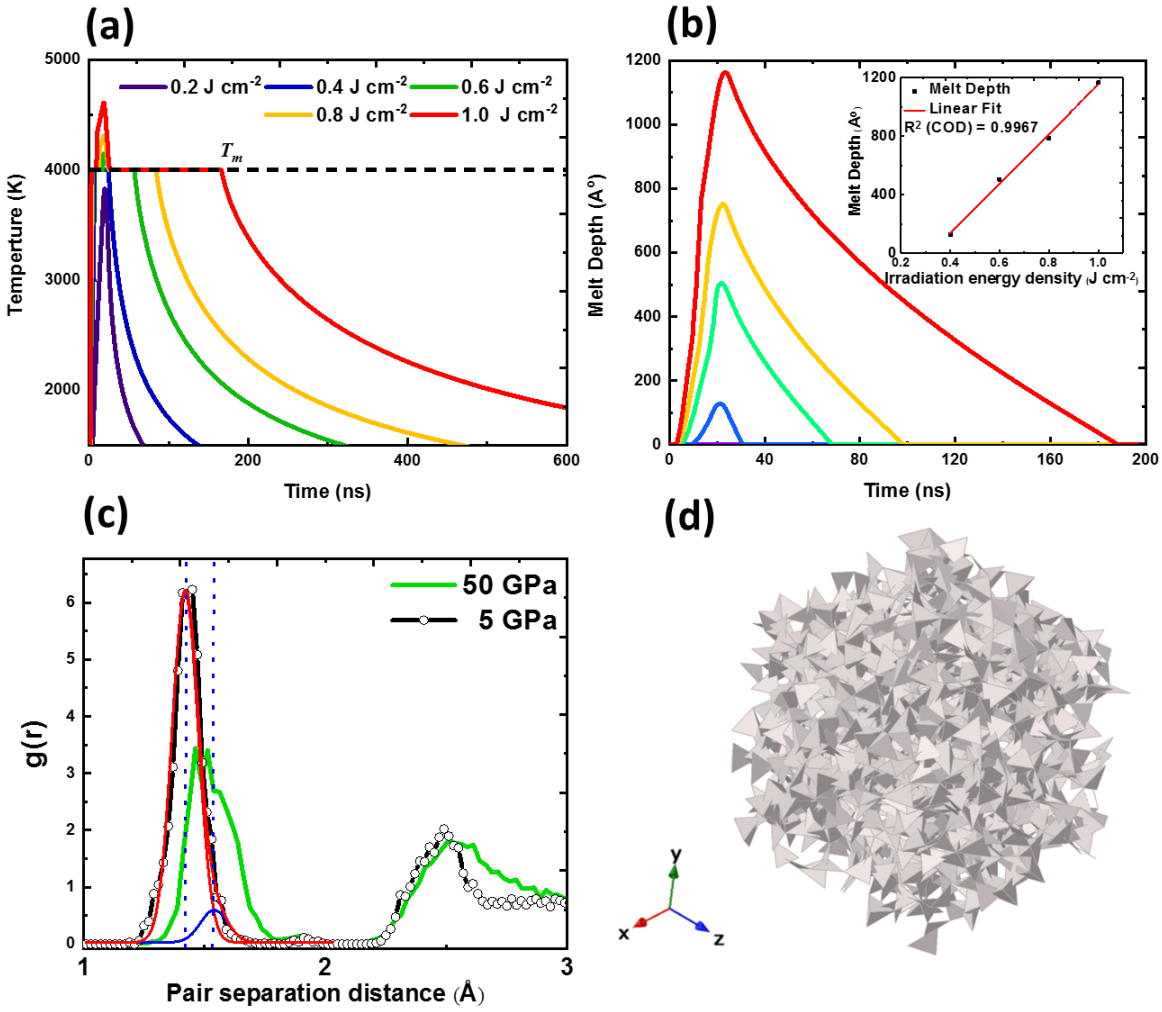

Figure 7. 5**:** Simulation of the Q-carbon melt regrown structure. (a) Simulated SLIM temperature *vs.* time thermal profiles for 70% sp^3 DLC thin films. (b) The melt depth as a function of time. (c) The radial distribution function plots for Q-carbon and α-carbon phases achieved as a function of applied isotropic pressures of 5 and 50 GPa, respectively; (d) the structural model of Q-carbon, revealing the prominently tetrahedral bonding in Q-carbon.

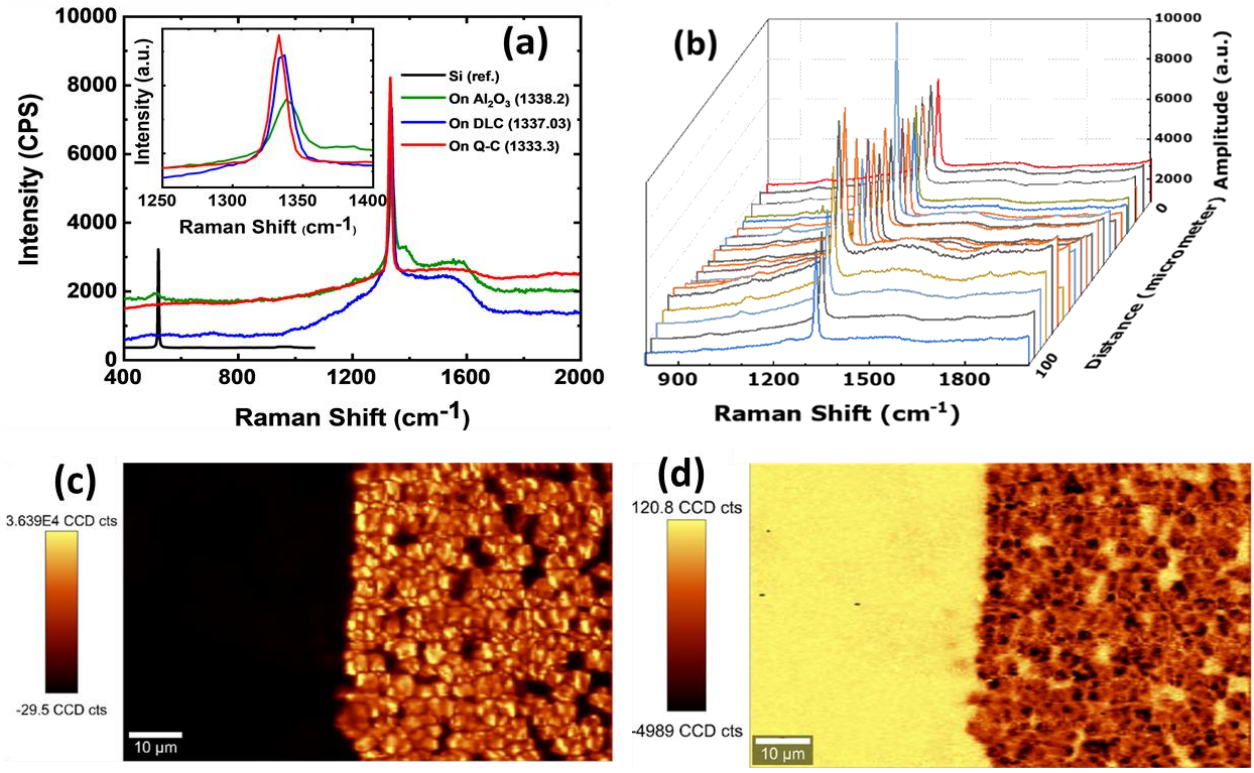

Figure 7. 6**:** (a) The Raman spectra of the diamond on Q-carbon coated Al_2O_3, DLC coated Al_2O_3, and uncoated Al_2O_3. The inset in (a) shows the position of the characteristic T_{2g} peaks of the corresponding spectra. (b) The line scan representation of the Raman spectra taken from 21 equidistance points on the film. (c) The Raman area mapping of the diamond peak illustrating the formation of the high-quality diamond film on the Q-carbon coated Al_2O_3 region (right side) and the absence of diamonds in the uncoated Al_2O_3 region. (d) The Raman area mapping of the graphitic peak depicts the presence of a graphitic entity in the uncoated Al_2O_3 region (left side). Almost complete absence of graphitic entity on the right side refers to the high-quality diamond deposition on the Q-carbon coated Al_2O_3.

References

[1] A. Doerr, Imaging: Diamonds for MRI, Nat. Methods. 12 (2015) 176. https://doi.org/10.1038/nmeth.3310.

[2] D. Ho, A. Zarrinpar, E.K.-H. Chow, Diamonds, Digital Health, and Drug Development: Optimizing Combinatorial Nanomedicine, ACS Nano. 10 (2016) 9087–9092. https://doi.org/10.1021/acsnano.6b06174.

[3] S. Yamasaki, E. Gheeraert, Y. Koide, Doping and interface of homoepitaxial diamond for electronic applications, MRS Bull. 39 (2014) 499–503. https://doi.org/10.1557/mrs.2014.100.

[4] K.-H. Hou, Han-TaoWang, H.-H. Sheu, M.-D. Ger, Preparation and wear resistance of electrodeposited Ni–W/diamond composite coatings, Appl. Surf. Sci. 308 (2014) 372–379. https://doi.org/10.1016/j.apsusc.2014.04.175.

[5] G. Karimi, J.R. Culham, Review and assessment of Pulsating Heat Pipe mechanism for high heat flux electronic cooling, in: Ninth Intersoc. Conf. Therm. Thermomechanical Phenom. Electron. Syst. IEEE Cat No04CH37543, 2004: pp. 52-59 Vol.2. https://doi.org/10.1109/ITHERM.2004.1318252.

[6] I. Friel, S.L. Geoghegan, D.J. Twitchen, G.A. Scarsbrook, Development of high quality single crystal diamond for novel laser applications, in: Opt. Photonics Counterterrorism Crime Fight. VI Opt. Mater. Def. Syst. Technol. VII, International Society for Optics and Photonics, 2010: p. 783819. https://doi.org/10.1117/12.864981.

[7] R.S. Balmer, J.R. Brandon, S.L. Clewes, H.K. Dhillon, J.M. Dodson, I. Friel, P.N. Inglis, T.D. Madgwick, M.L. Markham, T.P. Mollart, N. Perkins, G.A. Scarsbrook, D.J. Twitchen, A.J. Whitehead, J.J. Wilman, S.M. Woollard, Chemical vapour deposition synthetic diamond:

materials, technology and applications, J. Phys. Condens. Matter. 21 (2009) 364221. https://doi.org/10.1088/0953-8984/21/36/364221.

[8] N. Govindaraju, R.N. Singh, Processing of nanocrystalline diamond thin films for thermal management of wide-bandgap semiconductor power electronics, Mater. Sci. Eng. B. 176 (2011) 1058–1072. https://doi.org/10.1016/j.mseb.2011.05.042.

[9] A.V. Sumant, V.P. Godbole, S.T. Kshirsagar, Studies on hot filament chemical vapor deposition of diamond onto aluminum oxide, Mater. Sci. Eng. B. 39 (1996) L5–L9. https://doi.org/10.1016/0921-5107(96)01579-6.

[10] P.W. May, C.A. Rego, C.G. Trevor, E.C. Williamson, M.N.R. Ashfold, K.N. Rosser, N.M. Everitt, Deposition of diamond films on sapphire: studies of interfacial properties and patterning techniques, Diam. Relat. Mater. 3 (1994) 1375–1380. https://doi.org/10.1016/0925-9635(94)90153-8.

[11] K.G. Saw, I. Andrienko, A. Cimmino, P. Spizzirri, S. Prawer, J. du Plessis, Growth of diamond on α-(0001) sapphire substrates, Diam. Relat. Mater. 12 (2003) 1663–1669. https://doi.org/10.1016/S0925-9635(03)00189-4.

[12] J.B. Donnet, H. Oulanti, T.L. Huu, M. Schmitt, Synthesis of large single crystal diamond using combustion-flame method, Carbon. 44 (2006) 374–380. https://doi.org/10.1016/j.carbon.2005.06.041.

[13] Y. Tzeng, M. Yoshikawa, M. Murakawa, A. Feldman, Applications of Diamond Films and Related Materials: Proceedings of the First International Conference on the Applications of Diamond Films and Related Materials - ADC ’91, Auburn, Alabama, U.S.A., August 17-22, 1991, Elsevier, 2017.

[14] R.J. Meilunas, R.P.H. Chang, S. Liu, M.M. Kappes, Nucleation of diamond films on surfaces using carbon clusters, Appl. Phys. Lett. 59 (1991) 3461–3463. https://doi.org/10.1063/1.105678.

[15] J. Muller, F. Antoni, E. Fogarassy, F. Le Normand, HFCVD diamond nucleation and growth on DLC carbon films obtained by laser ablation, Carbon. 36 (1998) 565–568. https://doi.org/10.1016/S0008-6223(98)00067-0.

[16] L. Demuynck, J.C. Arnault, R. Polini, F. Le Normand, CVD diamond nucleation and growth on scratched and virgin Si(100) surfaces investigated by in-situ electron spectroscopy, Surf. Sci. 377–379 (1997) 871–875. https://doi.org/10.1016/S0039-6028(96)01501-4.

[17] Z. Feng, M.A. Brewer, K. Komvopoulos, I.G. Brown, D.B. Bogy, Diamond nucleation on unscratched silicon substrates coated with various non-diamond carbon films by microwave plasma-enhanced chemical vapor deposition, J. Mater. Res. 10 (1995) 165–174. https://doi.org/10.1557/JMR.1995.0165.

[18] P.E. Pehrsson, J. Glesener, A. Morrish, Chemical vapor deposition diamond nucleation induced by sp2 carbon on unscratched silicon, Thin Solid Films. 212 (1992) 81–90. https://doi.org/10.1016/0040-6090(92)90503-4.

[19] K. Tamaki, Y. Nakamura, Y. Watanabe, S. Hirayama, Effect of hydrogenated amorphous carbon films on nucleation of diamond particles by hot-filament chemical vapor deposition, J. Mater. Res. 10 (1995) 431–435. https://doi.org/10.1557/JMR.1995.0431.

[20] R. Meilunas, M.S. Wong, K.C. Sheng, R.P.H. Chang, R.P. Van Duyne, Early stages of plasma synthesis of diamond films, Appl. Phys. Lett. 54 (1989) 2204–2206. https://doi.org/10.1063/1.101124.

[21] M.M. Waite, S.I. Shah, X-ray photoelectron spectroscopy of initial stages of nucleation and growth of diamond thin films during plasma assisted chemical vapor deposition, Appl. Phys. Lett. 60 (1992) 2344–2346. https://doi.org/10.1063/1.107474.

[22] E. Abubakr, A. Zkria, Y. Katamune, S. Ohmagari, K. Imokawa, H. Ikenoue, T. Yoshitake, Formation of low resistivity layers on singlecrystalline diamond by excimer laser irradiation, Diam. Relat. Mater. 95 (2019) 166–173. https://doi.org/10.1016/j.diamond.2019.04.013.

[23] J. Steinbeck, G. Dresselhaus, M.S. Dresselhaus, The properties of liquid carbon, Int. J. Thermophys. 11 (1990) 789–796. https://doi.org/10.1007/BF01184345.

[24] M. Dixon, P. Hutchinson, A method for the extrapolation of pair distribution functions, Mol. Phys. 33 (1977) 1663–1670. https://doi.org/10.1080/00268977700101381.

[25] W.M. Yim, R.J. Paff, Thermal expansion of AlN, sapphire, and silicon, J. Appl. Phys. 45 (1974) 1456–1457. https://doi.org/10.1063/1.1663432.

[26] S.B. Qadri, C. Kim, E.F. Skelton, T. Hahn, J.E. Butler, Thermal expansion of chemical vapor deposition grown diamond films, Thin Solid Films. 236 (1993) 103–105. https://doi.org/10.1016/0040-6090(93)90651-5.

[27] R.K. Singh, D.R. Gilbert, J. Laveigne, Growth of adherent diamond films on optically transparent sapphire substrates, Appl. Phys. Lett. 69 (1996) 2181–2183. https://doi.org/10.1063/1.117158.

[28] J.J. Gracio, Q.H. Fan, J.C. Madaleno, Diamond growth by chemical vapour deposition, J. Phys. Appl. Phys. 43 (2010) 374017. https://doi.org/10.1088/0022-3727/43/37/374017.

[29] J.P. Hirth, J. Lothe, Theory of dislocations, McGraw-Hill, New York; London, 1968.

[30] J. Narayan, Recent progress in thin film epitaxy across the misfit scale (2011 Acta Gold Medal Paper), Acta Mater. 61 (2013) 2703–2724. https://doi.org/10.1016/j.actamat.2012.09.070.

[31] C.T. Kuo, C.R. Lin, H.M. Lien, Origins of the residual stress in CVD diamond films, Thin Solid Films. 290–291 (1996) 254–259. https://doi.org/10.1016/S0040-6090(96)09016-5.

[32] J.J. Gracio, Q.H. Fan, J.C. Madaleno, Diamond growth by chemical vapour deposition, J. Phys. Appl. Phys. 43 (2010) 374017. https://doi.org/10.1088/0022-3727/43/37/374017.

[33] R.K. Singh, J. Narayan, A novel method for simulating laser-solid interactions in semiconductors and layered structures, Mater. Sci. Eng. B. 3 (1989) 217–230. https://doi.org/10.1016/0921-5107(89)90014-7.

[34] R.K. Singh, J. Narayan, Pulsed-laser evaporation technique for deposition of thin films: Physics and theoretical model, Phys. Rev. B. 41 (1990) 8843–8859. https://doi.org/10.1103/PhysRevB.41.8843.

[35] A.H. Castro Neto, F. Guinea, N.M.R. Peres, K.S. Novoselov, A.K. Geim, The electronic properties of graphene, Rev. Mod. Phys. 81 (2009) 109–162. https://doi.org/10.1103/RevModPhys.81.109.

[36] J. Narayan, Interface instability and cell formation in ion-implanted and laser-annealed silicon, J. Appl. Phys. 52 (1981) 1289–1293. https://doi.org/10.1063/1.329753.

[37] J. Narayan, H. Naramoto, C.W. White, Cell formation and interfacial instability in laser-annealed Si-In and Si-Sb alloys, J. Appl. Phys. 53 (1982) 912–915. https://doi.org/10.1063/1.330559.

[38] J. Narayan, Interface structures during solid-phase-epitaxial growth in ion implanted semiconductors and a crystallization model, J. Appl. Phys. 53 (1982) 8607–8614. https://doi.org/10.1063/1.330457.

[39] V.S. Dozhdikov, A.Y. Basharin, P.R. Levashov, Quenching of liquid carbon under intensive heat transfer to the cold diamond substrate: Molecular-dynamic simulation, 653 (2015) 012091. https://doi.org/10.1088/1742-6596/653/1/012091.

[40] R. Ranganathan, S. Rokkam, T. Desai, P. Keblinski, Generation of amorphous carbon models using liquid quench method: A reactive molecular dynamics study, Carbon. 113 (2017) 87–99. https://doi.org/10.1016/j.carbon.2016.11.024.

[41] D.J. Evans, B.L. Holian, The Nose–Hoover thermostat, J. Chem. Phys. 83 (1985) 4069–4074. https://doi.org/10.1063/1.449071.

[42] R.L. Davidchack, R. Handel, M.V. Tretyakov, Langevin thermostat for rigid body dynamics, J. Chem. Phys. 130 (2009) 234101. https://doi.org/10.1063/1.3149788.

[43] J. Narayan, S. Gupta, A. Bhaumik, R. Sachan, F. Cellini, E. Riedo, Q-carbon harder than diamond, MRS Commun. 8 (2018) 428–436. https://doi.org/10.1557/mrc.2018.35.

[44] S. Gupta, R. Sachan, A. Bhaumik, J. Narayan, Enhanced mechanical properties of Q-carbon nanocomposites by nanosecond pulsed laser annealing, Nanotechnology. 29 (2018) 45LT02. https://doi.org/10.1088/1361-6528/aadd75.

[45] S. Mohapatra, A. Adhikary, K. Ghosh, A. Choudhury, Magnetically Frustrated Quaternary Chalcogenides with Interpenetrating Diamond Lattices, Inorg. Chem. 56 (2017) 7650–7656. https://doi.org/10.1021/acs.inorgchem.7b00121.

[46] R. Ramamurti, V. Shanov, R.N. Singh, S. Mamedov, P. Boolchand, Raman spectroscopy study of the influence of processing conditions on the structure of polycrystalline diamond films, J. Vac. Sci. Technol. A. 24 (2006) 179–189. https://doi.org/10.1116/1.2150228.

[47] R.J. Nemanich, J.T. Glass, G. Lucovsky, R.E. Shroder, Raman scattering characterization of carbon bonding in diamond and diamondlike thin films, J. Vac. Sci. Technol. A. 6 (1988) 1783–1787. https://doi.org/10.1116/1.575297.

[48] A.C. Ferrari, J. Robertson, Origin of the $1150\ensuremath{-}{\mathrm{cm}}^{\ensuremath{-}1}$ Raman mode in nanocrystalline diamond, Phys. Rev. B. 63 (2001) 121405. https://doi.org/10.1103/PhysRevB.63.121405.

[49] R. Pfeiffer, H. Kuzmany, P. Knoll, S. Bokova, N. Salk, B. Günther, Evidence for trans-polyacetylene in nano-crystalline diamond films, Diam. Relat. Mater. 12 (2003) 268–271. https://doi.org/10.1016/S0925-9635(02)00336-9.

[50] R. Akhvlediani, I. Lior, Sh. Michaelson, A. Hoffman, Nanometer rough, sub-micrometer-thick and continuous diamond chemical vapor deposition film promoted by a synergetic ultrasonic effect, Diam. Relat. Mater. 11 (2002) 545–549. https://doi.org/10.1016/S0925-9635(01)00646-X.

[51] V.G. Ralchenko, E.D. Obraztsova, K.G. Korotushenko, A.A. Smolin, S.M. Pimenov, V.G. Pereverzev, Stress in Thin Diamond Films on Various Materials Measured by Microraman Spectroscopy, MRS Online Proc. Libr. Arch. 383 (1995). https://doi.org/10.1557/PROC-383-153.

[52] C.A. Wolden, R.F. Davis, Z. Sitar, J.T. Prater, Low-temperature deposition of optically transparent diamond using a low-pressure flat flame, Diam. Relat. Mater. 6 (1997) 1862–1867. https://doi.org/10.1016/S0925-9635(97)00155-6.

[53] C.T. Kuo, C.R. Lin, H.M. Lien, Origins of the residual stress in CVD diamond films, Thin Solid Films. 290–291 (1996) 254–259. https://doi.org/10.1016/S0040-6090(96)09016-5.

[54] D. Das, R.N. Singh, A review of nucleation, growth and low temperature synthesis of diamond thin films, Int. Mater. Rev. 52 (2007) 29–64. https://doi.org/10.1179/174328007X160245.

[55] J. Narayan, V.P. Godbole, G. Matera, R.K. Singh, Enhancement of nucleation and adhesion of diamond films on copper, stainless steel, and silicon substrates, J. Appl. Phys. 71 (1992) 966–971. https://doi.org/10.1063/1.351322.

[56] Equilibrium between aluminum carbide and nitrogen at high temperatures | Journal of the American Chemical Society, (n.d.). https://doi.org/10.1021/ja01399a011.

[57] J. Narayan, A. Bhaumik, S. Gupta, A. Haque, R. Sachan, Progress in Q-carbon and related materials with extraordinary properties, Mater. Res. Lett. 6 (2018) 353–364. https://doi.org/10.1080/21663831.2018.1458753.

[58] K.V. Ravi, C.A. Koch, H.S. Hu, A. Joshi, The nucleation and morphology of diamond crystals and films synthesized by the combustion flame technique, J. Mater. Res. 5 (1990) 2356–2366. https://doi.org/10.1557/JMR.1990.2356.

[59] M.P. Siegal, T.A. Friedmann, J.P. Sullivan, Diamond and diamond-like carbon films for advanced electronic applications, Sandia National Labs., Albuquerque, NM (United States), 1996. https://doi.org/10.2172/206462.

[60] Q. Wei, J. Sankar, J. Narayan, Structure and properties of novel functional diamond-like carbon coatings produced by laser ablation, Surf. Coat. Technol. 146–147 (2001) 250–257. https://doi.org/10.1016/S0257-8972(01)01394-9.

[61] W.R.L. Lambrecht, C.H. Lee, B. Segall, J.C. Angus, Z. Li, M. Sunkara, Diamond nucleation by hydrogenation of the edges of graphitic precursors, Nature. 364 (1993) 607. https://doi.org/10.1038/364607a0.

[62] O. Ternyak, R. Akhvlediani, A. Hoffman, Study on diamond films with ultra high nucleation density deposited onto alumina, sapphire and quartz, Diam. Relat. Mater. 14 (2005) 323–327. https://doi.org/10.1016/j.diamond.2004.10.033.

[63] Z. Dai, C. Bednarski-Meinke, B. Golding, Heteroepitaxial diamond film growth: the a-plane sapphire–iridium system, Diam. Relat. Mater. 13 (2004) 552–556. https://doi.org/10.1016/j.diamond.2003.11.020.

8. Cost-effective synthesis of novel diamond microstructures and thin films from amorphous and graphitic carbon materials

Ariful Haque[a,#], Yanming Liu[a,b,#], and Jagdish Narayan[a,*]

[a]Department of Materials Science and Engineering, North Carolina State University, Raleigh, NC, 27695.7916, USA.

[b]Key Laboratory of Industrial Ecology and Environmental Engineering, School of Environmental Science and Technology, Dalian University of Technology, Dalian 116024, China.

8.1 Abstract

The synthesis of diamond with different microstructures is important for its various applications. Here we report the synthesis of novel diamond microstructures and coatings, including diamond microfibers, microspheres, tubes and large area thin film, using amorphous and graphitic carbon precursors by hot filament chemical vapor deposition. The characteristics of microstructures depend upon initial carbon precursors and their laser annealing pretreatments to provide nucleation sites for diamond growth. Low-cost and abundant carbon precursors act as diamond nucleation sites and accelerate diamond growth, while laser annealing can further promote further nucleation and growth of diamond. As a result, carbon microfibers are converted to diamond microfibers, while large diamond microspheres are formed from multi-pulse laser annealed carbon microfibers. Both of the diamond structures consist of fivefold twinned microcrystallites. Highly dense and phase-pure diamond films are observed using porous carbon seed, and individual diamond tubes with porous walls are obtained by using carbon nanotube hollow fiber. The electron backscatter diffraction and X-ray diffraction confirm diamond cubic

lattice structure, while sharp diamond peaks (1331-1333 cm^{-1}) in Raman spectra demonstrate the excellent diamond quality of prepared diamond microstructures.

8.2 Introduction

Diamond is one of the most fascinating materials due to its outstanding properties which include broad optical transparency, high mechanical hardness, excellent chemical stability, high thermal conductivity, low background current, and good biocompatibility.[1, 2] These unique properties of diamond make it a promising material for a variety of applications such as optics, electronic devices, tribology, thermal management, biomedicine, sensor, (photo-, electro-) catalysis.[3-7] To realize its wide applications, a simple and low-cost method for the synthesis of high-quality diamond is highly desirable. As different diamond structures are favorable for different applications, steering diamond structures is an effective method to adjust their properties and improve their respective performances. For example, diamond twins show higher hardness than single crystals;[8] a continuous diamond film covering the entire substrate is required for electrochemical applications;[9, 10] diamond structures with high surface areas and exposed sites can enhance its performance in sensor and catalysis applications.[11, 12]

The conventional methods of direct conversion of carbon into diamond requires very high-temperature (~5000K) and pressure (~12 GPa) in the form of diamond particles with limited yield. For the synthesis of diamond coatings, chemical vapor deposition (CVD) integrated with hot-filament, microwave and radio frequency plasma are used, where nano/microdiamond seeds sprinkled on substrates are often used for diamond nucleation.[13, 14] However, diamond is formed with low yield due to limited diamond nucleation and growth rates. Considerable efforts have been made to enhance diamond nucleation and growth. Our previous work shows the use of Q carbon as nucleation seeds which can stimulate diamond nucleation, leading to the rapid growth

of large-area diamond film via hot-filament CVD (HFCVD) on optically transparent substrates.[15] Nonequilibrium methods for direct conversion of nondiamond carbon into nanodiamond include shock-wave,[16] spark plasma sintering,[17] ballistic fracturing, [18] and laser annealing.[19-21] Our recent works show the direct conversion of carbon nanofibers/nanotubes into nanodiamonds by nanosecond laser annealing.[22, 23] The formed nanodiamonds provide effective nucleation sites to facilitate high-quality diamond film growth by HFCVD. The most common approach for preparing novel structured diamond is diamond growth on templates or reactive ion/plasma etching of planar diamond films. Porous diamond structures were obtained by diamond growth on the conductive polymer, SiO_2 spheres and SiC,[24-26] followed by chemical etching of the templates. Diamond nano-/microwires/rods/channels were synthesized with Si and carbon nanotubes as templates.[27-30] Meanwhile, reactive ion/plasma etching of planar diamond films was found to be effective for diamond nano-/microwires/cones/glasses preparation.[31, 32] The major obstacles limiting the preparation of various diamond structures with high quality are the complicated processes of these methods and low yield.

Here we report a promising strategy to synthesize novel structured diamond with high quality from amorphous and graphitic carbon materials via HFCVD. Carbon microfibers, porous carbon, and carbon nanotube hollow fibers are used as nucleation seeds to promote diamond growth. By using different carbon precursors and controlling the pulses of laser annealing carbon precursors, we have successfully prepared diamond with various microstructures, including diamond microfibers and diamond microspheres consisted of fivefold twinned microcrystallites, phase pure diamond film and diamond tube with porous tube wall. Laser annealing is effectively used to facilitate diamond growth and control the diamond morphology. The method proposed here for

novel structured diamond preparation is simple and cost-effective, which overcomes the complicated and time-consuming processes of commonly used methods, and increases the diamond nucleation and growth rate.

8.3 Results and discussion

8.3.1 Diamond microfibers and microspheres synthesized from carbon microfibers

The typical morphology of carbon microfibers used for diamond growth is shown in Fig. 8.1(a). The commercial carbon microfibers were cleaned by ultrasonication and furnace annealing at 800 ºC under Ar. The SEM image in Fig. 8.1(a) shows the smooth surface morphology of pristine carbon microfibers after cleaning. The diameter of the carbon fibers is approximately 7.0 μm. However, nanoparticles are found on the surfaces of carbon microfibers after 1 pulse of laser annealing at ambient temperature and pressure (Fig. 8.1(b)). Our previous works have demonstrated the direct conversion of carbon nanofibers/nanotubes into nanodiamond by laser annealing.[22, 23] The laser annealing melts the carbon nanofibers/nanotubes into a super undercooling state, and quenches rapidly to form nanodiamonds. The nanodiamonds can act as nucleation sites to accelerate diamond growth during HFCVD. Therefore, the nanoparticles observed on the surfaces of carbon microfibers should provide effective nucleation sites for subsequent diamond growth.

Fig. 8.2 shows the SEM images of diamond microfibers prepared from carbon microfibers using 3 h HFCVD. The carbon microfibers are completely converted to diamond microfibers even without laser annealing (Fig. 8.2(a-b)). It is interesting to note that the synthesized diamond crystallites are five-fold diamond twins with average grain size of ~2.0 μm. The diamond crystallites are preferentially nucleated at the carbon microfibers. The three-dimensional diamond growth enables the diamond microcrystallites to coalesce and form five-fold twinned diamond

microfibers. The diameter of diamond microfibers is approximately 2.6 μm. Here the carbon microfibers act as nucleation sites and facilitate the subsequent diamond growth during HFCVD, which leads to the formation of large diamond microcrystallites in a shorter time than conventional CVD techniques. As expected, diamond nucleation and growth can be further controlled by using laser annealing. As shown in Fig. 8.2(c-d), the formed diamond microfibers present significantly enhanced density of diamond twin microcrystallites when carbon microfibers are treated by 1 pulse of laser annealing. The diameter of diamond microfibers (3.0-3.5 μm) from the laser annealed carbon precursor is also larger than those without laser annealing. Laser annealing of carbon microfibers generates more nucleation sites (as revealed by the nanoparticles formed in Fig. 8.1(b)) for diamond growth, leading to higher diamond density and larger diamond microcrystallite size. The mechanism for fivefold diamond formation has been reported,[33, 34] which reveals that the origin of fivefold twin microcrystallites is the gap from ~70.5º subtended microcrystallites ($5 \times 70.5^\circ \approx 352.5 < 360^\circ$). For diamond microcrystallites without the gap, the misfit angle probably accommodated by elastic deformation and defects such as dislocations. Fivefold microcrystallites are nucleated at an edge dislocation. Once first microcrystallite is nucleated, the twinning process will occur, leading to the formation of others.

To elucidate the role of pulsed laser annealing on the formation of diamond, carbon microfibers with 5 and 10 pulses of laser annealing were used as precursors for diamond growth via 3 h HFCVD. The SEM images in Fig. 8.3(a-b) show the formation of large diamond microspheres accompanied with diamond microfibers from 5 pulses of laser irradiated carbon microfibers. The microsphere wall is a porous network composed of interconnected fivefold diamond twin microcrystallites. The size of diamond microspheres is in-between 10-20 μm. High magnification SEM image (inset in Fig. 8.3(b)) shows the existence of few diamond nanocrystallites on the

surface of diamond twins. When laser annealing is increased to 10 pulses, more diamond microspheres and less diamond microfibers are formed from carbon microfibers with the same HFCVD time (Fig. 8.3(c-d). It is noted that diamond nanocrystallites with a higher number density are present on the fivefold microcrystallite surfaces (inset in Fig. 8.3(d)). By increasing the number of laser pulses, the carbon microfibers can generate carbon microparticles during HFCVD and provide more nucleation sites for diamond growth. As diamond nucleates around the surfaces of formed carbon microparticles (Fig. S8.1), the rapid three-dimensional diamond growth results in the coalescence of fivefold diamond microcrystallites to form large diamond microspheres. Meanwhile, secondary nucleation occurs on the already formed fivefold diamond microcrystallites, leading to the formation of diamond nanocrystallites. The increased density of diamond nanocrystallites with 10 laser shots can be explained by that more laser pulses accelerate the diamond growth rate and promote secondary nucleation. These data provide a direct evidence that diamond growth rate and the formed diamond morphologies can be adjusted by controlling the laser annealing treatment of carbon microfibers.

Raman spectroscopy is employed to investigate the bonding characteristics of carbon microfibers, diamond microfibers, and microspheres. Two wide peaks centered at 1342 cm^{-1} and 1576 cm^{-1} are clearly observed in the Raman spectrum of carbon microfibers (Fig. 8.4(a)), corresponding to D and G vibrational modes of amorphous carbon, respectively. After carbon microfibers conversion by HFCVD, strong and sharp peaks appear at ~1332 cm^{-1} (D band) in the Raman spectra of both diamond microfibers and microspheres (Fig. 8.4(b)), which represent the characteristic diamond bonds. The additional peaks at ~1540-1560 cm^{-1} (G band), which are related to sp^2 carbon, are also present in their Raman spectra. As expected, the carbon peak is very

weak due to the presence of less graphitic content. These Raman data demonstrate the high diamond quality in the prepared diamond microfibers and microspheres.

The peak intensity ratio of D band and G band (I_D/I_G) is measured to reveal the nondiamond content. The I_D/I_G value of diamond microfibers prepared without laser annealing is 1.25 (Table S8.1), which increases slightly to 1.28 with 1 pulse of laser annealing. For diamond microspheres prepared from 5 pulses of laser annealed carbon microfibers, the I_D/I_G values is further increased to 1.42, highlighting their significantly reduced nondiamond component. However, the I_D/I_G values decrease to 1.28 with 10 pulses of laser annealing, which can be explained by the existence of a small amount of precursor residue inside the diamond microspheres. The nondiamond content is calculated by the equation $C_{nd}=1/(1+75\times I_D/I_G)\times 100\%$, which is in-between 1.03-1.05% for diamond microfibers and 0.93-1.03% for diamond microspheres. Such low nondiamond contents confirm their high diamond quality.

8.3.2 Diamond film synthesized from porous carbon

The morphology of mesoporous carbon used for diamond preparation is characterized by SEM and TEM images (Fig. 8.5(a-b) and S8.2). It is evident that abundant pores are presented on the surface of porous carbon film (Fig. 8.5(a-b)). Mesostructure with both tubular pores and interconnected pores is observed from its TEM image (Fig. 8.5(b)). A thin layer of porous carbon was drop-coated on Si substrate using porous carbon suspension (Fig. S8.3). The obtained porous carbon on Si was used as nuclei for diamond preparation by HFCVD. As shown in Fig. 8.5 (c-d), a dense and uniform film with well-faceted diamond microcrystallites is obtained after 3 h of HFCVD. The Si substrate is completely covered by the continuous diamond film without any crack or delamination. Fivefold diamond twin microcrystallites can be clearly observed (Fig. 8.5(d)). Diamond deposition on substrate usually uses micro-/nanodiamond as nucleation seeds. Here we

use the low-cost porous carbon to replace micro-/nanodiamond seeds. More importantly, a dense and continuous diamond film is formed in a short HFCVD time with high yield when porous carbon is used as a precursor, highlighting porous carbon can significantly enhance diamond nucleation and growth rate as well as diamond yield.

Raman spectroscopy is used to determine the characteristics of the porous carbon precursor and the quality of the prepared diamond film. Raman peaks appear at 1340 cm^{-1} (D band) and 1580 cm^{-1} (G band) for initial porous carbon, which illustrates its graphitic carbon feature. After HFCVD, only characteristic diamond peak at ~1333 cm^{-1} is observed, demonstrating that the phase-pure diamond film has been prepared from porous carbon without any pretreatment. Diamond preparation using carbon microfibers and porous carbon was performed under the same HFCVD conditions. A small amount of nondiamond carbon exists in the diamond microfibers and microsphere synthesized from carbon microfibers, while it is barely detected for the diamond film synthesized from porous carbon. The formed dense and phase-pure diamond film is probably attributed to the porous structure of carbon precursor, where its capillary effect can induce partial high pressure and trap gas molecules (H_2/CH_4) inside,[35, 36] thereby facilitating precursor dissociation and increasing diamond nucleation and growth rates.

8.3.3 Diamond tube synthesized from carbon nanotube hollow fibers

Fig. 8.7(a-b) show the SEM images of carbon nanotube (CNT) hollow fiber used for diamond synthesis. The CNT hollow fiber consists of interconnected CNTs. It has an outer diameter of ~740 μm and a wall thickness of ~150 μm. By using CNT hollow fiber as a precursor for diamond synthesis, diamond tube with relative high diamond coverage is obtained after 6 h HFCVD (Fig. 8.7 (c-d)), highlighting that CNT hollow fiber is also effective for promoting diamond nucleation and growth. A porous network containing microcrystallites with average grain sizes of ~2.9 μm is

clearly observed on the diamond tube wall. By laser annealing of CNT hollow fiber with 5 laser pulses, diamond tube with porous tube wall is still obtained after HFCVD (Fig. 8.7(e)). However, the diamond coverage on the tube surface is significantly increased, and the size of individual microcrystallites (~3.8 μm) is observed to be larger compared to that in the tube without laser annealing. Thus, diamond nucleation and growth rates are further increased by laser annealing of CNT hollow fiber, which agrees well with the results of diamond preparation from carbon microfibers.

Fig. 8.8 shows the Raman spectrum of CNT hollow fiber and diamond tubes. Raman peaks appear at 1345 cm^{-1} (D band) and 1575 cm^{-1} (G band) for initial CNT hollow fiber (Fig. 8.8(a)), illustrating its graphitic carbon feature. After HFCVD, the characteristic diamond peak appears at ~1331 cm^{-1} with high intensity for both diamond tubes (Fig. 8.8(b)). The peaks associated with graphitic carbon residue (1545-1560 cm^{-1}) are very week. The nondiamond content calculated from the I_D/I_G value is ~0.89% for diamond tube without laser annealing, which decreases to 0.78% for the one synthesized from 5 pulses laser annealed CNT hollow fiber. It is noted that both diamond tubes present low nondiamond content, illustrating high-quality diamond. It also confirms that laser annealing can promote diamond growth with improved quality.

8.4 Conclusions

Various novel diamond microstructures with high diamond quality have been prepared from low-cost amorphous and graphitic carbon materials by HFCVD. Carbon microfibers, porous carbon and CNT hollow fibers are effective for promoting diamond nucleation and growth during HFCVD, which can be further accelerated by laser annealing. The structures of the prepared diamond are dependent on the type of carbon precursors and laser annealing treatment. Diamond microfibers, consist of fivefold diamond twin microcrystallites, are obtained from carbon

microfibers by HFCVD. By multi-pulse laser annealing of carbon microfibers, the morphology changes to large diamond microspheres, which is also composed of fivefold diamond twins. A dense and phase-pure diamond film is synthesized from porous carbon, while diamond tube with porous structure is obtained from CNT hollow fibers. The methods presented here for novel structured diamond preparation and morphology control is simple and cost-effective, which will open a new frontier towards better design and understanding of diamond growth with desired nano-/microstructures and high quality for a variety of applications.

8.5 Experimental methods

Preparation of porous carbon and CNT hollow fibers. Porous carbon was prepared by the carbonization of phenol-formaldehyde resin.[37] Briefly, 0.53 mL 20 wt% NaOH was added into 3.05 g melted phenol, followed by slowly adding 5.0 mL formaldehyde solution (37 wt%). The obtained mixture solution was heated at 70 ºC for 1 h. The entire process was kept under stirring. After cooling to room temperature, the solution pH was adjusted to 7.0 by 0.6 M HCl, and vacuum dried at 50 ºC to form resin. Porous carbon was obtained by heating the resin at 100 ºC for 24 h and pyrolyzing the thermosetted resin at 750 ºC under Ar.

The CNT hollow fibers were prepared by wet-spinning method.[38] The commercial multi-wall CNTs (diameter of 60-100 nm, Shenzhen Nanotech Port Co. Ltd.) were oxidized by HNO_3 solution. The oxidized CNTs, dimethylacetamide and polyvinyl butyral were mixed with mass ratio of 2:1:17. The obtained suspension was dispensed by a spinneret equipped with an injection pump. The formed CNT hollow fibers were directly immersed into a water coagulation bath. Dimethylacetamide/water solution (v:v=75:25) was used as bore-fluid. The obtained CNT hollow fibers were dried and annealed at 800 °C under Ar.

Preparation of diamond microstructures. The commercial carbon microfibers were cleaned by ultrasonication in acetone solution and furnace annealing at 800 °C for 2 h under Ar. The cleaned carbon microfibers and CNT hollow fibers were pretreated by ArF laser annealing with the following conditions: wavelength 193 nm, pulse duration of 20 ns, energy density of ~0.65-0.75 J cm^{-2}. The above-mentioned carbon materials with or without laser annealing were used as precursors for diamond synthesis via HFCVD. The detailed HFCVD conditions are as follows: substrate temperature of 700 °C, tungsten filament temperature of ~2000 °C, gas mixture of 2 sccm CH_4/100 sccm H_2, the pressure of 20 Torr, deposition time 3-6 h.

Characterization. The morphology of carbon precursors and prepared diamond microstructures were characterized by SEM images acquired on a FEI Verios 460L SEM and TEM images recorded on FEI-Tecnai G^2 20. Their Raman spectra were measured on a WITec confocal Raman microscope system (Alpha 3000 M, 532 nm source) with a triple monochromator. A crystalline Si was used to calibrate the Raman system before the sample test. During Raman spectrum acquisition, an optimum laser power (~40 mW) was used to illuminate the sample and avoid heating.

8.6 Figures

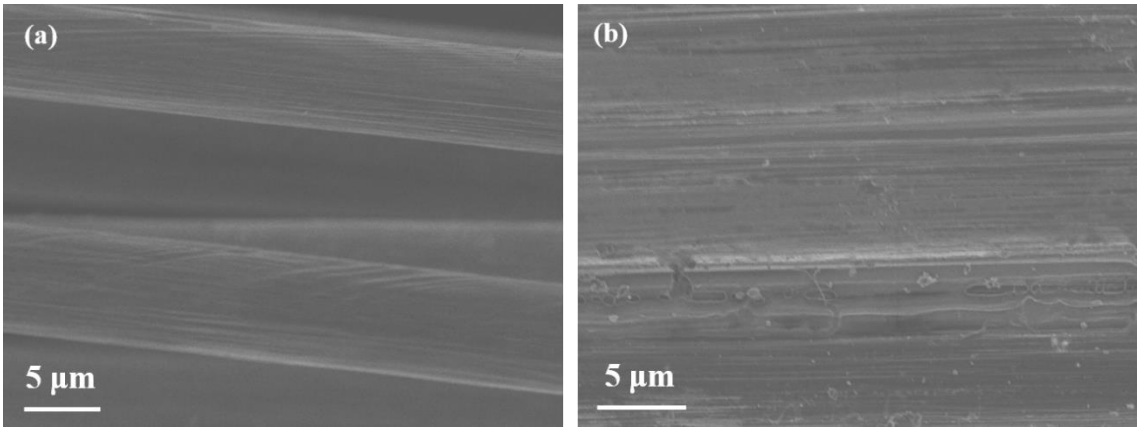

Figure 8. 1**:** SEM images of carbon microfibers: (a) without laser irradiation and (b) with 1 pulse of laser irradiation.

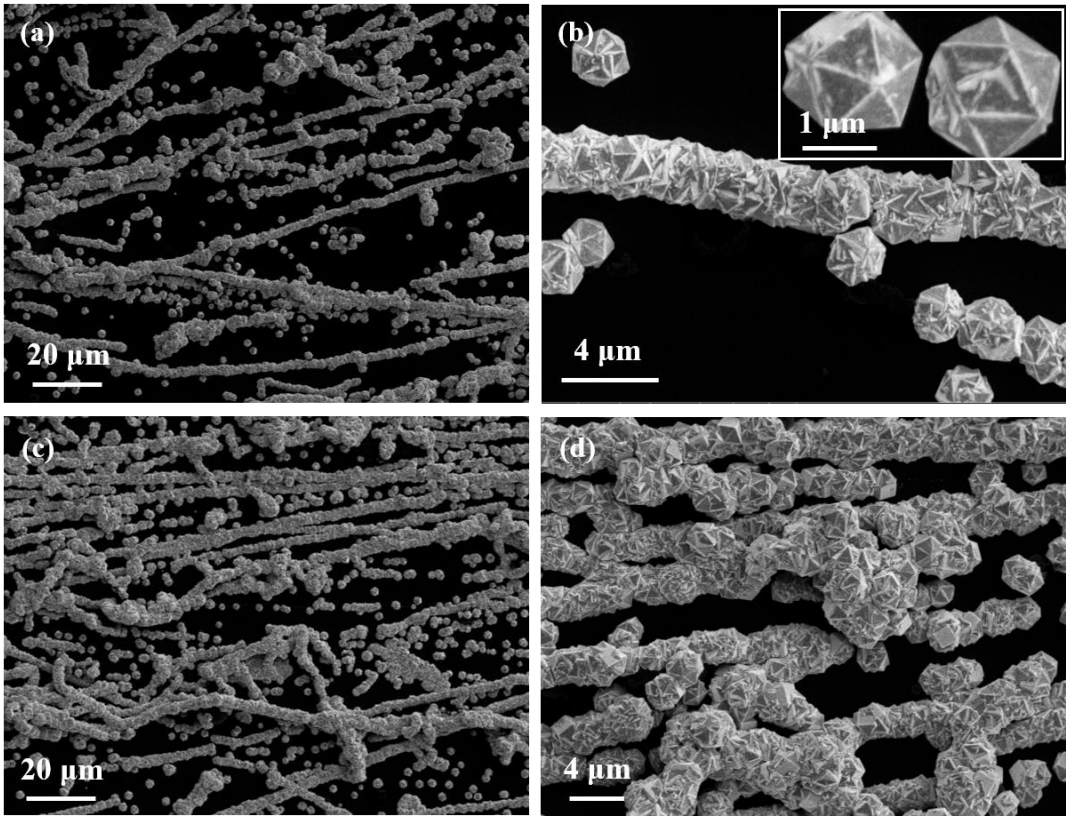

Figure 8. 2**:** SEM images of diamond microfibers synthesized from carbon microfibers: (a, b) without laser annealing and (c, d) with 1 pulse of laser annealing.

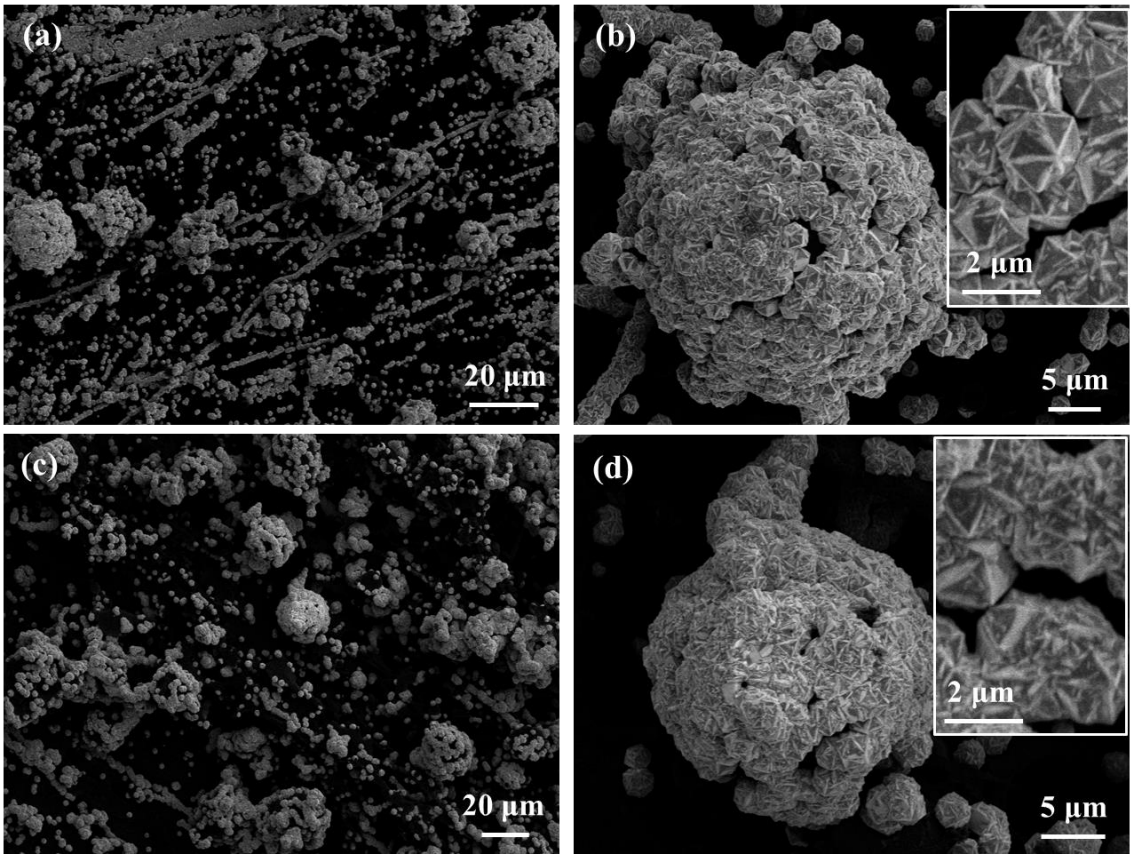

Figure 8. 3**:** SEM images of diamond synthesized from laser annealed carbon microfibers: (a, b) 5 laser pulses and (c, d) 10 laser pulses.

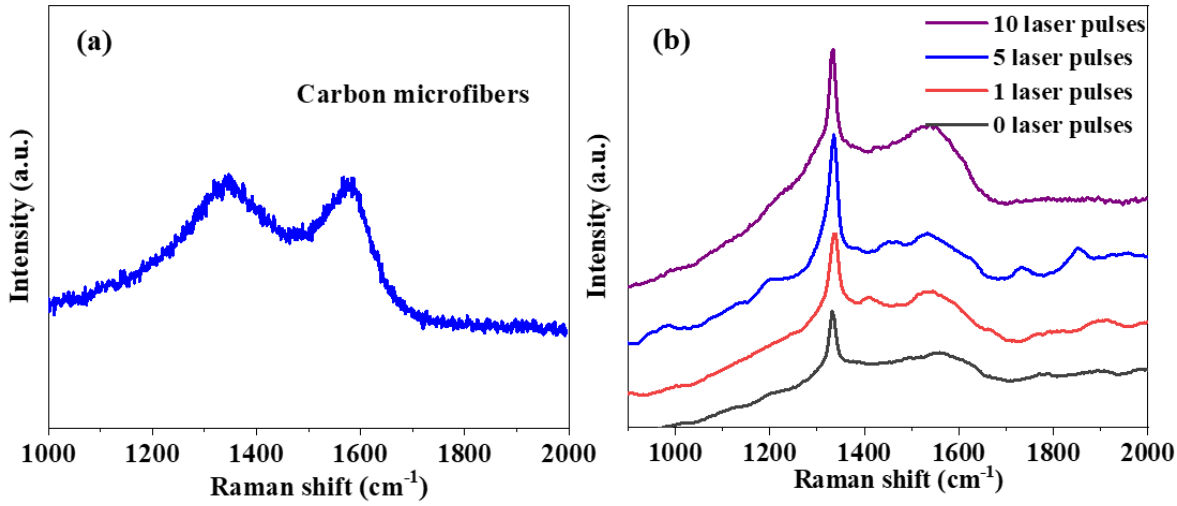

Figure 8. 4**:** Raman spectra of (a) carbon microfibers and (b) diamond synthesized from carbon microfibers with 0-10 pulses of laser annealing.

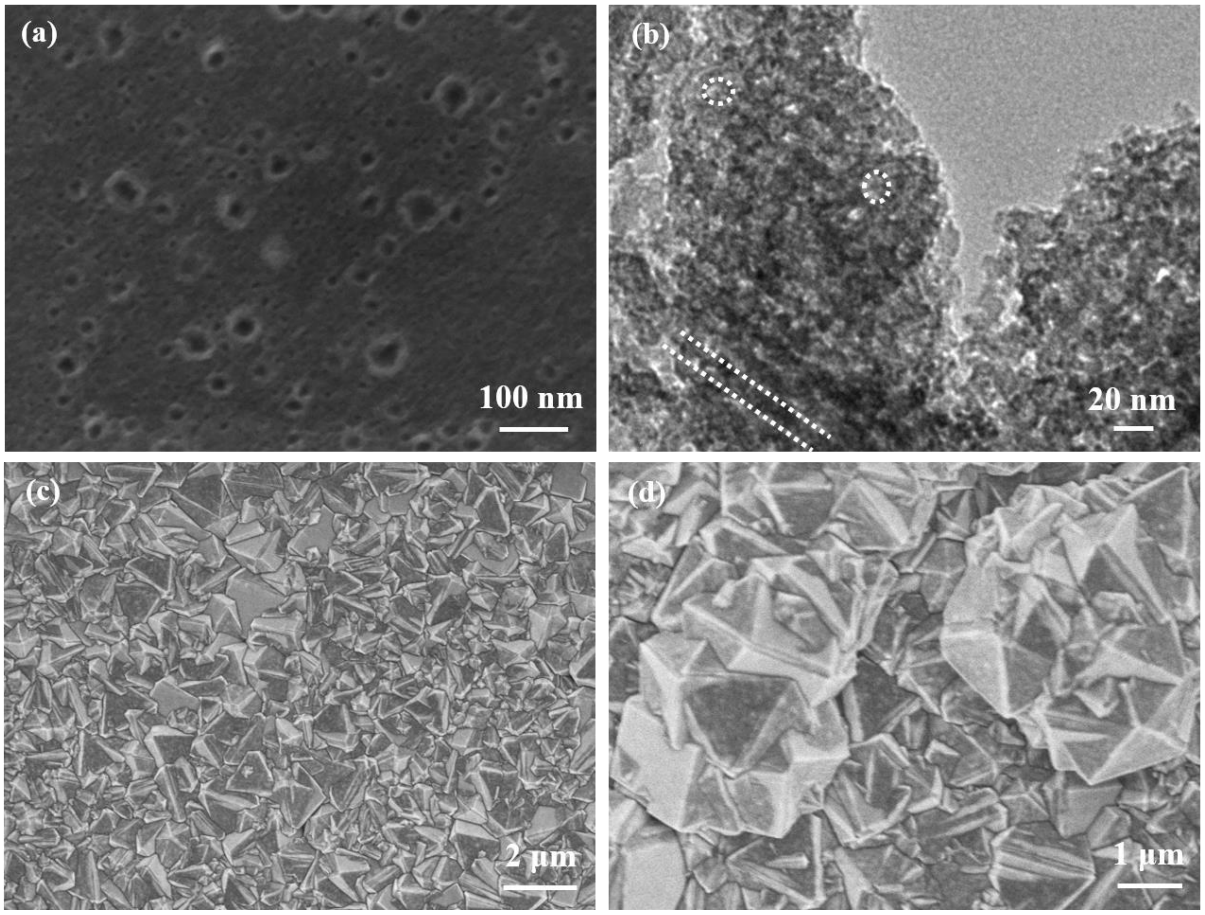

Figure 8. 5**:** (a) SEM image and (b) TEM image of porous carbon, (c, d) SEM images of diamond film synthesized from porous carbon at different magnifications.

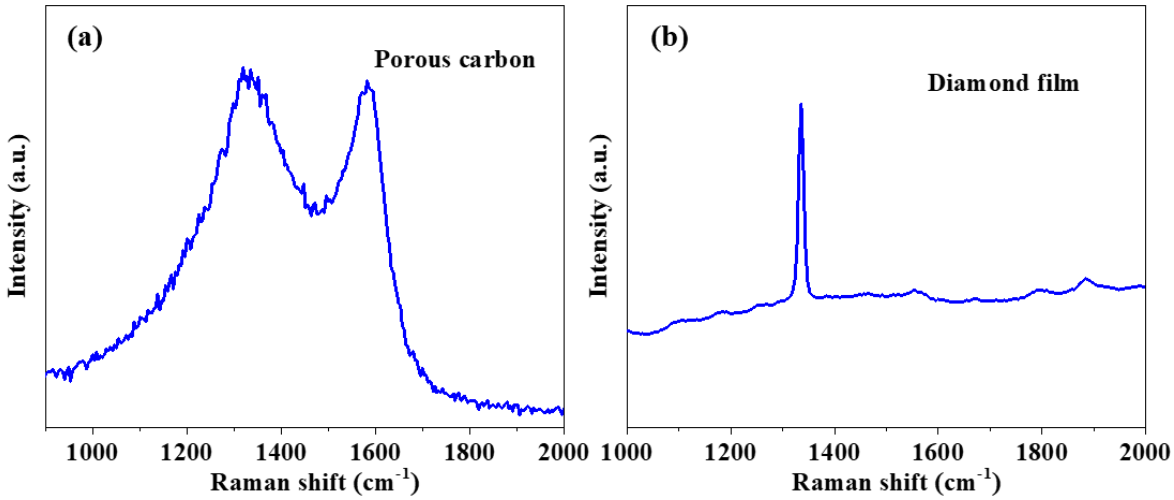

Figure 8. 6**:** Raman spectra of (a) porous carbon and (b) diamond synthesized from porous carbon.

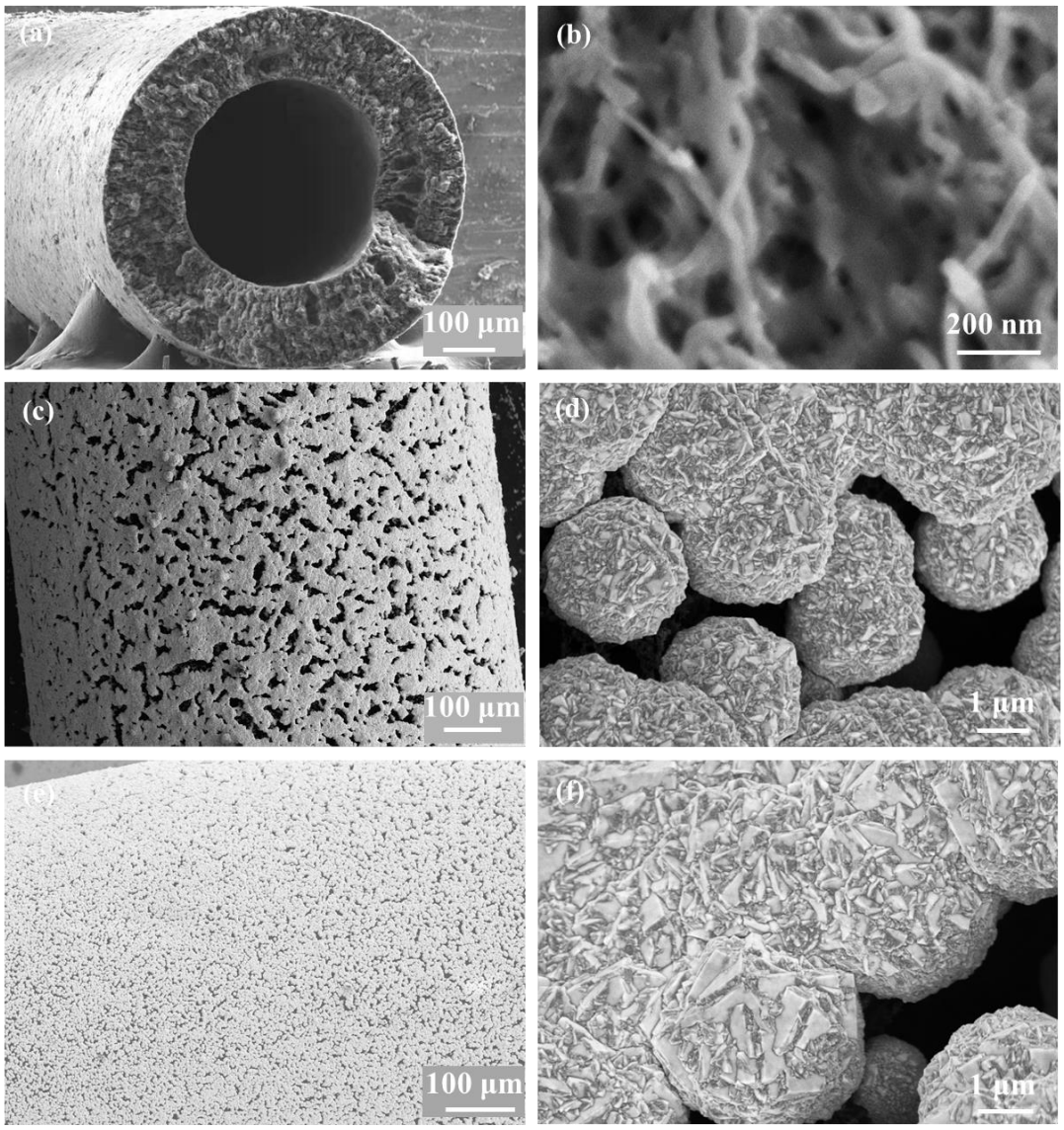

Figure 8. 7**:** SEM images of (a, b) CNT hollow fiber, diamond tubes synthesized from CNT hollow fibers by 6 h HFCVD: (c, d) without laser annealing and (e, f) with 5 pulses of laser annealing.

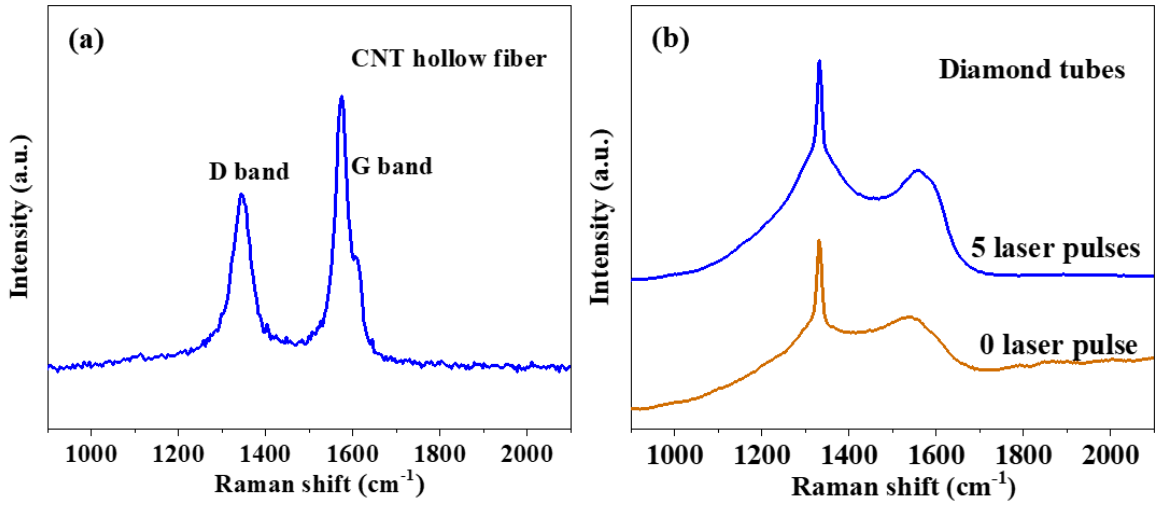

Figure 8. 8**:** Raman spectra of (a) CNT hollow fiber and (b) diamond tubes synthesized from CNT hollow fiber without and with 5 pulses of laser annealing.

References

[1] V.N. Mochalin, O. Shenderova, D. Ho, Y. Gogotsi, The properties and applications of nanodiamonds, Nat Nanotechnol 7(1) (2011) 11-23.

[2] Y. Lin, X. Sun, D.S. Su, G. Centi, S. Perathoner, Catalysis by hybrid sp(2)/sp(3) nanodiamonds and their role in the design of advanced nanocarbon materials, Chem Soc Rev 47(22) (2018) 8438-8473.

[3] R.E.E. A. Sipahigil, D. D. Sukachev, M. J. Burek, J. Borregaard, M. K. Bhaskar, C. T. Nguyen, J. L. Pacheco, H. A. Atikian, C. Meuwly, R. M. Camacho, F. Jelezko, E. Bielejec, H. Park, M. Lončar, M. D. Lukin, An integrated diamond nanophotonics platform for quantum-optical networks, Science 354 (2016) 847-850.

[4] P. Maletinsky, S. Hong, M.S. Grinolds, B. Hausmann, M.D. Lukin, R.L. Walsworth, M. Loncar, A. Yacoby, A robust scanning diamond sensor for nanoscale imaging with single nitrogen-vacancy centres, Nat Nanotechnol 7(5) (2012) 320-4.

[5] N. Yang, S. Yu, J.V. Macpherson, Y. Einaga, H. Zhao, G. Zhao, G.M. Swain, X. Jiang, Conductive diamond: synthesis, properties, and electrochemical applications, Chem Soc Rev 48(1) (2019) 157-204.

[6] N. Wachter, C. Munson, R. Jarosova, I. Berkun, T. Hogan, R.C. Rocha-Filho, G.M. Swain, Structure, Electronic Properties, and Electrochemical Behavior of a Boron-Doped Diamond/Quartz Optically Transparent Electrode, ACS Appl Mater Interfaces 8(42) (2016) 28325-28337.

[7] T. Sun, F.A.M. Koeck, C. Zhu, R.J. Nemanich, Combined visible light photo-emission and low temperature thermionic emission from nitrogen doped diamond films, Applied Physics Letters 99(20) (2011).

[8] Q. Huang, D. Yu, B. Xu, W. Hu, Y. Ma, Y. Wang, Z. Zhao, B. Wen, J. He, Z. Liu, Y. Tian, Nanotwinned diamond with unprecedented hardness and stability, Nature 510(7504) (2014) 250-3.

[9] C.A. Martinez-Huitle, M.A. Rodrigo, I. Sires, O. Scialdone, Single and Coupled Electrochemical Processes and Reactors for the Abatement of Organic Water Pollutants: A Critical Review, Chem Rev 115(24) (2015) 13362-407.

[10] Y. Liu, Y. Zhang, K. Cheng, X. Quan, X. Fan, Y. Su, S. Chen, H. Zhao, Y. Zhang, H. Yu, M.R. Hoffmann, Selective Electrochemical Reduction of Carbon Dioxide to Ethanol on a Boron- and Nitrogen-Co-doped Nanodiamond, Angew Chem Int Ed Engl 56(49) (2017) 15607-15611.

[11] L.W. Daibing Luo, and Jinfang Zhi, Fabrication of Boron-Doped Diamond Nanorod Forest Electrodes and Their Application in Nonenzymatic Amperometric Glucose Biosensing, ACS Nano 3 (2009) 2121-2128.

[12] T.A. Silva, H. Zanin, P.W. May, E.J. Corat, O. Fatibello-Filho, Electrochemical performance of porous diamond-like carbon electrodes for sensing hormones, neurotransmitters, and endocrine disruptors, ACS Appl Mater Interfaces 6(23) (2014) 21086-92.

[13] D. Das, R.N. Singh, A review of nucleation, growth and low temperature synthesis of diamond thin films, International Materials Reviews 52(1) (2013) 29-64.

[14] J.J. Gracio, Q.H. Fan, J.C. Madaleno, Diamond growth by chemical vapour deposition, Journal of Physics D: Applied Physics 43(37) (2010).

[15] A. Haque, P. Pant, J. Narayan, Large-area diamond thin film on Q-carbon coated crystalline sapphire by HFCVD, Journal of Crystal Growth 504 (2018) 17-25.

[16] O.A. Shenderova, I.I. Vlasov, S. Turner, G. Van Tendeloo, S.B. Orlinskii, A.A. Shiryaev, A.A. Khomich, S.N. Sulyanov, F. Jelezko, J. Wrachtrup, Nitrogen Control in Nanodiamond Produced by Detonation Shock-Wave-Assisted Synthesis, The Journal of Physical Chemistry C 115(29) (2011) 14014-14024.

[17] F. Zhang, J. Shen, J. Sun, Y.Q. Zhu, G. Wang, G. McCartney, Conversion of carbon nanotubes to diamond by spark plasma sintering, Carbon 43(6) (2005) 1254-1258.

[18] S. Ozden, L.D. Machado, C. Tiwary, P.A. Autreto, R. Vajtai, E.V. Barrera, D.S. Galvao, P.M. Ajayan, Ballistic Fracturing of Carbon Nanotubes, ACS Appl Mater Interfaces 8(37) (2016) 24819-25.

[19] L. Zhu, M. Yao, J. Dong, K. Hu, R. Liu, C. Gong, Y. Wang, B. Liu, Direct Conversion of Graphene Aerogel into Low-Density Diamond Aerogel Composed of Ultrasmall Nanocrystals, The Journal of Physical Chemistry C 122(24) (2018) 13193-13198.

[20] A. Bhaumik, J. Narayan, Nano-to-micro diamond formation by nanosecond pulsed laser annealing, Journal of Applied Physics 126(12) (2019).

[21] R. Ye, X. Han, D.V. Kosynkin, Y. Li, C. Zhang, B. Jiang, A.A. Marti, J.M. Tour, Laser-Induced Conversion of Teflon into Fluorinated Nanodiamonds or Fluorinated Graphene, ACS Nano 12(2) (2018) 1083-1088.

[22] J. Narayan, A. Bhaumik, R. Sachan, A. Haque, S. Gupta, P. Pant, Direct conversion of carbon nanofibers and nanotubes into diamond nanofibers and the subsequent growth of large-sized diamonds, Nanoscale 11(5) (2019) 2238-2248.

[23] A. Haque, R. Sachan, J. Narayan, Synthesis of diamond nanostructures from carbon nanotube and formation of diamond-CNT hybrid structures, Carbon 150 (2019) 388-395.

[24] F. Gao, M.T. Wolfer, C.E. Nebel, Highly porous diamond foam as a thin-film micro-supercapacitor material, Carbon 80 (2014) 833-840.

[25] C. Hébert, E. Scorsone, M. Mermoux, P. Bergonzo, Porous diamond with high electrochemical performance, Carbon 90 (2015) 102-109.

[26] H. Zhuang, N. Yang, H. Fu, L. Zhang, C. Wang, N. Huang, X. Jiang, Diamond network: template-free fabrication and properties, ACS Appl Mater Interfaces 7(9) (2015) 5384-90.

[27] M. Chandran, S. Elfimchev, S. Michaelson, R. Akhvlediani, O. Ternyak, A. Hoffman, Fabrication of microchannels in polycrystalline diamond using pre-fabricated Si substrates, Journal of Applied Physics 122(14) (2017).

[28] C. Hébert, J.P. Mazellier, E. Scorsone, M. Mermoux, P. Bergonzo, Boosting the electrochemical properties of diamond electrodes using carbon nanotube scaffolds, Carbon 71 (2014) 27-33.

[29] H. Zanin, P.W. May, D.J. Fermin, D. Plana, S.M. Vieira, W.I. Milne, E.J. Corat, Porous boron-doped diamond/carbon nanotube electrodes, ACS Appl Mater Interfaces 6(2) (2014) 990-5.

[30] Y. Liu, S. Chen, X. Quan, H. Yu, Efficient Electrochemical Reduction of Carbon Dioxide to Acetate on Nitrogen-Doped Nanodiamond, J Am Chem Soc 137(36) (2015) 11631-6.

[31] S. Kunuku, K.J. Sankaran, C.Y. Tsai, W.H. Chang, N.H. Tai, K.C. Leou, I.N. Lin, Investigations on diamond nanostructuring of different morphologies by the reactive-ion etching process and their potential applications, ACS Appl Mater Interfaces 5(15) (2013) 7439-49.

[32] C. Terashima, K. Arihara, S. Okazaki, T. Shichi, D.A. Tryk, T. Shirafuji, N. Saito, O. Takai, A. Fujishima, Fabrication of vertically aligned diamond whiskers from highly boron-doped diamond by oxygen plasma etching, ACS Appl Mater Interfaces 3(2) (2011) 177-82.

[33] J. Narayan, A.R. Srivatsa, K.V. Ravi, Mechanism of formation of 〈110〉 oriented fivefold microcrystallites in diamond films, Applied Physics Letters 54(17) (1989) 1659-1661.

[34] Y.M. Seiichiro Matsumoto, Electron microscopic observation of diamond particles grown from the vapour phase, J. Mater. Sci 18 (1983) 1785-1793.

[35] C.H. Hsu, S.G. Cloutier, S. Palefsky, J. Xu, Synthesis of diamond nanowires using atmospheric-pressure chemical vapor deposition, Nano Lett 10(9) (2010) 3272-6.

[36] C. Zhang, Y. Xu, P. Lu, X. Zhang, F. Xu, J. Shi, Capillary Effect-Enabled Water Electrolysis for Enhanced Electrochemical Ozone Production by Using Bulk Porous Electrode, J Am Chem Soc 139(46) (2017) 16620-16629.

[37] Y. Meng, D. Gu, F. Zhang, Y. Shi, H. Yang, Z. Li, C. Yu, B. Tu, D. Zhao, Ordered mesoporous polymers and homologous carbon frameworks: amphiphilic surfactant templating and direct transformation, Angew Chem Int Ed Engl 44(43) (2005) 7053-9.

[38] X. Fan, Y. Liu, X. Quan, S. Chen, Highly Permeable Thin-Film Composite Forward Osmosis Membrane Based on Carbon Nanotube Hollow Fiber Scaffold with Electrically Enhanced Fouling Resistance, Environ Sci Technol 52(3) (2018) 1444-1452.

Supplementary Information

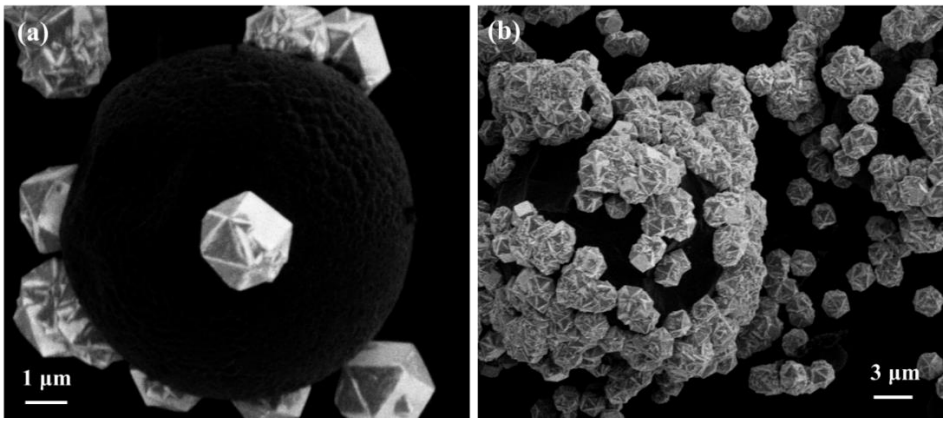

Figure S8.1: SEM images of diamond prepared from laser annealed carbon microfibers with (a) 1 laser pulse and (b) 5 laser pulses.

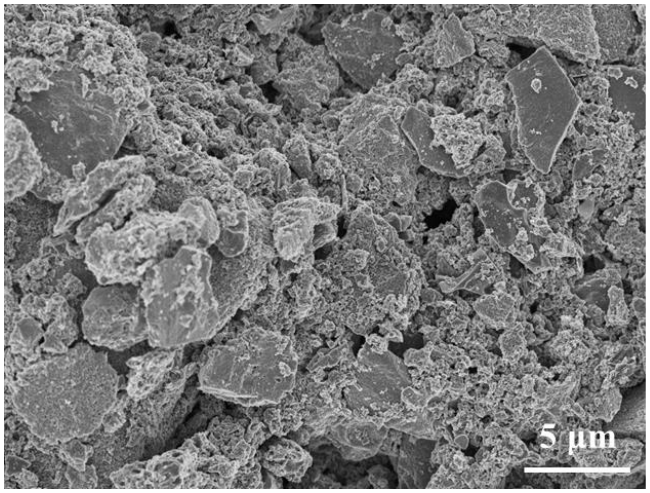

Figure S8.2: SEM images of porous carbon.

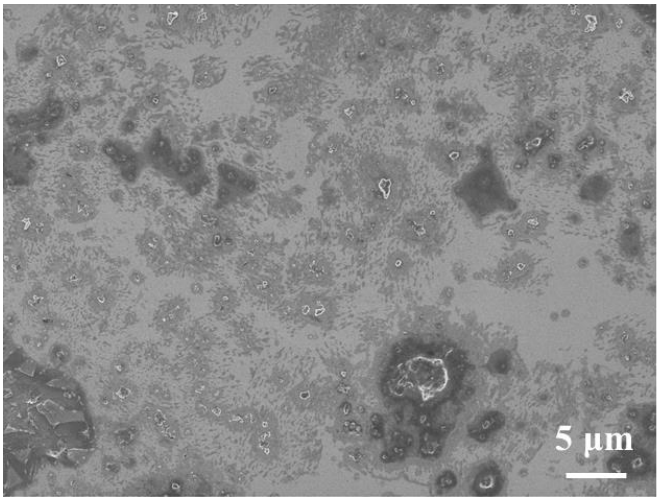

Figure S8.3: The SEM image of porous carbon dispersed on Si substrate.

Table S8.1. The intensity ratios of D and G peaks for different diamond structures.

Samples	I_D/I_G	% of sp^2 carbon
Diamond microfibers-0 PLA	1.25	1.05%
Diamond microfibers-1 PLA	1.28	1.03%
Diamond microspheres-5 PLA	1.42	0.93%
Diamond microspheres-10 PLA	1.28	1.03%
Diamond tubes-0 PLA	1.47	0.89%
Diamond tubes-5 PLA	1.70	0.78%

9. Synthesis of novel conductive tubular diamond structures with high electrochemical performance using CNT hollow fibers

Ariful Haque,[a,#] Yanming Liu,[a,b,#] Xinfei Fan[c] and Jagdish Narayan[a,*]

[a]*Department of Materials Science and Engineering, North Carolina State University, Raleigh, NC, 27695.7916, USA.*

[b]*Key Laboratory of Industrial Ecology and Environmental Engineering (Ministry of Education), School of Environmental Science and Technology, Dalian University of Technology, Dalian 116024, China.*

[c]*College of Environmental Science and Engineering, Dalian Maritime University, Dalian 116026, China.*

9.1 Abstract

Conductive diamond structures with high surface area are very appealing for various applications but their synthesis presents a great challenge. Here we report a simple one-step method for the synthesis of conductive diamond tube with porous tube wall from carbon nanotube (CNT) hollow fibers via pulsed laser annealing and hot filament chemical vapor deposition (HFCVD). These diamond tubes exhibit high double layer capacitances of 11.65-18.07 mF cm^{-2}, three orders of magnitudes higher than the equivalent flat diamond films. The scanning electron microscopy shows the presence of diamond microspheres composed of both microcrystallites and nanocrystallites on the entire tube after 3-6 h HFCVD. The number density of diamond, the average size of diamond microspheres, and nanocrystallite content on the microspheres can be controlled by HFCVD time and laser annealing parameters of CNT hollow fibers. The electron back scattered diffraction analysis shows the crystallographic orientation of the prepared diamond

along <101>. Raman spectra show a sharp characteristic diamond peak at ~1332 cm^{-1}, corresponding to unstrained high quality diamond. The magnificent electrochemical performances of these diamond tubes are explained by their significantly enhanced electroactive surface area and the presence of a very small fraction (0.73%-1.03%) of sp^2 carbon in diamond tubes for electron conduction.

9.2 Introduction

Diamond materials have exceptional optical and mechanical properties such as broad optical transparency, high thermal conductivity, mechanical hardness and biocompatibility [1–3], which have attracted great interests in the fields of quantum photonics, electron field emitters, nanoelectronics, sensor, drug delivery etc [4–9]. For optimally conductive diamond materials, they also possess unique electrochemical properties such as wide potential window, good electrocatalytic activity, and chemical stability [10,11]. Their applications can be widely expanded to the areas of electrocatalysis, electrosynthesis, water treatment, and energy storage and conversion [12,13]. The respective performances for applications can be optimized by the material structures and compositions [14,15]. Diamond materials with high surface areas, porous structure and good conductivity are highly desirable for various electrochemical applications, which can provide plenty of exposed active sites, fast mass transfer and rapid electron transfer rates for redox systems, leading to enhanced electrochemical performance.

The most common studied diamond structure is flat diamond film consisted of microcrystallites and nanocrystallites on silicon or metal substrates. Many efforts have been made to synthesize diamond materials with increased surface areas and/or porous structures, including diamond foam (also called network or porous diamond) with pore size ranging from nanometers to micrometers, nano-/microwires (also called rods, needles), cones, grasses etc [16]. Diamond

foam has been prepared by depositing diamond film on SiO_2 template and removing the template by chemical etching [17,18], and diamond films have been grown homoepitaxially on porous polymer and SiC to obtain composite materials [19,20]. Diamond nano-/microwires and cones are usually synthesized by top down and bottom up methods. In a top down method, diamond nano/micro-structure is obtained by reactive ion etching or plasma etching of diamond flat films with etching masks [21,22]. The gases used for etching are oxygen/tetrafluoromethane, argon/hydrogen and oxygen. The structures of as-prepared diamond are dependent upon the masks, etching conditions, initial morphologies, and microstructures of diamond films. In a bottom up technique, diamond nano-/microwires and cones are prepared from depositing diamond crystallites on templates such as Si nanowires/microrods [23,24], where the characteristic of as-prepared structures are determined by the morphology of templates. During these deposition processes, doping has been proved to be effective for enhancing diamond conductivity [24,25]. Moreover, these methods are complicated, time consuming, and cumbersome with low yield. Simple, template-free method with low-cost and high-throughput are needed for conductive diamond synthesis.

An alternative method for nano-/micro-structured diamond preparation is conversion of graphitic carbon materials [26,27], which can avoid the complicated etching process and the use of expensive templates/masks. Here we present a simple and cost-effective technique for the synthesis of three-dimensional structured diamond tube with porous tube wall from carbon nanotube (CNT) hollow fibers via pulsed laser annealing (PLA) and hot filament chemical vapor deposition (HFCVD). The PLA treated CNTs can provide nucleation sites to accelerate diamond growth. The optimum amount of residual unconverted carbon at the interfaces of diamond tubes endows them with desired electrical conductivity for electron transfer [28,29]. The effects of

HFCVD time and PLA on diamond tube growth and its electrochemical performance were investigated. Double layer capacitance measurements demonstrated that these diamond tubes have significantly enhanced electroactive surface area compared with the equivalent flat diamond films.

9.3 Results and discussion

9.3.1 Synthesis and characterization of diamond tubes

The scanning electron microscope (SEM) images in Fig. 9.1 show the cross-section and plan-view morphologies of CNT hollow fibers used for diamond tube growth. The cross-section view (Fig. 9.1(a)) shows the hollow tube structure with outer and inner diameters of ~740 μm and ~440 μm, respectively. The wall thickness is ~150 μm. The surface morphology of these tubes (Fig. 9.1(b-c)) shows the presence of fine porous structures and voids inside the wall. Figs. 9.1(d) show the top surface of CNT hollow fibers with increasing magnification. The CNTs are randomly distributed, and this distribution results in a spongelike structure with interconnected pores. The length of CNT hollow fibers can be up to tens of centimeters. For the present experiment of conversion of CNT hollow fibers into diamond, they were cut to the length of 3-4 cm. The inset of Fig. 9.1(d) shows the Kikuchi lines obtained from the electron back scattered diffraction (EBSD), which closely match up with the ideal CNT pattern. The indexed diffraction patterns in the Aztec software are shown by the blue lines. The possible solution for the crystalline orientation are sorted in the software library to find the best fit, and the relative orientation matrix is calculated which is shown in the sub-inset of Fig. 9.1(d).

A three-dimensional diamond tube was prepared by a simple one-step method using CNT hollow fibers (with or without nanosecond pulsed laser annealing at room temperature and normal pressure) as the growth precursor for HFCVD. Our previous works have demonstrated the

formation of nanodiamond crystals at CNT tips and bends via melting and ultrafast quenching after nanosecond pulsed laser annealing of CNTs [30,31]. The laser converted nanodiamonds at the tips and bends of CNTs can act as nucleation sites for diamond growth and accelerate diamond growth during HFCVD [26]. Fig. 9.2 shows the morphology of as prepared diamond tube from pulsed laser annealed CNT hollow fibers with 5 pulses and HFCVD time of 3 h (denoted as 5 PLA-3 h CVD). In the SEM images (Fig. 9.2 (a-b)), the porous diamond framework composed of microspheres is observed on the diamond tube surface. Diamond microspheres with average size about 2.0 μm are distributed uniformly on the entire tube surface. Some residual CNTs can be observed under the diamond film. Higher magnification SEM image (Fig. 9.2(c)) shows the diamond tube has very well defined diamond microcrystallites, and a small number of nanocrystallites also appear near the grain boundary. These results suggest that diamond tubes can be prepared efficiently by the facile and cost-effective PLA and HFCVD methods, which can avoid the processes of etching and usage of templates/substrates.

To gain more insight into the impact of HFCVD time on diamond growth, we extended the HFCVD time to 6 h (5 PLA). As shown in Fig. 9.2(d), porous diamond network with high diamond density is found on the tube surface. Three-dimensionally interconnected pores are homogeneously distributed on the tube although they have nonuniform features. Compared with the diamond tube synthesized under the same conditions but 3 h HFCVD, it possesses higher diamond coverage. The size of diamond microspheres is approximately 3.5-4.0 μm after 6 h HFCVD (Fig. 9.2(e)), larger than the one with 3 h HFCVD (~2.0 μm). The amount of residual CNTs has been significantly reduced with HFCVD time increased from 3 h to 6 h. In some areas of the tube surface, the diamond microspheres fuse together, resulting in the formation of dense diamond film. It is worth noting that more diamond

nanocrystallites are observed at the grain boundary for these diamond tubes with 6 h HFCVD (Fig. 9.2(e)). Diamond nanocrystallites have higher surface area than microcrystallites, which is more favorable to attain enhanced electrochemical performances for catalysis, sensor, energy conversion, water treatment and so on [32,33]. Therefore, the diamond coverage, particle size and nanocrystallites content can be tailored by HFCVD time during the process of converting CNT hollow fibers into diamond tubes.

To investigate the effect of pulsed laser annealing on diamond growth, diamond tubes were synthesized with 6 h HFCVD but different pulses of laser treated CNT hollow fibers. Without laser annealing, CNT hollow fibers also can be converted to diamond tubes (Fig. 9.3(a-c)). Compared with the diamond tube synthesized under the same conditions but treated with 5 PLA shots, the one without laser annealing exhibits lower diamond coverage. The size of microspheres is in the range of 2.7-3.1 μm, smaller than 3.5-4.0 μm obtained from laser treated samples with 5 PLA. Diamond nanocrystallites also can be observed at the grain boundaries. When laser annealing is increased to 10 pulses, the diamond coverage on the tube is further improved (Fig. 9.3(d)). As expected, the diamond microspheres (about 4.0-4.5 μm) contain both microcrystallites and nanocrystallites (Fig. 9.3(e)). It is interesting to note that micro- and nanodiamonds grow over the entire tube wall, as revealed by the cross section image in Fig. 9.3(f). The number density of diamond inside the wall is lower than that on the surface.

In the conventional CVD processes for diamond synthesis, diamond seeds are loaded on the substrate, which act as nucleation sites for diamond deposition. Here the CNT hollow fibers provide nucleation sites for diamond tube growth, which is expected to accelerate the growth rate of diamond. To verify the contribution of CNT hollow fibers for diamond

growth, diamond is also deposited on Si substrate under the same conditions (6 h, Fig. S9.1). The SEM image shows very low diamond coverage on the Si substrate, only few diamond microparticles are dispersed on the substrate. These results imply that the CNT hollow fibers contribute significantly to form diamond tubes by providing source for diamond nucleation and promote the formation of subsequent diamond crystallites.

The phase detection and the information about the crystallographic orientation of the fixed diamond structures in an SEM instrument by means of EBSD analysis are shown in the insets of Fig. 9.2(c), 9.2(f) and Fig. 9.3(c), 9.3(e). The Kikuchi patterns closely match up with the ideal diamond pattern after a quick analysis in the Aztec software and the indexed diffraction patterns are shown by the red lines. The possible solutions for the respective crystal orientations are sorted in the software library to find the best fit, and the orientation matrixes are calculated which are shown in the sub-insets of Fig. 9.2(c), 9.2(f) and Fig. 9.3(c), 9.3(e). Each of the diffraction patterns is bound to the crystal structure of the corresponding sample and as the crystal orientation changes the resultant diffraction pattern also changes. The positions of the Kikuchi bands can, therefore, be used to calculate the orientation of the diffracting crystal. As it is evident from all of the well-defined electron backscattered diffraction patterns, the out-of-plane orientation of the crystalline diamonds tip are along <101>.

Raman spectroscopy is very effective for determining the bonding characteristics of carbon-based materials. In the Raman spectrum of as prepared CNT hollow fibers (Fig. 9.4(a)), three characteristic Raman peaks centered at ~1345 cm^{-1}, ~1574 cm^{-1} and ~2685 cm^{-1} can be observed, which correspond to D, G and 2D peaks, respectively. The inset of Fig. 9.4(a) shows the absence of the radial breathing mode (RBM) associated with CNT hollow fibers. The RBM signal for large

diameter multi-wall CNTs is usually invisible [34]. After HFCVD performed on CNT hollow fibers with and without laser irradiation, sharp and strong peaks at ~1332 cm^{-1} are observed in their corresponding Raman spectra (Fig. 9.4(b)). This peak corresponds to the characteristic T_{2g} Raman mode of diamond crystals and highlights the successful formation of high quality diamond crystals after HFCVD. A small and broad peak at 1535-1560 cm^{-1} can be observed for each diamond tube sample, indicating the presence of a small amount of graphitic carbon in diamond tubes. This residual carbon is helpful for enhancing diamond conductivity and facilitating electron transfer [35,36].

The peak intensity ratio of T_{2g} Raman mode (diamond related peak) and G mode (graphitic carbon related peak), I_{T2g}/I_G, is 1.28 for diamond tubes prepared from 5 PLA-3 h HFCVD (Table S9.1). It is interesting to note that the I_{T2g}/I_G value increases to 1.71 when HFCVD time is extended to 6 h while laser irradiation is kept the same. The higher I_{T2g}/I_G value can be explained as follow: more CNTs are consumed for diamond growth with longer deposition time, which is consistent with the SEM observations (higher diamond coverage is achieved on diamond tubes with 6 h HFCVD). The I_{T2g}/I_G values of diamond tubes prepared from 6 h HFCVD but different laser annealing shots were also compared to explore the impact of laser treatment on diamond growth, which are 1.46 for diamond tube without laser annealing and 1.81 for the one with 10 PLA. These Raman results confirm that relatively high purity diamond tube is obtained from CNT hollow fibers even without laser irradiation, but laser annealing can further facilitate diamond growth.

The intensity ratio of T_{2g} and G peaks in the Raman spectra is used to estimate the amount of nondiamond content (C_{nd}) in each of the diamond tubes. The sensitivity of the Raman

signal from the non-diamond carbon phase is about 75 times of that for diamond [37]. The following equation is used to calculate the nondiamond contents:

$$C_{nd} = \frac{1}{1 + 75(\frac{I_d}{I_{nd}})}$$

Where I_d represents the Raman peak intensity for diamond entities, and I_{nd} represents the Raman peak intensity for the non-diamond carbon content. The calculated non-diamond content for all the representative diamond tubes vary in-between 0.73-1.03% (table S9.1), demonstrating that they have high-purity diamond crystals.

9.3.2 Electrochemical performance of diamond tube

The electrochemical performance of diamond tubes was investigated by measuring their double layer capacitances. Fig. 9.5(a) shows the cyclic voltammograms (CV) of diamond tube (10 PLA-6 h HFCVD) recorded in 0.05 M Na_2SO_4 at scan rates from 10 to 100 mV s^{-1}. All the CV curves exhibit quasi-rectangular shape at all the scan rates, revealing a good double layer capacitive feature of diamond tubes. This diamond tube provides a very high capacitive current density under the conditions applied. As expected, its capacitive current density increases with the increase of scan rate. The double layer capacitance is obtained from $C_{dl}=\Delta i/2v$ at 0.05 V (*vs* Ag/AgCl), where Δi is the difference between anodic current and cathodic current densities, and v is the corresponding scan rate. The calculated capacitance is 18.07 mF cm^{-2} for diamond tube with 10 PLA-6 h HFCVD (Fig. 9.5(b)), which is higher than the capacitances recently reported for diamond electrodes[17,38–42]. The double layer capacitance is proportional to the electroactive surface area. The high capacitance of diamond tube highlights its large electroactive surface area, which is favorable for enhancing performance for electrocatalysis, electrosynthesis,

energy conversion, electrochemical sensor, and so on. The CV curves in Fig. S9.2 for the diamond tubes prepared from 5 PLA-3 h HFCVD and 5 PLA-6 h HFCVD exhibit lower capacitive current than the one with 10 PLA-6 h HFCVD. The double layer capacitance is 14.61 mF cm^{-2} for diamond tubes with 5 PLA-6 h HFCVD, while it is 11.65 mF cm^{-2} for the one with 5 PLA-3 h HFCVD. These results reveal the diamond tubes grown under longer HFCVD time and more laser pulses possess much larger electroactive surface area, which could be attributed to the higher density of the diamond microcrystallites and increased amount of diamond nanocrystallites.

The advantage of diamond tube structure was revealed by comparing its electrochemical performance with that of equivalent flat diamond film. As comparison, flat diamond film was deposited on Si substrate under the same HFCVD conditions. The SEM image (in Fig. S9.3) shows a continuous and dense diamond film consisted of microcrystallites over the entire Si substrate using our seeding process. The CV curves of flat diamond electrode (Fig. 9.5(c)) show that its capacitive current is much lower than that of diamond tube. Its double layer capacitance is 0.034 mF cm^{-2}, three orders of magnitude lower than diamond tubes, demonstrating the significantly enhanced electroactive surface area of diamond tube compared with flat diamond electrodes. The high surface area of diamond tube could be mainly attributed to the tubular structure and porous tube wall with nano and microstructures.

9.4 Conclusion

Three dimensional diamond tubes with porous nano and microstructures have been prepared by a simple and cost-effective method which combines PLA with HFCVD. The CNT hollow fibers provide nucleation sites to accelerate the diamond growth. Diamond

microspheres composed of high quality diamond microcrystallites and nanocrystallites are observed on the entire tube even inside the tube wall. The diamond density, microsphere size and nanocrystallite content are significantly increased with increasing HFCVD time and laser pulses. These diamond tubes have high double layer capacitances, which are found to be dependent on the density of the diamond spheres, the porous tubular structure, nanocrystallite content and the quality of diamond. Its electroactive surface area is three orders of magnitude higher than flat diamond film. This effective method for the synthesis of diamond tubes having large surface area makes it an ideal candidate for electrochemical applications such as electrocatalysis, electrosynthesis, electroanalysis, energy storage and conversion.

9.5 Experimental

Preparation of CNT hollow fibers. The CNT hollow fibers were prepared by wet-spinning method [43], details as follows: the purchased multi-wall CNTs (diameter of 60-100 nm, Shenzhen Nanotech Port Co. Ltd.) were oxidized by H_2SO_4/HNO_3 solution. The oxidized CNTs were dispersed in dimethylacetamide solution, followed by adding polyvinyl butyral (mass ratio 2:1:17). The suspension was dispensed via a spinneret equipped with an injection pump, and the produced CNT hollow fibers were directly immersed into a water coagulation bath. DMAC/water solution (v:v=75:25) was used as bore-fluid. The obtained CNT hollow fibers were dried and annealed at 800 °C for 1 h under Ar.

Preparation of diamond tubes. The CNT hollow fibers with or without pulsed laser annealing were converted to diamond tubes via HFCVD. The prepared CNT hollow fibers were irradiated with 0-10 ArF laser pulses (wavelength=193 nm, pulse duration = 20 ns, energy density ~0.65-0.75 J cm^{-2}). The HFCVD was performed for 3-6 h at a substrate

temperature of 700 °C with 2 sccm CH_4 and 100 sccm H_2. At the beginning of the HFCVD, the tungsten filaments were gradually heated to a temperature of ~2000 °C. The pressure was kept at 20 Torr throughout the process. For comparison of the electrochemical property, flat diamond films were deposited on Si substrate under the same conditions using porous carbon film as nucleation seeds.

Characterization. The morphology of CNT hollow fibers and diamond tubes were characterized by high-resolution SEM images acquired on a FEI Verios 460L SEM. The non-destructive EBSD technique in the same Verios 460L SEM is used to determine the details of the crystallographic information of diamond and CNTs. During the EBSD data acquisition a beam of electrons (20KV & 5 nA) is directed at a point of interest on the tilted diamond structures. These electrons are diffracted to form a set of paired large-angle cones that correspond to each diffracting plane. The image produced on the phosphor screen contains characteristic Kikuchi bands of the corresponding diamond crystal, which are formed where the regions of enhanced electron intensity intersect the screen. The Raman active vibrational modes of CNT hollow fibers and diamond tubes were measured on a WITec confocal Raman microscope system (Alpha 3000 M, 532 nm source) with a triple monochromator, and gratings of 2400 lines/mm for high-resolution (spectrum resolution ~0.5 cm^{-1}). An optimum laser power (~40 mW) was used to illuminate the sample to avoid heating during the spectrum acquisition. A crystalline Si sample was used to calibrate the Raman system. Cyclic voltammetry (CV) was performed on Bio-Logic SP300 potentiostat (Bio-Logic, USA) with three-electrode system. The CNT hollow fibers or diamond tubes were used as the working electrode, whereas Pt wire and Ag/AgCl were used as counter

electrode and reference electrode, respectively. The CV curves for double layer capacitance were measured in 0.05 M Na_2SO_4 at 10-100 mV s^{-1}.

9.6 Figures

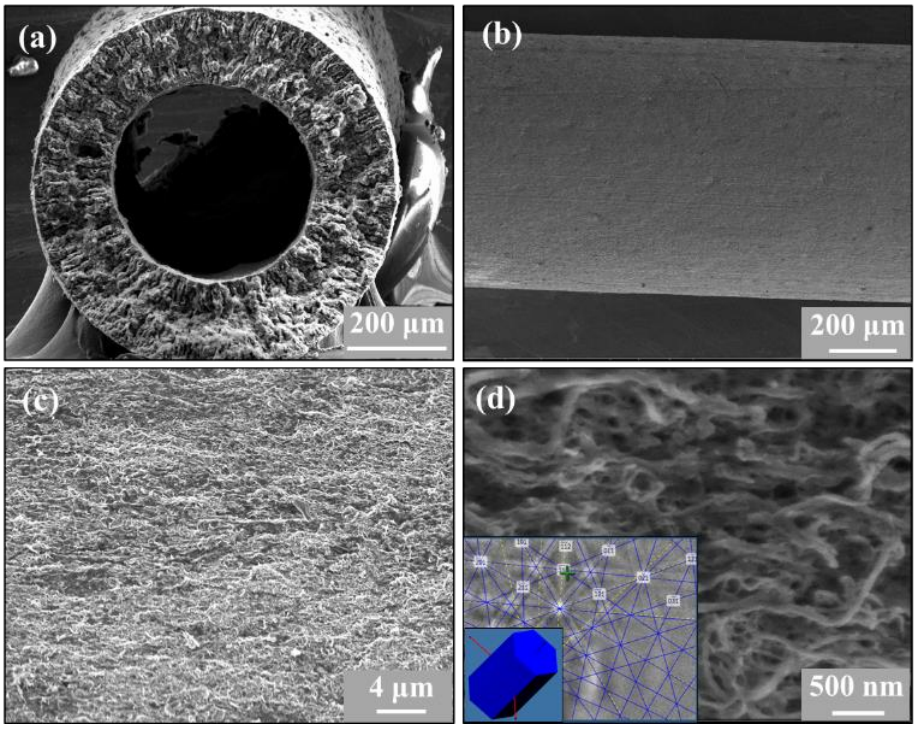

Figure 9. 1**:** SEM images of CNT hollow fibers: (a) cross section and (b, c, d) top view at different magnifications. The insets are EBSD pattern and relative orientation of CNT hollow fibers.

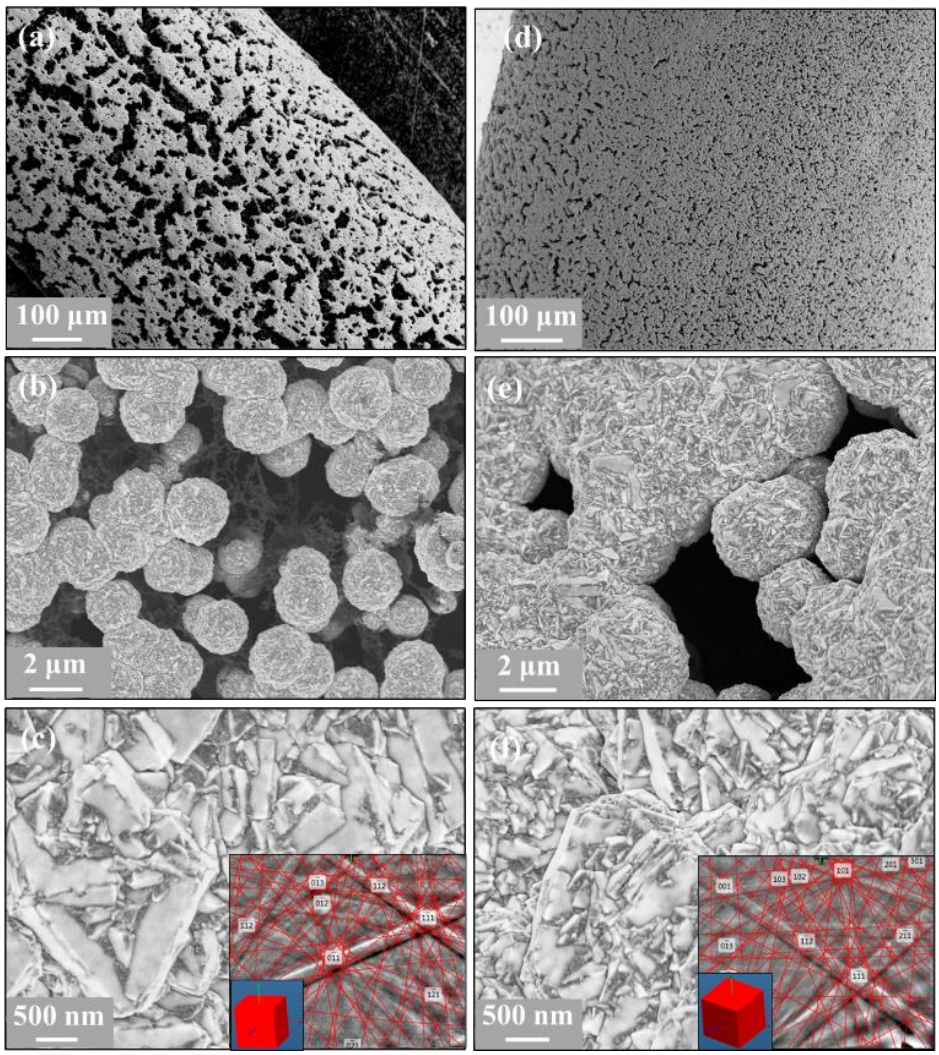

Figure 9. 2**:** SEM images of diamond tube with 5 PLA and growth time of (a, b, c) 3 h, (d, e, f) 6 h. The insets are EBSD pattern and relative orientation of diamond.

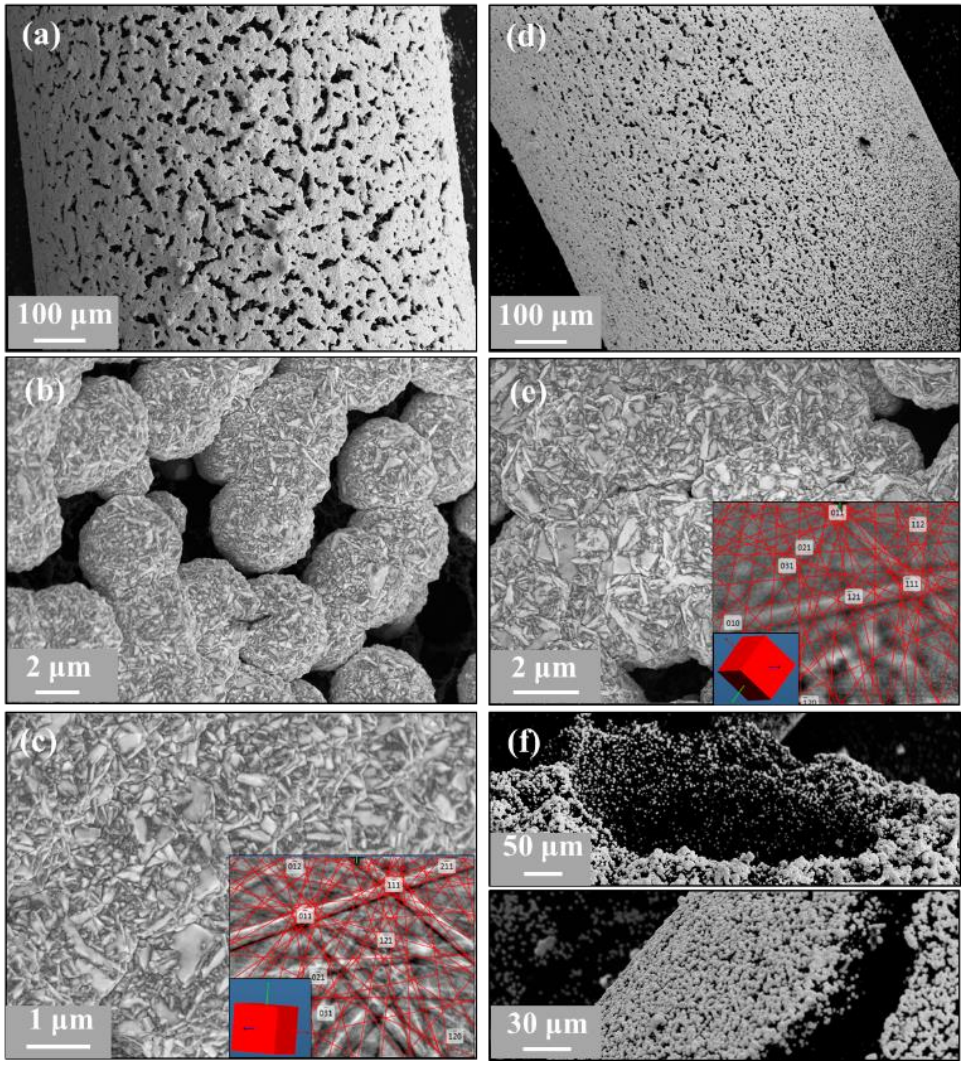

Figure 9. 3**:** SEM images of diamond tubes prepared from 6 h HFCVD and (a, b, c) without laser annealing, and (d, e, f) 10 PLA. The insets are EBSD pattern and relative orientation of diamond.

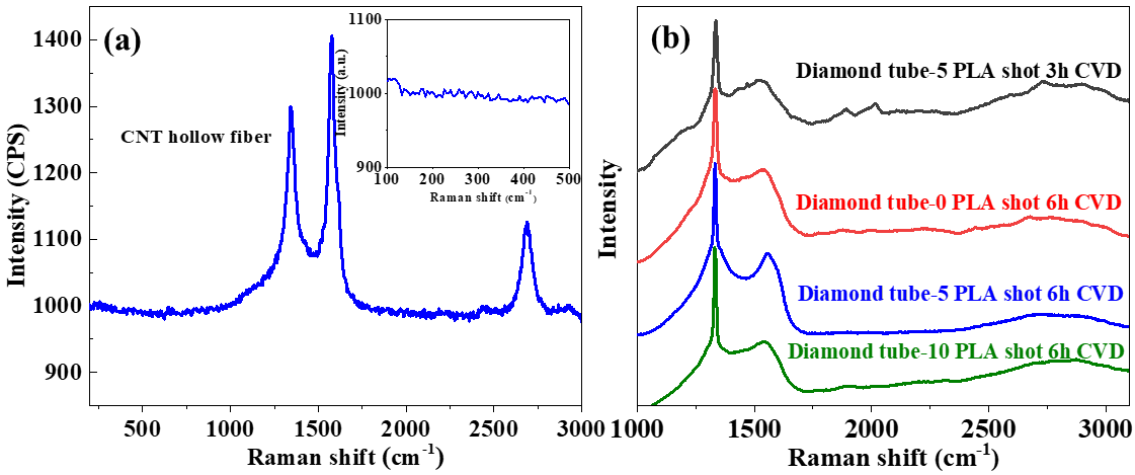

Figure 9. 4**:** Raman spectra of (a) CNT hollow fibers and (b) diamond tubes with 5 PLA-3 h CVD, 0 PLA-6 h CVD, 5 PLA-6 h CVD and 10 PLA-6 h CVD.

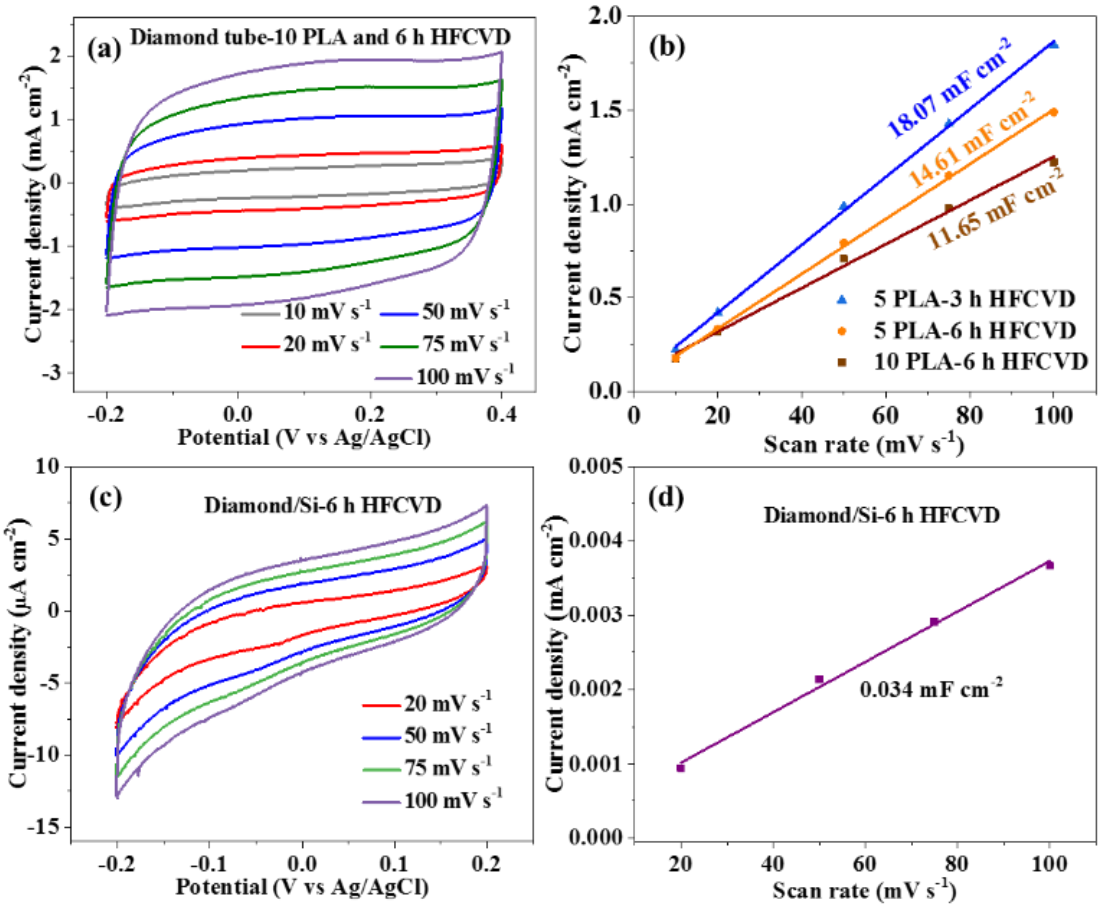

Figure 9. 5**:** (a) Cyclic voltammograms of diamond tube with 10 PLA-6 h CVD at 10-100 mV s^{-1}, (b) double layer capacitances for diamond tubes with 5 PLA-3 h CVD, 5 PLA-6 h CVD and 10 PLA-6 h CVD, (c) Cyclic voltammograms of flat diamond film at 20-100 mV s^{-1}, (d) double layer capacitance for flat diamond film (0.05 M Na_2SO_4).

References

[1] V.N. Mochalin, O. Shenderova, D. Ho, Y. Gogotsi, The properties and applications of nanodiamonds, Nat. Nanotechnol. 7 (2012) 11–23. https://doi.org/10.1038/nnano.2011.209.

[2] Q. Huang, D. Yu, B. Xu, W. Hu, Y. Ma, Y. Wang, Z. Zhao, B. Wen, J. He, Z. Liu, Y. Tian, Nanotwinned diamond with unprecedented hardness and stability, Nature. 510 (2014) 250–253. https://doi.org/10.1038/nature13381.

[3] T. Sun, F.A.M. Koeck, C. Zhu, R.J. Nemanich, Combined visible light photo-emission and low temperature thermionic emission from nitrogen doped diamond films, Appl. Phys. Lett. 99 (2011) 202101. https://doi.org/10.1063/1.3658638.

[4] A. Sipahigil, R.E. Evans, D.D. Sukachev, M.J. Burek, J. Borregaard, M.K. Bhaskar, C.T. Nguyen, J.L. Pacheco, H.A. Atikian, C. Meuwly, R.M. Camacho, F. Jelezko, E. Bielejec, H. Park, M. Lončar, M.D. Lukin, An integrated diamond nanophotonics platform for quantum-optical networks, Science. 354 (2016) 847–850. https://doi.org/10.1126/science.aah6875.

[5] P. Maletinsky, S. Hong, M.S. Grinolds, B. Hausmann, M.D. Lukin, R.L. Walsworth, M. Loncar, A. Yacoby, A robust scanning diamond sensor for nanoscale imaging with single nitrogen-vacancy centres, Nat. Nanotechnol. 7 (2012) 320–324. https://doi.org/10.1038/nnano.2012.50.

[6] T.M. Babinec, B.J.M. Hausmann, M. Khan, Y. Zhang, J.R. Maze, P.R. Hemmer, M. Lončar, A diamond nanowire single-photon source, Nat. Nanotechnol. 5 (2010) 195–199. https://doi.org/10.1038/nnano.2010.6.

[7] D. Zhu, L. Zhang, R.E. Ruther, R.J. Hamers, Photo-illuminated diamond as a solid-state source of solvated electrons in water for nitrogen reduction, Nat. Mater. 12 (2013) 836–841. https://doi.org/10.1038/nmat3696.

[8] W. Zhu, G.P. Kochanski, S. Jin, Low-Field Electron Emission from Undoped Nanostructured Diamond, Science. 282 (1998) 1471–1473. https://doi.org/10.1126/science.282.5393.1471.

[9] K.J. Pérez Quintero, S. Antipov, A.V. Sumant, C. Jing, S.V. Baryshev, High quantum efficiency ultrananocrystalline diamond photocathode for photoinjector applications, Appl. Phys. Lett. 105 (2014) 123103. https://doi.org/10.1063/1.4896418.

[10] N. Yang, J.S. Foord, X. Jiang, Diamond electrochemistry at the nanoscale: A review, Carbon. 99 (2016) 90–110. https://doi.org/10.1016/j.carbon.2015.11.061.

[11] N. Wächter, C. Munson, R. Jarošová, I. Berkun, T. Hogan, R.C. Rocha-Filho, G.M. Swain, Structure, Electronic Properties, and Electrochemical Behavior of a Boron-Doped Diamond/Quartz Optically Transparent Electrode, ACS Appl. Mater. Interfaces. 8 (2016) 28325–28337. https://doi.org/10.1021/acsami.6b02467.

[12] N. Yang, S. Yu, J. V. Macpherson, Y. Einaga, H. Zhao, G. Zhao, G. M. Swain, X. Jiang, Conductive diamond: synthesis, properties, and electrochemical applications, Chem. Soc. Rev. 48 (2019) 157–204. https://doi.org/10.1039/C7CS00757D.

[13] Yu.V. Pleskov, M.D. Krotova, V.V. Elkin, E.A. Ekimov, Electrochemical Behaviour of Boron-doped Diamond Compacts – a New Electrode Material, Electrochimica Acta. 201 (2016) 268–273. https://doi.org/10.1016/j.electacta.2015.09.075.

[14] S. Luo, B.C. Riggs, X. Zhang, J.T. Shipman, S. Adireddy, S.C. Sklare, B. Koplitz, D.B. Chrisey, Growth and microstructure of columnar Y-doped SrZrO3 films deposited on Pt-coated MgO by pulsed laser deposition, J. Appl. Phys. 118 (2015) 035310. https://doi.org/10.1063/1.4927158.

[15] A. Jeyaranjan, T.S. Sakthivel, C.J. Neal, S. Seal, Scalable ternary hierarchical microspheres composed of PANI/ rGO/CeO2 for high performance supercapacitor applications, Carbon. 151 (2019) 192–202. https://doi.org/10.1016/j.carbon.2019.05.043.

[16] K.D. Behler, A. Stravato, V. Mochalin, G. Korneva, G. Yushin, Y. Gogotsi, Nanodiamond-Polymer Composite Fibers and Coatings, ACS Nano. 3 (2009) 363–369. https://doi.org/10.1021/nn800445z.

[17] F. Gao, M.T. Wolfer, C.E. Nebel, Highly porous diamond foam as a thin-film micro-supercapacitor material, Carbon. 80 (2014) 833–840. https://doi.org/10.1016/j.carbon.2014.09.007.

[18] H. Kato, J. Hees, R. Hoffmann, M. Wolfer, N. Yang, S. Yamasaki, C.E. Nebel, Diamond foam electrodes for electrochemical applications, Electrochem. Commun. 33 (2013) 88–91. https://doi.org/10.1016/j.elecom.2013.04.028.

[19] H. Zhuang, N. Yang, H. Fu, L. Zhang, C. Wang, N. Huang, X. Jiang, Diamond Network: Template-Free Fabrication and Properties, ACS Appl. Mater. Interfaces. 7 (2015) 5384–5390. https://doi.org/10.1021/am508851r.

[20] C. Hébert, E. Scorsone, M. Mermoux, P. Bergonzo, Porous diamond with high electrochemical performance, Carbon. 90 (2015) 102–109. https://doi.org/10.1016/j.carbon.2015.04.016.

[21] S. Kunuku, K.J. Sankaran, C.-Y. Tsai, W.-H. Chang, N.-H. Tai, K.-C. Leou, I.-N. Lin, Investigations on Diamond Nanostructuring of Different Morphologies by the Reactive-Ion Etching Process and Their Potential Applications, ACS Appl. Mater. Interfaces. 5 (2013) 7439–7449. https://doi.org/10.1021/am401753h.

[22] C. Terashima, K. Arihara, S. Okazaki, T. Shichi, D.A. Tryk, T. Shirafuji, N. Saito, O. Takai, A. Fujishima, Fabrication of Vertically Aligned Diamond Whiskers from Highly Boron-Doped Diamond by Oxygen Plasma Etching, ACS Appl. Mater. Interfaces. 3 (2011) 177–182. https://doi.org/10.1021/am1007722.

[23] D. Luo, L. Wu, J. Zhi, Fabrication of Boron-Doped Diamond Nanorod Forest Electrodes and Their Application in Nonenzymatic Amperometric Glucose Biosensing, ACS Nano. 3 (2009) 2121–2128. https://doi.org/10.1021/nn9003154.

[24] Y. Liu, S. Chen, X. Quan, H. Yu, Efficient Electrochemical Reduction of Carbon Dioxide to Acetate on Nitrogen-Doped Nanodiamond, J. Am. Chem. Soc. 137 (2015) 11631–11636. https://doi.org/10.1021/jacs.5b02975.

[25] H. Zanin, P.W. May, D.J. Fermin, D. Plana, S.M.C. Vieira, W.I. Milne, E.J. Corat, Porous Boron-Doped Diamond/Carbon Nanotube Electrodes, ACS Appl. Mater. Interfaces. 6 (2014) 990–995. https://doi.org/10.1021/am4044344.

[26] A. Haque, R. Sachan, J. Narayan, Synthesis of diamond nanostructures from carbon nanotube and formation of diamond-CNT hybrid structures, Carbon. 150 (2019) 388–395. https://doi.org/10.1016/j.carbon.2019.05.027.

[27] A. Haque, P. Pant, J. Narayan, Large-area diamond thin film on Q-carbon coated crystalline sapphire by HFCVD, J. Cryst. Growth. 504 (2018) 17–25. https://doi.org/10.1016/j.jcrysgro.2018.09.036.

[28] Y. Lin, X. Sun, D. Sheng Su, G. Centi, S. Perathoner, Catalysis by hybrid sp 2 /sp 3 nanodiamonds and their role in the design of advanced nanocarbon materials, Chem. Soc. Rev. 47 (2018) 8438–8473. https://doi.org/10.1039/C8CS00684A.

[29] X. Duan, W. Tian, H. Zhang, H. Sun, Z. Ao, Z. Shao, S. Wang, sp2/sp3 Framework from Diamond Nanocrystals: A Key Bridge of Carbonaceous Structure to Carbocatalysis, ACS Catal. 9 (2019) 7494–7519. https://doi.org/10.1021/acscatal.9b01565.

[30] J. Narayan, A. Bhaumik, R. Sachan, A. Haque, S. Gupta, P. Pant, Direct conversion of carbon nanofibers and nanotubes into diamond nanofibers and the subsequent growth of large-sized diamonds, Nanoscale. 11 (2019) 2238–2248. https://doi.org/10.1039/C8NR08823C.

[31] J. Narayan, A. Bhaumik, A. Haque, Pseudo-topotactic growth of diamond nanofibers, Acta Mater. 178 (2019) 179–185. https://doi.org/10.1016/j.actamat.2019.08.008.

[32] J. Hees, R. Hoffmann, A. Kriele, W. Smirnov, H. Obloh, K. Glorer, B. Raynor, R. Driad, N. Yang, O.A. Williams, C.E. Nebel, Nanocrystalline Diamond Nanoelectrode Arrays and Ensembles, ACS Nano. 5 (2011) 3339–3346. https://doi.org/10.1021/nn2005409.

[33] I. Kovalenko, D.G. Bucknall, G. Yushin, Detonation Nanodiamond and Onion-Like-Carbon-Embedded Polyaniline for Supercapacitors, Adv. Funct. Mater. 20 (2010) 3979–3986. https://doi.org/10.1002/adfm.201000906.

[34] M.S. Dresselhaus, G. Dresselhaus, R. Saito, A. Jorio, Raman spectroscopy of carbon nanotubes, Phys. Rep. 409 (2005) 47–99. https://doi.org/10.1016/j.physrep.2004.10.006.

[35] Z. Zhai, N. Huang, B. Yang, C. Wang, L. Liu, J. Qiu, D. Shi, Z. Yuan, Z. Lu, H. Song, M. Zhou, B. Chen, X. Jiang, Insight into the Effect of the Core–Shell Microstructure on the Electrochemical Properties of Undoped 3D-Networked Conductive Diamond/Graphite, J. Phys. Chem. C. 123 (2019) 6018–6029. https://doi.org/10.1021/acs.jpcc.8b11865.

[36] J. Li, C.L. Bentley, S. Tan, V.S.S. Mosali, M.A. Rahman, S.J. Cobb, S.-X. Guo, J.V. Macpherson, P.R. Unwin, A.M. Bond, J. Zhang, Impact of sp2 Carbon Edge Effects on the Electron-Transfer Kinetics of the Ferrocene/Ferricenium Process at a Boron-Doped Diamond

Electrode in an Ionic Liquid, J. Phys. Chem. C. 123 (2019) 17397–17406. https://doi.org/10.1021/acs.jpcc.9b04519.

[37] C.T. Kuo, C.R. Lin, H.M. Lien, Origins of the residual stress in CVD diamond films, Thin Solid Films. 290–291 (1996) 254–259. https://doi.org/10.1016/S0040-6090(96)09016-5.

[38] S. Yu, J. Xu, H. Kato, N. Yang, A. Schulte, H. Schönherr, X. Jiang, Phosphorus-Doped Nanocrystalline Diamond for Supercapacitor Application, ChemElectroChem. 6 (2019) 1088–1093. https://doi.org/10.1002/celc.201801543.

[39] F. Gao, C.E. Nebel, Diamond-Based Supercapacitors: Realization and Properties, ACS Appl. Mater. Interfaces. 8 (2016) 28244–28254. https://doi.org/10.1021/acsami.5b07027.

[40] S. Yu, N. Yang, H. Zhuang, J. Meyer, S. Mandal, O.A. Williams, I. Lilge, H. Schönherr, X. Jiang, Electrochemical Supercapacitors from Diamond, J. Phys. Chem. C. 119 (2015) 18918–18926. https://doi.org/10.1021/acs.jpcc.5b04719.

[41] C. Hébert, J.P. Mazellier, E. Scorsone, M. Mermoux, P. Bergonzo, Boosting the electrochemical properties of diamond electrodes using carbon nanotube scaffolds, Carbon. 71 (2014) 27–33. https://doi.org/10.1016/j.carbon.2013.12.083.

[42] K. Takagi, K. Natsui, T. Watanabe, Y. Einaga, Increasing the Electric Double-Layer Capacitance in Boron-Doped Diamond Electrodes, ChemElectroChem. 6 (2019) 1683–1687. https://doi.org/10.1002/celc.201801702.

[43] X. Fan, Y. Liu, X. Quan, S. Chen, Highly Permeable Thin-Film Composite Forward Osmosis Membrane Based on Carbon Nanotube Hollow Fiber Scaffold with Electrically Enhanced Fouling Resistance, Environ. Sci. Technol. 52 (2018) 1444–1452. https://doi.org/10.1021/acs.est.7b05341.

Supplementary Information

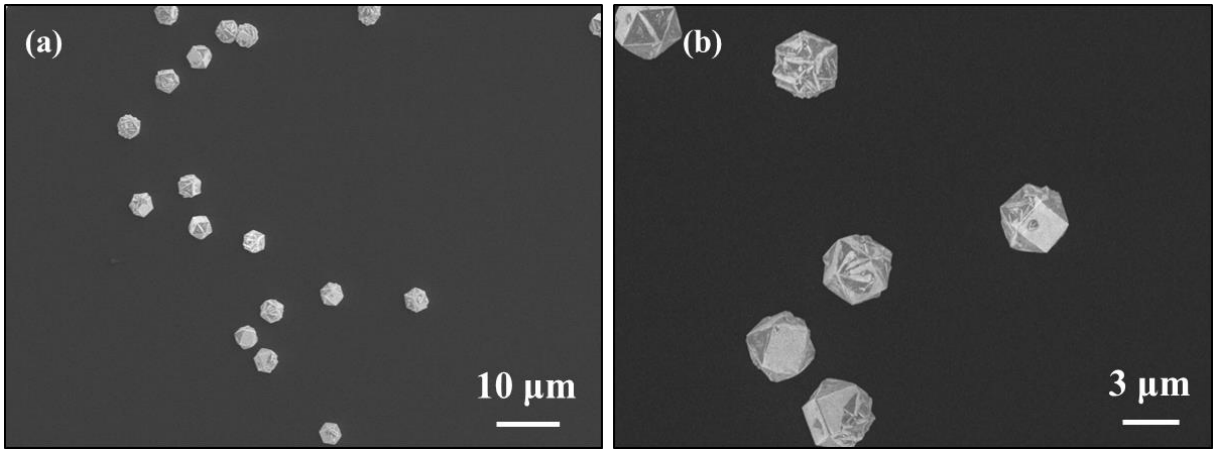

Figure S9.1: SEM images of diamond deposited on bare Si substrate with 6 h HFCVD at different magnifications, showing a very low amount of diamond coverage.

Table S9.1. The intensity ratios of T_{2g} and G peaks for different diamond tubes.

Samples	5PLA-3h	0pla-6h	5pla-6h	10pla-6h
I_D/I_G	1.28	1.46	1.71	1.81
% of sp^2 carbon	1.03%	0.91%	0.77%	0.73%

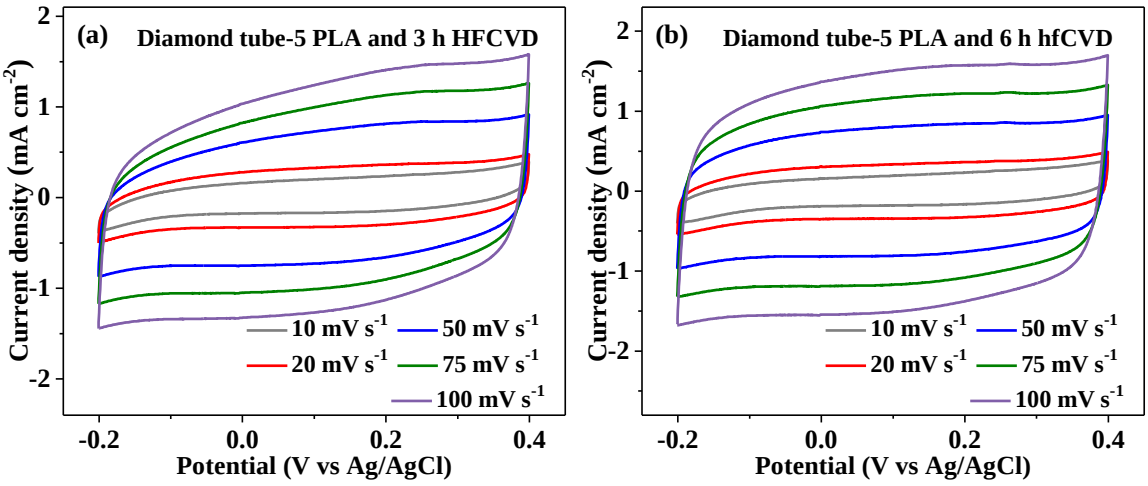

Figure S9.2: Cyclic voltammograms of diamond tubes with (a) 5 PLA-3 h CVD and (b) 5 PLA-6 h CVD at 0.05 M Na_2SO_4 and 10-100 mV s^{-1}.

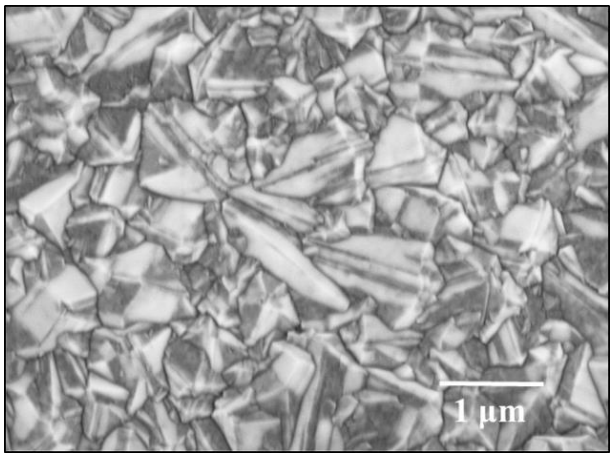

Figure S9.3: The SEM image of flat diamond film deposited on Si substrate with 6 h HFCVD. High amount of diamond coverage is due to the use of porous carbon film as nucleation seeds.

10. Electron field emission from Q-carbon

Ariful Haque and Jagdish Narayan

Materials Science and Engineering, North Carolina State University, Raleigh, North Carolina 27695.7916, USA

10.1 Abstract

We report field electron emission investigations in Q-carbon composite structures formed by pulsed laser annealing of amorphous carbon layers. Under the optimum fabrication conditions, a dense microstructured morphology of Q-carbon was obtained, which is important for local electric field enhancement in field-emission device applications. The turn-on field required to draw an emission current density of 1 μA/cm^2 is found to be 2.4 V/μm. The Q-carbon films show good electron emission stability as a function of time up to 4 hours. The microstructure and morphology of the field emitting Q-carbon films was analyzed by a variety of techniques, including field emission scanning electron microscope, Raman spectroscopy, and atomic force microscopy. Our results show a very high emission current density value of ~30 μA/cm^2 at an applied electric field of 2.65 V/μm, which is hysteresis-free and stable. The generated emission current has been found to have low fluctuations (<4%) and shows no generation of defects during repeated emission measurements on the sample. Our findings thus hold a great promise for the development of Q-carbon films in applications ranging from field emitters and frictionless motors to heterostructures for novel micro and nano-electronic devices.

10.2 Introduction

High-quality robust field emitting materials with stable emission over a long period of time are desirable for a wide range of applications such as flat panel displays, vacuum microwave amplifiers, contactless motors, microscopes operated by parallel electron beam sources, etc.[1–3]

Different forms of carbon such as diamond, carbon nanotubes, graphene, graphene oxide etc. were found to be good candidates for high current density at low applied electric field because of their negative electron affinity (NEA) or very low positive electron affinity.[4–7] For several decades, these carbon-based field emitters with different size, shape, aspect ratio, hybrid- nanostructures, and dopant types and doping concentrations have been studied extensively.[8–11] Robertson *et al.* investigated the band diagram of diamond and DLC surfaces for field emission and showed that DLC has a sizeable positive electron affinity (E_A), which could be tuned by nitrogen doping to enhance the field emission current density.[12] According to their results DLC has sizeable positive E_A values and the main barrier for electron emission is at the front surface, which is difficult to overcome. Doping DLC with nitrogen donor raises the Fermi level, which lowers the barrier and enhances the field emission. However, existing studies show that sometimes the emission current density can be proportional to the number of damaged sites induced by breakdown, implying that the FE is mainly originated from the undesirable damaged sites.[13] Recently, graphene field emitters with remarkable electrical, mechanical, and chemical properties have drawn attention for next-generation display technology.[14,15] Recently several methods have been developed to design and fabricate graphene for its potential application in field emission.[16,17] However, issues related to nanoscale thickness reliability, size optimization problems current stability, performance and yield challenges render the applications of graphene in practical FE devices.[18]

Theoretically, field-induced electrons could be emitted from a flat diamond crystal due to the negative electron affinity (NEA) of the diamond surface; however, the poor electrical conductivity of pristine wide bandgap diamond inhibits the electron transport through the bulk, which severely affects the FE current density from the surface. Measures, such as doping or introducing defects

into the diamond structure, have been implemented in the past to circumvent this problem. But incorporation of large amount of defects in the bulk diamond matrix is detrimental for the conditions necessary for the NEA of diamond. Moreover, incorporation of defects deteriorates the desirable physical and thermal properties of diamond, such as mechanical stability, chemical and radiation inertness and high thermal conductivity, which are necessary for reliable and robust device applications. Therefore, the uses of defective or doped diamond inhibit the realization of practical flat diamond based FE devices. The diamond microtip has shown promising results, where electrons move to the tip of the cathode via the surface states in the microtip structure.[19] However, the fabrication and formation process of such diamond microtips are very costly and extremely complicated in views of size and shape uniformity and distributions.[20] Additionally patterning a large area substrate with high packing density of these microtips is impractical with the present technology. Recently a new phase of carbon, named quenched carbon (Q-Carbon), has been discovered by our group, which shows excellent FE related properties, even superior to diamond. [21,22]

In this paper, we report excellent field emission properties of Q-carbon, which was fabricated from amorphous carbon films by nanosecond laser melting using a 193 nm laser pulse. This liquid phase mediated Q-carbon thin film is envisioned to have superior properties such as higher hardness than diamond (40% harder) [23], high-temperature record superconductivity (B-doped Q-carbon)[24], excellent chemical inertness, high thermal conductivity, excellent abrasion resistance, and room-temperature ferromagnetism.[22] This material can also be deposited at room temperature with a high deposition rate over a large area on different types of substrates such as Si, sapphire, WC, glass and polymers. Since Q-carbon composite structures have reasonable electron conductivity, the electrons travel unhindered and solid-state devices can be driven

electronically. Thus, Q-carbon films show a great potential for practical field-emitter applications. We used Raman spectroscopy, field emission scanning electron microscopy (FESEM), atomic force microscopy (AFM), and electrical transport property tests to investigate the correlation between FE and microstructural features. We also conducted a detailed analysis of the electron emission from Q-carbon grains using the modified electronic states at the surface in the presence of high applied electric field.

10.3 Experimental

A high quality compressed graphite target was used to deposit amorphous carbon/diamond like carbon (DLC) film with a mixture of sp^3/sp^2 bonding and with thickness ~500 nm on r-sapphire substrate using pulsed laser deposition (PLD) technique. The graphite was mounted on a rotating target holder at a distance of ~4 cm from the substrate. DLC thin film was deposited in a stainless steel chamber evacuated to a base pressure of $\sim 1 \times 10^{-6}$ torr. We used a pulsed krypton fluoride (KrF) excimer laser (λ = 248 nm, repetition rate 5 Hz/s, pulse width 20 ns, laser fluence of ~2 J/cm^2) during deposition. The DLC film was irradiated by ArF laser (wavelength = 193 nm, pulse duration = 20 ns) pulses with an energy density in-between 0.6 to 0.7 Jcm^{-2} for conversion into Q-carbon composite structure. During the pulsed laser annealing (PLA) process, the as-deposited films were melted in a super-undercooled state and subsequently quenched within 200-250 nanoseconds.

A WITec confocal Raman microscope system (alpha300M) with a maximum sensitivity excitation wavelength of 532.16 nm was used to characterize the DLC and Q-carbon. A crystalline Si sample (with characteristic Raman peak at 520.6 cm^{-1}) was used to calibrate the Raman spectra. Care was taken to avoid damaging the sample by the laser excitation. Field emission scanning electron microscopy (FESEM) imaging was performed using a FEI Verios 460L SEM, which

provides sub-nanometer resolution, to study the morphology of the Q-carbon composite structures. The atomic force microscopy (AFM) was performed using an Asylum MFP-3D classic Atomic Force Microscope (AFM). This instrument is capable of imaging an area up to 125 μm^2 and as small as a few tens of nm^2. The maximum spatial resolution of the instrument is such that the surface of the Q-carbon composite structure could be revealed. FE measurements were performed in an in-house setup shown in Fig. 10.1. The Q-carbon sample was placed in a parallel plate configuration with an anode of Tungsten separated by a 100μm glass spacer inside a clean high vacuum chamber at pressure < $2x10^{-7}$ Torr. The area of the composite sample was greater than 25 mm^2. No surface damage was observed after the measurements.

10.4 Results and discussion

10.4.1 Microstructure of Q-carbon

The Q-carbon provides an ideal platform for high field emission in view of its atomic structure and bonding characteristics. The Q-carbon consists of diamond tetrahedra which are closely packed with a packing efficiency of over 85%.[23] The bonding within the tetrahedron is sp^3 and in-between mostly sp^2 and some sp^3. The overall sp^3 fraction in Q-carbon is 80-85% and the rest is sp^2 carbon.[22] The Q-carbon structure is a new phase of carbon, which has an amorphous structure. The NEA of Q-carbon is higher than that of diamond like carbon. This unique mixed sp^3 and sp^2 bonded structure of Q-carbon is found to provide excellent electron emission efficiency. Fig. 10.2 (a-c) show FESEM images of the microstructure of Q-carbon composite sample used for the FE measurements. The brighter sp^3 rich regions are the Q-carbon structures and the rest (with dark region) is the amorphous carbon produced after the laser annealing treatment. Fig. 10.2 (a) shows the large area growth of Q-carbon composite structure, and Fig. 10.2 (b) shows that the sp^3 rich Q-carbon clusters are embedded in a sp^2 rich amorphous carbon matrix. Size of an individual

Q-carbon cluster may vary from 0.5 μm to 5μm. In Fig. 10.2(c) we can see the structural details inside the Q-carbon cluster. The cluster consists of sp^3 rich Q-carbon nano-structures surrounded by sp^2 rich boundaries. These sp^2 carbon containing boundaries are highly conductive in nature and provide pathways for the electrons to travel through individual Q-carbon nanocluster, which acts as a cathode, to ensure the continuous flow of electrons during the FE measurements. It is envisaged that the high density of the grain boundaries inside the Q-carbon clusters connected with the amorphous carbon matrix gives an efficient FE device. The areal density of Q-carbon in the composite structure was calculated from Fig. 10.2 (b-c) using ImageJ software. The actual area of Q-carbon clusters in the film is found to be around 12%. The low coverage of Q-carbon matrix in the film implies high emission current density during the FE measurements. Fig. 10.3 (d) represents a model diagram to show that Q-carbon mainly consists of sp^3 bonded carbon and the surrounding of a Q-carbon cluster mainly contains sp^2 rich amorphous carbon which provides pathway to the electrons taking part in the field emission process.

10.4.2 Raman spectroscopy

Micro Raman analysis has been performed on the DLC film (before annealing) and the Q-carbon composite sample (formed after annealing) used for FE measurements to correlate with sp^3 and sp^2 bonding characteristics. Fig. 10.3 (a) shows a Raman spectrum of the as deposited DLC film used to fabricate the Q-carbon composite structure. The calculated sp^3 fraction is found to be 55% in the as-deposited films. After laser annealing treatment, bright regions in the FESEM images refer to Q-carbon clusters and the corresponding Raman spectrum of those regions is shown in Fig. 10.3(c). The calculated sp^3 fraction from this spectrum is 82% for Q-carbon. No significant differences are found in the Raman spectra of Q-carbon features fabricated under the same conditions but with different cluster size. The Raman spectra of the intermediate region in-

between the Q-carbon clusters, amorphous carbon containing area, is shown in Fig. 10.3 (b). The fitting profile from this spectrum gives a sp^2 content of around 65%. A 65% sp^2 content implies the highly conductive nature of this region. Fig. 10.3 (d) represents a model diagram to show that Q-carbon mainly consists of sp^3 bonded carbon and the surrounding of a Q-carbon cluster mainly contains sp^2 rich amorphous carbon which provides pathway for the electrons taking part in the field emission process. The prominent D peak and the G peak (1573 cm^{-1}) in all the Raman spectra confirm the presence of carbonaceous structures in the film. The absence of the Raman peak at ~ 2160 cm^{-1} eliminates the possibility of any sp^1 sites present in the DLC film, Q-carbon structure or intermediate amorphous carbon region.[25]

10.4.3 AFM

The surface morphology of the as grown DLC and laser annealed Q-carbon film is studied by AFM imaging and presented in Fig. 10.4. The DLC film surface has a very smooth morphology, with the rms roughness of around 120 pm within the surface area of 1 μm^2, which is shown in Fig. 10.4 (a). However, the surface of the Q-carbon composite film is rougher than that of DLC, with rms surface roughness being approximately 41 nm over the scan area of 1 μm^2. The AFM data obtained on the Q-carbon sample shown in Fig. 10.4(b) reveal a nanotextured surface morphology. It also shows that the Q-carbon film is composed of distributed small grains, which are embedded randomly. The rms surface roughness increased after the laser annealing. Increased surface roughness means lots of nano-needle like or tiny round shaped Q-carbon structures, which can be compared to the nano-diamond or metal tips that exhibit higher current density at low applied electric field because of the shape effect.[26–28] From the 3D AFM imaging of Q-carbon film we estimate $4x10^7$ grains/1 mm^2 distributed inside the clusters. This refers to a high number density of the emission sites in the Q-carbon composite structure. Therefore Q-carbon nanocomposite film,

having such surface morphology, naturally lends itself to the field electron enhancement needed for field emission applications.

10.4.4 Field emission measurements

The FE measurement was performed with the Q-carbon sample as a cathode. The emission current density as a function of the applied electric field is shown in Fig. 10.5 (a). In this study, we define the turn-on electric field as the applied electric field to attain a current density of 1 $\boldsymbol{\mu}$A/cm^2. The turn-on field for Q-carbon FE device is found to be 2.4 V/$\boldsymbol{\mu}$m. A maximum current density of 32 $\boldsymbol{\mu}$A/cm^2 was observed at an applied field of 2.67 V/$\boldsymbol{\mu}$m. The field emission of the Q-carbon is very stable at this current density. The FE measurements were repeated at least 6 times on the sample and no change was observed in the turn-on electric field and the maximum current density indicating sample robustness and stability. Further, no surface damage was observed in the emitting regions suggesting a non-destructive FE mechanism. The field emission characteristics of the Q-carbon do not show any hysteresis during subsequent voltage cycles.

The mechanism of electron emission under an applied electric field is explained by the Fowler-Nordheim (F−N) theory, which describes the emission of electrons from the front surface of an emitter via tunneling to a suitable anode. The F-N theory for semiconductors is given by [29,30]

$$J = A\left(\frac{\beta^2 E^2}{\emptyset}\right) \exp\left(-\frac{B\emptyset^{3/2}}{\beta E}\right) \exp\left(-\frac{\Delta W^S - \Delta W^P}{2KT}\right) \quad (1)$$

Where, J is the emission current density, E is the applied electric field between the Q-carbon anode and the tungsten metal plate used as cathode. E is usually taken as E=V/d (V is the applied potential and d is the distance between the anode and cathode), Φ is the potential barrier height taken as work function, A and B are constants, A= 1.54 x 10^{-6} A eV V^{-2} and B=6.83 X 10^3 eV$^{-3/2}$ V^{-1} $\boldsymbol{\mu}$m; β is the field enhancement factor and reflects the ability of an FE surface to enhance the local electric field at the emission spots as compared to the average macroscopic value, k is the Boltzmann

constant, T is the absolute temperature, ΔW^S is the surface potential barrier for sp^3-bonded nanostructures due to surface states, and ΔW^P is the decrease of the surface potential barrier due to field penetration.

The experimental FE measurement values were fitted to the F-N model as described by equation (1) and plotted as shown in Fig. 10.5 (b). Based on this model we plotted the $ln\ (J/E^2)$ versus $1/E$, which gives two distinct regions. In the low voltage region (defined as region I) the F-N plot shows a linear behavior characteristic of the metallic conduction. At higher voltage (defined as region II) the current deviates from the linear behavior of region I to saturation. The saturation in region II can be explained by the theory for the FE property of semiconductors.[31] The deviation from a linear dependence to saturation has also been observed in several other FE experimental studies on diamond needles[32], Si[33] and SiC[34] nanowires. The linear behavior of the F-N plot in region I can be explained by the model diagram shown in Fig. 10.6 (a), where we show that the surface potential barrier decreases with increasing applied electric field resulting in a rapid increase in the FE current density. Fig. 10.6 (b) represents the energy bandgap diagram of region II at high electric field, where the field penetration surpasses the surface potential barrier and hence the slope of the FN plot in Fig. 10.5 (b) reduces. Wide bandgap In_2O_3 nanowires have been found to exhibit similar nonlinear characteristics in the F-N plot.[30]

The FE current density essentially depends upon two important parameters - work function (Φ) and the field enhancement factor (β). The FE current density increases with β and decreases with Φ. From the F−N plot, the β can be estimated at high and low applied electric field regions for a given value of Φ, taken as 3.5 eV. The β is normally expressed in terms of the ratio of local electric field (E_{local}) to the applied electric field (E). Large values of β can generate high local electric field at lower applied field to produce sizeable field emission. In the F-N plot the slope

($m=-B\,\Phi^{3/2}/\beta$) can be expressed by the combined effect of work function and local electric field enhancement. Using the expression for slope the calculated value of β was found to be 290 and 2936 at region I and II, respectively. The high value of β also explains the low threshold applied electric field for the FE from Q-carbon sample.

10.4.5 FE Stability

To remove the unwanted volatile/organic species from the surface of the Q-carbon sample, we heated the sample to 300 C for 1 minute before FE measurements. The room temperature FE current density was very stable in time after this preliminary heat treatment. Fig. 10.7 (a) shows the FE current density with time, which illustrates the dependence of the emission current on time for three different values of applied voltages. At high current densities the fluctuations were recorded for 4 hours. The measured fluctuation of the current density was less than ±4%. Additionally, no obvious degradation was observed in the sample after the FE measurements in the FESEM. Wang *et al.* observed applied electric field induced damage in the porous amorphic diamond films, which are very similar to the well-known diamond-like carbon (DLC) films except they consist of very high sp^3/sp^2 carbon ratio (73%-85% sp^3 carbon fraction).[35] The room-temperature *I-V* characteristics of amorphic diamond films were different before and after field emission test. Fig. 10.7 (b) shows almost no change in the room temperature *I-V* characteristics of Q-carbon sample before and after the FE measurements in the voltage range in-between -10V and 10V, which implies that no field induced damage occurred in the Q-carbon sample. The stable and persistent FE current from Q-carbon over a long period of time also supports aforementioned observation (the robustness nature of Q-carbon under high applied electric field).

10.4.6 Discussion

It is established that the amorphous and nanostructured carbon films show two types of field emission properties. First, the back contact controlled FE due to formation of leaky barrier at the film/back contact interface. This is shown in the low conductive polymer-like amorphous carbon films with a small amount of defects.[36] Second, front surface based FE property was observed in nanocrystalline DLC, which is attributed to high defect density and high conductivity of the film.[37] The field emission from Q-carbon shows the front surface based emission characteristics. Several models have been proposed to explain the FE from carbon-based structures, but a complete understanding is still lacking especially when the threshold field for FE is less than 5 V/μm. Similar to our findings $E_T \sim 3$ V/μm has been observed in nanodiamond samples and explained by defect induced conduction mechanism.[38] For $E_T < 10$ V/μm defects and localized states near the Fermi level help to obtain efficient FE devices.[39] These localized states near the Fermi level are observed due to the presence of sp^2 clusters in sp^3 matrix in the carbon-based materials. Q-carbon consists of sp^3 bonded tetrahedral with a packing efficiency of 80% and sp^2-bonded carbon atoms are distributed between sp^3-bonded tetrahedron. The liquid phase mediated growth of Q-carbon during non-equilibrium ultrafast laser annealing helps to attain a homogeneous mixture of the small sp^2 carbon (~18%) with tetrahedrally bonded carbon (~82%). This has a profound contribution in obtaining such low turn-on field and high current density at low applied electric field. The emission mechanism in Q-carbon cold cathode also involves a strong field enhancement at the emission surface. To understand the F-N emission process in the Q-carbon composite structures, it is critical to explain the origin of the large field enhancement factor, which is essential for lowering the barrier for electrons to tunnel towards the anode. In two different studies Guo *et al.*[40] and Carey *et al.*[41] explained that the sp^2 clusters present within the sp^3 matrix help to

raise the field enhancement in carbon-based films. The mixture of sp^2 and sp^3 bonding in Q-carbon structure creates dielectric inhomogeneity.[42] Therefore, the field enhancement in the film is higher in Q-carbon composite structures. Additionally the sp^2 carbon present within the sp^3 hybridized carbon matrix helps in a way that the energy levels of the former one located at or close to the Fermi level. These defect-induced bands near the Fermi level raise the level towards the conduction band and hence the work function decreases. Thus, combination of these two effects, (i) decrease in the work function and (ii) increase in the field enhancement factor due to the coexistence of sp^3-bonded carbon with the sp^2-bonded carbon at a definite ratio, result in improved FE characteristics from the Q-carbon composite film.

During the field emission property investigation of tetrahedral amorphous carbon, the sp^2/sp^3 ratio in the film was found to be one of the fundamental parameters to obtain a better understanding of its emission properties.[43] Although the sp^2 bonded carbon atoms help to raise the Fermi level towards the conduction band resulting in a low work function, however, it was found that the excessive amount of sp^2-bonded carbon atoms deteriorate the FE performance.[43] The optimum percentage of sp^2 bonded carbon atoms for enhanced field emission depends on the atomic features (cluster size and arrangement of the atoms) in the film, and these features depend upon the growth conditions and deposition routes. In the Q-carbon, which is formed by the liquid phase during non-equilibrium laser annealing treatment, the homogeneous mixture of the small sp^2 carbon with tetrahedrally bonded carbon has proven to be effective in attaining outstanding field-emission properties. Additionally, the AFM analysis revealed that the unique microstructure of Q-carbon nano composite has a definite advantage over the DLC films. This type of surface morphology of Q-carbon also causes for a geometric electric field enhancement in the local regions, which is another important factor affecting the field emission. Therefore, the turn-on field of the Q-carbon

film is lower than most of the conventional carbon-based field emitters. The high local field enhancement due to the combined effect of a suitable sp^3/sp^2 ratio and geometric effect facilitate electrons to easily tunnel into vacuum at low electric fields. Thus a turn-on electric field as low as 2.4 V/μm and field amplification factors up to several thousands were obtained from the Q-carbon field emitters. Since we obtain good current densities at low applied electric fields during FE tests in Q-carbon composite structure, a possible model pertaining to explain the excellent field electron emission property is shown in Fig. 10.2 (d). In this model, the sp^2 bonded conducting paths provide an access to electrons to travel the surrounding sp^3 rich Q-carbon structures, which are considered as less-conducting regions (compared to the sp^2 rich amorphous carbon). In a recent study, researchers observed low E_T and high J_E characteristics in diamond and CNT composite structures during the FE measurements, where the sp^3-bonded diamond grains act as sink to the heat produced in CNTs during the measurement and help to attain a more efficient field emission device.[44] Similarly, in the Q-carbon composite structure the sp^2-bonded conducting pathways generate heat due to the movement and scattering of free charge carriers through this region during the FE measurement. The highly thermally conductive sp^3 rich Q-carbon structures help to dissipate the heat fast and make the device more efficient.

This research on the development of Q-carbon cathodes is driven by several potential applications. The Q-carbon cathode film discussed here is operable at low electric-field, which can be easily fabricated within a very short time (250 nanoseconds) via an inexpensive route. The large area reproducibility of Q-carbon samples have potential applications in flat-panel display, fluorescent lighting, power-vacuum-switch to deal with thousands of amperes, frictionless motors, and so on. A current density of ~30 μA/cm^2 can be achieved at an applied field of 2.65 V/μm. This value is quite sufficient to meet the requirements of a field emission device. It is established that

Q-carbon is the hardest material ever known, which is ~40% harder than diamond.[23] The hard Q-carbon is embedded in the ductile amorphous carbon matrix, which provides a very unique combination. This hard and ductile large area nontoxic carbon thin film with excellent FE characteristics could be very attractive for flat panel display with higher flexibility without the usage of any toxic material. Compared to other emissive carbon films, the present films can be deposited, for example, onto WC, steel, glass, sapphire, and polymer substrates. This is a considerable advantage since it allows overcoming the limitations for thermal sensitivity, optical transparency, and/or flexibility of many substrates during the FE operation. The obtained FE properties of Q-carbon composite structure is outstanding compared to most of the carbon-based field emitters. Table 10.1 demonstrates the comparison between different field emission properties from Q-carbon nanocomposite structure and other carbon-based field emitters.

10.5 Summary

In this study, we focused on the design and fabrication process, characterization and field emission properties of large area Q-carbon composite thin films. We have shown that nanostructured Q-carbon films, fabricated from PLD grown DLC thin films followed by PLA, are excellent electron field emitters. It has been suggested that the rise of the Fermi level towards the conduction band due to the presence of sp^2 carbon in the sp^3 rich Q-carbon plays an important role in enhancing the electron field emission from the surface of the film. The low threshold field, hysteresis free extremely stable lifetimes (<±4% variation over 4 hours) and room-temperature and nonequilibrium processing make these nanostructured Q-carbon films very suitable for display device applications. Our findings could provide an in-depth insight to understand field emissions from Q-carbon composite system on other substrates as well. Thus, Q-carbon-based films provide highly efficient platform for high-performance FE devices.

Table 10. 1**:** Comparison between different field emission properties from Q-carbon nanocomposite structure and other form of carbon-based field emitters.

Field emitters	Turn on field (V/μm)	Threshold field (V/μm)	Field enhancement factor (β)	Ref.	Year
Q-carbon	2.4 (1 μA/cm^2)	2.65 (30 μA/cm^2)	2936	This study	2018
Diamond	4.27 (0.1 μA/cm^2)	7.6 (113.2 μA/cm^2)	1000	[45,46]	2003 & 1996
Nano-diamond films	2.2 (1 μA/cm^2)	6.4 (0.72 mA/cm^2)	-	[47]	2003
Graphene nanosheet array	2.6 (10 μA/cm^2)	5.8 (1 mA/cm^2)	3788	[48]	
DLC/Si	5.6 (0.01 μA/cm^2)	14.3 (15.2 μA/cm^2)	-	[49]	2000
Carbon nanotubes (CNT) arrays	0.85 (0.1μA/cm^2)	1.67 (1 mA/cm^2)	3517	[50]	2008
Carbon nanowalls	4.7 (0. 1mA/cm^2)	6 (1mA/cm^2)	1399	[51]	2015
Vertically aligned CNT/DLC	2.0 (undefined)	2.1 (10 μA /cm^2)	2529	[52]	2013

10.6 Figures

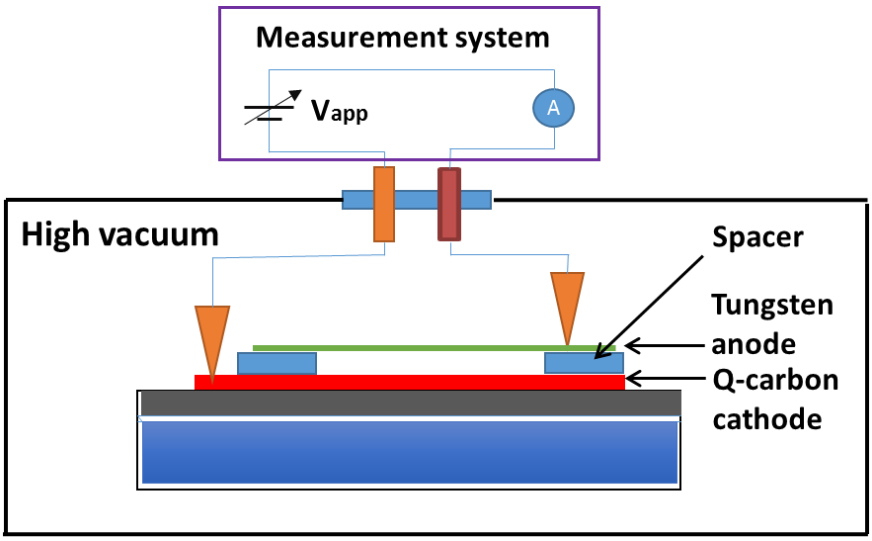

Figure 10. 1**:** Field emission setup used for electron emission measurements of Q-carbon sample.

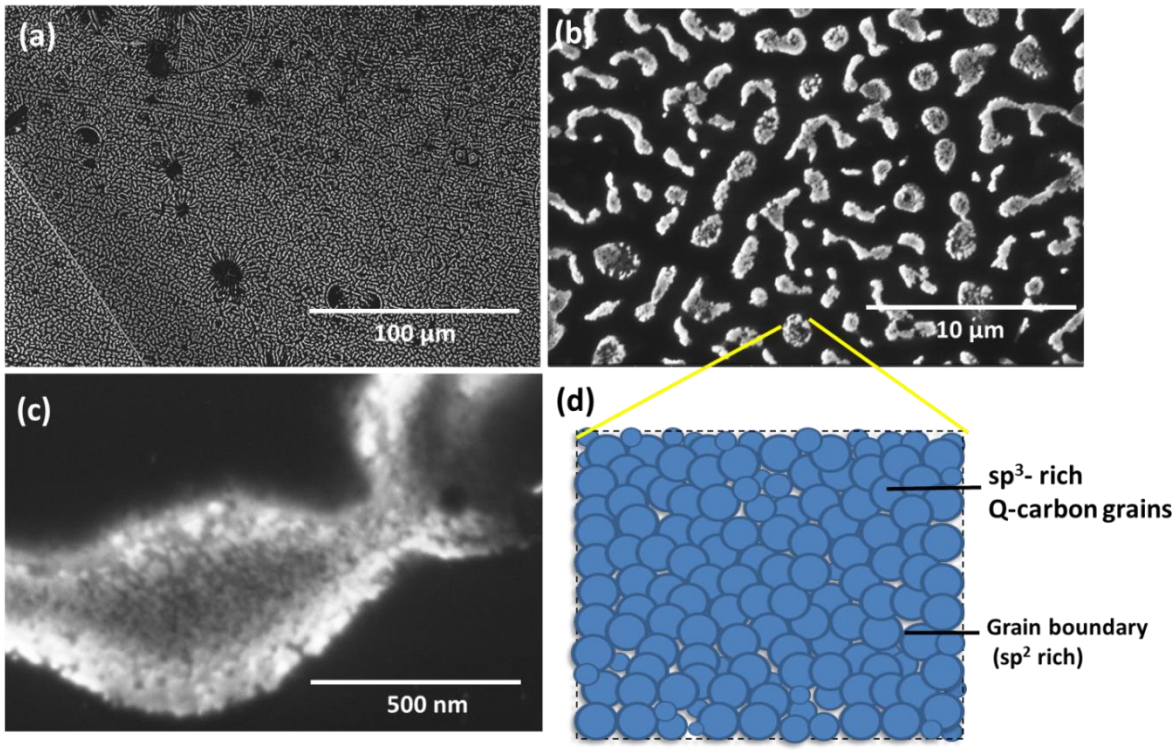

Figure 10. 2**:** (a) SEM image of large area Q-carbon composite structure, (b) high magnification image of the same film, (c) an individual Q-carbon cluster consisting of four-way bonded (sp^3) carbon rich Q-carbon surrounded by sp^2-rich amorphous carbon, (d) Proposed model where Q-

carbon grains are considered as emission regions and amorphous carbon rich boundaries are considered as conducting pathways.

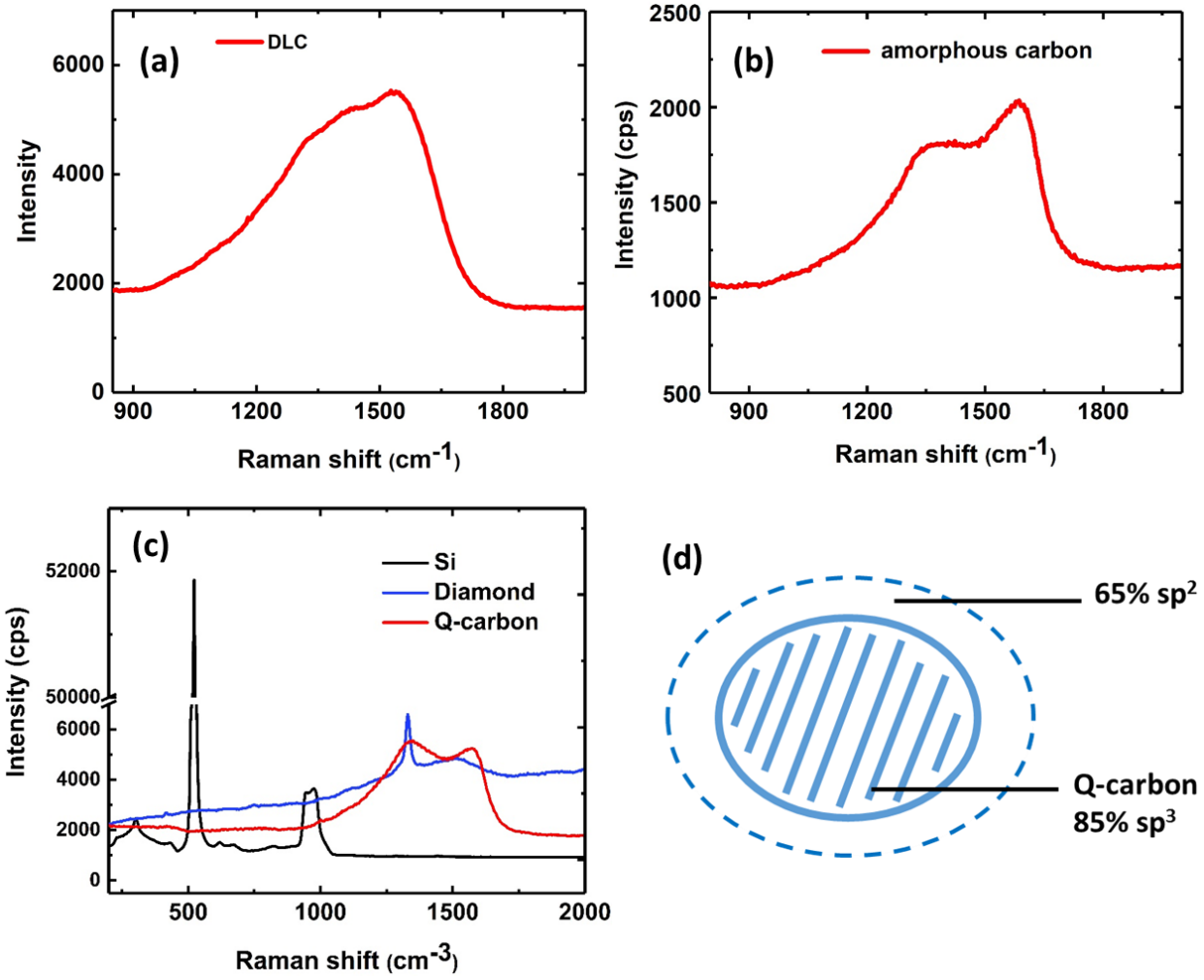

Figure 10. 3**:** Micro-Raman spectra of (a) DLC film, (b) amorphous carbon region, and (c) Q-carbon along with the Si standard (520 cm^{-1}) and diamond (1333 cm^{-1}). (d) A model diagram depicts the sp^2 and sp^3 carbon fractions in a Q-carbon cluster and its surrounding.

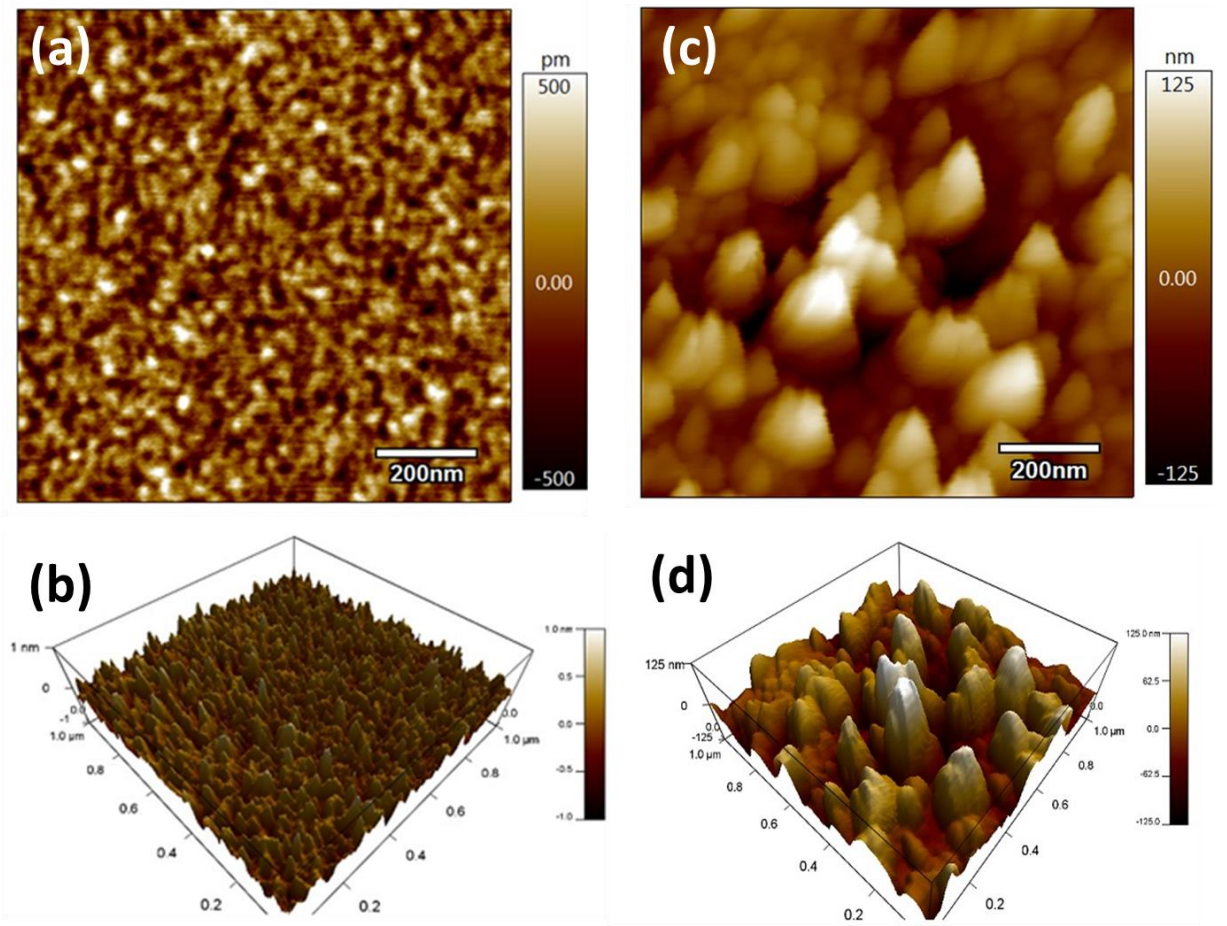

Figure 10. 4**:** Surface morphology analysis of (a) DLC film and (b) Q-carbon composite film. 3D AFM image of (c) PLD grown DLC film, and (d) Q-carbon film with an areal density of emission sites.

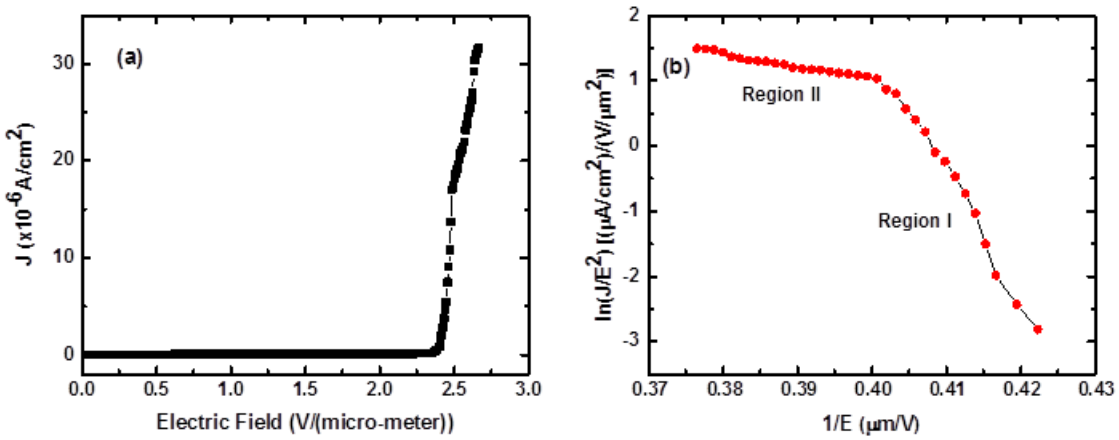

Figure 10. 5**:** (a) Field emission plot of Q-carbon thin film (*J*−*E* characteristics). (b) F−N plot shows nonlinear behavior with two distinct slopes at high and low applied electric fields.

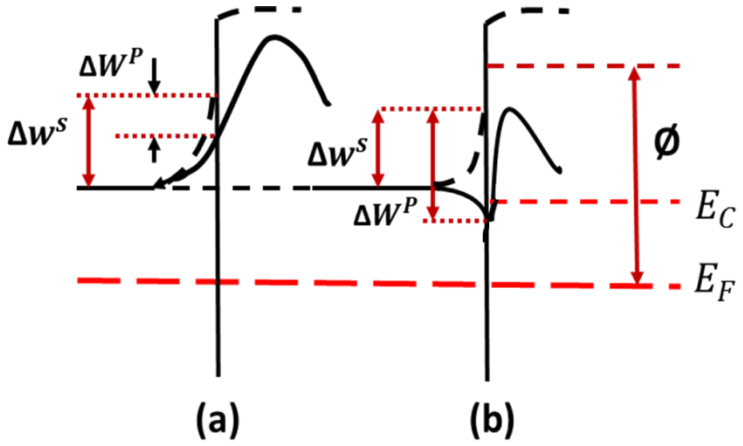

Figure 10. 6**:** Energy band diagram of Q-carbon near the emission surface under different applied electric fields producing (a) $\Delta w^s > \Delta W^P$ and (b) $\Delta w^s < \Delta W^P$.

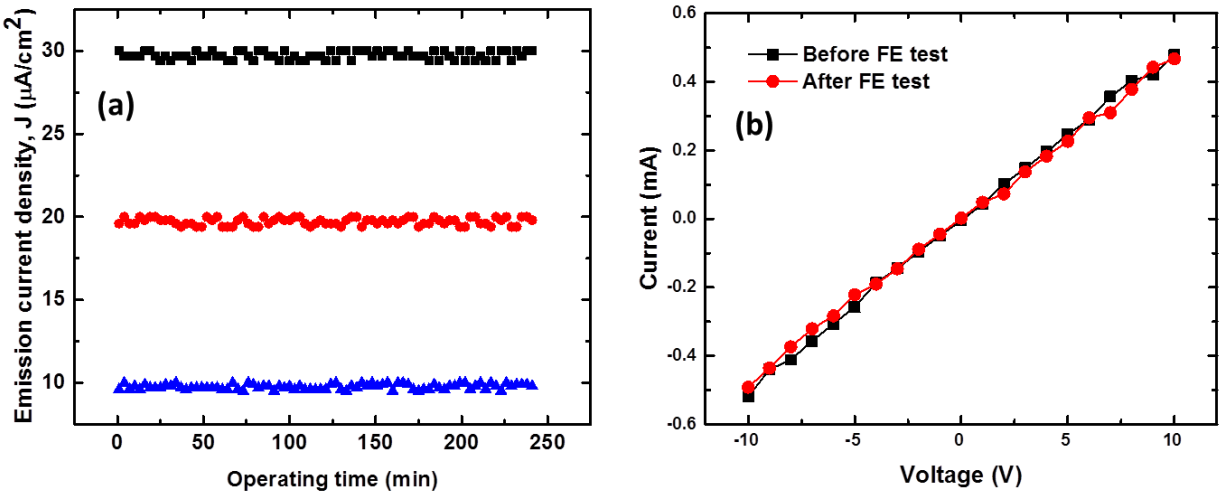

Figure 10. 7**:** (a) Field emission current stability test data shows the emission current density (*J*) *vs* operating time (*T*) characteristics of Q-carbon field emitter under three constant applied electric fields. The long-term fluctuations observed from these results are ±4 %. (b) Current-voltage curves before and after FE tests on the Q-carbon sample.

References

[1] W.I. Milne, K.B.K. Teo, G. a. J. Amaratunga, P. Legagneux, L. Gangloff, J.-P. Schnell, V. Semet, V.T. Binh, O. Groening, Carbon nanotubes as field emission sources, J. Mater. Chem. 14 (2004) 933–943. https://doi.org/10.1039/B314155C.

[2] Y. Saito, S. Uemura, Field emission from carbon nanotubes and its application to electron sources, Carbon. 38 (2000) 169–182. https://doi.org/10.1016/S0008-6223(99)00139-6.

[3] J. Kennedy, F. Fang, J. Futter, J. Leveneur, P.P. Murmu, G.N. Panin, T.W. Kang, E. Manikandan, Synthesis and enhanced field emission of zinc oxide incorporated carbon nanotubes, Diam. Relat. Mater. 71 (2017) 79–84. https://doi.org/10.1016/j.diamond.2016.12.007.

[4] F.J. Himpsel, J.A. Knapp, J.A. VanVechten, D.E. Eastman, Quantum photoyield of diamond(111)-A stable negative-affinity emitter, Phys. Rev. B. 20 (1979) 624–627. https://doi.org/10.1103/PhysRevB.20.624.

[5] J. Robertson, Mechanisms of electron field emission from diamond, diamond-like carbon, and nanostructured carbon, J. Vac. Sci. Technol. B Microelectron. Nanometer Struct. Process. Meas. Phenom. 17 (1999) 659–665. https://doi.org/10.1116/1.590613.

[6] C. Wenger, J. Kitzmann, A. Wolff, M. Fraschke, C. Walczyk, G. Lupina, W. Mehr, M. Junige, M. Albert, J.W. Bartha, Graphene based electron field emitter, J. Vac. Sci. Technol. B Nanotechnol. Microelectron. Mater. Process. Meas. Phenom. 33 (2015) 01A109. https://doi.org/10.1116/1.4905937.

[7] E. Manikandan, G. Kavitha, J. Kennedy, Epitaxial zinc oxide, graphene oxide composite thin-films by laser technique for micro-Raman and enhanced field emission study, Ceram. Int. 40 (2014) 16065–16070. https://doi.org/10.1016/j.ceramint.2014.07.129.

[8] C. Nützenadel, O.M. Küttel, O. Gröning, L. Schlapbach, Electron field emission from diamond tips prepared by ion sputtering, Appl. Phys. Lett. 69 (1996) 2662–2664. https://doi.org/10.1063/1.117551.

[9] A. Wisitsora-at, W.P. Kang, J.L. Davidson, Y. Gurbuz, D.V. Kerns, Field emission enhancement of diamond tips utilizing boron doping and surface treatment, Diam. Relat. Mater. 8 (1999) 1220–1224. https://doi.org/10.1016/S0925-9635(99)00008-4.

[10] E. Manikandan, J. Kennedy, G. Kavitha, K. Kaviyarasu, M. Maaza, B.K. Panigrahi, U.K. Mudali, Hybrid nanostructured thin-films by PLD for enhanced field emission performance for radiation micro-nano dosimetry applications, J. Alloys Compd. 647 (2015) 141–145. https://doi.org/10.1016/j.jallcom.2015.06.102.

[11] D.E. Motaung, M.K. Moodley, E. Manikandan, N.J. Coville, In situ optical emission study on the role of C2 in the synthesis of single-walled carbon nanotubes, J. Appl. Phys. 107 (2010) 044308. https://doi.org/10.1063/1.3311563.

[12] J. Robertson, M.J. Rutter, Band diagram of diamond and diamond-like carbon surfaces, Diam. Relat. Mater. 7 (1998) 620–625. https://doi.org/10.1016/S0925-9635(97)00257-4.

[13] J. Robertson, Amorphous carbon cathodes for field emission display, Thin Solid Films. 296 (1997) 61–65. https://doi.org/10.1016/S0040-6090(96)09381-9.

[14] W. Lei, C. Li, M.T. Cole, K. Qu, S. Ding, Y. Zhang, J.H. Warner, X. Zhang, B. Wang, W.I. Milne, A graphene-based large area surface-conduction electron emission display, Carbon. 56 (2013) 255–263. https://doi.org/10.1016/j.carbon.2013.01.004.

[15] V.P. Verma, S. Das, I. Lahiri, W. Choi, Large-area graphene on polymer film for flexible and transparent anode in field emission device, Appl. Phys. Lett. 96 (2010) 203108. https://doi.org/10.1063/1.3431630.

[16] Z. Xiao, J. She, S. Deng, Z. Tang, Z. Li, J. Lu, N. Xu, Field Electron Emission Characteristics and Physical Mechanism of Individual Single-Layer Graphene, ACS Nano. 4 (2010) 6332–6336. https://doi.org/10.1021/nn101719r.

[17] S. Santandrea, F. Giubileo, V. Grossi, S. Santucci, M. Passacantando, T. Schroeder, G. Lupina, A. Di Bartolomeo, Field emission from single and few-layer graphene flakes, Appl. Phys. Lett. 98 (2011) 163109. https://doi.org/10.1063/1.3579533.

[18] L. Chen, H. Yu, J. Zhong, L. Song, J. Wu, W. Su, Graphene field emitters: A review of fabrication, characterization and properties, Mater. Sci. Eng. B. 220 (2017) 44–58. https://doi.org/10.1016/j.mseb.2017.03.007.

[19] M.Y. Chen, K.Y. Wu, J. Hwang, M.T. Chang, L.J. Chou, C.S. Kou, Field emission from diamond nanotips treated with nitrogen plasma immersion ion implantation, Nanotechnology. 18 (2007) 455706. https://doi.org/10.1088/0957-4484/18/45/455706.

[20] V.I. Kleshch, S.T. Purcell, A.N. Obraztsov, Single Crystal Diamond Needle as Point Electron Source, Sci. Rep. 6 (2016) 35260. https://doi.org/10.1038/srep35260.

[21] J. Narayan, A. Bhaumik, S. Gupta, A. Haque, R. Sachan, Progress in Q-carbon and related materials with extraordinary properties, Mater. Res. Lett. 6 (2018) 353–364. https://doi.org/10.1080/21663831.2018.1458753.

[22] J. Narayan, A. Bhaumik, Novel phase of carbon, ferromagnetism, and conversion into diamond, J. Appl. Phys. 118 (2015) 215303. https://doi.org/10.1063/1.4936595.

[23] J. Narayan, S. Foo, A. Bhaumik, R. Sachan, F. Cellini, E. Reido, Q-carbon is harder than diamond, MRS Commun. Submitt. (2018). https://doi.org/10.1016/j.proeng.2017.04.118.

[24] A. Bhaumik, R. Sachan, S. Gupta, J. Narayan, Discovery of High-Temperature Superconductivity (Tc = 55 K) in B-Doped Q-Carbon, ACS Nano. 11 (2017) 11915–11922. https://doi.org/10.1021/acsnano.7b06888.

[25] E. Barborini, P. Piseri, A. Li Bassi, A.C. Ferrari, C.E. Bottani, P. Milani, Synthesis of carbon films with controlled nanostructure by separation of neutral clusters in supersonic beams, Chem. Phys. Lett. 300 (1999) 633–638. https://doi.org/10.1016/S0009-2614(98)01449-3.

[26] W. Wei, K. Jiang, Y. Wei, P. Liu, K. Liu, L. Zhang, Q. Li, S. Fan, LaB6 tip-modified multiwalled carbon nanotube as high quality field emission electron source, Appl. Phys. Lett. 89 (2006) 203112. https://doi.org/10.1063/1.2388862.

[27] G. Ulisse, F. Brunetti, A. Vomiero, M.M. Natile, G. Sberveglieri, A. Di Carlo, Hybrid thermal-field emission of ZnO nanowires, Appl. Phys. Lett. 99 (2011) 243108. https://doi.org/10.1063/1.3670331.

[28] O. Gröning, O.M. Küttel, Ch. Emmenegger, P. Gröning, L. Schlapbach, Field emission properties of carbon nanotubes, J. Vac. Sci. Technol. B Microelectron. Nanometer Struct. Process. Meas. Phenom. 18 (2000) 665–678. https://doi.org/10.1116/1.591258.

[29] R. Stratton, Field Emission from Semiconductors, Proc. Phys. Soc. Sect. B. 68 (1955) 746. https://doi.org/10.1088/0370-1301/68/10/307.

[30] S.Q. Li, Y.X. Liang, T.H. Wang, Nonlinear characteristics of the Fowler–Nordheim plot for field emission from In2O3 nanowires grown on InAs substrate, Appl. Phys. Lett. 88 (2006) 053107. https://doi.org/10.1063/1.2159092.

[31] L.M. Baskin, O.I. Lvov, G.N. Fursey, General features of field emission from semiconductors, Phys. Status Solidi B. 47 (1971) 49–62. https://doi.org/10.1002/pssb.2220470105.

[32] V.I. Kleshch, S.T. Purcell, A.N. Obraztsov, Single Crystal Diamond Needle as Point Electron Source, Sci. Rep. 6 (2016) 35260. https://doi.org/10.1038/srep35260.

[33] M. Choueib, R. Martel, C.S. Cojocaru, A. Ayari, P. Vincent, S.T. Purcell, Current Saturation in Field Emission from H-Passivated Si Nanowires, ACS Nano. 6 (2012) 7463–7471. https://doi.org/10.1021/nn302744e.

[34] M. Choueib, A. Ayari, P. Vincent, S. Perisanu, S.T. Purcell, Evidence for Poole–Frenkel conduction in individual SiC nanowires by field emission transport measurements, J. Appl. Phys. 109 (2011) 073709. https://doi.org/10.1063/1.3556736.

[35] W.N. Wang, N.A. Fox, D. Richardson, G.M. Lynch, J.W. Steeds, Field emission properties of diode devices based on amorphic diamond-Si heterojunctions, J. Appl. Phys. 81 (1997) 1505–1508. https://doi.org/10.1063/1.363915.

[36] N. Dwivedi, S. Kumar, R.K. Tripathi, J.D. Carey, H.K. Malik, M.K. Dalai, Structural and Electronic Characterization of Nanocrystalline Diamondlike Carbon Thin Films, ACS Appl. Mater. Interfaces. 4 (2012) 5309–5316. https://doi.org/10.1021/am301252e.

[37] J.D. Carey, Engineering the next generation of large-area displays: prospects and pitfalls, Philos. Trans. R. Soc. Lond. Math. Phys. Eng. Sci. 361 (2003) 2891–2907. https://doi.org/10.1098/rsta.2003.1283.

[38] T. Ikeda, K. Teii, Origin of low threshold field emission from nitrogen-incorporated nanocrystalline diamond films, Appl. Phys. Lett. 94 (2009) 143102. https://doi.org/10.1063/1.3115767.

[39] J.D. Carey, R.D. Forrest, S.R.P. Silva, Origin of electric field enhancement in field emission from amorphous carbon thin films, Appl. Phys. Lett. 78 (2001) 2339–2341. https://doi.org/10.1063/1.1366369.

[40] P.S. Guo, Z. Sun, S.M. Huang, Y. Sun, Temperature effect on field emission properties and microstructures of polymer-based carbon films, J. Appl. Phys. 98 (2005) 074906. https://doi.org/10.1063/1.2084310.

[41] J.D. Carey, R.D. Forrest, R.U.A. Khan, S.R.P. Silva, Influence of sp2 clusters on the field emission properties of amorphous carbon thin films, Appl. Phys. Lett. 77 (2000) 2006–2008. https://doi.org/10.1063/1.1312202.

[42] J.D. Carey, R.D. Forrest, S.R.P. Silva, Origin of electric field enhancement in field emission from amorphous carbon thin films, Appl. Phys. Lett. 78 (2001) 2339–2341. https://doi.org/10.1063/1.1366369.

[43] B.S. Satyanarayana, A. Hart, W.I. Milne, J. Robertson, Field emission from tetrahedral amorphous carbon, Diam. Relat. Mater. 7 (1998) 656–659. https://doi.org/10.1016/S0925-9635(97)00296-3.

[44] D. Varshney, B.R. Weiner, G. Morell, Growth and field emission study of a monolithic carbon nanotube/diamond composite, Carbon. 48 (2010) 3353–3358. https://doi.org/10.1016/j.carbon.2010.05.025.

[45] C. Nützenadel, O.M. Küttel, O. Gröning, L. Schlapbach, Electron field emission from diamond tips prepared by ion sputtering, Appl. Phys. Lett. 69 (1996) 2662–2664. https://doi.org/10.1063/1.117551.

[46] E.S. Cho, S.J. Kwon, H.C. Yang, H.S. Uh, Y.H. Kim, B.-G. Park, J.D. Lee, Fabrication and characterization of phosphorus-implanted mold-type diamond field-emitter arrays, Thin Solid Films. 435 (2003) 324–328. https://doi.org/10.1016/S0040-6090(03)00342-0.

[47] S.G. Wang, Q. Zhang, S.F. Yoon, J. Ahn, Q. Zhou, Q. Wang, D.J. Yang, J.Q. Li, S. Zhang Shanyong, Electron field emission enhancement effects of nano-diamond films, Surf. Coat. Technol. 167 (2003) 143–147. https://doi.org/10.1016/S0257-8972(02)00901-5.

[48] L. Li, W. Sun, S. Tian, X. Xia, J. Li, C. Gu, Floral-clustered few-layer graphene nanosheet array as high performance field emitter, Nanoscale. 4 (2012) 6383–6388. https://doi.org/10.1039/C2NR31524F.

[49] D.S. Mao, X. Wang, W. Li, X.H. Liu, Q. Li, J.F. Xu, K. Okano, Electron field emission from a patterned diamond-like carbon flat thin film using a Ti interfacial layer, J. Vac. Sci. Technol. B Microelectron. Nanometer Struct. Process. Meas. Phenom. 18 (2000) 2420–2423. https://doi.org/10.1116/1.1289926.

[50] G. Chen, D.H. Shin, T. Iwasaki, H. Kawarada, C.J. Lee, Enhanced field emission properties of vertically aligned double-walled carbon nanotube arrays, Nanotechnology. 19 (2008) 415703. https://doi.org/10.1088/0957-4484/19/41/415703.

[51] L. Cui, J. Chen, B. Yang, D. Sun, T. Jiao, RF-PECVD synthesis of carbon nanowalls and their field emission properties, Appl. Surf. Sci. 357 (2015) 1–7. https://doi.org/10.1016/j.apsusc.2015.08.252.

[52] H. Zanin, P.W. May, M.H.M.O. Hamanaka, E.J. Corat, Field Emission from Hybrid Diamond-like Carbon and Carbon Nanotube Composite Structures, ACS Appl. Mater. Interfaces. 5 (2013) 12238–12243. https://doi.org/10.1021/am403386a.

11. Characteristics of electron field emission in Q-carbon

Ariful Haque and Jagdish Narayan

Materials Science and Engineering, North Carolina State University, Raleigh, North Carolina 27695.7916, USA

11.1 Abstract

In this study, we have investigated electron field emission (EFE) characteristics of Q-carbon at room temperature and above. At room temperature the Q-carbon requires only ~2.4V/μm applied electric field to turn-on the EFE. The EFE properties of the Q-carbon composite structure improve with temperature by lowering the turn-on field and increasing the current density. At 500 K we observed a turn-on field of ~ 2.34V/μm, and a maximum current density was found to be ~ 53μA/cm^2 at 2.66V/μm. The Q-carbon field emitters also show a very stable EFE characteristics (within 7% fluctuations) over time for current intensities between 7.5μA/cm^2 and 47μA/cm^2.

11.2 Introduction

Electron field emission (EFE) is considered as the only electron emission process compatible with the vacuum electronics due to the fast response time, low power consumption, cathode-ray tube like colors and wide viewing angles [1,2]. However, incorporation of cold field emitters in practical electronic devices is still quite challenging due to the stringent requirements of long cathode lifetime with high stability. Since the discovery of the excellent EFE properties of Q-carbon composite structure [3], there has been significant increase of interest in studying the emission stability of this material for practical device applications. The carbon-based field emitters such as diamond, diamond-like carbon (DLC), nano-diamond, and carbon nanotubes have been investigated, however, reliable commercial devices such as field emission lighting elements, frictionless motors, flat panel displays, etc. are still challenging to develop due to several barriers

[4]. Over the decades, diamond has been considered as one of the most promising materials for cold-cathode applications owing to its negative electron affinity (NEA) [5,6]. However, the ideal single crystal diamond cannot provide the required amount of electrons for the field emission, and the band structure of diamond is unsuitable for the transport of those electrons to the surface. Usually the diamond surface is terminated by hydrogen to obtain NEA for enhanced EFE properties. But exposing the hydrogen-terminated diamond surface to high fields and to oxygen ambient for several days is enough to replace some of the surface hydrogen with different oxygen groups. This diminish the NEA and thereby reduces the percentage of the emitting surface area, and worsen the EFE performance [7]. Therefore, researchers have tried nanometer size or highly defective crystallites having much degraded physical properties than the crystalline diamond, such as polycrystalline diamond, nitrogen-incorporated ultrananocrystalline diamond, and DLC [8–11]. The EFE characteristics from the DLC and amorphous carbon can be compared to vacuum breakdown at high electric field and the electron affinity was found to be positive in these materials, which is undesirable for good field emission characteristics [12,13]. The field emission from DLC film has been found to be related to the surface roughness [14]. But the roughness in the DLC film is quite low and not easy to control. A change to the sp^2 surface bonding characteristics at a relatively low applied electric field was also observed in the DLC film during the EFE measurements, which significantly affects the EFE properties [14]. The poor thermal stability and high intrinsic stress in DLC films lead to the degradation of electrical and optical properties and result in peeling of the film from the substrate during high temperature EFE tests [15]. Moreover, damages on the surface, such as the formation of crater, tip-hill-like structures, cracking, amorphization or just traces of surface melting, have been observed after EFE measurements from DLC and CVD diamond [16,17]. These factors significantly affect the EFE

performance and cause serious problems in different EFE related applications of these materials [18]. The carbon nanotube has also been considered as a promising material for field emission applications [19,20]. However, the fabrication and alignment of carbon nanotubes are found to be quite difficult. The growth mechanism of both carbon nanotube and diamond require high temperature and very precise environments.[21] Additionally, the dependence of EFE characteristics on the quantity and type of adsorbed molecules present in the carbon nanotubes and a considerable spread in electronic properties of carbon nanotubes are responsible for the lack of control and uncertainty in the emission characteristics [22]. So far, EFE has only been observed from the edges of graphene and graphene oxide sheets [23,24]. Since the field emission is only from edges, nanotubes and graphene composites display nonuniformity which is difficult to control for device applications [25,26]. Researchers also observed local peeling of the graphene edge from the substrate due to the ponderomotive force during the field emission [25]. Overall, poor uniformity, lack of control during fabrication and field emission, low current stability, and structural instability and poor robustness during emission measurements have hindered the commercial development of the aforementioned carbon based field emitters.

The discovery of Q-carbon heralds a new era for field-emission devices, as it can address the problems related to the structural and emission instability with its excellent mechanical robustness, chemical inertness, and excellent emission properties [27]. Q-carbon is fabricated by the ultrafast quenching of amorphous carbon using pulsed laser annealing over a large area on different substrates. Studies on Q-carbon have shown that it is harder than diamond (40% harder) [28], has high thermal conductivity, robust ferromagnetism at room temperature [27], and it shows extraordinary Hall effect [29], and record BCS high-temperature superconductivity upon doping with B [28]. Q-carbon overcomes the aforementioned problems related to the carbon-based

practical EFE devices. Q-carbon is considered among the most promising candidates for large area field emitter applications because of its easy fabrication processes and an outstanding field emission characteristics such as low threshold voltage for electron emission and high field enhancement factor [3]. Q-carbon films can be deposited using a laser scanning system with a high deposition rate at room temperature over a large area. This is a prerequisite for producing wide, commercial flat-panel displays for practical applications. Another hindrance for the practical realization of carbon-based field emitters is the absence of long-term field emission stability. Most of the studies have been conducted on the low threshold fields, high field emission current densities, and failure of the emission device. However, complete studies on the fundamental factors that contribute to the field emission stability are still lacking. In this paper, we report the study on the long-term stability of the field emission current density from Q-carbon using different techniques such as Raman spectroscopy, high resolution scanning electron microscopy, and electrical measurements. We obtained very high stability of EFE current over time at different current density levels and over a large range of temperatures.

11.3 Experimental

A high quality compressed graphite target was used to deposit DLC film with a mixture of sp^3/sp^2 bonding and with thickness ~500 nm on the r-sapphire substrate. The graphite was mounted on a rotating target holder at a distance of ~4 cm from the substrate. Commercially available 2-inch wafer of c-plane sapphire was cut into 1 cm x 1 cm as a substrate. The substrate was ultrasonically cleaned with acetone for 10 minutes, with methanol for 5 minutes, and dried with nitrogen gas. The DLC thin film was deposited on this substrate in a stainless steel chamber which evacuated to a base pressure of $\sim 1 \times 10^{-6}$ torr. We used a pulsed krypton fluoride (KrF) excimer laser (λ = 248 nm, repetition rate 5 Hz/s, pulse width 20 ns, laser fluence of ~2 J/cm^2) during

deposition. The DLC films were irradiated by an ArF laser (wavelength = 193 nm, pulse duration = 20 ns) pulses with an energy density in-between 0.6 Jcm^{-2} and 0.7 Jcm^{-2} for conversion into Q-carbon composite structure. During the laser annealing process, the as-deposited films were melted in a super-undercooled state and subsequently quenched within 200-250 nanoseconds.

A WITec confocal Raman microscope system (alpha300M) with a maximum sensitivity excitation wavelength of 532.16 nm was used to identify the characteristics of DLC and Q-carbon. A crystalline Si sample (with characteristic Raman peak at 520.6 cm^{-1}) was used to calibrate the Raman spectrum. Care was taken to avoid damaging the sample by the laser excitation. Field emission scanning electron microscopy (FESEM) imaging was performed using an FEI Verios 460L SEM, which provides sub-nanometer resolution, to study the morphology of the Q-carbon composite structures. Using ImageJ software, we calculated the percentage of the actual coverage of the Q-carbon in the sp^2 rich amorphous carbon matrix.

We performed EFE measurements on the Q-carbon sample in the parallel plate configuration with an anode of Tungsten and a 100 µm spacer made of glass inside a clean high vacuum chamber at below 5×10^{-7} Torr pressure. The measurements were carried out at a distance of 100μm between the Q-carbon film cathode and the anode. We did not use any further processing treatment to obtain emission from the Q-carbon film. After the test, we did not observe any macroscopic surface damage on the film, which is expected as the applied field was kept low and the film was found to be robust. The area of the film was greater than 25 mm^2. A complete set-up for the EFE measurements of Q-carbon has been shown in our previous work [3].

11.4 Analyses of the results

11.4.1 FESEM

Fig. 11.1 (a-c) show field-emission scanning electron microscopy (FESEM) images of the Q-carbon composite structures at different magnifications. The low-magnification image shown in Fig. 11.1 (a) indicates that the laser annealed Q-carbon composite structure can be fabricated over a large area. Fig. 11.1 (b), a high magnification image of the same structure, shows individual Q-carbon clusters. The sp^2 rich amorphous carbon surrounds the sp^3 rich Q-carbon grains in each of these clusters. The amount of Q-carbon coverage (in the form of clusters) in the amorphous carbon matrix is considerably less, which is evident from these two figures. Fig. 11.1 (c) is a very high magnification image of the same structure, which shows the presence of Q-carbon grains inside a cluster. The sp^2-rich grain boundaries present in-between the grains, which provide the conducting pathway to the electrons during the EFE measurements. The high density of the grain boundaries inside the Q-carbon clusters connected with the amorphous carbon matrix gives an efficient EFE device.

11.4.2 Raman spectroscopy

Fig. 11.2 shows the Raman spectrum of the Q-carbon structure. This spectrum confirms the presence of both D and G peak at 1343 and 1568 cm^{-1}, respectively, meaning that the Q-carbon film consists of sp^3-bonds mixed with sp^2-bonds [30]. The peak fitting of the Raman spectrum using the Gaussian distribution function gives the percentage of sp^3 carbon of around 80-82%. The rest of the carbon remains in sp^2 form. These results are in agreement with the early studies on Raman and EELS analyses of Q-carbon structures [27,31]. The Raman spectrum of the carbon structures is also sensitive to the ratios of bonds present in the structure and the local environment as well. Deconvolution of the Raman spectrum also reveals that the position of the G-band, occurs

at 1582 cm^{-1} for PLD grown DLC film, is shifted to 1568 cm^{-1} after the pulsed laser annealing. The red shift in the G-band of Raman spectrum is due to the increase in the sp^3-bonds in the amorphous carbon structure [32]. The higher sp^3 fraction in the Q-carbon structure could be responsible for very low or negative electron affinity. The sp^2 bonded carbon present in the structure provides the conductivity to the charge carriers taking part in the electron emission process. As a result, the Q-carbon composite structure provides an ideal platform for excellent EFE characteristics. The Raman spectra of the DLC film before laser annealing and the amorphous carbon region (in between the Q-carbon clusters) are provided in the supplementary information.

11.4.3 Electron field emission properties

Fig. 11.3 (a-e) show the field emission current density-electric field (*J*-*E*) characteristics of the Q-carbon composite film at room temperature and above (up to 500 K). These EFE plots demonstrate exponential characteristics for the applied field values above the turn-on field. Such a fine field emission property can be ascribed to the coexistence of sp^3-bonded carbon with the sp^2-bonded carbon at a suitable ratio in the Q-carbon clusters, providing an ideal platform for excellent EFE. The Q-carbon consists of sp^3 bonded tetrahedra which are packed with 80% packing efficiency [28]. The sp^2-bonded carbon exists in-between sp^3-bonded tetrahedron. The tetrahedrally bonded carbon acts as field emitters, whereas the sp^2-bonded carbon provide a good conduction path for transporting electrons during the EFE tests [33]. The observed EFE capacity of Q-carbon field emitter (J~53 μA/cm^2 at E~2.66 V/μm) is significantly larger than other forms of carbon-based field emitters [33]. The EFE experiment was repeated several times, and the magnitude of the turn-on electric field and the maximum current density did not fluctuate with time. The EFE characteristics were reproducible during subsequent voltage cycles without any hysteresis effects.

The data from the EFE measurements were plotted in accordance with the Fowler-Nordheim (F-N) coordinates and shown in the insets of corresponding *J-E* plots in Fig. 11.3 (a-e). The F-N theory for semiconductors is given by [34,35] the following equation.

$$J = A\left(\frac{\beta^2 E^2}{\emptyset}\right) \exp\left(-\frac{B\emptyset^{3/2}}{\beta E}\right) \exp\left(-\frac{\Delta W^S - \Delta W^P}{2KT}\right) \quad (1)$$

Where, *J* is the emission current density, *E* is the applied electric field between the Q-carbon anode and the tungsten metal plate used as cathode. *E* is usually taken as E=V/d (*V* is the applied potential and *d* is the distance between the anode and cathode), Φ is the potential barrier height taken as work function, *A* and *B* are constants, *A*= 1.54 x 10^{-6} A eV V^{-2} and *B*=6.83 X 10^3 $eV^{-3/2}$ V^{-1} $\boldsymbol{\mu}$m; β is the field enhancement factor and reflects the ability of an electron emission surface to enhance the local electric field at the emission spots as compared to the average macroscopic value, *k* is the Boltzmann constant, *T* is the absolute temperature, ΔW^S is the surface potential barrier for sp^3-bonded nanostructures due to surface states, and ΔW^P is the decrease of the surface potential barrier due to field penetration. The *J–E* plots in Fig. 11.3 (a-e) fit well to the F–N relation at the low field region and it deviates from the linearity due to the current saturation of Q-carbon after a certain applied electric field. This saturation region is marked as region II in the F-N plots. Such type of current saturation is also observed in high resistivity Si and Ge [36], wide bandgap In_2O_3 nanowires[37], and CNT emitters [38]. In accordance with the classical field emission model, the slope of the F-N plots can be determined by the combined parameter ($\varphi^{3/2}/\beta$), where φ is the workfunction of the Q-carbon emitter, and β is the field enhancement factor for the emitting spots. In those plots, this parameter varied between 22 $eV^{3/2}$ and 203 $eV^{3/2}$. The EFE current density increases with β or decreases with φ. The β is the ability of an EFE surface to enhance the local electric field at the emission spots. The β is normally expressed in terms of the ratio of local electric field (E_{local}) to the applied electric field (*E*), which justifies its association with the generation of

the local field rather than the applied field. At low electric field (region I) the EFE property mainly depends on the surface states of the Q-carbon structure. The F-N plots deviate from the linearity when the applied electric field is above a critical field value. The critical field values thus obtained are tabulated in table 11.1, which varies in-between 2.41 V/μm and 2.51 V/μm. We have explained this nonlinear behavior by an electronic model in our earlier work, where the surface potential barrier decreases with increasing applied electric field and hence the emission current density increases rapidly after a critical value of the applied electric field [3]. The field penetration surpasses the surface potential barrier at this critical value and lowers the barrier height tremendously for the electrons to overcome during the EFE process. Therefore, region II is the slow current variation region also termed as “saturation” region [39]. Although the operating voltage is an important parameter for different EFE related applications, the stability of emission current density and the durability of the emitter are also essential. Degradation of the emission performances can be evaluated by measuring the stability of the EFE current intensity with time at constant applied voltage.

11.4.4 Temperature dependence of field emission

We analyzed the temperature-dependent EFE characteristics of the Q-carbon composite structure. Studies have shown that in p-type semiconductors and in some highly resistive n-type semiconductors a highly resistive depletion zone is formed with the penetration of electric field at the surface of the emitter during EFE measurements [40]. Similar to the operation mechanism of a reverse biased diode, this depletion region limits the current flow and produces a saturation region. Therefore, region II in the F-N plot shows saturation behavior of the EFE device due to limited supply of carriers in the depletion region. Since the thermal generation of free charge carriers in the depletion zone strongly affects the supply of the charge carriers to the emitter

surface, this model predicts a strong dependence of the current density on operating temperature. Accordingly, we observed an increase in the emission current density (1.58 times at 2.65 V/μm applied electric field) with *in situ* heating of the Q-carbon composite sample from room temperature to 500K. In this region, the dependence of the EFE current density on temperature follows Arrhenius law, $J \sim exp(-E_a/kT)$, where E_a is the characteristic activation energy in the Q-carbon sample and k is the Boltzmann constant. At constant applied electric field (in the middle of region II) the $ln(J)$ vs. $1/kT$ demonstrates a linear behavior with slope equal to 0.032, which has been shown in Fig. 11.3 (g). This slope represents the thermal activation energy in eV during the electron emission tests of Q-carbon samples. We also observed a slight decrease in the activation energy with decrease of the applied electric field. The total difference of the activation energy (ΔE_a) in the Q-carbon composite sample at the beginning and the end of the region II is ~ 2 meV. The observed increase in the emission current density with temperature from Q-carbon field emitter is related to the interband states. These states might have small activation energy possibly due to the different energy levels in the band gap. At high temperature, the electrons from these states could be elevated to the conduction band due to the dependence of free carrier density on the thermal energy. Another possibility could be the emission of electrons towards the anode via vacuum medium directly from those interband states, however, the probability for this phenomenon to take place is less [41].

11.4.5 Stability analysis

(i) Stability over time: The stability experiments on a Q-carbon EFE device determine the reliability of the emission device and therefore the robustness of the emitter. We analyzed the stability of the Q-carbon field emitter by measuring the variation in the field emission current density as a function of time and at different temperatures. Fig. 11.4 (a) and (c) represent the time evolution of the emission current density from Q-carbon composite sample at different emission

current densities. The emission current density was found to be very stable even after 500 minutes of continuous operation, which is significantly superior to the EFE stability of many other carbon-based EFE devices [42]. In all the stability analyses the emission current fluctuations were less than 7%.

(ii) Stability at different current levels: Fig. 11.4 (a) represents the room-temperature current stability for three different field emission current densities at different applied electric fields. The current data was collected at every minute for more than 500 minutes. It can be observed that the fluctuation increases with increasing field emission current density. We fitted the Gaussian function in the distribution of current densities at different current levels, which has been shown in Fig. 11.4 (b). From this analysis, we obtained important parameters such as the mean value, standard deviation and FWHM (full width at half max) for the Q-carbon composite sample. These parameters along with the corresponding applied electric field are presented in table 11.2. We observed an increase in the standard deviation, ~5 times for the current density from 7.5 $\mu A/cm^2$ to 30.1 $\mu A/cm^2$, and broadening in the FWHM with increasing EFE current density. The field emission parameters obtained from this study implies better stability of the EFE current even at high level of current density.

(iii) Stability at different temperatures: We also analyzed the current histories of the Q-carbon field emitter device at different temperatures by studying the fluctuation behavior of the current density using the Gaussian function. Fig. 11.4 (c) presents the emission current density as a function of time at 300K, 400K and 500K under the constant applied electric field (2.64 V/μm). We fitted the Gaussian function in the distribution of field emission current densities, which gives us continuous probability distributions. Fig. 11.4 (d) shows the corresponding probability distribution plots. The mean value, standard deviation and FWHM for the Q-carbon field emitter

are important parameters, which have been extracted from the fitted curves. Table 11.2 summarizes the fitted values for comparison. It is evident from this study that the room-temperature field emission current density has less distribution compared to that at elevated temperatures. The FWHM broadens with temperature meaning that the current fluctuation increases with EFE operating temperature. The standard deviation from the Gaussian fitting profile also increases with temperature. Nevertheless from room-temperature to 500 K, the fluctuations in the current density are within the limit that can be considered as good for practical applications.

The relatively narrower field emission current distributions from the Q-carbon film during all the measurements imply the highly stable field emission characteristics along with no physical degradation over time of operation. At the end of this study, we examined the surface of the emitter by optical and electron microscopy to ensure structural stability and did not observe any physical damage. We also performed *I-V* tests before and after the EFE measurements. No significant variations in the *I-V* plots before and after the EFE tests also confirm the robustness of the Q-carbon sample during the electron emission process. The *I-V* plots before and after the EFE tests are shown in the supplementary information section.

11.4.6 Discussion

The excellent EFE stability in Q-carbon can be attributed to the unique bonding characteristics of this novel phase of carbon. One of the key mechanisms behind the field emission current fluctuations from carbon-based cold-cathodes is the adsorption of gaseous species onto the emitting surface. These types of contaminants can modify the local work function of carbon structures at the emitting surface, which may cause a change in the field emission current density over time. Due to its superior chemical inertness with high atomic packing fraction, the Q-carbon composite film is less susceptible to the adsorption of contaminant gases or other organic/inorganic

species [43]. Therefore only a small amount of change occurs in the work function (in the local regions) during the EFE tests over time, which has a negligible effect on the emission current density. Thus, the Q-carbon shows excellent stability during the field emission measurements with excellent lifetime of this emitter.

Similar to the polycrystalline diamond the composite structure presented in this work has sp^3 rich Q-carbon grains, which are surrounded by sp^2 rich grain boundaries (amorphous carbon). In the sp^3 rich Q-carbon composite structures, the sp^2 bonded carbon provides the percolation path, which helps to attain more current density during the EFE measurements. From the Raman analysis, it is confirmed that the Q-carbon consists of a small fraction of sp^2-bonded carbon atoms which are uniformly distributed among the highly packed sp^3-bonded carbon tetrahedron [43]. This unique structure of Q-carbon provides the necessary conduction to the free carriers inside the Q-carbon grains during the electron emission process. Since sp^3 bonded carbon structure usually exhibits very low or negative electron affinity, the electron in the Q-carbon face a very negligible potential barrier for emission and the Q-carbon device can emit electrons easily at a very low applied electric field. In fact, negative electron affinity for Q-carbon was established using Kelvin probe force microscopy in our earlier studies [27]. When an external electric field is applied, the large local electric field is generated around the sp^2-bonded amorphous carbon structure due to the termination of the field lines [44]. This helps to obtain efficient EFE devices from the Q-carbon composite structure, where sp^2 and sp^3-bondings play an important role in the complementary process. The optimum amount of sp^2 and sp^3 bonding in the Q-carbon as well as in surrounding amorphous carbon structure are needed for efficient field emission from the Q-carbon based field emitter device. Due to the high thermal conductivity, the sp^3 rich grains act as a heat sink and help to maintain an efficient EFE process. Additionally, the distribution of sp^2 carbon in sp^3 matrix

creates a dielectric inhomogeneity, which enhances the field enhancement factor [45]. Furthermore, the energy levels of the sp^2 carbon are located close to the Fermi level of the material and raise the Fermi level towards the conduction band. Thus the presence of uniformly distributed sp^2 carbon reduces the work-function and thereby helps to obtain good EFE properties of the Q-carbon composite structure [46,47]. Earlier we investigated the correlation between excellent EFE properties and morphology of Q-carbon composite structure [3]. The electron emission from Q-carbon grains is explained by a band diagram model where we proposed the modification in the electronic states at the surface of Q-carbon under the presence of an applied electric field. The observed increase in current density and the decrease in turn-on field in Q-carbon field emitter with temperature could be due to the further modification in the electronic structures, such as the activation of acceptor-like levels or impurity levels which facilitate the transportation of electrons through sp^3-bonds. This could be one of the predominant factors affecting the EFE characteristics due to the change in temperature of the emitter. Moreover, the optimum sp^3-to-sp^2 ratio is also another important factor, which is explained as follows [42]. In Q-carbon the sp^3 bonded C tetrahedra confers the low or negative electron affinity of diamond and also a physical and chemical inertness, which are pre-requisite for field emission display applications [48]. The excess amount of sp^2 bonded C, which provides the conduction pathway to the electrons, reduces the enhanced properties of the sp^3 rich structure for the EFE. Therefore, maintaining an optimum sp^3/sp^2 ratio is very crucial in an EFE device, which seems to be present in the Q-carbon structure. A preliminary FESEM study of the samples after the high-temperature EFE experiments did not reveal any noticeable structural change. At the same time, we cannot rule out a minor change due to the rise in temperature that causes electrical property change leading to better field emission properties. Raman spectroscopy was employed to characterize the microstructure changes of the

Q-carbon composite structure after the temperature-dependent studies. No appreciable changes in the position of the D band and G bands and the ratio between these two peak intensities were observed, implying a highly stable microstructural feature of Q-carbon.

11.5 Summary

Detailed microstructural analysis and field emission current stability measurements have been carried out for the Q-carbon composite sample fabricated by PLA of amorphous carbon thin film. The characteristics of the emission current from the Q-carbon cold-cathode at different current levels over a long time have been studied. It is found that the fluctuation in emission current density increases with increasing current density level. The effect of the operating temperature on the stability of the EFE current density has also been investigated. Particularly the current in the saturation region has been found to be sensitive to temperature and increased by ~58% with temperature from 300 K to 500 K. This was attributed to the interband defect levels. Along with the excellent emission stability, the Q-carbon composite structure demonstrates outstanding thermal sensitivity during EFE tests, which can open new frontiers for applications in sensor and heat controlled electron sources. The fundamental study reported here improves our understanding of electron emission from Q-carbon, and can thus serve as a platform to understand other important characteristics of Q-carbon field emitters for display device application.

Table 11. 1**:** Field enhancement factor in the temperature range from 300K to 500K.

Temperature, K	Critical field (V/μm)	Maximum current density ($\mu A/cm^2$)	β (region-I)	β (region-II)
300	2.51	31.62	2936	290
350	2.48	36.8	1724	220
400	2.41	42.9	1090	237
450	2.44	46.1	1193	244
500	2.43	53.1	1160	333

Table 11. 2**:** Mean, standard deviation and FWHM obtained from the Gaussian fitting of the Q-carbon EFE data.

Operating conditions	Mean ($\mu A/cm^2$)	Standard deviation ($\mu A/cm^2$)	FWHM ($\mu A/cm^2$)	Operating conditions	Mean ($\mu A/cm^2$)	Standard deviation	FWHM ($\mu A/cm^2$)
2.6 V/µm at 300K	30.1	0.68	0.76	2.6 V/µm at 300K	30.1	0.68	0.76
V/µm at 300K	15.05	0.37	0.51	2.6 V/µm at 400K	37.05	0.94	1.38
V/µm at 300K	7.5	0.14	0.17	2.6 V/µm at 500K	47.2	1.37	2.12

11.6 Figures

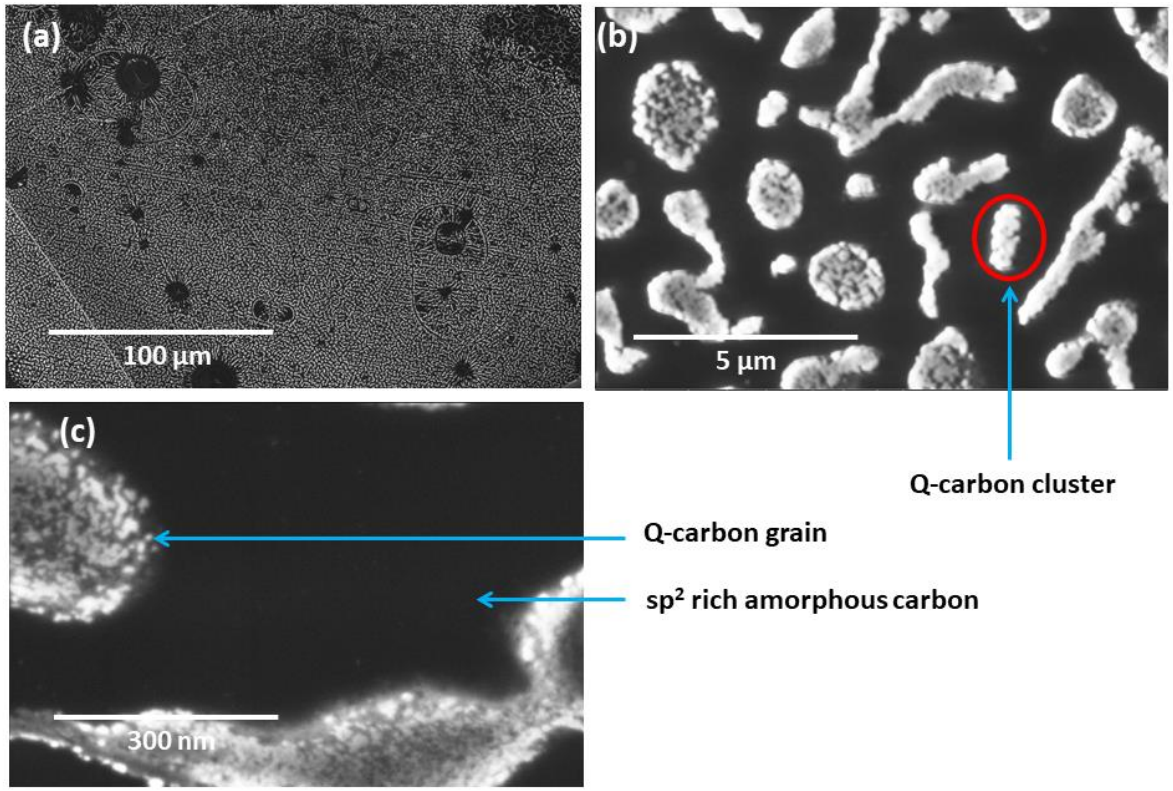

Figure 11. 1**:** (a) Large area Q-carbon composite film on c-sapphire substrate. (b) Shows the Q-carbon clusters and the amorphous carbon in-between the clusters. (c) High magnification image of the Q-carbon composite structure showing individual Q-carbon grains in a cluster.

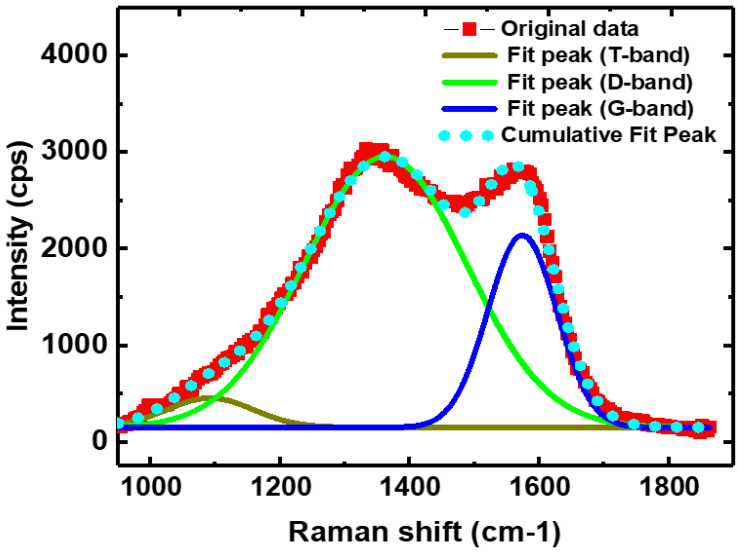

Figure 11. 2**:** Raman spectrum of Q-carbon.

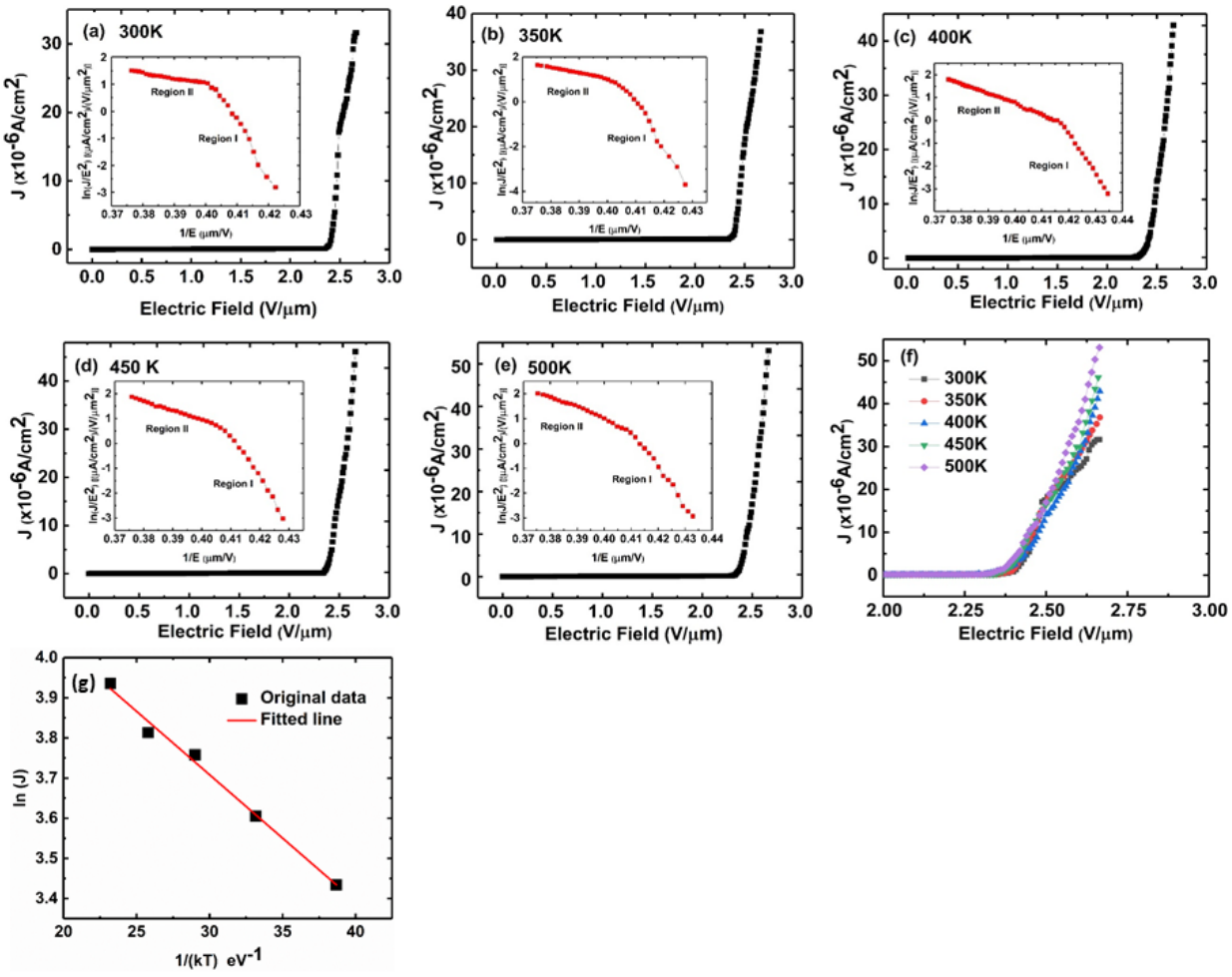

Figure 11. 3**:** The field emission current density vs. applied electric field plots at (a) 300K, (b) 350K, (c) 400K, (d) 450K, and (e) 500 K. Inset in figures (a) - (e) represent the F-N plots of the corresponding EFE data. (f) Shows the field emission current density vs. applied electric field plots in the same frame measured at 5 different operating temperatures. (g) *Arrhenius plot* of the of the EFE current density for the Q-carbon field emitter. The solid line is the linear approximations of the experimental points obtained at different temperatures under a constant applied electric field.

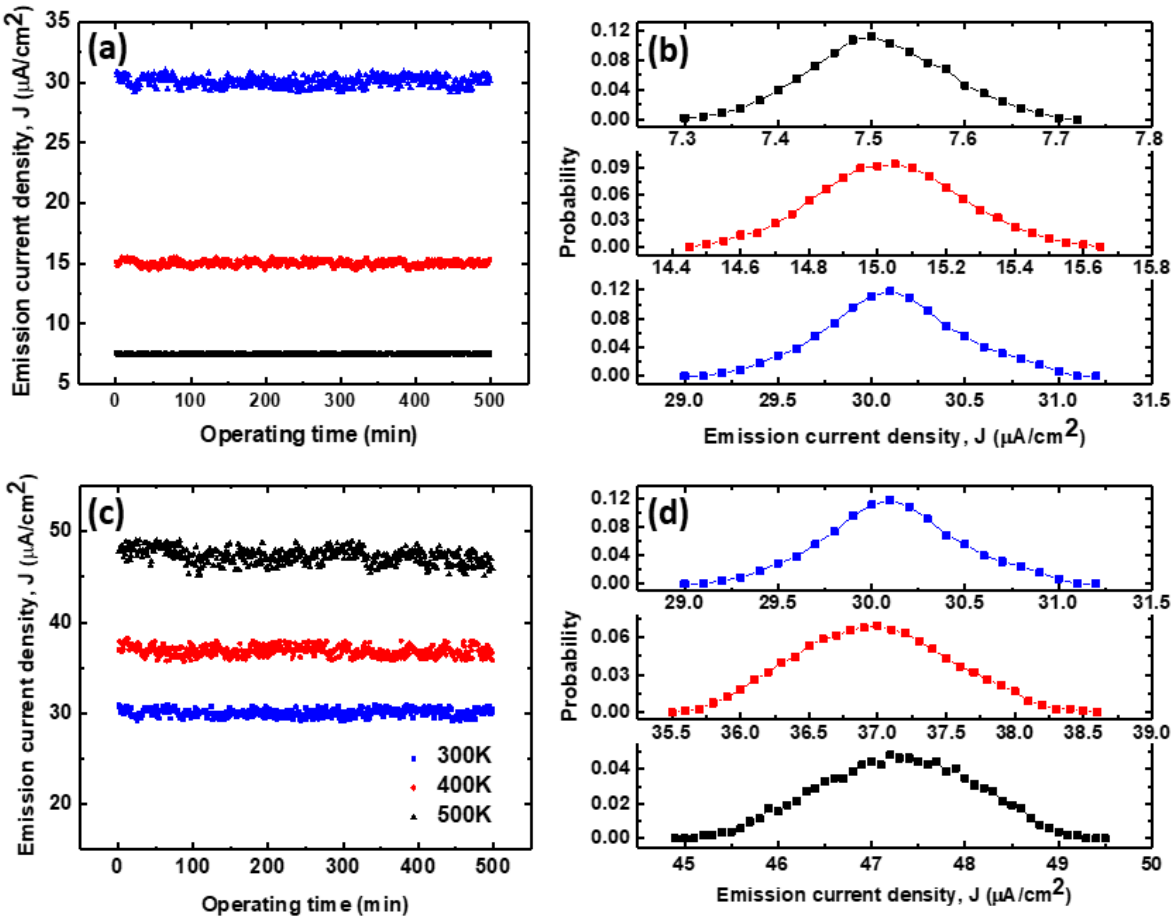

Figure 11. 4**:** (a) Room-temperature emission current densities as a function of time. (b) Probability distribution of corresponding emission current densities fitted by Gaussian function. (c) Emission current densities at 2.64 V/μm under different operating temperatures (300 K, 400K and 500K) as a function of time. (d) Probability distribution of corresponding emission current densities fitted by Gaussian function.

References

[1] S. Itoh, M. Tanaka, T. Tonegawa, Development of field emission displays, J. Vac. Sci. Technol. B Microelectron. Nanometer Struct. Process. Meas. Phenom. 22 (2004) 1362–1366. https://doi.org/10.1116/1.1691409.

[2] A.A. Talin, K.A. Dean, J.E. Jaskie, Field emission displays: a critical review, Solid-State Electron. 45 (2001) 963–976. https://doi.org/10.1016/S0038-1101(00)00279-3.

[3] A. Haque, J. Narayan, Electron field emission from Q-carbon, Diam. Relat. Mater. 86 (2018) 71–78. https://doi.org/10.1016/j.diamond.2018.04.008.

[4] E. Manikandan, J. Kennedy, G. Kavitha, K. Kaviyarasu, M. Maaza, B.K. Panigrahi, U.K. Mudali, Hybrid nanostructured thin-films by PLD for enhanced field emission performance for radiation micro-nano dosimetry applications, J. Alloys Compd. 647 (n.d.) 141–145.

[5] J. van der Weide, Z. Zhang, P.K. Baumann, M.G. Wensell, J. Bernholc, R.J. Nemanich, Negative-electron-affinity effects on the diamond (100) surface, Phys. Rev. B. 50 (1994) 5803–5806. https://doi.org/10.1103/PhysRevB.50.5803.

[6] J.B. Cui, J. Ristein, L. Ley, Electron Affinity of the Bare and Hydrogen Covered Single Crystal Diamond (111) Surface, Phys. Rev. Lett. 81 (1998) 429–432. https://doi.org/10.1103/PhysRevLett.81.429.

[7] R.L. Harniman, O.J.L. Fox, W. Janssen, S. Drijkoningen, K. Haenen, P.W. May, Direct observation of electron emission from grain boundaries in CVD diamond by PeakForce-controlled tunnelling atomic force microscopy, Carbon. 94 (2015) 386–395. https://doi.org/10.1016/j.carbon.2015.06.082.

[8] J.W. Glesener, A.A. Morrish, Investigation of the temperature dependence of the field emission current of polycrystalline diamond films, Appl. Phys. Lett. 69 (1996) 785–787. https://doi.org/10.1063/1.117891.

[9] O. Chubenko, S.S. Baturin, K.K. Kovi, A.V. Sumant, S.V. Baryshev, Locally Resolved Electron Emission Area and Unified View of Field Emission from Ultrananocrystalline Diamond Films, ACS Appl. Mater. Interfaces. 9 (2017) 33229–33237. https://doi.org/10.1021/acsami.7b07062.

[10] K. Okano, S. Koizumi, S.R.P. Silva, G.A.J. Amaratunga, Low-threshold cold cathodes made of nitrogen-doped chemical-vapour-deposited diamond, Nature. 381 (1996) 140–141. https://doi.org/10.1038/381140a0.

[11] W. Zhu, G.P. Kochanski, S. Jin, Low-Field Electron Emission from Undoped Nanostructured Diamond, Science. 282 (1998) 1471–1473. https://doi.org/10.1126/science.282.5393.1471.

[12] High Voltage Vacuum Insulation: Basic Concepts and Technological Practice, Elsevier, 1995.

[13] W.T. Diamond, New perspectives in vacuum high voltage insulation. I. The transition to field emission, J. Vac. Sci. Technol. A. 16 (1998) 707–719. https://doi.org/10.1116/1.581051.

[14] J. Robertson, Mechanisms of electron field emission from diamond, diamond-like carbon, and nanostructured carbon, J. Vac. Sci. Technol. B Microelectron. Nanometer Struct. Process. Meas. Phenom. 17 (1999) 659–665. https://doi.org/10.1116/1.590613.

[15] R. Isono, T. Tanimoto, Y. Iijima, S.A. Kusumawan, T. Harigai, Y. Suda, H. Takikawa, M. Kamiya, S. Kaneko, S. Kunitsugu, M. Taki, Improvement of adhesion of hydrogen-free DLC film by employing an interlayer of tungsten carbide, AIP Conf. Proc. 1929 (2018) 020019. https://doi.org/10.1063/1.5021932.

[16] A.A. Talin, T.E. Felter, T.A. Friedmann, J.P. Sullivan, M.P. Siegal, Electron field emission from amorphous tetrahedrally bonded carbon films, J. Vac. Sci. Technol. A. 14 (1996) 1719–1722. https://doi.org/10.1116/1.580326.

[17] O. Gröning, O.M. Küttel, E. Schaller, P. Gröning, L. Schlapbach, Vacuum arc discharges preceding high electron field emission from carbon films, Appl. Phys. Lett. 69 (1996) 476–478. https://doi.org/10.1063/1.118145.

[18] C.H.P. Poa, S.R.P. Silva, R.G. Lacerda, G. a. J. Amaratunga, W.I. Milne, F.C. Marques, Effects of applying stress on the electron field emission properties in amorphous carbon thin films, Appl. Phys. Lett. 86 (2005) 232102. https://doi.org/10.1063/1.1940129.

[19] K. Ghosh, M. Kumar, T. Maruyama, Y. Ando, Tailoring the field emission property of nitrogen-doped carbon nanotubes by controlling the graphitic/pyridinic substitution, Carbon. 48 (2010) 191–200. https://doi.org/10.1016/j.carbon.2009.09.003.

[20] J. Kennedy, F. Fang, J. Futter, J. Leveneur, P.P. Murmu, G.N. Panin, T.W. Kang, E. Manikandan, Synthesis and enhanced field emission of zinc oxide incorporated carbon nanotubes, Diam. Relat. Mater. 71 (2017) 79–84. https://doi.org/10.1016/j.diamond.2016.12.007.

[21] D. Das, R.N. Singh, A review of nucleation, growth and low temperature synthesis of diamond thin films, Int. Mater. Rev. 52 (2007) 29–64. https://doi.org/10.1179/174328007X160245.

[22] G.S. Bocharov, A.V. Eletskii, Theory of Carbon Nanotube (CNT)-Based Electron Field Emitters, Nanomaterials. 3 (2013) 393–442. https://doi.org/10.3390/nano3030393.

[23] D. Ye, S. Moussa, J.D. Ferguson, A.A. Baski, M.S. El-Shall, Highly Efficient Electron Field Emission from Graphene Oxide Sheets Supported by Nickel Nanotip Arrays, Nano Lett. 12 (2012) 1265–1268. https://doi.org/10.1021/nl203742s.

[24] E. Manikandan, G. Kavitha, J. Kennedy, Epitaxial zinc oxide, graphene oxide composite thin-films by laser technique for micro-Raman and enhanced field emission study, Ceram. Int. 40 (2014) 16065–16070. https://doi.org/10.1016/j.ceramint.2014.07.129.

[25] V.I. Kleshch, D.A. Bandurin, A.S. Orekhov, S.T. Purcell, A.N. Obraztsov, Edge field emission of large-area single layer graphene, Appl. Surf. Sci. 357 (2015) 1967–1974. https://doi.org/10.1016/j.apsusc.2015.09.160.

[26] S. Fujii, S. Honda, H. Machida, H. Kawai, K. Ishida, M. Katayama, H. Furuta, T. Hirao, K. Oura, Efficient field emission from an individual aligned carbon nanotube bundle enhanced by edge effect, Appl. Phys. Lett. 90 (2007) 153108. https://doi.org/10.1063/1.2721876.

[27] J. Narayan, A. Bhaumik, Novel phase of carbon, ferromagnetism, and conversion into diamond, J. Appl. Phys. 118 (2015) 215303. https://doi.org/10.1063/1.4936595.

[28] J. Narayan, A. Bhaumik, S. Gupta, A. Haque, R. Sachan, Progress in Q-carbon and related materials with extraordinary properties, Mater. Res. Lett. 6 (2018) 353–364. https://doi.org/10.1080/21663831.2018.1458753.

[29] A. Bhaumik, S. Nori, R. Sachan, S. Gupta, D. Kumar, A.K. Majumdar, J. Narayan, Room-Temperature Ferromagnetism and Extraordinary Hall Effect in Nanostructured Q-Carbon: Implications for Potential Spintronic Devices, ACS Appl. Nano Mater. 1 (2018) 807–819. https://doi.org/10.1021/acsanm.7b00253.

[30] F.Y. Chuang, C.Y. Sun, H.F. Cheng, C.M. Huang, I.N. Lin, Enhancement of electron emission efficiency of Mo tips by diamondlike carbon coatings, Appl. Phys. Lett. 68 (1996) 1666–1668. https://doi.org/10.1063/1.115899.

[31] A. Haque, J. Narayan, Electron field emission from Q-carbon, Diam. Relat. Mater. 86 (2018) 71–78. https://doi.org/10.1016/j.diamond.2018.04.008.

[32] V.L. Humphreys, J. Khachan, Spatial correlation of electron field emission sites with non-diamond carbon content in CVD diamond, Electron. Lett. 31 (1995) 1018–1019. https://doi.org/10.1049/el:19950698.

[33] C.-M. Lin, S.-J. Chang, M. Yokoyama, F.-Y. Chuang, C.-H. Tsai, W.-C. Wang, I.-N. Lin, Electron Field Emission Characteristics of Planar Field Emission Array with Diamondlike Carbon Electron Emitters, Jpn. J. Appl. Phys. 38 (1999) 890. https://doi.org/10.1143/JJAP.38.890.

[34] R. Stratton, Field Emission from Semiconductors, Proc. Phys. Soc. Sect. B. 68 (1955) 746. https://doi.org/10.1088/0370-1301/68/10/307.

[35] S.Q. Li, Y.X. Liang, T.H. Wang, Nonlinear characteristics of the Fowler–Nordheim plot for field emission from In2O3 nanowires grown on InAs substrate, Appl. Phys. Lett. 88 (2006) 053107. https://doi.org/10.1063/1.2159092.

[36] Borzyak P. G., Yatsenko A. F., Miroshnichenko L. S., Photo-Field-Emission from High-Resistance Silicon and Germanium, Phys. Status Solidi B. 14 (2006) 403–411. https://doi.org/10.1002/pssb.19660140218.

[37] S.Q. Li, Y.X. Liang, T.H. Wang, Nonlinear characteristics of the Fowler–Nordheim plot for field emission from In2O3 nanowires grown on InAs substrate, Appl. Phys. Lett. 88 (2006) 053107. https://doi.org/10.1063/1.2159092.

[38] S.C. Lim, H.J. Jeong, Y.M. Shin, K.S. Kim, W.S. Kim, Y.S. Park, Y.C. Choi, K.H. An, D.J. Bae, Y.H. Lee, Saturation of emission current from carbon nanotube field emission array, AIP Conf. Proc. 590 (2001) 221–224. https://doi.org/10.1063/1.1420094.

[39] G.N. Fursey, Field Emission in Vacuum Microelectronics, Springer US, New York, 2005. doi:10.1007/b139052.

[40] Baskin L. M., Lvov O. I., Fursey G. N., General features of field emission from semiconductors, Phys. Status Solidi B. 47 (2006) 49–62. https://doi.org/10.1002/pssb.2220470105.

[41] J. Chen, N.Y. Huang, X.W. Liu, S.Z. Deng, N.S. Xu, Analysis of the field-electron energy distribution from amorphous carbon-nitride films, J. Vac. Sci. Technol. B Microelectron. Nanometer Struct. Process. Meas. Phenom. 21 (2003) 567–570. https://doi.org/10.1116/1.1527599.

[42] F.Y. Chuang, C.Y. Sun, H.F. Cheng, C.M. Huang, I.N. Lin, Enhancement of electron emission efficiency of Mo tips by diamondlike carbon coatings, Appl. Phys. Lett. 68 (1996) 1666–1668. https://doi.org/10.1063/1.115899.

[43] J. Narayan, S. Gupta, A. Bhaumik, R. Sachan, F. Cellini, E. Riedo, Q-carbon harder than diamond, MRS Commun. (2018) 1–9. https://doi.org/10.1557/mrc.2018.35.

[44] J.D. Carey, R.D. Forrest, R.U.A. Khan, S.R.P. Silva, Influence of sp2 clusters on the field emission properties of amorphous carbon thin films, Appl. Phys. Lett. 77 (2000) 2006–2008. https://doi.org/10.1063/1.1312202.

[45] J.D. Carey, R.D. Forrest, S.R.P. Silva, Origin of electric field enhancement in field emission from amorphous carbon thin films, Appl. Phys. Lett. 78 (2001) 2339–2341. https://doi.org/10.1063/1.1366369.

[46] B.S. Satyanarayana, A. Hart, W.I. Milne, J. Robertson, Field emission from tetrahedral amorphous carbon, Diam. Relat. Mater. 7 (1998) 656–659. https://doi.org/10.1016/S0925-9635(97)00296-3.

[47] P.S. Guo, Z. Sun, S.M. Huang, Y. Sun, Temperature effect on field emission properties and microstructures of polymer-based carbon films, J. Appl. Phys. 98 (2005) 074906. https://doi.org/10.1063/1.2084310.

[48] J. Robertson, Electron affinity of carbon systems, Diam. Relat. Mater. 5 (1996) 797–801. https://doi.org/10.1016/0925-9635(95)00505-6.

[49] W.N. Wang, N.A. Fox, D. Richardson, G.M. Lynch, J.W. Steeds, Field emission properties of diode devices based on amorphic diamond-Si heterojunctions, J. Appl. Phys. 81 (1997) 1505–1508. https://doi.org/10.1063/1.363915.

Supplementary Information

Micro Raman analyses have been performed on the DLC film (before annealing) and the Q-carbon composite sample (formed after annealing) used for FE measurements. Fig. S11.1 (a) shows a Raman spectrum of the as deposited DLC film used to fabricate the Q-carbon composite structure. The Raman spectrum of the intermediate region in-between the Q-carbon clusters, amorphous carbon containing area, is shown in Fig. S11.1 (b). The Raman spectrum of the PLD target (graphite) is shown in Fig. S11.1 (c). The micro-Raman optical image of the Q-carbon composite film is shown in Fig. S11.1 (d). The dark spots in this image refer to the Q-carbon clusters.

The stable and persistent EFE current density obtained from Q-carbon over a long period of time supports the robust nature of Q-carbon under high applied electric field. In the porous amorphic diamond field emitters, researchers observed field induced damages during the EFE tests [49]. They also observed a change in the electrical properties of the emitter after the test. The room-temperature *I-V* characteristics of amorphic diamond films were different before and after the field emission test. Fig. S11.2 shows almost no change in the room temperature *I-V* characteristics of Q-carbon sample before and after the EFE measurements in the voltage range in-between -10V and 10V, which implies that no field induced damage occurred in the Q-carbon sample.

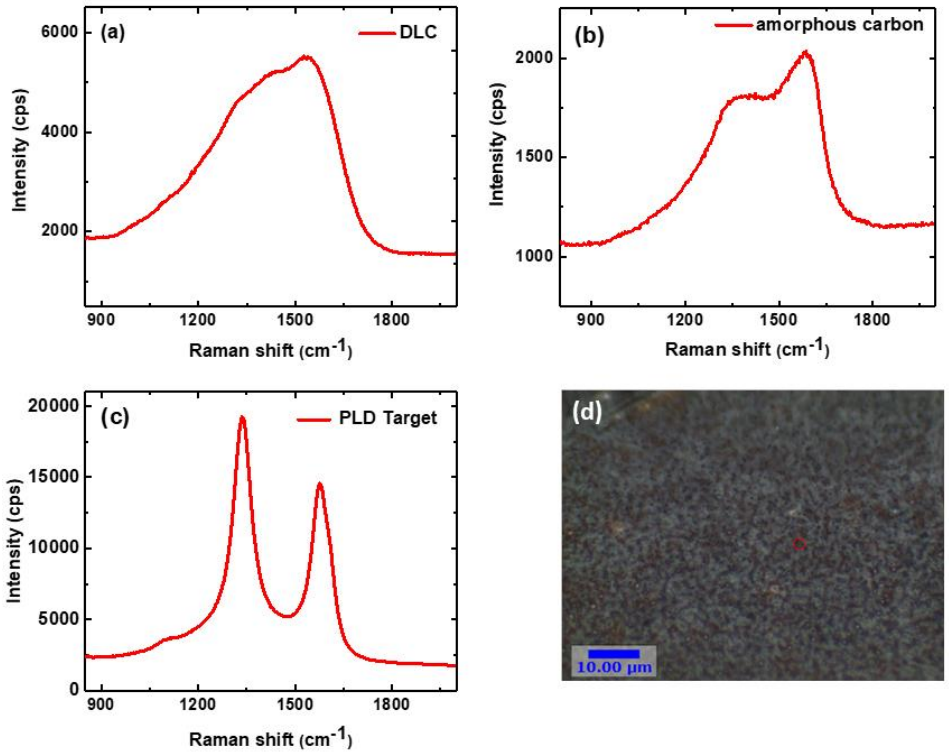

Figure S11.1: Raman spectra of (a) the DLC film (before laser annealing), (b) amorphous carbon region in-between the Q-carbon clusters after laser annealing, (c) graphite target used for PLD, and (d) presents the micro-Raman optical image of the Q-carbon composite film.

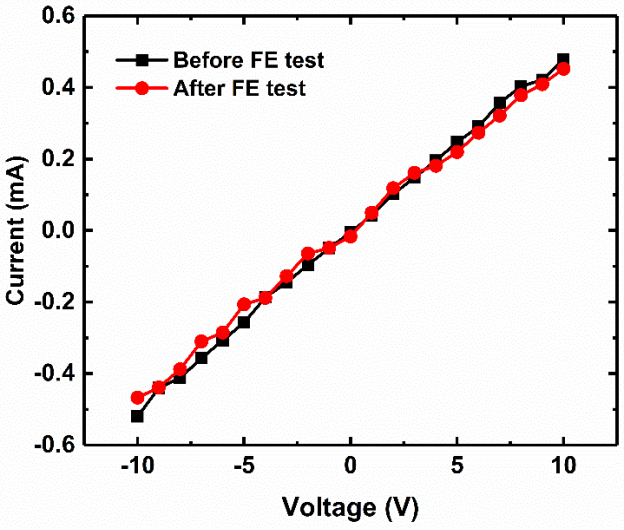

Figure S11.2: *I-V* plots before and after EFE tests on the Q-carbon composite sample.

12. Conclusions

In this study, I have investigated the fabrication processes, characterization, structural property correlation, and applications of Q-carbon and diamond with emphasizes in the magnificent field emission characteristics and improved electrocatalytic properties. Different carbon-based structures, in particular Q-carbon and diamond, have demonstrated immense potential to meet the demands of next generation field emission displays and devices. The transformation of one phase of carbon to another is subject to an important investigation from the economical and scientific point of view which has been addressed in detail in this work. By controlling the nucleation and growth processes from the liquid phase of carbon (mainly sp^2 rich), we can control formation of defects and create diamond structures with reduced defect density. This is a very important consideration in diamond fabrication as defect annealing temperatures exceed 1700° C, above which high pressure is needed to stabilize diamond and anneal out defects. Such high temperatures and pressures needed for annealing defects in diamond render CVD grown diamonds unsuitable for the fabrication of solid-state devices. Upon laser annealing, the laser fluence and laser-CNT or laser-CNF interaction dictates the melt penetration and temperature, and hence the size of the diamond crystals on the tips and bends of CNTs/CNFs. This liquid phase mediated growth leads to the direct bonding characteristics between the CNT and diamond which will facilitate to obtain improved electron field emission efficiency due to low interfacial resistance, fabricate high load bearing capacity hybrids, etc. Moreover, with increasing the number of nanosecond laser pulses, the entire CNT and CNF can be converted into diamond nanorods. We have shown that the first laser pulse converts tips of nanofibers and nanotubes into diamond, and subsequent laser pulses subsequently convert the rest of the carbon structures, while not affecting already formed diamond. With different complementary characterization techniques we have shown that our evidences are

sufficient to prove the conversion of CNTs and CNFs into nanodiamond structures by nanosecond pulsed laser annealing through the first order phase transformation. Analogous diamond formation was conducted previously by laser annealing of amorphous carbon thin film consisting sp^2 and sp^3-bonded carbon on different substrates. However, the proposed process is novel in a way that the CNTs mainly consist of sp^2 bonded carbon and they have completely different thermal and optical properties compared to the amorphous carbon film. The mechanism for forming the cubic diamond nanostructures (via the non-equilibrium route) at the tips and bends along the radial directions of CNTs is also studied by detailed electron microscopy, SLIM, and MD simulations. This highly nonequilibrium phase transformation is ideal for the formation of single crystal diamond and this single crystal diamond can be doped with dopants of both p and n-types at doping concentration far greater than the thermodynamic solubility limit owing to the liquid phase mediated growth. Single crystal diamond with such high level of doping concentration has several exciting applications, i.e. high-temperature superconductivity, power electronics, and efficient field emission devices. Attaining such high doping concentration (otherwise impossible to realize) in single crystal diamond is only possible by this novel discovery of the controlled, direct, ultrafast, and non-equilibrium transformation of carbon into diamond. The present synthesis of diamond from CNT is unique for obtaining single crystal diamond topped CNTs having distinct size, shape and aspect ratio for novel solid-state devices, high-efficiency field emitters, drug delivery, optoelectronics, and cellular- and bio-sensors. Moreover, the diamond and CNT have attracted extensive interest in recent years because of their unique quantum properties and potential applications as nanoconnectors and nanoscale devices. Especially the non-equilibrium conversion of diamond from graphitic phases has tremendous implication due to its considerable scientific and industrial importance.

Furthermore, we established a novel laser method for enhancing the nucleation and for improving the quality of diamond films on optically transparent c-Al_2O_3 substrate deposited by HFCVD. We have found that the DLC tetrahedra act as nuclei for diamond growth, their number density determines the areal coverage of grown diamond crystals. The average size of diamond crystallites on DLC and Q-carbon is found to be the same (~5 μm), which is somewhat larger than on bare Al_2O_3. From our observation, we have concluded that diamond crystallites grow on DLC tetrahedra whose density is much higher in Q-carbon than DLC films. The smaller size on bare Al_2O_3 is related to incubation period needed to form DLC tetrahedra during HFCVD, which provide nucleation sites for diamond growth. Although the diamond thin films on uncoated sapphire using the HFCVD process does not show any peak splitting, the XRD and Raman analysis shows a considerable amount of in-plane compressive stress. A possible approach to overcome the generation of stress in the diamond film on sapphire is the utilization of an interlayer. The feasibility of Q-carbon as an interlayer has been demonstrated in this study and compared with DLC interlayer. The critical nucleation and growth related results obtained in this work are described as follow: (1) The nucleation and growth of diamond crystals and films by the HFCVD method are found to be strongly related to the nature of the substrate surface on which diamond synthesis is performed. (2) A DLC interlayer on sapphire results in dramatic changes in the nucleation density and the morphology of the subsequently deposited diamond. However, this layer itself is not sufficient to yield a continuous diamond thin film over the entire sapphire substrate. (3) The use of a Q-carbon layer for nucleation enhancement has been shown to increase nucleation density by several orders of magnitude and thus we have been able to produce large area diamond thin film on the entire sapphire substrate after 6 hours HFCVD. (4) The improvement in adhesion is also accomplished owing to the liquid phase mediated growth of diamond tetrahedra

in the Q-carbon on which the diamond nucleation and growth take place. (5) Furthermore, the formation of a carbide layer is not necessary in attaining the beneficial effects of carbon pretreatment on diamond nucleation. It is envisaged that the diamond tetrahedra present in the amorphous Q-carbon layer provide nucleation sites for diamond growth on which the large diamond crystallites grew. The improved diamond nucleation and growth of continuous diamond film on Q-carbon/sapphire not only develop our understanding on diamond growth on substrates with no affinity to the formation of carbide but also it will help to realize many machine, tool and infrared window related practical applications. In fact, diamond has been promoted as the 'ultimate' optical material, however, the limiting factors must be taken into consideration to realize its practical applications.

Furthermore, various novel diamond microstructures with high diamond quality have been prepared from low-cost amorphous and graphitic carbon materials by HFCVD. Carbon microfibers, porous carbon and CNT hollow fibers are effective for promoting diamond nucleation and growth during HFCVD, which can be further accelerated by laser annealing. The structures of the prepared diamond are dependent on the type of carbon precursors and laser annealing treatment. Diamond microfibers, consist of fivefold diamond twin microcrystallites, are obtained from carbon microfibers by HFCVD. By multi-pulse laser annealing of carbon microfibers, the morphology changes to large diamond microspheres, which is also composed of fivefold diamond twins. A dense and phase-pure diamond film is synthesized from porous carbon, while diamond tube with porous structure is obtained from CNT hollow fibers. The methods presented here for novel structured diamond preparation and morphology control is simple and cost-effective, which will open a new frontier towards better design and understanding of diamond growth with desired nano-/microstructures and high quality for a variety of applications. In addition to that, three

dimensional diamond tubes with porous nano and microstructures have been prepared by a simple and cost-effective method which combines PLA with HFCVD. The CNT hollow fibers provide nucleation sites to accelerate the diamond growth. Diamond microspheres composed of high quality diamond microcrystallites and nanocrystallites are observed on the entire tube even inside the tube wall. The diamond density, microsphere size and nanocrystallite content are significantly increased with increasing HFCVD time and laser pulses. These diamond tubes have high double layer capacitances, which are found to be dependent on the density of the diamond spheres, the porous tubular structure, nanocrystallite content and the quality of diamond. Its electroactive surface area is three orders of magnitude higher than flat diamond film. This effective method for the synthesis of diamond tubes having large surface area makes it an ideal candidate for electrochemical applications such as electrocatalysis, electrosynthesis, electroanalysis, energy storage and conversion.

In this study, we have also demonstrated a simple and low-cost approach for the large-scale synthesis of Q-carbon nano-composite films with excellent FE performances, which could be used in the future cold cathode based electronic devices. After studying and comparing the emission properties of carbon-based field emitters one can determine how the characteristics of emission are affected by the structural characteristics, localized states, and field penetration which depends on the electrical conductivity of the emitters, on the presence of adsorbed/bonded species and on the polarizability of the structure. The present challenges to the commercialization of carbon based field emitters are the uniformity in the field emission, reliability and material lifetime. Some other major drawbacks of many of the carbon-based field emitters are instability under high applied electric field, short lifetime at high current density, complex and expensive fabrication process, poor field emission uniformity from the surface of the emitter, and pixel-to-pixel inconsistency.

This is due to the reason that fundamental understanding of the field emission properties of these materials is far from complete. Therefore a rationale is someway required between the field emission properties, on one part, and chemical, structural, morphological and electronic properties of the carbon nanostructures on another part. In order to obtain low turn-on and threshold fields, a high enhancement factor and good emission stability, most of the researches mainly have devoted their efforts on optimizing the properties of field emitters such as tailoring the morphology structure, modulating work function and/or tuning relative orientation of the carbon sheets with respect to the substrate and anode. However little efforts had been devoted to investigate the other aspects of carbon-based materials such as tailoring the density of states near the Fermi level, changing the mass density or tuning the sp^3/sp^2 ratio and other electronic properties. The large scale and uniform Q-carbon nano-composite films were fabricated on transparent r-cut Al_2O_3 substrates at room temperature by successive PLD and PLA processes, and the transparency of the substrate adds beneficial features for display device applications. The Q-carbon field emitters show very low turn-on electric fields and very stable electron emissions up to 500K. The emission current density of the Q-carbon field emitters can be controlled by the applied field and it also depends on the operation temperature. Two regimes were inferred from the F-N linearizations and fitting analyses, each corresponds to a distinct field enhancement factor which varies with temperature. The highly efficient and stable field emission performance is attributed to the enhanced electron conductivity owing to the optimum sp^3/sp^2 ratio, enhancement in the local electric field owing to the large field enhancement factors, and highly stable structure which is unperturbed at high applied electric field, temperature, and most importantly during the high-density electron emission. Furthermore, the outstanding field emission properties can also be attributed to the sp^2-bonded carbon atoms with their corresponding midgap states in the sp^3 carbon

rich Q-carbon and enhancement of the spatial conductivity in the surrounding amorphous carbon region due to the sp^2 carbon rich network. These analyses and findings certainly have advanced the understanding of the field-emission mechanisms that occur in such nanostructured Q-carbon composite and/or electrical heterogeneous systems.